

The production of metal-organic frameworks by micro-fluidic synthesis

Tom William Bailey

Submitted in accordance with the requirements for the
degree of *Doctor of Philosophy*

The University of Leeds

School of Chemical and Process Engineering

September 2023

Intellectual Property and Publication Statements

The candidate confirms that the work submitted is his own, except where work which has formed part of jointly authored publications has been included. The contribution of the candidate and the other authors to this work has been explicitly indicated below. The candidate confirms that appropriate credit has been given within the thesis where reference has been made to the work of others.

Chapters 4, 5,6 and 7 are comprised of jointly authored material. The details for each of these works and the authors contributions are summarised below. An overall thesis summary is provided in Chapter 1.6.

Chapter 4: Continuous microfluidic synthesis of zirconium-based UiO-67 using a coiled flow inverter reactor, *Tom Bailey, Merwyn Pinto, Nicole Hondow, Ke-Jun Wu*, Published in *MethodsX* in January 2021

Tom Bailey performed the synthesis and characterisation of the materials discussed, alongside building the reactor. AutoCAD work was performed by Merwyn Pinto to generate the images shown in the article. Work was supervised by Nicole Hondow and Ke-Jun Wu.

Chapter 5: The controlled microfluidic formation of stable mixed phase HCP/FCC-UiO-67(Zr)-Benzoic acid through modification of water concentration, *Tom Bailey, Lina Yang, Eleanor Humphreys, Faye Esat, Ben Douglas, Nicole Hondow*, Published in *Journal of Porous Materials* in September 2023.

Tom Bailey performed the majority of synthesis and characterisation within this article. Lina Yang assisted in some synthesis, alongside Eleanor Humphreys. Faye Esat assisted in the XRD of the synthesis products. Ben Douglas assisted with the N₂ isotherm analysis in this work. Nicole Hondow assisted in the TEM analysis while also supervising the overall project.

Chapter 6: Attempts at microfluidic synthesis of UiO-67 with incorporated Pd nanoparticles, *Tom Bailey, Dario Fernandez Ainaga, Andrew Britton, Nicole Hondow*, Submitted to Journal of Porous materials in September 2023

Tom Bailey performed all synthesis and analysis on the products. Dario Fernandez Ainaga assisted in the TEM and EDX analysis of the synthesis products. Andrew Britton assisted in the XPS analysis. Nicole Hondow also assisted in the TEM and the EDX, alongside supervising this work.

Chapter 7: Gradient boosted machine learning model to predict H₂, CH₄ and CO₂ uptake in metal organic frameworks using experimental data, *Tom Bailey, Adam Jackson, Razvan-Antonio Berbece, Kejun Wu, Nicole Hondow, Elaine Martin*, Published in Journal of Chemical Information and Modelling in July 2023

Tom Bailey performed most modelling, modelling refinement, alongside recalculation of any literature values where necessary. Adam Jackson performed most of the database collection, with Tom Bailey assisting to collect further data. Razvan-Antonio Berbece assisted in the modelling and model refinement. Kejun Wu and Nicole Hondow supported this project through supervision. Elaine Martin assisted in the creation and testing of the final model, including principle component analysis, alongside supervision of the project.

This copy has been supplied on the understanding that it is copyright material and that no quotation from the thesis may be published without proper acknowledgement.

The right of Tom William Bailey to be identified as Author of this work has been asserted by Tom William Bailey in accordance with the Copyright, Designs and Patents Act 1988

Acknowledgments

There are a wide range of people I would like to thank for helping me throughout my PhD, both professionally and non-professionally.

I would firstly like to thank my supervisor, Dr Nicole Hondow, for all her help throughout my PhD, be it assistance with the scientific side, such as talking through my work and helping with electron microscope characterisation, or on the non-scientific side, by making sure I was doing okay and reassuring me that I was on track. This thesis would not have been possible without her and I'm so grateful for her taking me on when I would have been left without a supervisor.

I would like to thank a wide range of researchers/lecturers/technicians, who without their expertise and assistance, much of my work would not have been possible. These include Elaine Martin, for her extensive help in the computational side of my work, Ben Douglas, who assisted with all the gas isotherm data collected, and Faye Esat, who's expertise in X-Ray Diffraction was necessary for much of the analysis present in the work.

I would like to thank the EPSRC for funding this project and allowing me the freedom to direct the research in the directions I felt most strongly about.

Alongside the scientific help, there are many people who helped throughout my thesis that I will thank here. I'd like to thank my parents, for supporting me so much throughout my work. Living back at home for the last year of my project helped greatly and allowed me to focus purely on my work, which I appreciate massively.

I'd like to thank a wide variety of friends here: Joe Gilbody, Ferdinand Otter-Sharp, Archie Vipani, Yasmine Sandholme, Theo Wilcocks, Tommy Parker, Asheleigh Buck, Mallika Rana, Rob Williamson, and so many different people in the Post Graduate Chemistry Society, with many I haven't mentioned, I'm sure. You all genuinely wanted to know how my work was going and how I was doing mentally. Your support has made this work far easier than it could have been.

Finally, I'd like to thank my girlfriend, Casey, for all her help in the last few months. The support and consideration for this last stretch have meant the world and I'm extremely grateful for all of it. Your understanding of my stresses and worries have helped me navigate through this period with relative ease and I only hope I can do the same when it comes time for you to submit your thesis.

Abstract

Metal-Organic Frameworks (MOFs), particularly Zirconium based UiO type MOFs, have been developed for a wide variety of applications in the past, such as gas storage and supporting catalysts. However, they are limited by traditionally being synthesised in long batch reactions, leading to high energy cost and potential batch to batch variations. Microfluidic synthesis can address these issues, as continuous flow reactors with increased mass/heat transfer, leading to reduced synthesis times and greater reaction control. Microfluidic synthesis has been used in this thesis to synthesise, modify, and investigate MOFs/UiO-67 in varying ways, presented in a papers format.

The first paper was published in *MethodsX* and describes the microfluidic synthesis of UiO-67 using a coiled flow inverter reactor. The second paper, published in the *Journal of Porous Materials*, describes how the crystal phase of UiO-67 can be controlled using water in the microfluidic reactor, resulting in a new product, HCP/FCC-UiO-67-Benzoic acid, being formed for the first time. The third paper, which has been submitted to the *Journal of Porous Materials*, describes the attempted microfluidic synthesis of Pd(0)-UiO-67-BPYDC and the several insights made on the complications present within this attempted synthesis. The final paper, which was published in the *Journal of Chemical Information and Modelling*, describes the formation of a machine learning model to predict the gravimetric uptake of several gasses (CO₂, CH₄ and H₂) in MOF materials at varying pressures and temperatures. This model was fitted using experimental literature uptake data and descriptors that could be acquired without pre done modelling, to form an accurate, flexible and easy to use model for a new researcher.

This project was a success, with novel research into MOF materials through a lens of microfluidics being produced and resulting in several publications. Specific results and conclusions have been formed in each publication alongside more overarching deductions on the effects of microfluidic synthesis on MOF materials. The insights formed within this thesis may be used in future research into MOF materials and the use of microfluidics for their synthesis.

Contents

Intellectual Property and Publication Statements	1
Acknowledgments.....	3
Abstract	4
Figures	11
Tables	18
Supplementary Figures	19
Supplementary Tables	21
Abbreviations.....	22
Chapter 1 Introduction.....	23
1.1 Metal-Organic Frameworks	23
1.2 Synthesis of MOFs.....	30
1.3 Microfluidic Reactors	31
1.4 Microfluidic Synthesis of MOFs.....	33
1.5 Gas Storage in MOFs.....	34
1.6 Machine Learning for MOFs	39
1.7 Aims	41
1.8 Thesis Summary.....	42
1.9 References.....	43
Chapter 2 Materials and Methods.....	49
2.1 Section overview.....	49
2.2 Microfluidic Reactors	49
2.3 Characterisation techniques	50

2.3.1 X-Ray Diffraction (XRD)	50
2.3.2 Gas Adsorption Isotherms	51
2.3.3 Electron Microscopy	52
2.3.4 X-ray Photoelectron Spectroscopy (XPS).....	53
2.4 Machine Learning methods.....	53
2.5 References.....	55
Chapter 3 MethodsX Journal Article, “Continuous microfluidic synthesis of zirconium-based UiO-67 using a coiled flow inverter reactor”, Published Jan 2021, https://doi.org/10.1016/j.mex.2021.101246	
3.1 Abstract	56
3.2 Graphical Abstract	57
3.3 Abbreviations	57
3.4 Background	58
3.5 Overview of the method.....	61
3.6 Materials	62
3.6.1 Chemicals.....	62
3.6.2 Equipment.....	62
3.7 Equipment Setup.....	63
3.7.1 Coiled Flow Inverter Reactor	63
3.7.2 Microfluidic connections	66
3.7.3 Slurry delivery system	68
3.7.4 Controlling the residence time	69
3.8 Experimental Procedure.....	70

3.9 Timing.....	71
3.10 Anticipated results.....	72
3.10.1 XRD Patterns	72
3.10.2 SEM Images.....	74
3.11 Declaration of interests:	75
3.12 References.....	76
Chapter 4 Journal of Porous Materials Article,” The controlled microfluidic formation of stable mixed phase HCP/FCC-UiO-67(Zr)-Benzoic acid through modification of water concentration”, Published September 2023, https://doi.org/10.1007/s10934-023-01513-4 ..	
4.1 Abstract.....	77
4.2 Introduction.....	77
4.3 Materials and Methods.....	83
4.3.1 Chemicals.....	83
4.3.2 Microfluidic synthesis of UiO-67 products.....	83
4.3.3 Traditional Batch synthesis of UiO-67 [Batch].....	84
4.3.4 Batch synthesis: 30 minutes, 140 °C, 60 equivalent water [Batch60eq].....	84
4.3.5 Characterisation	85
4.4 Results and Discussion	86
4.4.1 Structure analysis	86
4.4.2 Gas uptake.....	92
4.4.3 Difficulties present in this synthesis	99
4.5 Conclusions.....	102
4.6 Declarations	103

4.7 References.....	103
4.8 Supporting Information.....	105
Chapter 5 Journal of Porous Materials Article, “Attempts at microfluidic synthesis of UiO-67 with incorporated Pd nanoparticles”, Submitted September 2023.....	112
5.1 Abstract.....	112
5.2 Introduction.....	112
5.3 Materials and Methods.....	114
5.3.1 Materials	114
5.3.2 Microfluidic Reactor.....	115
5.3.3 Microfluidic synthesis of UiO-67-BPDC.....	115
5.3.4 Attempted Microfluidic synthesis of Pd@UiO-67-BPYDC	116
5.3.5 Attempted Batch Synthesis of Pd@UiO-67-BPYDC	116
5.3.6 Reduction of Pd(II)-UiO-67-BPYDC using NaBH ₄ /H ₂ O	117
5.3.7 Reduction of Pd(II)-UiO-67-BPYDC using NaBH ₄ /DMF.....	117
5.3.8 Reduction of Pd(II)-UiO-67-BPYDC using NaBH ₄ /DMF (increased reducing agent)	117
5.3.9 Reduction of Pd(II)-UiO-67-BPYDC using NaBH ₄ /DMF (increased solvent) .	117
5.3.10 Attempted Two Stage Batch synthesis of Pd(0)-UiO-67-BPYDC.....	118
5.3.11 Characterisation.....	118
5.4 Results and Discussion	119
5.4.1 Transfer of synthesis to microfluidics.....	119
5.4.2 Attempt to incorporate Pd(0) using microfluidic synthesis.....	121
5.4.3 Batch synthesis.....	126

5.4.4 Two stage batch synthesis	128
5.5 Conclusions.....	131
5.6 References.....	132
5.7 Supporting Information.....	133
Chapter 6 Journal of Chemical Information and Modelling Article, “Gradient boosted machine learning model to predict H ₂ , CH ₄ and CO ₂ uptake in metal organic frameworks using experimental data”, Published July 2023, https://doi.org/10.1021/acs.jcim.3c00135	136
6.1 Abstract.....	136
6.2 Introduction.....	137
6.3 Methods and materials	140
6.4 Results and discussion	143
6.5 Conclusions.....	151
6.6 References.....	152
6.7 Supporting Information.....	153
Table S 6.1 MOF structures with literature H ₂ uptakes.....	153
Table S 6.2 MOF structures with literature CH ₄ uptakes	161
Table S 6.3 MOF structures with literature CO ₂ uptakes	166
Table S 6.4 Individual coefficient of determination values for each fold in the 10 runs	176
Hyperparameters for other machine learning models	177
6.8 References for uptake data.....	178
Chapter 7 Overall Discussion and Future work	188
7.1 Progress achieved.....	188
7.2 Difficulties encountered in the research.....	189

7.3 Conclusions..... 191

7.4 Future Research 191

7.5 References..... 193

Figures

Figure 1.1: Number of papers relating to “UiO-66” each year since 2009. Data collected from WebOfScience on 25/07/2023.....	24
Figure 1.2: $[\text{Zr}_6(\text{OH})_4\text{O}_4]^{12+}$ SBU for UiO type MOFs with a generic carboxylic acid linker bonded on the right-hand side. Various linker lengths shown, with the corresponding MOF name given. Figure drawn using Chemdraw Prime 22.	25
Figure 1.3: a) Powder XRD patterns for UiO-67 synthesised using increasing amounts of benzoic acid. b) SEM image of 0 equivalent UiO-67 sample, c) SEM image of 3 equivalents UiO-67 sample, d) SEM image of 30 equivalents UiO-67 sample. Figure adapted from work by Shaate <i>et al.</i> ¹⁴	26
Figure 1.4: Varying crystal phases for UiO type MOFs with blue circles representing SBUs and the purple lines representing linker units. a) Face Centred Cubic (fcc) structure, b) ReO_3 (reo) structure, c) 2d representation of larger fcc structure, d) 2d representation of Hexagonal Centred Planar (hcp) structure.....	28
Figure 1.5: Basic schemes for laminar and turbulent flow patterns. Laminar flow shows a parallel flow pattern, with frictional forces on the tubing walls causing the flow rate to decrease in these areas. Mixing will only occur between these layers through diffusion. Turbulent flow shows a random flow pattern with different layers crossing and mixing throughout the tube. Frictional forces play less of an impact in the flow, as the layers are constantly crossing over and changing position in the tube.....	32
Figure 1.6: Scheme of Faustini <i>et al.</i> 's two-phase microfluidic droplet reactor. Figure adapted from Faustini <i>et al.</i> ⁷⁵	33
Figure 1.7: CO_2 absorption isotherms for various MOF materials at 298k. Figure adapted from work by Millward and Yaghi. ⁸⁴	35
Figure 1.8 Hydrogen adsorption isotherm for MOF-5 at A) 78 K and B) 298 K. Figure adapted from work by Rosi <i>et al.</i> ⁹²	37

Figure 1.9: Main Graph: Hydrogen Capacity for Mg and Mg/ZIF-67 in relation to cycle number. Inset Graph: Hydrogen desorption of Mg and Mg doped materials in relation to time, at 300 °C. Figure adapted from work by Wang <i>et al.</i> ⁹⁴	38
Figure 2.1: Basic schematic of a CFIR, highlighting the change in the centrifugal force direction when inverting the tubing by 90°. Coloured circles represent the centrifugal hotspots and their direction on each side of the CFIR. Orange dashed arrows show the direction of the centrifugal force on each side of the CFIR.	50
Figure 2.2: Scheme depicting the principle of XRD. X-rays (curved blue lines) hit the atoms (blue circles) at angle θ and are diffracted. The distance between the atom layers is given as d.	51
Figure 2.3 Scheme showing the general adsorption trends seen in a) Type I isotherms and b) Type IV isotherms.	52
Figure 3.1: Representation of a MOF structure, with SBUs and linker units highlighted	58
Figure 3.2: Basic reaction scheme for the synthesis of UiO-67	59
Figure 3.3: Schematic of protocol, showing the workflow from the syringe pump to the product.	62
Figure 3.4: Series of steps used to form the basic helix shape in AutoCAD.....	63
Figure 3.5: Wireframe CFIR structure, with the inlet/outlet corner highlighted.....	64
Figure 3.6: Sequence of AutoCAD steps used to sweep through the wireframe structure and form the 3D cylinders	64
Figure 3.7: (A) structure with circle swept through the helix wireframe, and (B) structure with the channel formed through the subtraction of the helical sweep through.....	65
Figure 3.8: (A) Structure with inlet/outlet lines swept through by the 1.6 mm circle, (B) Structure with these sweep throughs subtracted.	65
Figure 3.9: (A) Image highlighting the line drawn through the support square in the inlet/outlet corner, (B) Inlet/Outlet corner once the square has been swept through using this line.	66

- Figure 3.10** (A) The CFIR with tubing pressed through the corner inlet, (B) the CFIR with the tubing wrapped around 1 side, and (C) the fully completed CFIR with the tubing now pressed through the second corner hole. 67
- Figure 3.11** (A) Tubing with fitting and ferrule attached (B) Photo showing the syringe, luer adaptor and tubing with the ferrule now tightly attached. (C) Luer adaptor now screwed onto the end of the tubing. (D) Tubing now connected to the syringe. 67
- Figure 3.12:** (A) Syringe and magnet next to each-other, (B) Image showing syringe with plunger removed, (C) Image showing syringe with magnet placed inside. 68
- Figure 3.13:** Scheme showing the general setup for the slurry delivery system, with the grey rectangle representing the magnetic stirrer plate and the smaller grey cuboid representing the magnetic stirrer bar. 69
- Figure 3.14:** (Top to bottom) PXRD patterns for: Microfluidic synthesised UiO-67, Batch synthesised UiO-67 at 140 °C for 30 minutes, traditionally batch synthesised UiO-67 (24 hours, 120 °C), simulated UiO-67 performed by Vesta. All patterns are over $2\theta = 5 - 45^\circ$... 73
- Figure 3.15:** (A) SEM image for UiO-67 product formed through traditional 24 hours 120 °C batch process, (B) SEM image for UiO-67 product formed through microfluidic CFIR process. 74
- Figure 3.16:** SEM image for UiO-67 product from 30 minutes 140 °C batch synthesis..... 75
- Figure 4.1:** a) General 2D representation of face centred cubic (fcc) and hexagonal centred planar (hcp) structures. Blue circles represent SBU's and purple lines represent linkers. b) Crystal structure of FCC-UiO-67 unit cell, with polyhedra highlighted in green. c) Crystal structure of HCP-UiO-67, with double cluster structure visible. 80
- Figure 4.2** Simulated XRD patterns for a) HCP UiO-67 and b) FCC UiO-67. Patterns were simulated in VESTA. CIF for HCP is from Cliffe *et al*'s SI.¹⁹ CIF for the FCC pattern was obtained from the Cambridge Structural Database, from a paper by Goodenough *et al*²⁴.... 81
- Figure 4.3** XRD patterns for microfluidic UiO-67 products, with the equivalents of H₂O used varying from 0 to 60. Baseline was removed in Highscore using Sonneveld and Visser baseline reduction. 87

- Figure 4.4** HCP and FCC peak positions for microfluidically formed UiO-67, from 20-60 equivalents of water. 20 EQ sample only shows one clear peak, so the centre of this is listed as the HCP peak. 88
- Figure 4.5** XRD patterns for microfluidically synthesised HCP-UiO-67 using 60 equivalents H₂O (**MF60eq**), UiO-67 synthesised in a batch setting using similar reaction conditions to the microfluidic reaction (**Batch60eq**; 60 equivalents H₂O, 30 minutes heating, 140 °C) and FCC-UiO-67 synthesised using the traditional batch method (**Batch**; 0 equivalents of water, 24 hours heating, 120 °C). Key diffraction peaks for the HCP are highlighted at 4.0° 2θ (002) and 5.3° 2θ (100), and for FCC phase at 5.7° 2θ (111) and 6.6° 2θ (200). Baseline was removed in Highscore using Sonneveld and Visser baseline reduction. 90
- Figure 4.6** XRD pattern for **MF60eq** product. Hashed lines highlight areas corresponding to different diffraction peak contributions. Baseline was removed in Highscore using Sonneveld and Visser baseline reduction. 91
- Figure 4.7** Maximum quantity of N₂ adsorbed (cm³/g) vs the molar equivalents of water used in the microfluidic reaction 92
- Figure 4.8** N₂ isotherms for microfluidically synthesised HCP-UiO-67 using 60 equivalents H₂O (**MF60eq**), batch synthesised UiO-67 with 60 equivalents of H₂O (**Batch60eq**) and FCC-UiO-67 synthesised using the traditional batch method (**Batch**; 0 equivalents of water, 24 hours heating, 120 °C). Dashed lines are for N₂ desorption. 93
- Figure 4.9** Plot showing how BET, Microporous, Mesoporous and External Surface Area (m²/g) change with the increasing concentration of water in the reaction solution. BET surface area is calculated through Brunauer, Emmett and Teller (BET) calculations, with error bars shown for these. The microporous and external areas have been calculated using t-plot calculations. The mesoporous surface area has been calculated through Barrett, Joyner, and Halenda (BJH) adsorption calculations, giving the surface area for pores with diameters between 1.7 nm and 300 nm. Trendlines for each data set are present to guide the eye. 95
- Figure 4.10** XRD pattern for 3 on the day after the initial drying and 3 months after this point. Measured between 3° 2θ and 10° 2θ. Key diffraction peaks for the HCP are highlighted at 4.0°

2 θ (002) and 5.3° 2 θ (100), and for FCC phase at 5.7° 2 θ (111) and 6.6° 2 θ (200). Baseline was removed in Highscore using Sonneveld and Visser baseline reduction 98

Figure 4.11 XRD patterns for the 50 equivalent H₂O UiO-67 product and for the product formed under the same reaction conditions, except fouling was found to have been present in the reactor. Key diffraction peaks for the HCP are highlighted at 4.0° 2 θ (002) and 5.3° 2 θ (100), and for FCC phase at 5.7° 2 θ (111) and 6.6° 2 θ (200). Baseline was removed in Highscore using Sonneveld and Visser baseline reduction 100

Figure 4.12 XRD pattern for **MF60eq** when using 96 hours washing and for **MF60eq** when using 48 hours washing. Key diffraction peaks for the HCP are highlighted at 4.0° 2 θ (002) and 5.3° 2 θ (100), and for FCC phase at 5.7° 2 θ (111) and 6.6° 2 θ (200). Baseline was removed in Highscore using Sonneveld and Visser baseline reduction 101

Figure 5.1: Reaction scheme for the incorporation of Pd(0) nanoparticles into UiO-67, using the experimental procedure given by Chen *et al.*⁷ Scheme has been drawn in ChemDraw22. 113

Figure 5.2: XRD patterns for microfluidically synthesised UiO-67-BPDC under varying conditions with simulated patterns for both HCP and FCC phases. All microfluidic products have a residence time ~ 1 hour. a) Microfluidically produced UiO-67-BPDC, HCl volume = 0.5 ml. b) Microfluidically produced UiO-67-BPDC, HCl volume = 1.875 ml. c) Microfluidically produced UiO-67-BPDC, HCl volume = 4.5 ml. d) Simulated XRD pattern for HCP UiO-67-BPDC. Pattern was simulated in VESTA, using a CIF file obtained from Cliff *et al.*'s SI.¹⁶ e) Simulated XRD pattern for FCC UiO-67-BPDC. Pattern was simulated in VESTA, using a CIF file obtained from the Cambridge Structural Database, from a paper by Goodenough *et al.*¹⁷ Key diffraction peaks for the HCP are highlighted at 4.0° 2 θ (002) and 5.3° 2 θ (100), and for FCC phase at 5.7° 2 θ (111) and 6.6° 2 θ (200). Volumes of HCl are related to the specific experimental procedure used, when volume of DMF = 15 ml. 120

Figure 5.3: a) XRD pattern for microfluidically synthesised Pd(II)-UiO-67-BPYDC. b) HAADF STEM image of microfluidically synthesised Pd(II)-UiO-67-BPYDC. c) EDX map

for Pd present in microfluidically synthesised Pd(II)-UiO-67-BPYDC. d) EDX map for Zr present in microfluidically synthesised Pd(II)-UiO-67-BPYDC. 122

Figure 5.4: X-Ray Photoelectron Spectra for microfluidically formed Pd(II)-UiO-67-BPYDC products. a) XPS for microfluidically formed Pd(II)-UiO-67-BPYDC. b) XPS for microfluidically formed Pd(II)-UiO-67-BPYDC post reduction by NaBH₄/water. c) XPS for microfluidically formed Pd(II)-UiO-67-BPYDC post reduction by NaBH₄/DMF. Blue dashed lines correspond to Zr based signals, green dashed lines correspond to Pd²⁺ based signals. 123

Figure 5.5: a) TEM image of microfluidically synthesised Pd(II)-UiO-67-BPYDC post 24 hours heating in DMF, with Pd particles of 61 ± 11 nm. b) HAADF STEM image of a different area for the same material, with areas for EDX spectra highlighted. c) EDX spectrum for Area #1 with key peaks labelled with a high concentration of palladium labelled compared to d) EDX spectrum for Area #2 with key peaks labelled. 124

Figure 5.6: a) TEM image of batch synthesised Pd(II)-UiO-67-BPYDC. b) Higher magnification TEM image of batch synthesised Pd(II)-UiO-67-BPYDC. 126

Figure 5.7: X-ray photoelectron spectra for batch synthesised Pd(II)-UiO-67-BPYDC products. a) XPS for batch synthesised Pd(II)-UiO-67-BPYDC. b) XPS for batch synthesised Pd(II)-UiO-67-BPYDC post reduction by NaBH₄/DMF. c) XPS for waste collected from NaBH₄/DMF reduction of batch synthesised Pd(II)-UiO-67-BPYDC. 127

Figure 5.8: TEM image for solid found in the waste solution from the NaBH₄/DMF reduction of batch synthesised Pd(II)-UiO-67-BPYDC following separation of the MOF material... 128

Figure 5.9: a) TEM image of two stage batch synthesised Pd(II)-UiO-67-BPYDC with Pd nanoparticles of 21 ± 13 nm, EDX areas are highlighted. b) EDX spectrum taken over Area #1. c) EDX spectrum taken over Area #2. 129

Figure 5.10: a) STEM image of two stage batch synthesised Pd(II)-UiO-67-BPYDC. b) EDX map of Zr present in two stage batch synthesised Pd(II)-UiO-67-BPYDC. c) EDX map of Pd present in two stage batch synthesised Pd(II)-UiO-67-BPYDC, d) TEM image for two stage batch synthesised Pd(II)-UiO-67-BPYDC. The darker features in this TEM image are due to thickness effects. 130

Figure 6.1: Regression plots for the developed ML models a) linear model; b) SVM; c) DT model; d) GBDT model. Each plot uses the average predictions for each datapoint (over 10 runs) versus the real experimental wt% values found in literature. The black line is $y=x$, with the R^2 around this line calculated and shown in black text. The red line is a fitted line of best fit, with the R^2 for this shown in red text. 144

Figure 6.2. Estimated mean squared prediction error vs number of PLS components. The datapoint at 5 components has been highlighted. 148

Figure 6.3. Variable importance scores for each of the 51 descriptors. Those with a score > 0.5 are labelled and highlighted in red. 149

Tables

Table 5.1: BET surface area was calculated using several points in the adsorption isotherm. Microporous and External areas are given by the t-plot for each isotherm, with errors provided through the errors on the t-plot intercept and slope. Mesoporous surface area is calculated using the BJH method, giving the surface area for pores with diameters between 1.7 nm and 300 nm. Overall uptake and working capacity are given in cm ³ /g of N ₂ at standard pressure and temperature (STP). Working capacity is determined by the difference in uptakes from 0.1 to 1 bar.	95
Table 5.2: Average pore diameter (nm), Micropore Volume (cm ³ /g) and Mesoporous volume (cm ³ /g) for Batch , Batch60eq , MF60eq . Average pore diameter and Mesoporous volume are calculated by BJH adsorption. Micropore volume is calculated through the t-plot, with errors.	96
Table 6.1 A list of the descriptors used in the machine learning models.....	142
Table 6.2 R ₂ , Validation MSE (KFold Loss), MAE and MAPE for each of the machine learning models used.....	144
Table 6.3 Relative Standard Deviation (%) for R ² , KFold Loss, MAE and MAPE across the 10 runs.....	145
Table 6.4: Average MAE and Average MAPE when fitting data for each gas in the GBDT model, over 10 runs.....	146
Table 6.5 Comparison of R ₂ , Adjusted R ₂ , Kfold loss, average MAE, average MAPE when different combinations of primary building unit (PBU), secondary building unit (SBU) and physical conditions (PHYS) were used in the fitting of the GBDT model.	147
Table 6.6 R ² , Adjusted R ² , Kfold Loss, MAE and MAPE for GBDT models fitting using only the descriptors with VIPScores >1, VIPScores > 0.5 and fitting using all 51 descriptors. ...	150

Supplementary Figures

Figure S 4.1 TEM image (left) and FFT (middle) of MF60EQ product. The FFT is taken from the whole TEM image, with the red circles correspond to 14 angstrom spacings (which correspond to $7.2^\circ 2q$ in the XRD pattern), blue circle corresponds to 12 angstrom spacing (which correspond to $6.1-6.3^\circ 2q$ in the XRD pattern). FFT of one of the larger particles (top right) has spacing corresponding to 14 angstrom spacings (which correspond to $7.2^\circ 2q$ in the XRD pattern), indicating likely structure is HCP	105
Figure S 4.2 TEM image of MF60EQ product showing 2 distinct particles sizes, and table of average sizes	105
Figure S 4.3 TEM images for a) MF40eq product and b) MF50eq product, alongside a table of average particle size for the larger HCP particles.....	106
Figure S 4.4 TEM images for a) Batch60eq product and b) Batch product.....	106
Figure S 4.5 N ₂ Absorption isotherm of MF0EQ product.....	107
Figure S 4.6 N ₂ Absorption isotherm of MF10EQ product.....	107
Figure S 4.7 N ₂ Absorption isotherm of MF20EQ product.....	108
Figure S 4.8 N ₂ Absorption isotherm of MF30EQ product.....	108
Figure S 4.9 N ₂ Absorption isotherm of MF40EQ product.....	109
Figure S 4.10 N ₂ Absorption isotherm of MF50EQ product.....	109
Figure S 4.11 N ₂ Absorption isotherm of MF70EQ product.....	110
Figure S 4.12 N ₂ Absorption isotherm of MF60EQ product (48 hours in methanol)	110
Figure S 4.13 Comparative N ₂ isotherm graph for all microfluidic products	111
Figure S 5.1: XPS spectrum for rewashed microfluidically synthesised Pd-UiO-67-BPYDC that underwent further reduction with 24hrs heating at 130 °C in DMF	133
Figure S 5.2: TEM images of Pd(II)-UiO-67-BPYDC sample where further reduction was attempted with 0.1 M NaBH ₄ /DMF on an unwashed microfluidic synthesis sample. a) Lower magnification TEM image. b) higher magnification TEM image.....	134

Figure S 5.3: TEM images of two further reduction samples on the batch synthesis product when the literature method was followed exactly (0.5 ml HCl). a) 5 ml 0.1 M NaBH₄/DMF solution in 2 ml DMF, 4 hours in an ice bath. b) 15 ml 0.1 M NaBH₄/DMF solution in 20 ml DMF, 4 hours in ice bath..... 134

Figure S 5.4: N1s XPS spectra for: a) batch synthesised Pd(II)-UiO-67-BPYDC. b) batch synthesised UiO-67-BPYDC. Both show similar pattern shape, with the broadening to higher energies being unrelated to the Pd present. 135

Supplementary Tables

Table S 6.1 MOF structures with literature H ₂ uptakes	153
Table S 6.2 MOF structures with literature CH ₄ uptakes	161
Table S 6.3 MOF structures with literature CO ₂ uptakes	166
Table S 6.4 Individual coefficient of determination values for each fold in the 10 runs.....	176

Abbreviations

BPDC	Biphenyl-4,4-dicarboxylic acid
BPYDC	2,2'-bipyridine-5,5'-dicarboxylic acid
CFIR	Coiled Flow Inversion Reactor
DFT	Density Functional Theory
DMF	Dimethyl Formamide
DT	Decision Trees
EDX	Electron dispersive X-Ray
FCC	Face-Centred Cubic
GBDT	Gradient Boosted Decision Tree
GCMC	Grand Canonical Monte Carlo
H ₂ BDC	Terephthalic Acid
HCl	Hydrochloric acid
HCP	Hexagonal Centred Planar
MAE	Mean Absolute Error
MAPE	Mean Average Percentage Error
ML	Machine Learning
MOF	Metal-Organic Framework
MSE	Mean Squared Error
PBU	Primary Building Unit
PCA	Principle Component Analysis
PDMS	poly(dimethylsiloxane)
PHYS	Physical Conditions
PLS	Partial Least Squares
PTFE	Polytetrafluoroethylene
RF	Random Forest
RTD	Residence Time Distribution
SBU	Secondary Building Units
SEM	Scanning Electron Microscopy
SVM	Support Vector Mechanism
TEM	Transmission Electron Microscopy
UiO	Universitet i Oslo
VIPScore	Variable Importance Score
wt%	Weight Percentage
XPS	X-Ray Photoelectron Spectroscopy
XRD	X-Ray Diffraction

Chapter 1 Introduction

1.1 Metal-Organic Frameworks

MOFs were first reported in 1959 with the synthesis of Cu^+ complexes joined by bis(alkylnitrilo) units of varying length by Saito *et al*, with the length of these linker units influencing the dimensionality of the product formed.¹⁻³ Shorter length linkers, such as succinonitrile resulted in a 1D structure, increasing the linker length with glutaronitrile resulted in a layered structure and finally increasing the length further with adiponitrile resulted in a 3D crystalline structure being formed. This was a cationic framework stabilised by the encapsulation of nitrile ions within its pores. Research continued into these repeating crystal structures,⁴ referred to as coordination polymers, but it wasn't until 1995 that the term Metal Organic Framework (MOF) was established by Yaghi *et al*.⁵ MOFs at this stage were instable and did not support a permanent porosity when guest molecules (e.g. solvent) were removed. A key development was made by Yaghi *et al* in 1999 with the development of Zn(II) based MOF-5, which showed a permanent porosity when solvent was removed and a thermal stability of up to 300 °C.⁶ The wide range of potential SBU/linker combinations and ordered porous structures has led to MOFs being synthesised for a wide range of applications: catalysis, gas storage/capture, drug delivery etc.⁷ A key limitation for MOFs in these applications was a relatively low thermal and chemical stability when compared to other porous materials (Zeolites).⁸

To counteract this limitation, the Zr (IV) based Universitet i Oslo (UiO)type MOF was formed by Cavka *et al* in 2008.⁹ UiO-66 and its analogues have been used widely since their inception,¹⁰ with the number of papers relating to UiO-66 increasing year on year (Error! Reference source not found.).

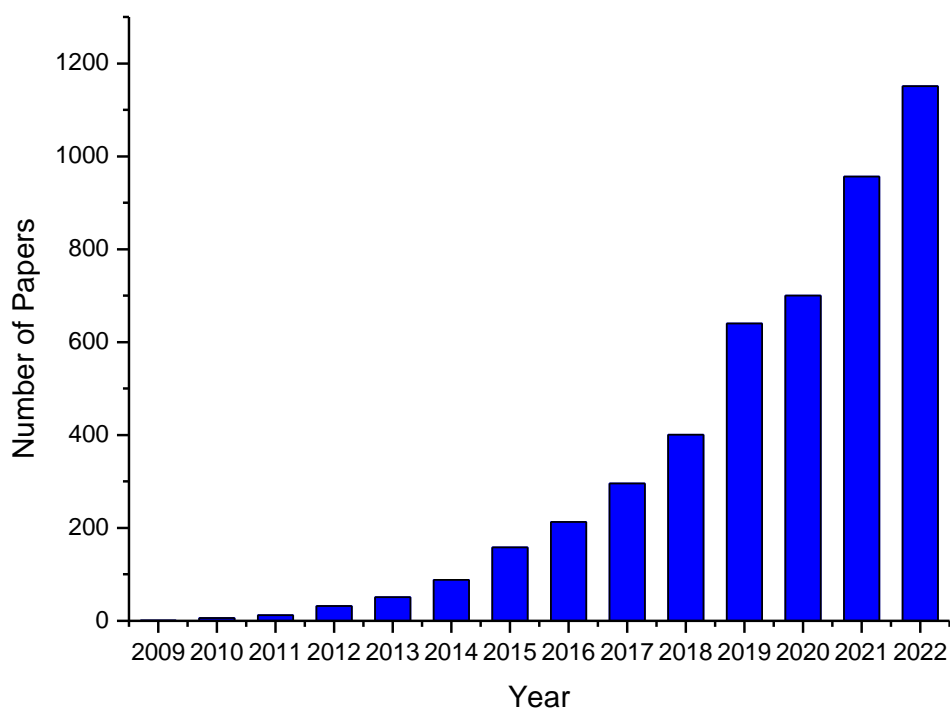


Figure 1.1: Number of papers relating to “UiO-66” each year since 2009. Data collected from WebOfScience on 25/07/2023.

UiO MOFs are composed of $[\text{Zr}_6(\text{OH})_4\text{O}_4]^{12+}$ SBUs joined together by dicarboxylic acid linker groups containing phenyl rings, with the number of phenyl rings denoting the name of the MOF, as shown in **Figure 1.2**.

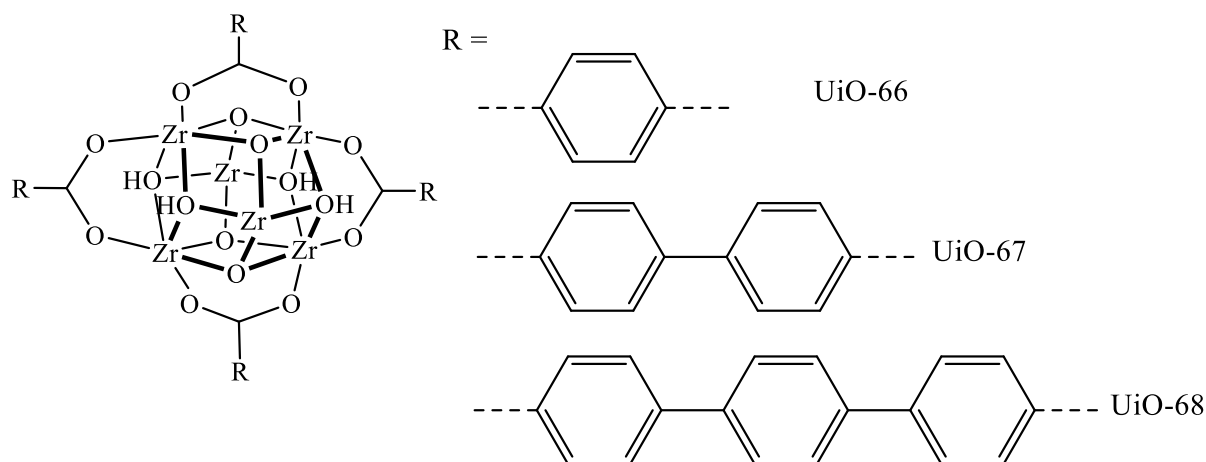


Figure 1.2: [Zr₆(OH)₄O₄]¹²⁺ SBU for UiO type MOFs with a generic carboxylic acid linker bonded on the right-hand side. Various linker lengths shown, with the corresponding MOF name given. Figure drawn using Chemdraw Prime 22.

In the work by Cavka *et al* in 2008,⁹ UiO-66 in was observed to show extremely high thermal and chemical stability when compared to other MOFs. This high stability is a key feature of Zr(IV) based MOFs, with strong acid/base bonds formed between the cationic SBU units and the anionic linker units and the high level of connectivity in the framework contributing to this.¹¹ This addresses a key limitation found in many non-Zr(IV) based MOFs, being the relatively low thermal/chemical stability, limiting their use in industrial applications.⁸

Early synthesis of UiO MOFs followed a basic batch solvothermal synthesis procedure, with low concentrations of the metal salt or linker used, with no additive species present.¹² The first synthesis of UiO-66 involved mixing ZrCl₄ and terephthalic acid (H₂BDC) in dimethylformamide (DMF), in a molar ratio of reactants:DMF of 1:~1500.⁹ Without the presence of acid modulators or deprotonating agents, higher reactant concentrations led to rapid nucleation and interconnection, resulting in an amorphous product rather than a crystalline powder. An amorphous product will not be consistent in size, shape, or porosity, limiting the ease of use in a desired application, though recent research has aimed to purposefully create amorphous MOFs to exploit certain attributes.¹³ Increased reactant concentrations would be desired to increase the turnover yield of the MOF synthesis. Key works by Schaate *et al* and Zhao *et al* introduced the used of acid modulators and deprotonating agents respectively.^{14,15}

Acid modulators are typically single carboxylic acid groups connected to a varying carbon chain group (R-COOH), with R varying from methyl (acetic acid), benzene (benzoic acid) etc.¹⁶ These groups compete with the linker groups to reversibly bind with the SBUs, causing a slower crystal nucleation as well as controlled crystal growth.¹⁷ This was initially found in

the work by Schaate *et al*, with UiO-66, UiO-66-NH₂, UiO-67 and UiO-68-NH₂ all synthesised while varying the concentration of acid modulator used, being acetic acid or benzoic acid.¹⁴ Schaate *et al* found that the presence of an acid modulator would increase the crystallinity and the crystal size of the UiO products formed as the modulator concentration was increased (**Figure 1.3**). While crystalline UiO-66 could be synthesised without the presence of an acid modulator, the larger UiO-67 and UiO-68-NH₂ analogues required their presence, otherwise resulting in a non-crystalline product.

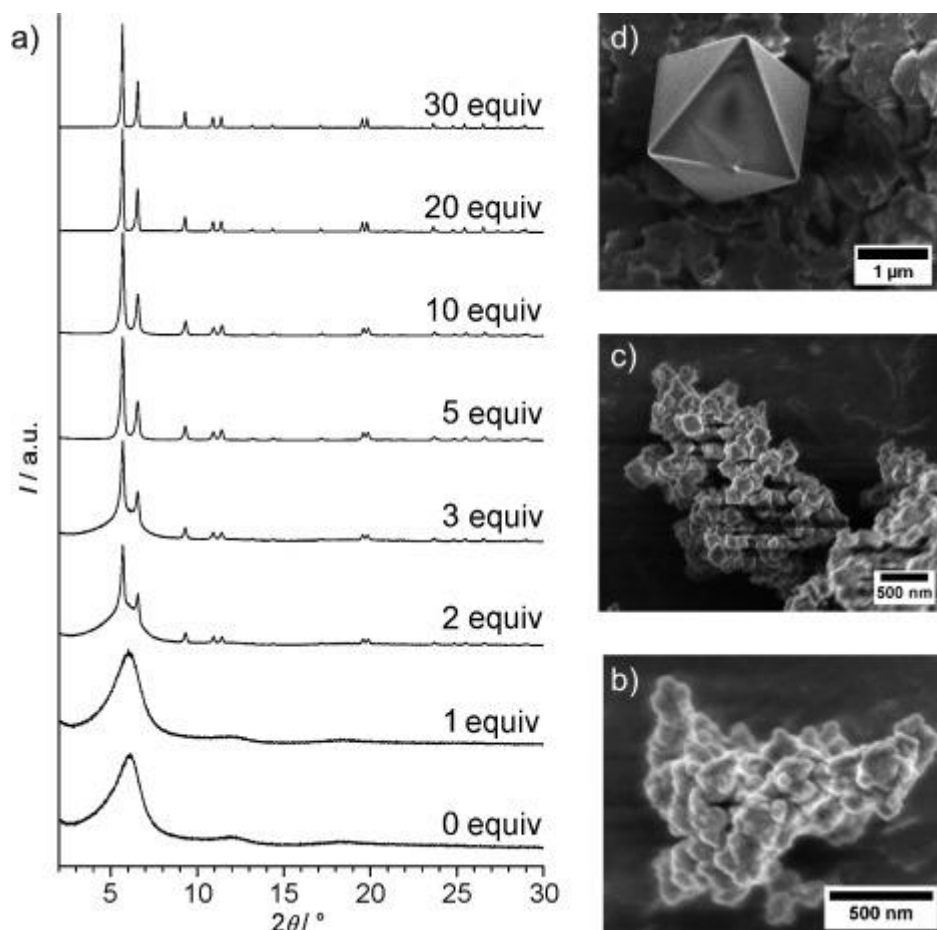


Figure 1.3: a) Powder XRD patterns for UiO-67 synthesised using increasing amounts of benzoic acid. b) SEM image of 0 equivalent UiO-67 sample, c) SEM image of 3 equivalents UiO-67 sample, d) SEM image of 30 equivalents UiO-67 sample. Figure adapted from work by Shaate *et al*.¹⁴

Deprotonating agents act in the opposite way, by activating the linkers and increasing the rate of nucleation.¹⁰ These are used in a conjunction with acid modulation to form smaller crystalline products. Zhao *et al* used triethylamine in conjunction with acetic acid to form UiO-66 with a controllable size, by promoting the release of hydrogen from the biphenyldicarboxylic acid (BPDC) linkers, with the acetic acid still competing with them for SBU connections.¹⁰ Decreasing the crystallite size is beneficial for many applications, as it increases the diffusion of species through the MOF pores.¹⁸ However, increasing the

concentration of a deprotonating agent too much will start to interfere with the intended effect of the acid modulator unit.

Alongside acid modulation and deprotonating units, there are two other key additives that may be present in the reactant solution to control the synthesis occurring: HCl and water. HCl has become an additive of interest in the synthesis of UiO MOFs, with its addition to the reaction mixture improving the synthesis in two opposing ways to ensure a better product. On the one hand, the addition of the acidic HCl will decrease the rate of linker deprotonation by decreasing the pH, leading to a better formed crystalline product, in the same way the monocarboxylic acid modulators slow down the linker bonds being formed.¹⁹ On the other hand, the crystallisation rate is increased due to the presence of another additive present in a HCl solution, water. Water has been shown to act as a capping agent, like monocarboxylic acid modulators, but will increase the rate of formation for the MOF product rather than decrease it.²⁰ This increase in formation rate is due to the added oxygen increasing the rate of formation for the SBUs.¹⁴

UiO type MOFs can undergo modification for specific applications through three key methods: Defects, morphology control and functionalisation. Defects, specifically missing linker and cluster defects are introduced into UiO MOFs through a variety of influences and have been shown to increase the surface area and adsorption properties of MOFs while decreasing the stability.^{18,21,22} Missing linker defects may occur using acid modulators, with the monocarboxylic groups taking up a site where a linker group may usually bond.^{15,17,23–27} Acid modulator groups with higher acidity have been shown to form a higher number of defects.²⁵ These missing linker defects can increase the catalytic performance by making the zirconium metal sites to be more readily available.²⁸ These defects were reported as early as 2011, with Valenzano *et al* reporting the synthesis of UiO-66 material that showed a smaller than expected thermogravimetric profiles for the linker combustion step, prompting the conclusion that this result was due to a lower number of linkers than expected.²⁹ This was followed up with theoretical calculations by Hajek *et al* on the use of UiO-66 as a heterogeneous catalyst for the cross-aldol condensation of benzaldehyde and heptanal, which revealed that the catalytic reaction could only proceed with missing linker sites being present, allowing for Lewis Acidic coordination sites on the Zr⁴⁺ SBU to be accessed.^{30,31} Purposeful introduction of the missing linker defects was first performed by Vermoortele *et al* and followed up with another publication by Wu *et al* achieving the same, using an excess of monocarboxylic acid modulators, replacing the dicarboxylic acid linker units.^{26,28} This method of varying the concentration of modulator to control the concentration of missing linker defects present offers a way to directly control certain properties of the MOF, such as pore size and volume.³²

The other key class of defects present in UiO MOFs are missing cluster defects, in which a whole $[\text{Zr}_6\text{O}_4(\text{OH})_4]^{12+}$ SBU is removed, with these first synthesised by Cliffe *et al* in 2014.³³ The extra space created within the UiO-66 structure can be used to store larger functional molecules, such as ferrocene.³⁴ High concentrations of missing linker or cluster defects may lead to UiO products with different crystal phases than their usual face centred cubic (**fcc**) formation (Error! Reference source not found.). The formation of different structures of UiO-66/67 allowed for various benefits to be discovered such as increased catalytic activity due to a higher density of defect sites,³⁵ or altering their structures to give different types of adsorption isotherm with a larger working capacity, with mesopores introduced that will only fill at higher pressures.³⁶

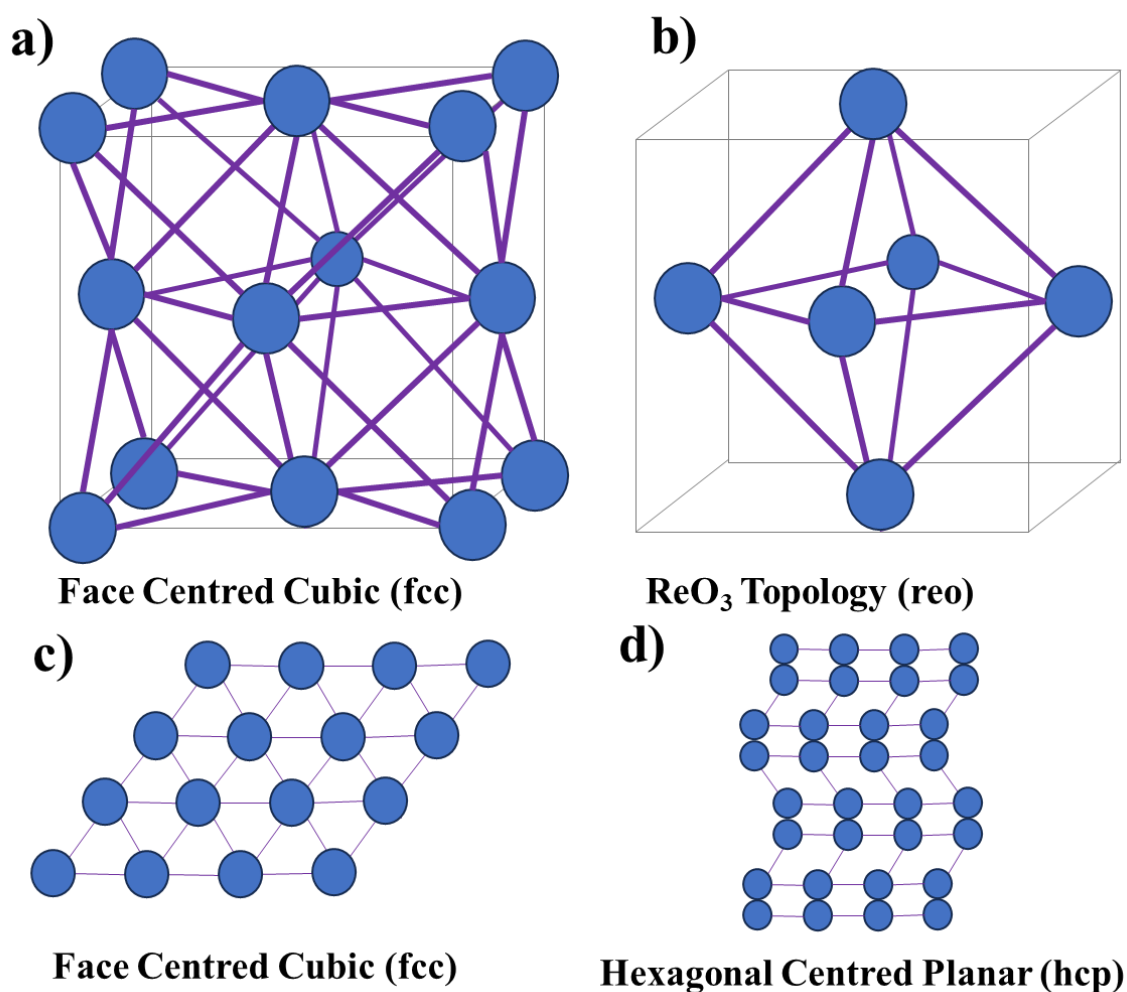


Figure 1.4: Varying crystal phases for UiO type MOFs with blue circles representing SBUs and the purple lines representing linker units. a) Face Centred Cubic (**fcc**) structure, b) ReO_3 (**reo**) structure, c) 2d representation of larger **fcc** structure, d) 2d representation of Hexagonal Centred Planar (**hcp**) structure.

Increasing the appearance of missing cluster defects, through modifying the concentration of formic acid present, led to areas of ReO_3 like topology (**reo**) within UiO-66.^{33,37,38} Controlling

the topology/crystal phase that formed was further developed in a follow up piece of work by Cliffe *et al.*, in which the larger analogue of UiO-67 was subjected to a similar synthesis procedure with high concentrations of formic acid, resulting in a new crystal phase, hexagonal close packed (**hcp**) UiO-67 being formed.³⁸ The high levels of formic acid lead to an increased number of missing linker defects within the UiO-67 structure, causing the SBU to change from 12 linker coordinated $M_6O_4(OH)_4$ SBU to the 18 linker coordinated $M_{12}O_8(OH)_{14}$ SBU, with M being Hf in the case of the work by Cliffe *et al.*³⁷ The presence of water has been shown to play a key role in forming these other phases of UiO MOFs, with Cliffe *et al.* finding the by increasing the concentration of water present would drive the reaction towards a **hcp** UiO-67 product, even when using a volume of acid modulator that would usually form a **fcc** product.³⁸ Excess of HCl has also been shown to promote the formation of a crystalline **hcp** product.¹⁷ Higher temperatures will also promote the formation of metal-oxide clusters with higher nuclearity, with the formation rate of **fcc** being higher at lower temperatures.³⁸

However, for HCP-UiO-67 in particular, it has only been synthesised in the past using formic acid as the modulator group, for both the Hf and Zr versions.^{36,38} Achieving this structure while using different modulator groups would allow for the incorporation of different functional groups, increasing the number of potential applications for the phase controlled product.³⁹ Functionalisation, which can range from bonding NH_2 groups to the linker unit all the way to immobilisation of catalytic molecule, of UiO MOFs has been performed to create MOFs for a wide range of applications.^{40,41} Functionalisation may also be achieved through encapsulation of an active molecule, where it is held in the pores through non-covalent forces, such as the encapsulation of Crabtree's catalyst in MIL-101.⁴² These encapsulated species may also be metal nanoparticles.

Nanoparticles are of key interest due to their high surface area/volume ratio, leading to a larger chemically active surface available for reactions. However, with this high surface energy, the nanoparticles are thermodynamically unstable and will coalesce, i.e. the nanoparticles will combine with each other. To counteract this, nanoparticles can be synthesised in the presence of supporting materials, with the nanoparticle immobilised on the support to prevent aggregation.⁴³ MOFs have been used a support material for various metal nanoparticles, with their high surface areas, porosity and ordered structures making them suitable materials.⁴³ For example, several MOF supports have been used to immobilise gold,⁴⁴⁻⁴⁶ platinum,^{41,47,48} and other metal nanoparticles for various applications.⁴⁹

These nanoparticles can be attached to the MOF structure using a variety of different methods. Metal nanoparticles may be synthesised within already formed MOF structures, by infiltration of the nanoparticle precursors, through either liquid or gas phase methods.⁵⁰ The precursor

molecules are then converted into the nanoparticles through the application of heat, reducing agents or radiation.⁵¹ This is the most common method of encapsulating nanoparticles in MOFs and has been used for Pd,⁵² Ag,⁵³ and many other metals.⁵⁴ A potential disadvantage to this method would be that the MOF already has to be fully formed before the encapsulation can occur, resulting in a multiple step synthesis.

An alternative method of nanoparticle incorporation is by forming the MOF cage around already synthesised metal nanoparticles.⁵⁵ An advantage over the previous method is that the metal nanoparticles are of a known size when they are incorporated into the MOF, with the size potentially modified to suit certain applications. However, a key disadvantage is that controlled synthesis of these metal nanoparticles would need to be performed with a different capping agent beforehand.⁵⁶

1.2 Synthesis of MOFs

Generally, solvothermal or hydrothermal synthesis are the most common methods for producing MOFs, with the reactants placed into a reaction vessel, such as an autoclave, with water/solvent (typically DMF) and heated for a set period.⁵⁷ This technique was first used by Yaghi *et al* in 1995,⁵⁸ and has since found success in forming a variety of MOF families.⁵⁷ This is still the most common reaction method used in the synthesis of MOFs. By using a sealed vessel, the reaction solutions can be heated to past their boiling point, ensuring the reactants, which can be initially insoluble, dissolve into the solution and react. As the reactants dissolve into the solution, a required nucleation concentration will be reached, which will then lead to crystal growth.⁵⁹ These reactions are generally easy to perform in a laboratory setting, with very few steps needed. However, scaling these processes up comes with several limitations: long reactions times,⁶⁰ batch to batch variability, and inconsistency within the same batch.⁶¹⁻⁶³ Increasing the mixing present in the system could reduce the time needed for the reaction, while changing it from a batch to continuous system would allow for a steady stream of the product. Microfluidic reactors may be used to address these limitations.

1.3 Microfluidic Reactors

Microfluidic reactors are a class of reactor with liquids flowing through microchannels, with potentially continuous synthesis leading to several advantages over larger scale batch reactors.⁶⁴ Firstly, the high surface area to volume ratio allows for higher mass and heat transfer of the reactants.⁶⁵ Secondly, the small amount of reagent being heated at any one time is safer than that of larger vessels. Finally, it allows for a greater amount of reaction control, with precise and consistent reaction times/heating for the reactants, limiting batch to batch variability.

Fluids in microfluidics reactors are almost exclusively under a laminar flow pattern rather than a turbulent flow pattern.⁶⁶ This is due to the Reynolds number (Error! Reference source not found.) for these reactors being low, due to the low value for L (being the reactor diameter).

$$\text{Re} = \frac{\rho u L}{\mu} \quad \text{Equation 1}$$

Equation 1.1: Reynolds number equation. Re = Reynolds number, ρ = density of the fluid (kg/m^3), u = flow speed (m/s), L = characteristic linear dimension (m), μ = dynamic fluid viscosity ($\text{kg}/(\text{m} \cdot \text{s})$).

Laminar flow consists of a parallel flow pattern, with mixing only occurring through diffusion between the layers (**Figure 1.5**). It also does not have consistent residence times, with the fluid closer to the reactor walls moving slower due to frictional forces at work.

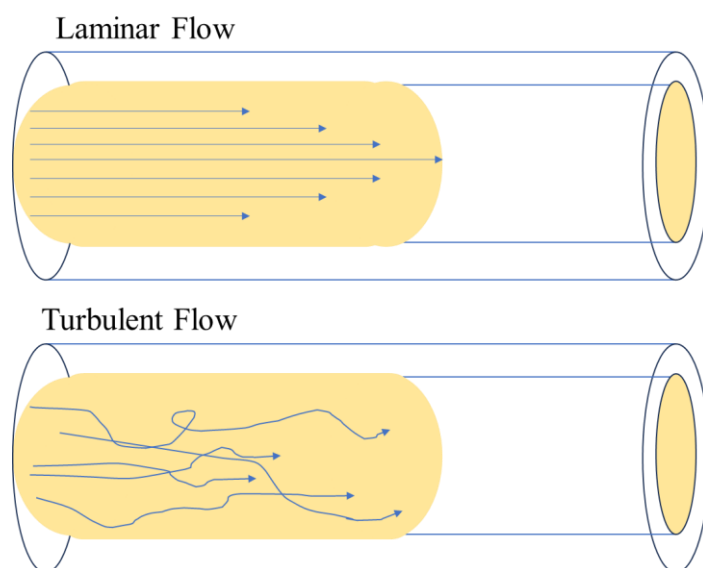


Figure 1.5: Basic schemes for laminar and turbulent flow patterns. Laminar flow shows a parallel flow pattern, with frictional forces on the tubing walls causing the flow rate to decrease in these areas. Mixing will only occur between these layers through diffusion. Turbulent flow shows a random flow pattern with different layers crossing and mixing throughout the tube. Frictional forces play less of an impact in the flow, as the layers are constantly crossing over and changing position in the tube.

Several developments in microfluidic reactors have been made to address these two issues through micromixing technologies. Micromixing technologies can be split into two categories: Active, in which external energy is being used to increase the mixing efficiency, and Passive, in which no external energy is being used to enhance the mixing.⁶⁷ Active mixers include the application of acoustic/ultrasonic waves, electrochemical forces, and thermal influence.⁶⁸ While these techniques have achieved high levels of mixing, the difficulty in fabrication as well as the need for an external energy source during use are key disadvantages that passive techniques address.⁶⁷

Passive techniques rely on the reactor design inducing mixing between the reactants, by increasing the contact area between the reactant solutions and thus increasing the level of diffusion.⁶⁹ This can be achieved through various methods, such as splitting and recombining the solution, introducing chaotic advection or by using a coiled flow.⁶⁹

Coiled flow is used in micro-tubular reactors to ensure a consistent level of mixing by enhancing the Dean vortices, a secondary flow pattern which narrows the residence time

distribution.⁷⁰ However, if the tubing is coiled in one direction, then mixing hotspots will appear in the tubing due to enhanced centrifugal forces.⁷¹ This can be solved by inverting the direction of the tubing by 90° four times, with the hotspots averaging out to give consistent mixing.⁷² This type of reactor is referred to as a Coiled Flow Inversion Reactor (CFIR) and was first developed by Saxena and Nigam.⁷³ More details on the CFIR are given in Section 2.2.

1.4 Microfluidic Synthesis of MOFs

Ameloot *et al* were the first to successfully use microfluidic technologies to synthesise a MOF material in 2011, with the formation of hollow HKUST-1 capsules using a droplet based microtubular reactor, with an aqueous reactant solution being injected as droplets into a denser continuous reactant solution.⁷⁴ The crystallisation of the MOF would occur at the droplet-carrier interface, forming the hollow capsules. Following this, in 2013, Faustini *et al* adapted this droplet base method to perform the solvothermal synthesis of various MOFs (HKUST-1, MOF-5, IRMOF-3 and UiO-66), with the reactant solution being carried through a heated area as microdroplets, carried by a denser continuous phase (silicon oil) (**Figure 1.6**).⁷⁵ Due to the benefits of microfluidic synthesis previously mentioned, these MOFs were formed in considerably lower reaction times than their batch counterparts, while also showing consistent sizes and shapes due to the passive mixing present in the droplets.⁷⁵

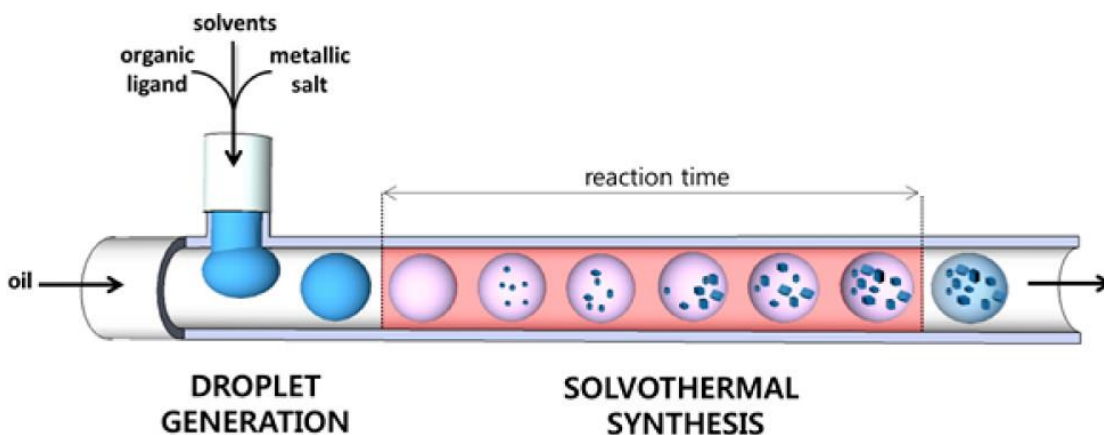


Figure 1.6: Scheme of Faustini *et al*'s two-phase microfluidic droplet reactor. Figure adapted from Faustini *et al*.⁷⁵

Following this, several other pieces of work have focused the synthesis and modification of UiO-66 through microfluidic processes.⁷⁶⁻⁷⁸ In 2016, Tai *et al* published work detailing the microfluidic formation of nano-UiO-66 and nano-UiO-66-NH₂.⁷⁸ This work used a single-phase coiled flow reactor to form UiO-66 in a matter of minutes, with the residence time being altered to control the product size. By achieving the formation of the UiO-66 in a single-phase reactor, it gave a synthesis protocol that is easier to follow for new researchers, with the washing/separation of a denser secondary phase no longer an issue. Before the start of this work, no successful microfluidic synthesis of the larger analogue, UiO-67, had been published. The closest success has been found by Vo *et al* in 2020, in which UiO-67 was formed in a continuous reactor with microwave irradiation as the heat source used.⁷⁹ This reactor is different to a microfluidic reactor in a key way, being that the tubing is too wide (2 mm) to be considered microfluidic and so does not carry the same benefits as found in those methods. It also still does not provide a method through standard heating means (oil bath) for a researcher to achieve the synthesis of UiO-67 in a microfluidic setting.

1.5 Gas Storage in MOFs

A key application for MOFs and one that will be revisited throughout this thesis is that of gas storage and separation. When compared to other porous materials, such as zeolites, MOFs are more suited to these applications due to their high surface areas, high porosity and the ability to tune their functionality and structure.⁸⁰ They also have a lack of “dead space”, being areas in a porous material, such as zeolites, that are inaccessible for storage/reactions, giving them more accessible space to use when compared to zeolites.⁸¹

The first attempts to use MOFs in fuel gas storage, CH₄ in this case, can be traced back to 1997 in work by Kondo *et al*.⁸² Following this, developments have been made to capture and store a variety of gasses, including CO₂, CH₄ and H₂. Recent advancements for the storage/capture for each these gasses are given below.

Carbon Dioxide emissions play a key role in the onset of global warming, and so the reduction of these emissions is currently an important area of research.⁸⁰ While transitioning to cleaner sources of energy should be a priority, the use of Carbon Capture Solutions (CCS) is important in the time taken for this transition, or for industries where CO₂ emissions may be unavoidable.⁸³ Two key aims for CCS materials are that the CO₂ uptake is fully reversible and that the material can be fine-tuned with functionalisation to achieve maximum uptake in a given scenario.⁸⁴ MOFs fulfil both of these requirements, which was recognised by Millward and Yaghi in 2005 where they tested a range of MOFs for the room temperature absorption of CO₂.⁸⁴ The isotherms gathered were all Type I isotherms, suggesting monolayer adsorption of CO₂ (Figure 1.7).

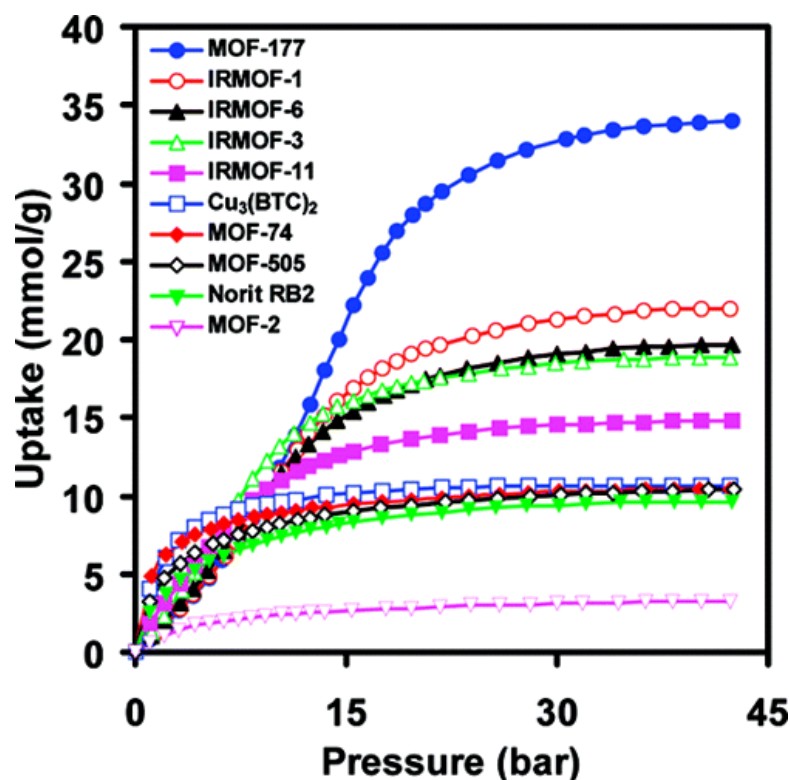


Figure 1.7: CO₂ absorption isotherms for various MOF materials at 298K. Figure adapted from work by Millward and Yaghi.⁸⁴

The MOFs used in this work were pure products, with no defects or extra functionalisation introduced. Subsequent works following this focused on modifying the MOF structures to ensure increased CO₂ uptake. One line of interest is the introduction of amine groups, which may act as a Lewis Base to attract the Lewis Acidic CO₂.⁸⁵ Serra *et al* performed a comparative

study for the uptake of CO₂ into MIL-101(Al) and NH₂-MIL-101(Al), finding an increased uptake in CO₂ with the amine modified MOF.⁸⁶ Adding too many amine groups to the linker unit may lead to a lack of space for the CO₂ to bind, with a balance needing to be found.⁸⁷

Hydrogen is an alternative energy source with a high amount of interest surrounding it, due to lack of CO₂ in its combustion products and a higher gravimetric energy density compared fossil fuels.^{88,89} However, storing the high volumes of gas needed for use in transport and other sectors is an area of difficulty, with either extremely high pressures (~700 bar) for delivery as a gas at room temperature or extremely low temperatures (~20 K) needed to deliver the hydrogen in liquid form at atmospheric pressure.^{90,91} The use of solid porous absorbents, such as MOFs, is to reduce these pressure and temperature barriers to a point when H₂ becomes a viable fuel source. The first use of MOFs for Hydrogen storage was performed by Yaghi's group in 2003, in which the hydrogen absorption of MOF-5 was tested at both 78K and at ambient temperatures, with a gravimetric uptake of ~4% achieved at 78 K (**Figure 1.8**).⁹² Following this work, various advancements have been made in the use of MOFs for H₂ storage.

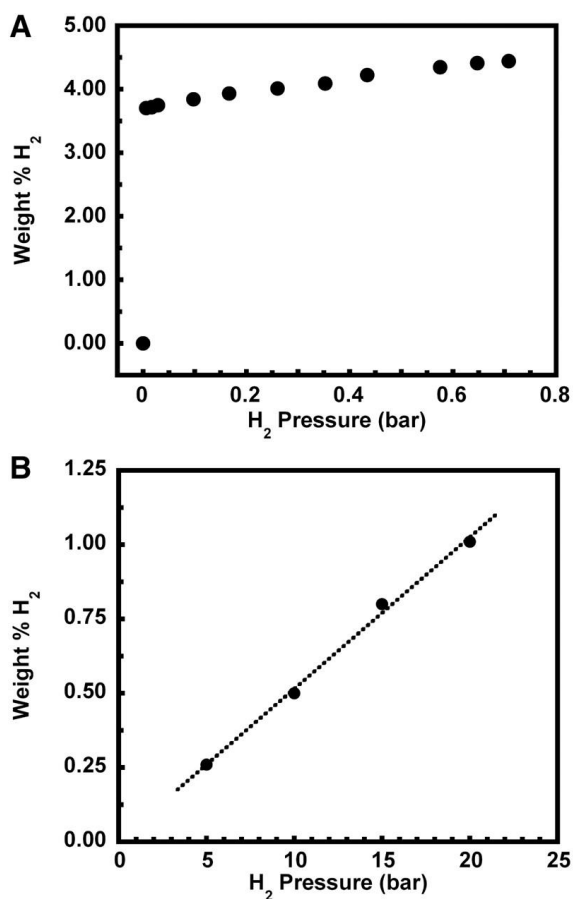


Figure 1.8 Hydrogen adsorption isotherm for MOF-5 at A) 78 K and B) 298 K. Figure adapted from work by Rosi et al.⁹²

One such method has been to dope the structures of MOFs with metal nanoparticles, which will strengthen their interactions with H₂, leading to an increased uptake at room temperature.⁹³ Wang *et al* doped several MOF structures (MOF-74, ZIF-8, ZIF-67) with magnesium nanoparticles using deposition reduction, finding an increase in the uptake of H₂ at high temperatures when compared to pure magnesium.⁹⁴ The doped MOFs also showed a higher level of reusability, with the uptake over many cycles staying consistent and a quicker release and capture of the hydrogen when necessary (**Figure 1.9**).

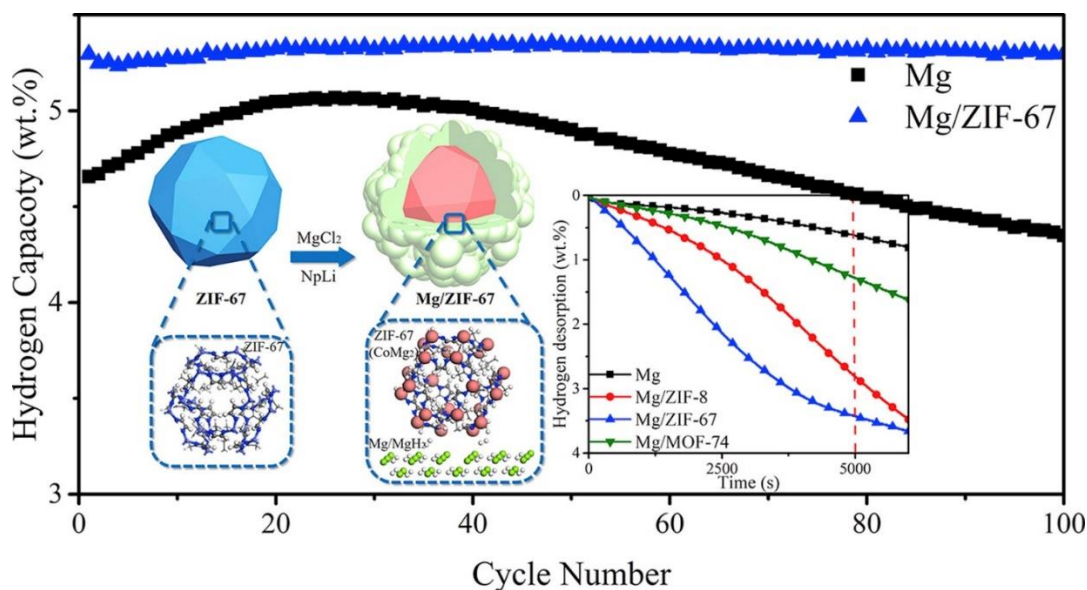


Figure 1.9: Main Graph: Hydrogen Capacity for Mg and Mg/ZIF-67 in relation to cycle number. Inset Graph: Hydrogen desorption of Mg and Mg doped materials in relation to time, at 300 °C. Figure adapted from work by Wang *et al.*⁹⁴

Alongside CO₂ and H₂ capture/storage, the storage of CH₄ in MOFs has also been of particular interest. Similar to H₂, CH₄ can be used as a potential replacement for petroleum in vehicles, which also being greener to burn and can be produced renewably.^{95,96} However, the storage and delivery of CH₄ falls into the same issues that H₂ has; low densities at room temperature requiring extremely high pressures to store it.⁹⁷ Using a porous material, such as MOFs, can reduce the temperature and pressure barriers present to change CH₄ into a viable fuel source. The uptake of CH₄ into MOFs can be enhanced by exploiting electrostatic interactions between the CH₄ and open metal sites, ideally using a MOF which naturally has a high number of these sites. Wu *et al* tested the CH₄ uptake of MOF-74 while changing the metal used in forming the MOF (Mg, Mn, Co, Ni, Zn) and found a drastically increased uptake of CH₄ when compared to MOF-5, which has a reduced number of open metal sites (Ni-MOF-74 = 190 cm³/cm³, MOF-5 = 110 cm³/cm³).⁹⁷

For gas absorption in general, there has been interest in the use of UiO type MOFs, due to their ability to withstand high temperatures and pressures when storing and releasing gasses.⁹⁸ In the past however, a limitation has been the UiO MOFs microporosity and low density, which results in high overall gas uptakes but a low working capacity.⁹⁹ The uptake occurs quickly at

low pressures and then remaining constant, which is a Type I isotherm. To address this issue, Connolly *et al* synthesised monolithic UiO-66, with mesopores and macropores introduced to the structure.⁹⁹ This structure showed an increased N₂ working capacity, with these larger pores being filled at higher pressures. Introduction of mesopores has also been performed UiO-67 by Xydias *et al*, with a SO₂ modified linker leading to increased pore size and CO₂ uptake.¹⁰⁰ However, the enhanced capture of CO₂ is attributed to the polar SO₂ groups included within the structure, rather than larger pores being present, as the N₂ adsorption actually decreases from the standard UiO-67. Forming mesoporous UiO-67 in a similar vein to the work by Connolly *et al* would allow for increased working capacities for the structure for N₂ storage.

1.6 Machine Learning for MOFs

Due to the high number of potential SBU and linker combinations, it can be difficult to test all the potential MOF materials for their desired application (catalytic performance, gas adsorption, etc.). Using computational methods, such as machine learning (ML), may allow rapid screening of a wide range of potential MOF materials, with the model giving a predicted property (catalytic activity, gas uptake etc.) for a given MOF material.¹⁰¹ Building these ML models requires several key components: collecting a wide range of MOF descriptors and output values of interest to train the model, before finally training a ML model to predict new data.

Extensive data collection is key to forming a ML model with high predictive performance; this can be conducted via analysis of experimental literature data or through hypothetical MOF databases.¹⁰¹ This data includes the output value of interest for many MOFs to help train the model, alongside descriptor values so that the ML model can “learn” and find patterns between the MOFs. These descriptors can range from simple chemical properties, such as the type of metal present in the SBU, to more complicated structural descriptors, such as the pore size.¹⁰¹ Values for these structural descriptors are obtained through either literature values, or more commonly, through molecular simulation e.g. Grand Canonical Monte Carlo.¹⁰² For the output data, experimental data is more reliable, but values are sparse; many MOFs have no

data available, and the few that do are lacking in quantity. Conversely, there is an abundance of theoretical MOF database values, due to the widespread number of descriptors available, but as these values are obviously calculated, they are based on assumptions and lack the reliability real-life data has. Use of computational, theoretical data to construct a model that will also serve to provide predicted data will evidently lead to inaccuracies within these predictions. New researchers will also have to find the descriptors for the material they want to make predictions on, so having to use other modelling techniques beforehand lengthens the process.

A focus of these screening processes has been to predict the materials gas adsorption ability, be it for fuel cell applications (H_2 and CH_4 uptake),^{103,104} or for carbon capture purposes (CO_2 uptake).¹⁰⁵⁻¹⁰⁷ Previous screening techniques through Density Functional Theory (DFT) or Grand Canonical Monte Carlo (GCMC) simulations were time consuming processes when looking at vast MOF databases.¹⁰⁸ To improve upon this, machine learning techniques were used to screen larger amounts of data quickly. For example, Pardakhti *et al* built a random forest model for the prediction of CH_4 uptake in MOFs.¹⁰⁴ This model was accurate ($R^2 = 0.98$) when predicting the gravimetric uptake, with a dataset of $\sim 130,000$ hypothetical MOF structures used for training and testing the model, with only 8% of the dataset needed in training the model to give this high accuracy. However, several limitations are present in this work, which have been developed on in future works. The ability to only predict for one gas, at one temperature, and at one pressure, reduces the flexibility of the model for future researchers. The work by Fanourgakis *et al* developed on this, with a random forest model built to predict for both the uptake of CH_4 and CO_2 in MOF structures, using a dataset of 78,000 hypothetical MOFs.¹⁰⁵ This model could also predict the uptake of the gases at varying pressures, improving on the models flexibility. For both of these models however, the use of both hypothetical MOF structures and descriptors gained through GCMC simulation (pore size, surface area etc.) limits their applicability to real world results in two key ways. Firstly, the use of data from previous GCMC simulations for the training of a machine learning model

will cause all the results to be affected by the errors present in the initial simulations. Secondly, the ease of use for new researchers is reduced by firstly requiring GCMC simulations on their products of interest before predictions with the machine learning model can be performed.

The Computation-Ready Experimental Metal-Organic Framework (CoRE MOF) dataset was formed in 2014, with the GCMC simulated descriptors, such as surface area and pore size, for ~5000 experimentally synthesised 3D MOFs,¹⁰⁹ with the database updated in 2019 to include ~14,000 3D MOFs.¹¹⁰ This database provided an opportunity for researchers to access data more in line with the real world and use it in building their own predictive models, as many hypothetical MOFs may not be stable when synthesised.¹¹¹ Several research projects have used this database in the formation of their models.^{108,112–114} However, as was reported in the formation of the 2014 database, the use of this data for predicting the surface area of MOF structures leads to overprediction of these when compared to real world uptake values. Using these overpredicted values in machine learning to predict features such as gas uptake will lead to a discrepancy. The formation of a machine learning model that can predict for multiple gases/temperatures/pressures, which is trained using experimentally determined output values and with descriptors that do not require GCMC modelling should be the next stage in development for these methods.

1.7 Aims

The aim of this thesis is to further the study of MOF materials, with a focus on microfluidic synthesis. In particular, the production of UiO-67 using a CFIR, while using the intrinsic characteristics of microfluidic synthesis to affect the UiO-67 properties. Firstly, UiO-67 has been synthesised through this microfluidic method, to ensure a good basis for the rest of the work. Following this, the phase modification of the UiO-67 has been attempted by controlling the water content present in the reaction, with the mixed phased product showing a Type IV N₂ isotherm with an increased working capacity. The microfluidic growth of Pd(0) nanoparticles in the UiO-67 material has been attempted by following and modifying literature methods. Alongside this work, a machine learning model has been developed to predict the

gas uptake of MOF materials, using literature experimental data and easily obtainable chemical descriptors to form a model that is not reliant on other computational predictions, in contrast to previous models formed in the literature.

1.8 Thesis Summary

This thesis is composed of a materials and methods chapter detailing the synthesis and characterisation used in this work, followed by four journal articles, each at different stages of publication, before drawing conclusions and suggestion of potential future work within this field.

The first article is titled "Continuous microfluidic synthesis of zirconium-based UiO-67 using a coiled flow inverter reactor", which was published in *MethodsX* in 2021. The article describes the synthesis of UiO-67 in a microfluidic reactor while using benzoic acid as the acid modulator of choice alongside details for creating a CFIR in AutoCAD to be then 3D printed.

Following this is an article titled "The controlled microfluidic formation of stable mixed phase HCP/FCC-UiO-67(Zr)-Benzoic acid through modification of water concentration", which was published by the *Journal of Porous Materials* in September 2023. The focus of this work was to form UiO-67- benzoic acid microfluidically, while the FCC to HCP phase ratio of the resulting UiO-67 product was controlled through adjusting the water content present within the reaction. Products with varying crystallinity and phase ratios were collected and analysed through X-Ray Diffraction (XRD), N₂ adsorption isotherms and Transmission Electron Microscopy (TEM).

The third article is titled "Attempts to incorporate Pd(0) nanoparticles into UiO-67 using a two stage temperature controlled microfluidic synthesis" and is currently under review with the *Journal of Cluster Science*. This article details the attempted incorporation of Pd(0) nanoparticles within the pores of microfluidically formed UiO-67, with the aim to build off the success of the previous microfluidic synthesis and adapt a literature batch synthesis of

Pd(0)-UiO-67 to this new setting. Many synthesis procedures were performed, with investigation into these products performed by XRD, TEM and X-ray photoelectron spectrometry (XPS).

The final article is titled “Gradient boosted machine learning model to predict H₂, CH₄ and CO₂ uptake in metal organic frameworks using experimental data”, which has been published by the Journal of Chemical Information and Modelling in 2023. This article details the formation of a gradient boosted decision tree model to predict the gravimetric uptakes of H₂, CH₄ and CO₂ into MOF structures at a wide range of temperatures and pressures. This model was trained using literature uptake data and only using chemical descriptors that could be obtained without the need for previous modelling by a researcher.

To conclude, a short section will follow these papers to discuss potential future work in this field while addressing the overall success of using microfluidic synthesis in the production of MOFs.

1.9 References

1. Kinoshita, Y., Matsubara, I., Higuchi, T., Saito, Y. *Bull. Chem. Soc. Jpn.*, 1959, **32**, 1221–1226.
2. Kinoshita, Y., Matsubara, I., Saito, Y. *Bull. Chem. Soc. Jpn.*, 1959, **32**, 1216–1221.
3. Kinoshita, Y., Matsubara, I., Saito, Y. *Bull. Chem. Soc. Jpn.*, 1959, **32**, 741–747.
4. Hoskins, B. F., Robson, R. *J. Am. Chem. Soc.*, 1990, **112**, 1546–1554.
5. Yaghi, O. M., Li, H. *J. Am. Chem. Soc.*, 1995, **117**, 10401–10402.
6. Li, H., Eddaoudi, M., O’Keeffe, M., Yaghi, O. M. *Nature*, 1999, **402**, 276–279.
7. Gangu, K. K., Maddila, S., Mukkamala, S. B., Jonnalagadda, S. B. *Inorganica Chim. Acta*, 2016, **446**, 61–74.
8. Li, J. R., Tao, Y., Yu, Q., Bu, X. H., Sakamoto, H., Kitagawa, S. *Chem. - A Eur. J.*, 2008, **14**, 2771–2776.
9. Cavka, J. H., Jakobsen, S., Olsbye, U., Guillou, N., Lamberti, C., Bordiga, S., Lillerud, K. P. *J. Am. Chem. Soc.*, 2008, **130**, 13850–13851.
10. Winarta, J., Shan, B., McIntyre, S. M., Ye, L., Wang, C., Liu, J., Mu, B. *Cryst. Growth Des.*, 2020, **20**, 1347–1362.
11. Bai, Y., Dou, Y., Xie, L. H., Rutledge, W., Li, J. R., Zhou, H. C. *Chem. Soc. Rev.*, 2016, **45**, 2327–2367.

12. Garibay, S. J., Cohen, S. M. *Chem. Commun.*, 2010, **46**, 7700–7702.
13. Fonseca, J., Gong, T., Jiao, L., Jiang, H. L. *J. Mater. Chem. A*, 2021, **9**, 10562–10611.
14. Schaate, A., Roy, P., Godt, A., Lippke, J., Waltz, F., Wiebcke, M., Behrens, P. *Chem. - A Eur. J.*, 2011, **17**, 6643–6651.
15. Zhao, Y., Zhang, Q., Li, Y., Zhang, R., Lu, G. *ACS Appl. Mater. Interfaces*, 2017, **9**, 15079–15085.
16. Øien, S., Wragg, D., Reinsch, H., Svelle, S., Bordiga, S., Lamberti, C., Lillerud, K. P. *Cryst. Growth Des.*, 2014, **14**, 5370–5372.
17. Clark, C. A., Heck, K. N., Powell, C. D., Wong, M. S. *ACS Sustain. Chem. Eng.*, 2019, **7**, 6619–6628.
18. Taddei, M., Dümbgen, K. C., Van Bokhoven, J. A., Ranocchiari, M. *Chem. Commun.*, 2016, **52**, 6411–6414.
19. Ragon, F., Horcajada, P., Chevreau, H., Hwang, Y. K., Lee, U. H., Miller, S. R., Devic, T., Chang, J. S., Serre, C. *Inorg. Chem.*, 2014, **53**, 2491–2500.
20. Zahn, G., Zerner, P., Lippke, J., Kempf, F. L., Lilienthal, S., Schröder, C. A., Schneider, A. M., Behrens, P. *CrystEngComm*, 2014, **16**, 9198–9207.
21. Goodenough, I., Devulapalli, V. S. D., Xu, W., Boyanich, M. C., Luo, T. Y., De Souza, M., Richard, M., Rosi, N. L., Borguet, E. *Chem. Mater.*, 2021, **33**, 910–920.
22. Bambalaza, S. E., Langmi, H. W., Mokaya, R., Musyoka, N. M., Ren, J., Khotseng, L. E. *J. Mater. Chem. A*, 2018, **6**, 23569–23577.
23. Zhao, Q., Du, Q., Yang, Y., Zhao, Z., Cheng, J., Bi, F., Shi, X., Xu, J., Zhang, X. *Chem. Eng. J.*, 2022, **433**, 134510.
24. Atzori, C., Shearer, G. C., Maschio, L., Civalleri, B., Bonino, F., Lamberti, C., Svelle, S., Lillerud, K. P., Bordiga, S. *J. Phys. Chem. C*, 2017, **121**, 9312–9324.
25. Shearer, G. C., Chavan, S., Bordiga, S., Svelle, S., Olsbye, U., Lillerud, K. P. *Chem. Mater.*, 2016, **28**, 3749–3761.
26. Wu, H., Chua, Y. S., Krungleviciute, V., Tyagi, M., Chen, P., Yildirim, T., Zhou, W. *J. Am. Chem. Soc.*, 2013, **135**, 10525–10532.
27. Gutov, O. V., Hevia, M. G., Escudero-Adán, E. C., Shafir, A. *Inorg. Chem.*, 2015, **54**, 8396–8400.
28. Vermoortele, F., Bueken, B., Le Bars, G., Van De Voorde, B., Vandichel, M., Houthoofd, K., Vimont, A., Daturi, M., Waroquier, M., Van Speybroeck, V., Kirschhock, C., De Vos, D. E. *J. Am. Chem. Soc.*, 2013, **135**, 11465–11468.
29. Valenzano, L., Civalleri, B., Chavan, S., Bordiga, S., Nilsen, M. H., Jakobsen, S., Lillerud, K. P., Lamberti, C. *Chem. Mater.*, 2011, **23**, 1700–1718.
30. Hajek, J., Vandichel, M., Van De Voorde, B., Bueken, B., De Vos, D., Waroquier, M., Van Speybroeck, V. *J. Catal.*, 2015, **331**, 1–12.
31. Vermoortele, F., Vimont, A., Serre, C., De Vos, D. *Chem. Commun.*, 2011, **47**, 1521–1523.
32. Fang, Z., Bueken, B., De Vos, D. E., Fischer, R. A. *Angew. Chemie - Int. Ed.*, 2015, **54**, 7234–7254.

33. Cliffe, M. J., Wan, W., Zou, X., Chater, P. A., Kleppe, A. K., Tucker, M. G., Wilhelm, H., Funnell, N. P., Coudert, F. X., Goodwin, A. L. *Nat. Commun.*, 2014, **5**, 1–8.
34. Shan, B., McIntyre, S. M., Armstrong, M. R., Shen, Y., Mu, B. *Ind. Eng. Chem. Res.*, 2018, **57**, 14233–14241.
35. Chen, X., Lyu, Y., Wang, Z., Qiao, X., Gates, B. C., Yang, D. *ACS Catal.*, 2020, **10**, 2906–2914.
36. Ma, C., Zheng, L., Wang, G., Guo, J., Li, L., He, Q., Chen, Y., Zhang, H. *Aggregate*, 2022, **3**, 1–15.
37. Firth, F. C. N., Cliffe, M. J., Vulpe, D., Aragonés-Anglada, M., Moghadam, P. Z., Fairen-Jimenez, D., Slater, B., Grey, C. P. *J. Mater. Chem. A*, 2019, **7**, 7459–7469.
38. Cliffe, M. J., Castillo-Martínez, E., Wu, Y., Lee, J., Forse, A. C., Firth, F. C. N., Moghadam, P. Z., Fairen-Jimenez, D., Gaultois, M. W., Hill, J. A., Magdysyuk, O. V., Slater, B., Goodwin, A. L., Grey, C. P. *J. Am. Chem. Soc.*, 2017, **139**, 5397–5404.
39. Vahabi, A. H., Norouzi, F., Sheibani, E., Rahimi-Nasrabadi, M. *Coord. Chem. Rev.*, 2021, **445**, 214050.
40. Benseghir, Y., Lemarchand, A., Duguet, M., Mialane, P., Gomez-Mingot, M., Roch-Marchal, C., Pino, T., Ha-Thi, M. H., Haouas, M., Fontecave, M., Dolbecq, A., Sassoie, C., Mellot-Draznieks, C. *J. Am. Chem. Soc.*, 2020, **142**, 9428–9438.
41. Xiao, J. D., Shang, Q., Xiong, Y., Zhang, Q., Luo, Y., Yu, S. H., Jiang, H. L. *Angew. Chemie - Int. Ed.*, 2016, **55**, 9389–9393.
42. Grigoropoulos, A., McKay, A. I., Katsoulidis, A. P., Davies, R. P., Haynes, A., Brammer, L., Xiao, J., Weller, A. S., Rosseinsky, M. J. *Angew. Chemie Int. Ed.*, 2018, **57**, 4532–4537.
43. Wang, X., Wang, Y., Ying, Y. *TrAC - Trends Anal. Chem.*, 2021, **143**, 116395.
44. Dhakshinamoorthy, A., Navalón, S., Asiri, A. M., Garcia, H. *ChemMedChem*, 2020, **15**, 2236–2256.
45. Esken, D., Turner, S., Lebedev, O. I., Van Tendeloo, G., Fischer, R. A. *Chem. Mater.*, 2010, **22**, 6393–6401.
46. Sharma, A. S., Kaur, H., Shah, D. *RSC Adv.*, 2016, **6**, 28688–28727.
47. Ling, P., Qian, C., Yu, J., Gao, F. *Biosens. Bioelectron.*, 2020, **149**, 111838.
48. Proch, S., Herrmannsdörfer, J., Kempe, R., Kern, C., Jess, A., Seyfarth, L., Senker, J. *Chem. Eur. J.*, 2008, **14**, 8204–8212.
49. Dhakshinamoorthy, A., Garcia, H. *Chem. Soc. Rev.*, 2012, **41**, 5262–5284.
50. Falcaro, P., Ricco, R., Yazdi, A., Imaz, I., Furukawa, S., MasPOCH, D., Ameloot, R., Evans, J. D., Doonan, C. J. *Coord. Chem. Rev.*, 2016, **307**, 237–254.
51. Rösler, C., Fischer, R. A. *CrystEngComm*, 2015, **17**, 199–217.
52. Zlotea, C., Campesi, R., Cuevas, F., Leroy, E., Dibandjo, P., Volkringer, C., Loiseau, T., Ferey, G., Latroche, M. *J. Am. Chem. Soc.*, 2010, **132**, 2991–2997.
53. He, L., Dumée, L. F., Liu, D., Velleman, L., She, F., Banos, C., Davies, J. B., Kong, L. *RSC Adv.*, 2015, **5**, 10707–10715.
54. Hermes, S., Schröder, F., Amirjalayer, S., Schmid, R., Fischer, R. A. *J. Mater. Chem.*,

- 2006, **16**, 2464–2472.
55. Chen, L., Chen, X., Liu, H., Bai, C., Li, Y. *J. Mater. Chem. A*, 2015, **3**, 15259–15264.
 56. Chen, L., Chen, H., Li, Y. *Chem. Commun.*, 2014, **50**, 14752–14755.
 57. Rubio-Martinez, M., Avci-Camur, C., Thornton, A. W., Imaz, I., MasPOCH, D., Hill, M. R. *Chem. Soc. Rev.*, 2017, **46**, 3453–3480.
 58. Yaghi, O. M., Li, G., Li, H. *Nature*, 1995, **378**, 703–706.
 59. Stock, N., Biswas, S. *Chem. Rev.*, 2012, **112**, 933–969.
 60. Hu, Z., Zhao, D. *Dalt. Trans.*, 2015, **44**, 19018–19040.
 61. Dunne, P. W., Lester, E., Walton, R. I. *React. Chem. Eng.*, 2016, **1**, 352–360.
 62. Hu, G., Yang, L., Li, Y., Wang, L. *J. Mater. Chem. B*, 2018, **6**, 7936–7942.
 63. Jambovane, S. R., Nune, S. K., Kelly, R. T., McGrail, B. P., Wang, Z., Nandasiri, M. I., Katipamula, S., Trader, C., Schaef, H. T. *Sci. Rep.*, 2016, **6**, 1–9.
 64. Whitesides, G. M. *Nature*, 2006, **442**, 368–373.
 65. Hung, L. H., Lee, A. P. *J. Med. Biol. Eng.*, 2007, **27**, 1–6.
 66. Whitesides, G. M., Stroock, A. D. *Phys. Today*, 2001, **54**, 42.
 67. Nguyen, N. T., Wu, Z. *J. Micromechanics Microengineering*, 2005, **15**.
 68. Fan, J., Li, S., Wu, Z., Chen, Z. In *Microfluidics for Pharmaceutical Applications* Elsevier 2018; pp. 79–100.
 69. Bayareh, M., Ashani, M. N., Usefian, A. *Chem. Eng. Process. - Process Intensif.*, 2020, **147**, 1–19.
 70. Singh, J., Srivastava, V., Nigam, K. D. P. *Ind. Eng. Chem. Res.*, 2016, **55**, 3861–3870.
 71. Asrami, M. R., Tran, N. N., Nigam, K. D. P., Hessel, V. *Sep. Purif. Technol.*, 2021, **262**, 118289.
 72. Wu, K. J., Torrente-Murciano, L. *React. Chem. Eng.*, 2018, **3**, 267–276.
 73. Saxena, A. K., Nigam, K. D. P. *AIChE J.*, 1984, **30**, 363–368.
 74. Ameloot, R., Vermoortele, F., Vanhove, W., Roeffaers, M. B. J., Sels, B. F., De Vos, D. E. *Nat. Chem.*, 2011, **3**, 382–387.
 75. Faustini, M., Kim, J., Jeong, G. Y., Kim, J. Y., Moon, H. R., Ahn, W. S., Kim, D. P. *J. Am. Chem. Soc.*, 2013, **135**, 14619–14626.
 76. Fu, Q., Niu, W., Yan, L., Xie, W., Jiang, H., Zhang, S., Yang, L., Wang, Y., Xing, Y., Zhao, X. *Mater. Lett.*, 2023, **343**, 134344.
 77. Yuanlei, S., Jokar, Z., Khedri, E., Khanaman, P. M., Mohammadgholian, M., Ghotbi, M., Shafiee, S., Li, Z. X., Inc, M. *Eng. Anal. Bound. Elem.*, 2023, **149**, 166–176.
 78. Tai, S., Zhang, W., Zhang, J., Luo, G., Jia, Y., Deng, M., Ling, Y. *Microporous Mesoporous Mater.*, 2016, **220**, 148–154.
 79. Vo, T. K., Quang, D. T., Song, M., Kim, D., Kim, J. *Microporous Mesoporous Mater.*, 2020, **306**, 110405.
 80. Li, H., Wang, K., Sun, Y., Lollar, C. T., Li, J., Zhou, H. C. *Mater. Today*, 2018, **21**,

- 108–121.
81. Czaja, A. U., Trukhan, N., Müller, U. *Chem. Soc. Rev.*, 2009, **38**, 1284–1293.
 82. Kondo, M., Yoshitomi, T., Matsuzaka, H., Kitagawa, S., Seki, K. *Angew. Chemie Int. Ed. English*, 1997, **36**, 1725–1727.
 83. Sumida, K., Rogow, D. L., Mason, J. A., McDonald, T. M., Bloch, E. D., Herm, Z. R., Bae, T.-H., Long, J. R. *Chem. Rev.*, 2012, **112**, 724–781.
 84. Millward, A. R., Yaghi, O. M. *J. Am. Chem. Soc.*, 2005, **127**, 17998–17999.
 85. Liu, Y., Wang, Z. U., Zhou, H.-C. *Greenh. Gases Sci. Technol.*, 2012, **2**, 239–259.
 86. Serra-Crespo, P., Ramos-Fernandez, E. V., Gascon, J., Kapteijn, F. *Chem. Mater.*, 2011, **23**, 2565–2572.
 87. Ghanbari, T., Abnisa, F., Daud, W. M. A. W. *Sci. Total Environ.*, 2020, **707**, 135090.
 88. van den Berg, A. W. C., Areán, C. O. *Chem. Commun.*, 2008, 668–681.
 89. Chen, Z., Kirlikovali, K. O., Idrees, K. B., Wasson, M. C., Farha, O. K. *Chem*, 2022, **8**, 693–716.
 90. Durbin, D. J., Malardier-Jugroot, C. *Int. J. Hydrogen Energy*, 2013, **38**, 14595–14617.
 91. Allendorf, M. D., Hulvey, Z., Gennett, T., Ahmed, A., Autrey, T., Camp, J., Cho, E. S., Furukawa, H., Haranczyk, M., Head-Gordon, M., others *Energy Environ. Sci.*, 2018, **11**, 2784–2812.
 92. Rosi, N. L., Eckert, J., Eddaoudi, M., Vodak, D. T., Kim, J., O’Keeffe, M., Yaghi, O. M. *Science (80-.)*, 2003, **300**, 1127–1129.
 93. Shet, S. P., Shanmuga Priya, S., Sudhakar, K., Tahir, M. *Int. J. Hydrogen Energy*, 2021, **46**, 11782–11803.
 94. Wang, Y., Lan, Z., Huang, X., Liu, H., Guo, J. *Int. J. Hydrogen Energy*, 2019, **44**, 28863–28873.
 95. Miguel, C. V., Soria, M. A., Mendes, A., Madeira, L. M. *Chem. Eng. J.*, 2017, **322**, 590–602.
 96. Chynoweth, D. P., Owens, J. M., Legrand, R. *Renew. energy*, 2001, **22**, 1–8.
 97. Kumar, K. V., Preuss, K., Titirici, M.-M., Rodríguez-Reinoso, F. *Chem. Rev.*, 2017, **117**, 1796–1825.
 98. Li, L., Tang, S., Wang, C., Lv, X., Jiang, M., Wu, H., Zhao, X. *Chem. Commun.*, 2014, **50**, 2304–2307.
 99. Connolly, B. M., Aragonés-Anglada, M., Gandara-Loe, J., Danaf, N. A., Lamb, D. C., Mehta, J. P., Vulpe, D., Wuttke, S., Silvestre-Albero, J., Moghadam, P. Z., Wheatley, A. E. H., Fairen-Jimenez, D. *Nat. Commun.*, 2019, **10**, 1–11.
 100. Xydias, P., Spanopoulos, I., Klontzas, E., Froudakis, G. E., Trikalitis, P. N. *Inorg. Chem.*, 2014, **53**, 679–681.
 101. Demir, H., Daglar, H., Gulbalkan, H. C., Aksu, G. O., Keskin, S. *Coord. Chem. Rev.*, 2023, **484**, 215112.
 102. Chong, S., Lee, S., Kim, B., Kim, J. *Coord. Chem. Rev.*, 2020, **423**, 213487.
 103. Ahmed, A., Seth, S., Purewal, J., Wong-Foy, A. G., Veenstra, M., Matzger, A. J.,

- Siegel, D. J. *Nat. Commun.*, 2019, **10**, 1568.
104. Pardakhti, M., Moharreri, E., Wanik, D., Suib, S. L., Srivastava, R. *ACS Comb. Sci.*, 2017, **19**, 640–645.
105. Fanourgakis, G. S., Gkagkas, K., Tylianakis, E., Froudakis, G. E. *J. Am. Chem. Soc.*, 2020, **142**, 3814–3822.
106. Yu, J., Xie, L. H., Li, J. R., Ma, Y., Seminario, J. M., Balbuena, P. B. *Chem. Rev.*, 2017, **117**, 9674–9754.
107. Fernandez, M., Barnard, A. S. *ACS Comb. Sci.*, 2016, **18**, 243–252.
108. Altintas, C., Altundal, O. F., Keskin, S., Yildirim, R. *J. Chem. Inf. Model.*, 2021, **61**, 2131–2146.
109. Chung, Y. G., Camp, J., Haranczyk, M., Sikora, B. J., Bury, W., Krungleviciute, V., Yildirim, T., Farha, O. K., Sholl, D. S., Snurr, R. Q. *Chem. Mater.*, 2014, **26**, 6185–6192.
110. Chung, Y. G., Haldoupis, E., Bucior, B. J., Haranczyk, M., Lee, S., Zhang, H., Vogiatzis, K. D., Milisavljevic, M., Ling, S., Camp, J. S., Slater, B., Siepmann, J. I., Sholl, D. S., Snurr, R. Q. *J. Chem. Eng. Data*, 2019, **64**, 5985–5998.
111. Borboudakis, G., Stergiannakos, T., Frysali, M., Klontzas, E., Tsamardinos, I., Froudakis, G. E. *npj Comput. Mater.*, 2017, **3**, 1–6.
112. Zhang, Z., Cao, X., Geng, C., Sun, Y., He, Y., Qiao, Z., Zhong, C. *J. Memb. Sci.*, 2022, **650**, 120399.
113. Daglar, H., Keskin, S. *ACS Appl. Mater. Interfaces*, 2022, **14**, 32134–32148.
114. Luo, Y., Bag, S., Zaremba, O., Cierpka, A., Andreo, J., Wuttke, S., Friederich, P., Tsotsalas, M. *Angew. Chemie - Int. Ed.*, 2022, **61**.

Chapter 2 Materials and Methods

2.1 Section overview

This section will outline the general synthesis, characterisation and machine learning methods that have been used throughout this work, with a focus on why certain techniques have been chosen and what information they can provide. This includes Microfluidic Reactors, X-ray Diffraction (XRD), Gas Adsorption Isotherms, Electron Microscopy, X-ray Photoelectron Spectroscopy (XPS) and the various machine learning techniques. Specific experimental details are given within the papers that follow.

2.2 Microfluidic Reactors

Microfluidic reactors provide the continuous flow of reactants through microchannels, with the high surface area to volume ratio leading to certain benefits as described in Chapter 1.2. There are two key categories of microreactor: micro-channel reactors and micro-tubular reactors. Micro-channel reactors are traditionally formed of poly(dimethylsiloxane) (PDMS), by soft lithography with this giving a high level of reactor design, allowing the introduction of many passive mixing elements.¹ However, a key disadvantage for these reactors is in the building process, as soft lithography requires the use of a clean room.² 3D printing avoids this problem, as with a 3D printer and appropriate software (AutoCAD for example), any shape designed can be formed easily. 3D printing also allows for the formation of more complex structures, which would not be easily made using lithography, such as coils. The key barrier in the use of 3D printed microreactors is the low resolution of 3D printing as compared to soft lithography techniques. The maximum resolution for 3D printing is around 100 μm diameter channels, whereas for PDMS lithography is approximately 5 μm diameter channels as standard (but can be lower using different photo masks).² 3D printing can be further used to form scaffolds for microtubular reactors, which give various advantages. The main advantage is that these scaffolds will hold a specific length of tubing in place, meaning that if this reaction is to be repeated in the future, the flow pattern should be identical. Depending on how this tubing is arranged, it may influence the flow pattern in a specific way, such as CFIRs, which were discussed in Chapter 1.2. This reactor for this work was chosen due to the ease of development, repeatability with the tubing held in place and ease for modification of the reactor, such as printing a larger CFIR unit or stacking units to increase the reactor length.

The CFIR, as briefly mentioned in Chapter 1.2, is an improvement on a standard coiled tubing reactor in several keyways. While the coiled reactor will provide a higher level of passive mixing than a straight tubing reactor, with enhanced Dean vortices present, if it is only coiled

in a single direction then certain hotspots will appear in the mixing due to centrifugal forces.³ To give consistent mixing throughout the reactor, inverting the direction of the tubing by 90° four times will result in these hotspots averaging out (**Figure 2.1**). The consistent tubing pattern from the frame should also give more repeatable results, with researchers looking at this work being able to exactly replicate the flow patterns through printing an identical CFIR piece.

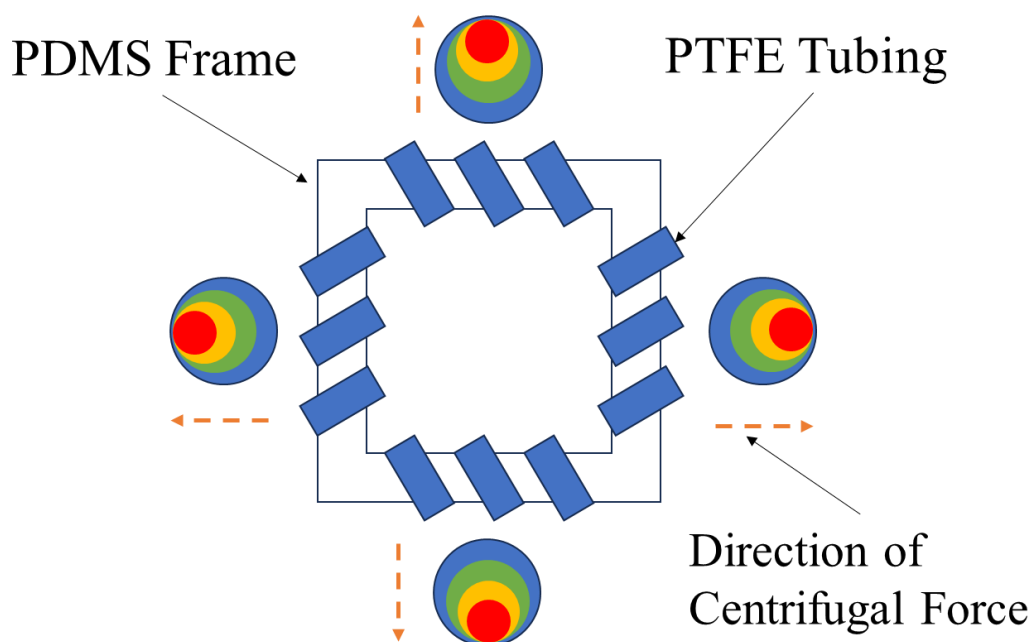


Figure 2.1: Basic schematic of a CFIR, highlighting the change in the centrifugal force direction when inverting the tubing by 90°. Coloured circles represent the centrifugal hotspots and their direction on each side of the CFIR. Orange dashed arrows show the direction of the centrifugal force on each side of the CFIR.

2.3 Characterisation techniques

2.3.1 X-Ray Diffraction (XRD)

XRD is a non-destructive analysis technique that provides information on the crystallographic structure of a given material.⁴ In general terms, X-rays are emitted towards a sample at a set angle (θ), with a detector following at the same angle. As X-rays interact with the atoms in the sample, the X-rays will be diffracted by the atomic planes in the crystal lattice. As the wavelength of X-rays is on a same order as atomic distances, 0.1 – 10 Å, constructive interference of these waves may occur if the atoms are present in an ordered format. Bragg's law can be used to explain this phenomenon (**Equation 2.1**). **Figure 2.2** shows a basic scheme

of this process. The long-range order of a crystalline structure will cause a high level of constructive interference, resulting in the high intensity peaks seen in a XRD pattern.

$$n\lambda = 2d \sin\theta \quad \text{Equation 2.1}$$

Equation 2.1: Bragg Equation. n = diffraction order, λ = wavelength (Å), d = spacing of atomic layers (Å), θ = angle of x-ray incidence.

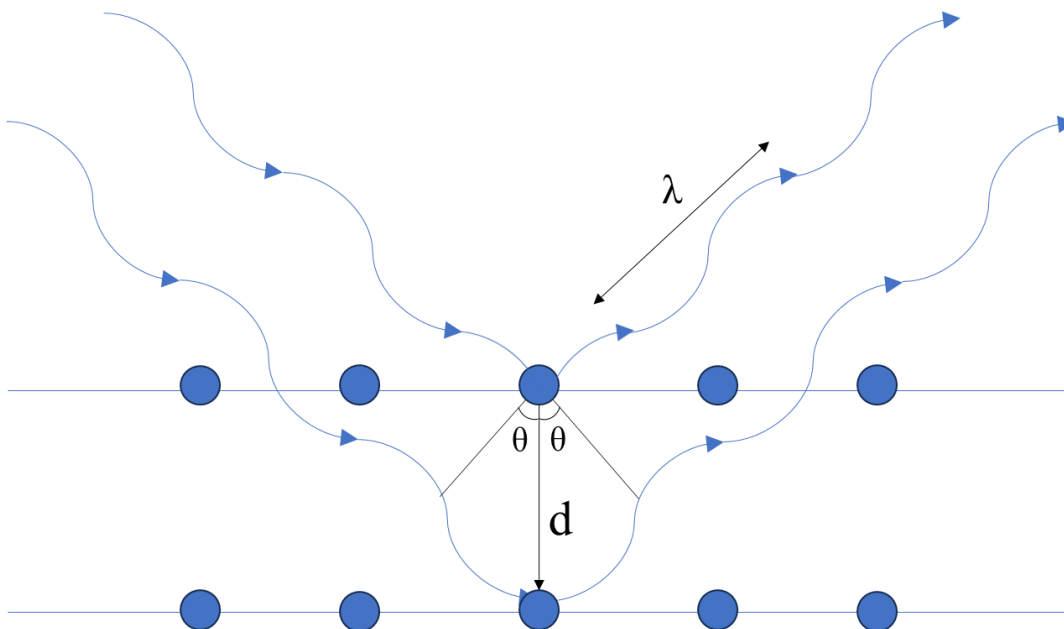


Figure 2.2: Scheme depicting the principle of XRD. X-rays (curved blue lines) hit the atoms (blue circles) at angle θ and are diffracted. The distance between the atom layers is given as d .

The angle and intensity of the diffracted X-rays can give certain information about the d spacing of the parallel crystal cell units as well as the crystal unit type present. This is the key reason it's used in the analysis of MOF structures, giving the crystal phases present in the MOF material, through measurement of d -spacing and subsequent identification of the miller indices.⁵ As this is the dominant characterisation technique for MOFs, it can be used for confirmation of a product through literature comparison, so has been used throughout this work.

2.3.2 Gas Adsorption Isotherms

Gas adsorption isotherms are a key characterisation method for porous materials, in the determination of pore size and surface area.⁶ This is routinely performed with N_2 at 77 K, but

can be performed with other gases to determine how a material adsorbs different gases. The difference between the volume of N₂ pumped in and the known volume of the sample tube will be the volume adsorbed by the MOF material, with this data represented by a graph of relative pressure versus volume adsorbed. The relationship between the pressure and the volume adsorbed can be used to calculate the surface area or pore sizes, with the software able to make these calculations automatically.

N₂ adsorption isotherms have been used in this work to determine the MOF materials surface areas, pore sizes and as a point of comparison between the products formed in this work and in literature, as it is a routine characterisation technique in the field of MOFs. The shape of the adsorption isotherm will also give details on the distribution of pore sizes within the MOF and if the N₂ is adsorbing in a mono- or multi-layer mechanism. For example, in a microporous material, a Type I isotherm (**Figure 2.3a**) would be expected, with a sudden increase in uptake as gas pressure increases and then staying constant, which suggests a monolayer coverage of the gas.⁷ In a mesoporous material, a Type IV isotherm (**Figure 2.3b**) will be present, in which there is a sudden increase in uptake at the start as a monolayer coverage is achieved, followed by a gradual increase as multilayer adsorption starts, followed by another sharp uptake increase as the mesopores are filled completely at higher pressures through capillary condensation.⁸

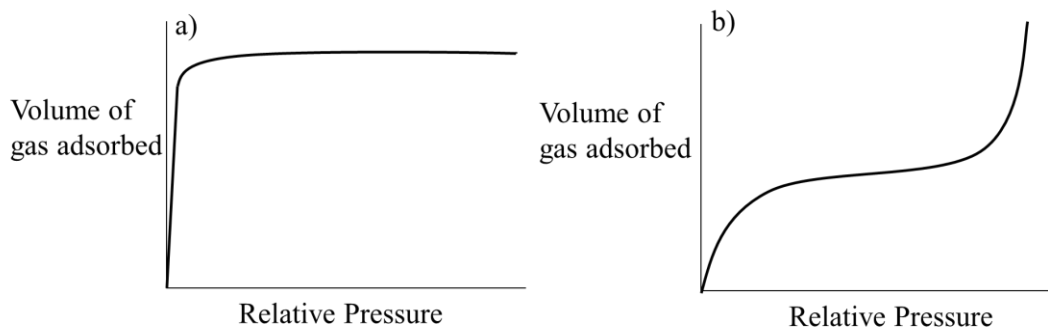


Figure 2.3 Scheme showing the general adsorption trends seen in a) Type I isotherms and b) Type IV isotherms.

2.3.3 Electron Microscopy

Scanning electron microscopy (SEM) and transmission electron microscopy (TEM) are used to image MOF materials to analyse the particle sizes, size distributions and shape, to then be compared to literature analogues.⁵

SEM is used for surface sensitive imaging of MOFs, allowing particle sizes and morphology measurements through the detection of secondary electrons emitted from the samples surface following irradiation with the electron beam.⁹ TEM produces higher resolution 2D projection images of MOF samples, using a higher energy electron beam which passes through the

sample to a detector. TEM can be used to determine certain internal features of a material, such as the presence of encapsulated nanoparticles in a MOF or direct imaging of a crystal lattice.¹⁰ While SEM requires less sample preparation (thicker samples can be used),⁹ TEM has been used primarily throughout this work due to the extra information gained and the small particle sizes encountered.

Alongside TEM, energy dispersive X-ray (EDX) spectroscopy can be used to detect and map the presence of specific elements within a sample.^{7,9} The high energy electrons that are fired at the sample for imaging also result in element specific X-ray emission being released from the sample and detected.⁶ This can be used to produce a map of the elements present, to determine if the elemental composition is consistent throughout a sample. EDX spectroscopy and mapping has been used in this work to confirm the elemental composition and distribution of elements within the synthesised materials.

2.3.4 X-ray Photoelectron Spectroscopy (XPS)

In XPS, high energy X-rays are fired at the surface of sample, causing electrons to be excited and released.¹¹ The specific kinetic energy of the electrons released will relate to the atoms element and oxidation state. These photoelectrons that are released have low energies, with electrons deep within the material unable to escape the material and reach the detector.¹² This is why only surface electrons will reach the detector, which results in a surface sensitive technique, with electrons detected that are only affected by the element/oxidation state of the atoms, with no bonding influences.¹¹

This technique has been used to determine the oxidation state of elements within the MOF material.¹⁰ For this reason, XPS has been used in the work relating to Pd nanoparticles.

2.4 Machine Learning methods

“Machine learning” is considered an development of artificial intelligence, with models formed that, when given a series of data to train with, can recognise and form patterns between the input and output data, through repeated iterations.¹³ It has been used in previous work relating to MOFs as described in the Chapters 1.4 and 2.5, with the high number of potential linker and SBU combinations leading to screening processes being necessary to find the ideal MOF for a given application. These models may output the data via Classification (discrete values, such as “High”, “Medium” “Low” etc.) or through Regression (continuous numerical values, such as the gravimetric uptake of a given gas). This work focuses on Regression techniques.

The simplest form of machine learning is through Linear Regression. In its most basic form, it is fitting a straight line to existing data, with the $y = mx + c$ equation formed being used to

predict new y values.¹⁴ This line is fit using “Least Squares”, which aims to reduce the squared residuals from the plotted line. This extends to modelling datasets with many independent x variables in Multivariate Linear Regression, with a new dimension being added to the graph for each new dependent variable, with the line of best fit now becoming a plane or other higher dimension shape.¹⁴

Decision trees are a simple but effective class of machine learning, where all the data starts at a root node and is sequentially split by internal nodes until it reaches terminal nodes (leaves).¹⁵ These internal nodes will split the data by containing a binary question that can be applied to the input descriptors. A key potential issue with decision trees is the possibility of overfitting the model to the training data. If the data keeps being split until each output has a separate leaf, this will result in a high accuracy for this set of data, but it may not adapt well to new data.¹⁶ To counter this, the “minimum leaf size” can be increased so each terminal leaf corresponds to the average of several outputs rather than just one. This will result in a loss of accuracy to the training set, but it should increase the generalisation of the model to new data.¹⁷

To counter this loss in accuracy, while ensuring that overfitting is avoided, techniques which aggregate the results of multiple decision trees have been formed, such as Gradient Boosted Decision Trees (GBDTs).¹⁵ GBTDs focus on using high numbers of DTs to increase the accuracy and generalisation of the model. GBTDs have DTs that are formed based on their previous iteration to slowly approach an accurate model.¹⁸ This is achieved by the model firstly taking the average of all the output data and then finding the difference of the output values to this average, with these differences being pseudo residuals. The model will then form a tree to predict for these residuals and not the actual outputs. This process is then repeated until the desired number of trees is formed.

To further reduce any overfitting in machine learning, cross validation techniques can be used. The most common form of validation is to randomly split the data set into 2 distinct categories: training and testing sets.¹⁹ The majority of the data will be used in the training set to form the model. The model will then perform predictions on the test set, to see how it performs with new data. As this set has not interacted with the model at all and no modifications have been made to try and improve its fitting, it is completely blind to the model, giving the most accurate representation of how the model will perform with new data in the future. By randomly selecting the data, no personal bias comes into play as well. However, since the data is selected at random, if a certain datapoint needs to be part of the training to ensure a good model is formed, it may be missed, meaning this method may be best for large datasets, where not having a specific datapoint in the training may not have a large impact.

A more modern technique for cross validation is K-Fold validation.¹⁹ This involves splitting the data into equal “folds”, with the model fitting and prediction being repeated so each dataset can be used as a “testing” set. For example, if the number of folds was set to 5, the whole dataset would be split into 5 and the fitting would be repeated 5 times, with each fitting using four sets for training and one set for testing. This ensures that all the datapoints will be used in both the training and the testing of the model, which is necessary for smaller datasets. However, the drawback of this method is the extra computational power required, with each fold added meaning a new model must be fitted.

Within this work, all these techniques described were used in order to confirm and build the best model possible.

2.5 References

1. Song, Y., Hormes, J., Kumar, C. S. S. R. *Small*, 2008, **4**, 698–711.
2. Bhattacharjee, N., Urrios, A., Kang, S., Folch, A. *Lab Chip*, 2016, **16**, 1720–1742.
3. Asrami, M. R., Tran, N. N., Nigam, K. D. P., Hessel, V. *Sep. Purif. Technol.*, 2021, **262**, 118289.
4. Raja, P. B., Munusamy, K. R., Perumal, V., Ibrahim, M. N. M. In *Nano-Bioremediation: Fundamentals and Applications* Elsevier 2022; pp. 57–83.
5. Schaate, A., Roy, P., Godt, A., Lippke, J., Waltz, F., Wiebcke, M., Behrens, P. *Chem. - A Eur. J.*, 2011, **17**, 6643–6651.
6. Sing, K. *Colloids Surfaces A Physicochem. Eng. Asp.*, 2001, **187–188**, 3–9.
7. Leng, Y. *Materials Characterization: Introduction to Microscopic and Spectroscopic Methods*, Wiley-VCH, Weinheim, 2nd edn., 2009.
8. Schneider, P. *Appl. Catal. A, Gen.*, 1995, **129**, 157–165.
9. Goodhew, P. J., Humphreys, J., Beanland, R. *Electron Microscopy and Analysis*, CRC press, London, 3rd edn., 2000.
10. Chen, L., Chen, X., Liu, H., Bai, C., Li, Y. *J. Mater. Chem. A*, 2015, **3**, 15259–15264.
11. Lee, Y.-G., Moon, H. R., Cheon, Y. E., Suh, M. P. *Angew. Chemie*, 2008, **120**, 7855–7859.
12. Stevie, F. A., Donley, C. L. *J. Vac. Sci. Technol. A*, 2020, **38**, 5–6.
13. Helm, J. M., Swiergosz, A. M., Haeberle, H. S., Karnuta, J. M., Schaffer, J. L., Krebs, V. E., Spitzer, A. I., Ramkumar, P. N. *Curr. Rev. Musculoskelet. Med.*, 2020, **13**, 69–76.
14. Maulud, D., Abdulazeez, A. M. *J. Appl. Sci. Technol. Trends*, 2020, **1**, 140–147.
15. Elith, J., Leathwick, J. R., Hastie, T. *J. Anim. Ecol.*, 2008, **77**, 802–813.
16. Kotsiantis, S. B. *Artif. Intell. Rev.*, 2013, **39**, 261–283.
17. Bramer, M. *Princ. Data Min.*, 2007, 119–134.
18. Schapire, R. E. *Nonlinear Estim. Classif.*, 2003, 149–171.

19. Yadav, S., Shukla, S. *Proc. - 6th Int. Adv. Comput. Conf. IACC 2016*, 2016, 78–83.

Chapter 3 MethodsX Journal Article, “Continuous microfluidic synthesis of zirconium-based UiO-67 using a coiled flow inverter reactor”, Published Jan 2021, <https://doi.org/10.1016/j.mex.2021.101246>

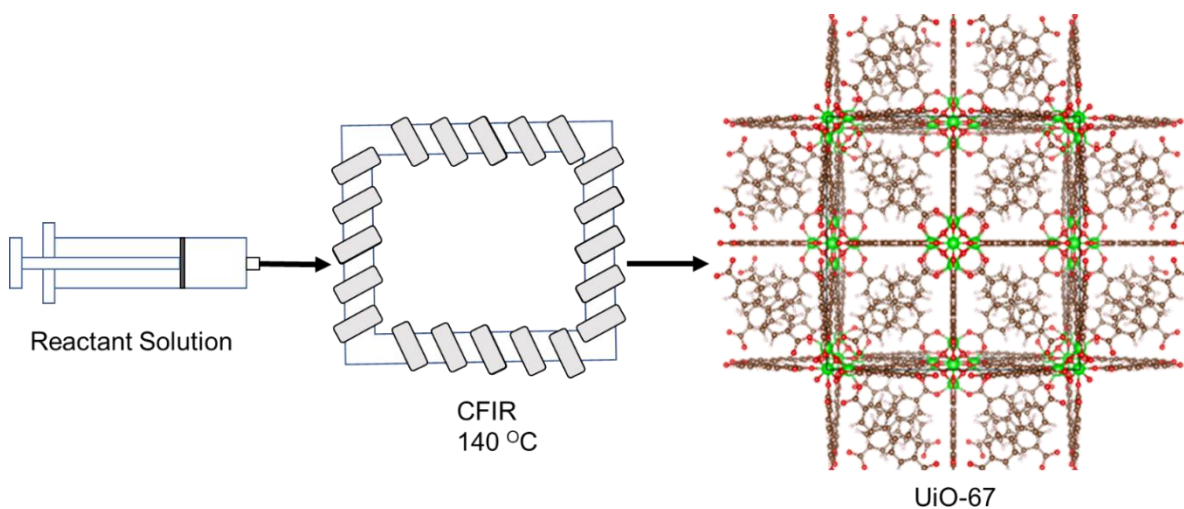
Tom Bailey, Merwyn Pinto, Nicole Hondow, Ke-Jun Wu

School of Chemical and Process Engineering, The University of Leeds, United Kingdom

3.1 Abstract

Metal-organic frameworks (MOFs), particularly Zirconium based, have a wide variety of potential applications, such as catalysis and separation. However, these are held back by traditionally only being synthesised in long batch reactions, which causes the process to be expensive and limit the amount of reaction control available, leading to potential batch to batch variation in the products, such as particle size distributions. Microfluidics allows for batch reactions to be performed with enhanced mass/heat transfer, with the coiled flow inverter reactor (CFIR) setup narrowing the residence time distribution, which is key in controlling the particle size and crystallinity. In this work, a Zirconium based MOF, UiO-67, has been synthesised continuously using a microfluidic CFIR, which has allowed for the product to be formed in 30 minutes, a fraction of the traditional batch heating time of 24 hours. The microfluidically synthesised UiO-67 is also smaller product with a narrower particle size distribution ($\approx 200\text{nm}$ to $\approx 400\text{ nm}$) than its batch counterpart ($\sim 500\text{ nm}$ to over $3\text{ }\mu\text{m}$).

3.2 Graphical Abstract



3.3 Abbreviations

BPDC: Biphenyl-4,4-dicarboxylic acid

CFIR: Coiled flow inverter reactor

DMF: Dimethylformamide

MOFs: Metal organic frameworks

PXRD: Powder X-Ray Diffraction

RTD: Residence Time Distribution

SBU: Secondary Building Unit

SEM: Scanning Electron Microscopy

UiO: Universitetet i Oslo

3.4 Background

Metal-organic frameworks (MOFs) are a class of porous coordination polymer, discovered in 1990 with the appearance of a $[\text{N}(\text{CH}_3)_4][\text{CuZn}(\text{CN})_4]$ cubic structure.¹ These materials are composed of metal containing secondary building units (SBUs) and organic linker units, with a general representation in **Figure 3.1**. Due to being made up of these combinations, there is almost an unlimited number of structures theoretically available, with MOFs also prone to modification after synthesis. These MOFs can be used in a wide variety of applications, such as gas capture/separation, catalysis and drug delivery.^{2,3}

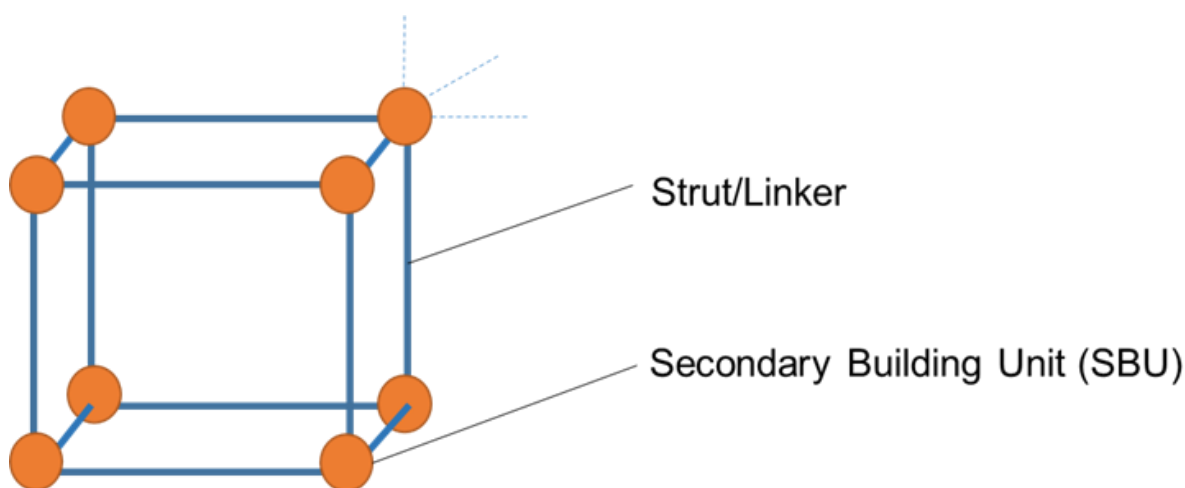


Figure 3.1: Representation of a MOF structure, with SBUs and linker units highlighted

Zirconium based MOFs, such as the University of Oslo (UiO) type MOFs, are of interest due to their relatively high thermal and acid/base stabilities, comparatively to non-Zr(IV) carboxylate containing MOFs.⁴ They have previously been used in a range of applications, such as hydrogenation catalysis,⁵ adsorption of illegal organic dyes,⁶ modified for gas storage and many others.⁷ UiO-67 was chosen for this work due to a lack of work on its microfluidic synthesis being present, when compared to the other main member of this group, UiO-66.^{8,9} UiO-67 is a larger analogue of the UiO group, so will have a higher surface area and be more efficient in absorption than UiO-66. A typical synthetic protocol for UiO-67, is represented in the **Figure 3.2**. An issue with these MOFs however, is that their production is traditionally through the use of a lengthy batch process, with *Schaate et al* reporting a 24 hour reaction

time, followed by time taken to wash and dry the product.¹⁰ Another issue with batch processes is the lack of reaction control present, which can lead to wider particle size distributions. Previous work by Zhang et al has shown that the particle size distribution of UiO-67 directly affects its absorption abilities, with a narrower distribution enhancing the absorption of organic dyes, so control over this is important.¹¹ A way to speed up this synthesis process and allow for further reaction control could be using microfluidic reactors.

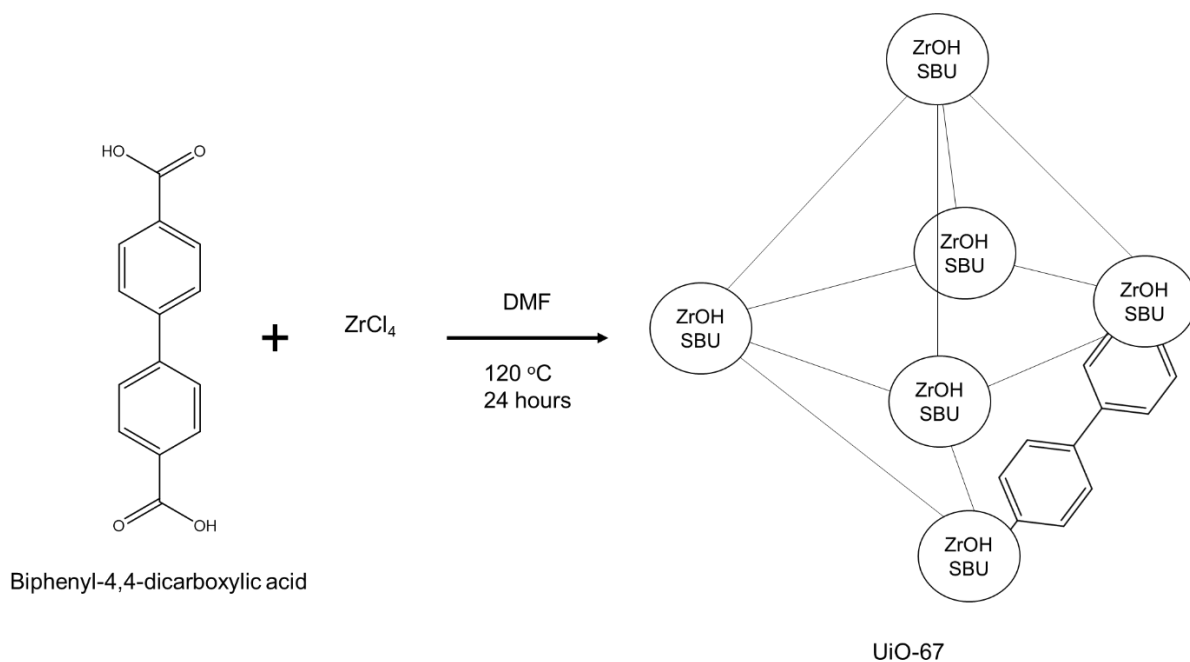


Figure 3.2: Basic reaction scheme for the synthesis of UiO-67

Microfluidic synthesis occurs within micrometre sized channels, causing higher levels of mixing and heat transfer due to the higher surface area to volume ratio.¹² This higher mixing efficiency allows for greater control over the reaction, which means greater control of nanoparticle size for example.¹³ Microfluidic reactors have been used to synthesis a variety of materials, such as: metal nano-rods,¹⁴ quantum dots and more recently MOFs.^{8,9,15} A key development in the microfluidic synthesis of MOFs was published by Faustini et al, in which several MOF structures, including UiO-66, were successfully synthesised through the use of two-phase droplet synthesis, with reactant/DMF droplets being carried through a reactor by silicon oil.⁸ This showed that crystalline MOFs could be formed in lower reaction times when a microfluidic system was used, but showed the system could be still improved. Mainly, the

use of two phases will increase the costs of production, with large amounts of silicon oil (in a 5:1 ratio with the reactant mixture) will be used and will be largely unrecoverable for synthesis of UiO-66 at 140 °C. To simplify these systems, while still ensuring the high level of micro-mixing present in droplet reactors would be a key challenge. Following this work, Tai et al were successful in synthesising UiO-66 in a single phase microfluidic reaction, where it was found that by varying the residence time, a certain level of control could be achieved over the particle size.⁹ Higher flowrates/shorter residence times results in smaller UiO-66 particles, so ensuring this residence time distribution is narrow would be key for ensuring the particle size distribution would also be narrow. Further work has been performed on other MOF groups, such as ZIF-8, which was synthesised in a microfluidic process by Kolomykov et al, while ensuring size control also through variation of the residence time.¹⁶ They were successful in generally controlling the size through the variation of reaction conditions, but their relative particle size distributions were still high, with enhanced mixing for this system potentially being a solution. So, by adapting previous work of microfluidic based MOF synthesis, and combining it with the batch method used for the synthesis of UiO-67, it should be possible to form UiO-67 in a continuous method, while using enhanced mixing from reactor design to narrow the particle size distributions. This reactor design could then be used with future materials that would also benefit from consistent particle size.

While heat and mass transfer are improved in microfluidic systems, mixing is limited to molecular diffusion, due to the laminar flow of the system. Laminar flow also has a relatively large residence time distribution (RTD), as fluid near the channel walls will travel slower due to friction forces. To improve the mixing present in microtubular systems, the tubing can be arranged in specific patterns which may influence the mixing. One example of this is through the use of coiled flow inverter reactors (CFIRs), which arrange the tubing in helical patterns, while also including 90° inversions in the flow, which enhance the mixing through secondary flow patterns appearing in the system.¹⁷ These secondary flow patterns are called Dean Vortices and they enhance the radial mixing in the system, narrowing the RTD.¹⁸ The 90° turns

cause the direction of the centrifugal force to change across the fluid, which flattens the laminar flow pattern and eliminates stagnant mixing zones in the system, which further reduces the RTD. Work performed by Wu and Torrente-Murciano found that size distribution of silver nanoparticles synthesized in this system were narrower than their straight helical counterparts, showing the enhanced mixing and lower RTDs.¹⁷ Using this CFIR system should give MOF particles with narrower particle size distributions in a continuous method, which would be ideal for future applications where particle size will be important (e.g. absorption).

This paper describes the construction and application of a continuous CFIR microfluidic reactor for the production of UiO-67, which is a relatively small system that can be placed on a laboratory benchtop. Success in forming UiO-67 in a relatively short time, due to enhanced mixing and heat transfer in the system, highlights the potential use of this system for the formation of other MOFs in quick and continuous processes, with the reaction times and temperatures easily variable. The produced UiO-67 also showed a narrower particle size distribution, due to the enhanced mixing from the CFIR.

3.5 Overview of the method

Figure 3.3 shows a schematic overview of the protocol. The CFIR is composed of polytetrafluoroethylene (PTFE) tubing (0.79 mm ID, 1/16" OD) coiled around 3D printed support fabricated with commercial high-temperature resin. The CFIR is placed into an oil bath, to be heated by a magnetic stirrer hotplate. The inlet to this reactor is connected to a syringe via IDEX flangeless fittings and threaded luer adapters (exact models provided in the Equipment section), with the syringe then sitting in the syringe pump once the reactant solution has been drawn up. This is then pumped through the heated system at a constant rate, with the product collected in a 100 ml glass flask at the end. This product then requires washing with fresh DMF and methanol and then drying to remove any solvent present in the materials pores. The UiO-67 is then analysed by PXRD and SEM.

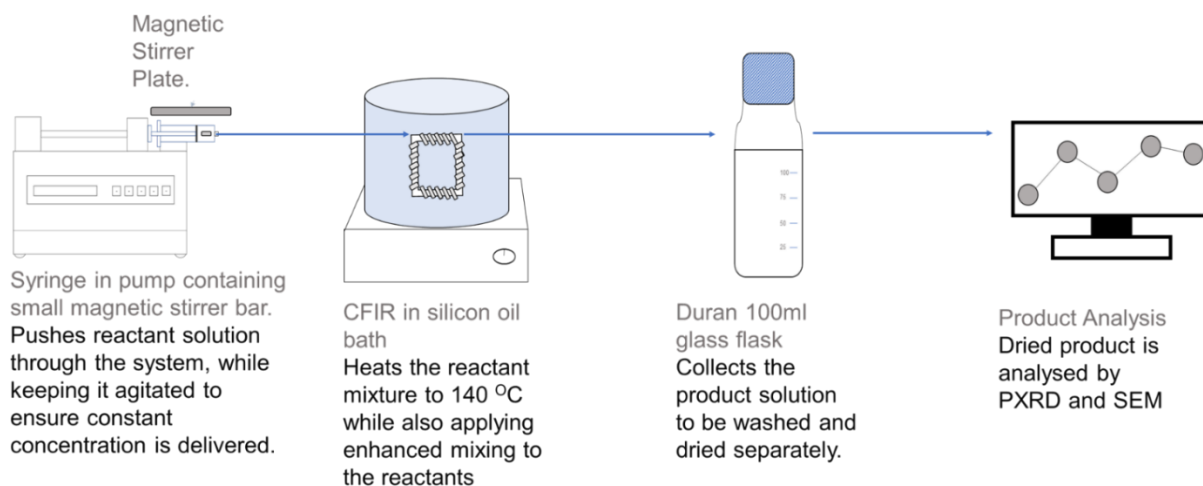


Figure 3.3: Schematic of protocol, showing the workflow from the syringe pump to the product.

3.6 Materials

3.6.1 Chemicals

Zirconium chloride (98%, Cat number: L14891) and silicon oil (Cat number: A12728.36) were purchased from Alfa Aesar. Benzoic acid (99%, Cat number: 237766) and biphenyl dicarboxylic acid (BPDC; 95%, Cat number: 091522) were purchased from Fluorochem. Methanol (>99.9%, Cat number: 34860-2.5L-R) and dimethylformamide (DMF; >99.9%, Cat number: 27054) were purchased from Sigma Aldrich. All the reagents were used as received without further purification.

3.6.2 Equipment

- Syringe pumps (Fusion 101, Chemyx)
- Magnetic Stirrers (IKA, C-MAG HS7) with Electronic contact thermometer (IKA, ETS-D5, resolution of 0.1 °C)
- Tubing (PTFE, 1/32 ID 1/16 OD, Adtech)
- Centrifuge (Centurion 2000 Series)
- X-Ray Diffractor (Bruker D8 ,1.54 Å, $2\theta = 5^\circ - 45^\circ$)
- Flangeless Fitting (PEEK, 1/16" OD, IDEX Health & Science), Catalogue number: XP-283
- Luer Adapter (Female Luer x Female 1/4-28 Flat Bottom, IDEX Health & Science), Catalogue number: P-628
- Syringe (10 ml HSW Air Tite All Plastic)
- Scanning Electron Microscope (Carl Zeiss EVO MA15)

3.7 Equipment Setup

3.7.1 Coiled Flow Invertor Reactor

The design of the CFIR requires a skeleton-based structure to be formed using AutoCAD software initially, so a 2D wireframe view was therefore selected as the preferred visual style to begin with. A typical procedure to draw the skeleton-based structure (helix diameter: 5 mm, pitch distance: 3 mm, and total length: about 3.16 m) involves:

1. A circle of radius 5 mm is first created. A helix, of height 75 mm, is then created with a base and top radius identical to the initial circle. The helix turn properties are altered to 25 turns with a turn height of 3 mm. The centre of the helix is then translated a distance 10 directly above the centre of the initial circle. This sequence of steps is illustrated below in **Figure 3.4**.

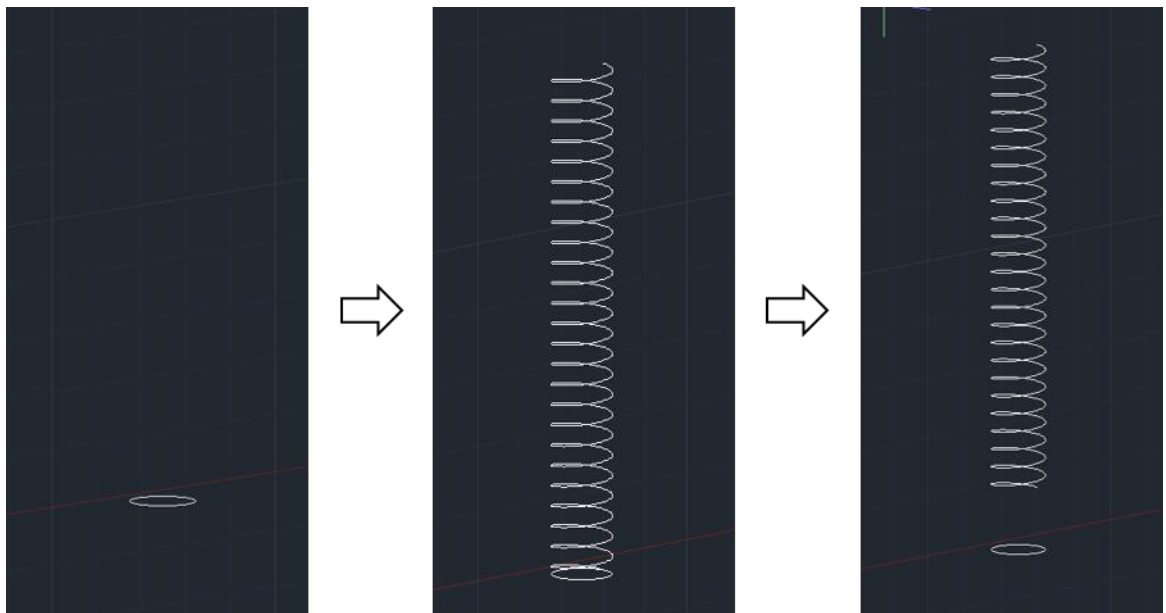


Figure 3.4: Series of steps used to form the basic helix shape in AutoCAD.

2. This assembly is copied, rotated horizontally, and aligned in a manner to ensure a continuous link is formed between the helixes and is repeated to complete the four flow inversions. It is important to ensure that the helixes meeting in one of the corners (in this case the top right) do not meet, as that will be where the inlet and outlet holes are placed. At this corner, a straight line is placed at the end of the helixes, which will be removed from the final structure to form

the inlet and outlet channels, shown in **Figure 3.5**. Also included in a support square of 2.5 mm x 2.5 mm x 10 mm that is placed adjacent to the inlet and outlet lines, to affixed at a later stage. This support square is where the inlet/outlet tubing will pass through and be held securely in the structure. Once these steps have been finished, the wireframe is complete, which will be used to form the final structure through extrusion.

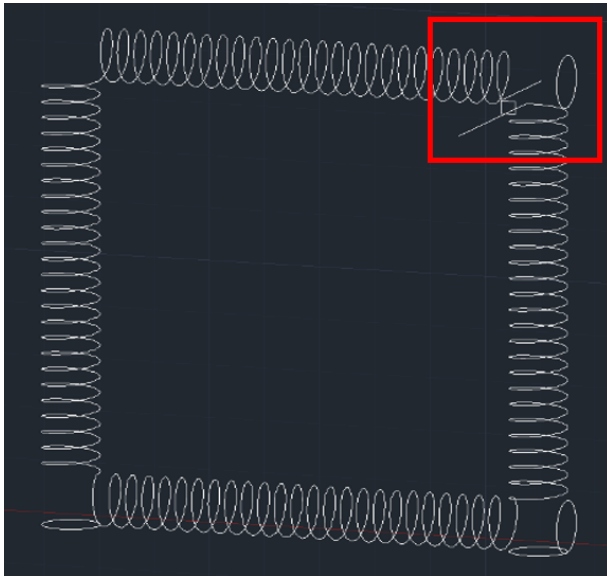


Figure 3.5: Wireframe CFIR structure, with the inlet/outlet corner highlighted.

3. To build the cylindrical supports, sweep paths need to be defined in the structure. To achieve this, firstly create a line of length 95 mm from the centre of each stand-alone circle through the centre of the helix. Then, using the ‘Sweep’ operator, select the circle as the object to sweep and then use the line drawn as the path for the sweep. Repeat this for each of the 4 circles/helices. This sequence of steps is shown below in **Figure 3.6**.

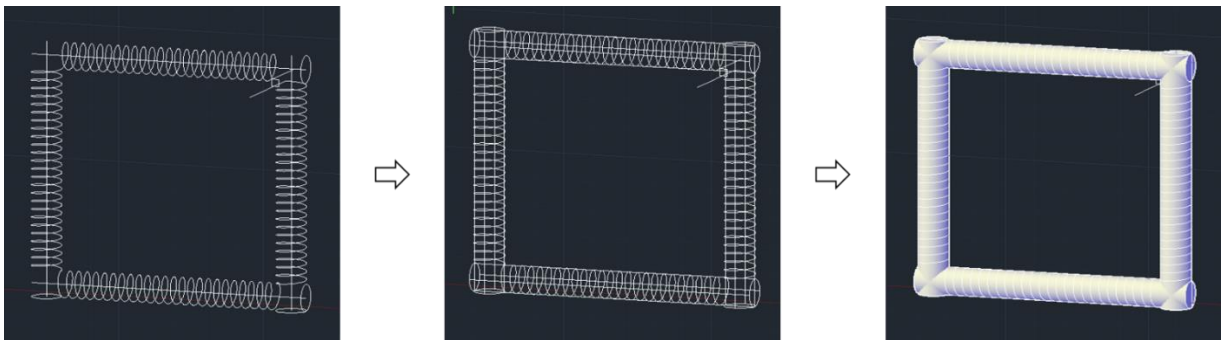


Figure 3.6: Sequence of AutoCAD steps used to sweep through the wireframe structure and form the 3D cylinders

4. Draw a circle of radius 1.6 mm, then using the ‘Sweep’ operator again, sweep the circle through the structure using the helixes as a path. Once this has been done for each of the four helixes, subtract this structure from each cylinder using the ‘solid subtract’ function. This will leave a path for the tubing in the structure (**Figure 3.7**).

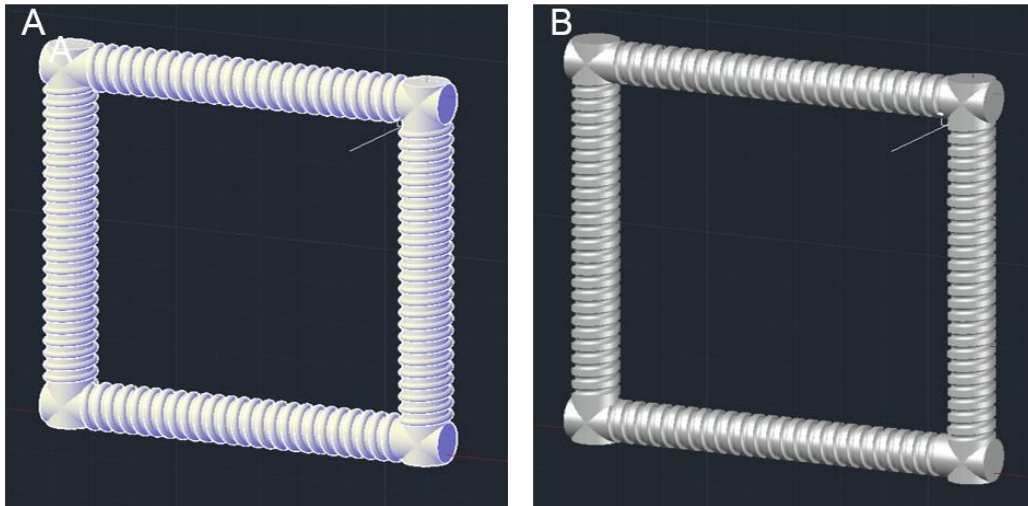


Figure 3.7: (A) structure with circle swept through the helix wireframe, and (B) structure with the channel formed through the subtraction of the helical sweep through.

5. Using this same method, the inlet and outlet channels can be formed. By sweeping through the 1.6 mm circle and subtracting the structure, it forms two holes in the piece, which will be used to secure the tubing. This is shown in **Figure 3.8**.

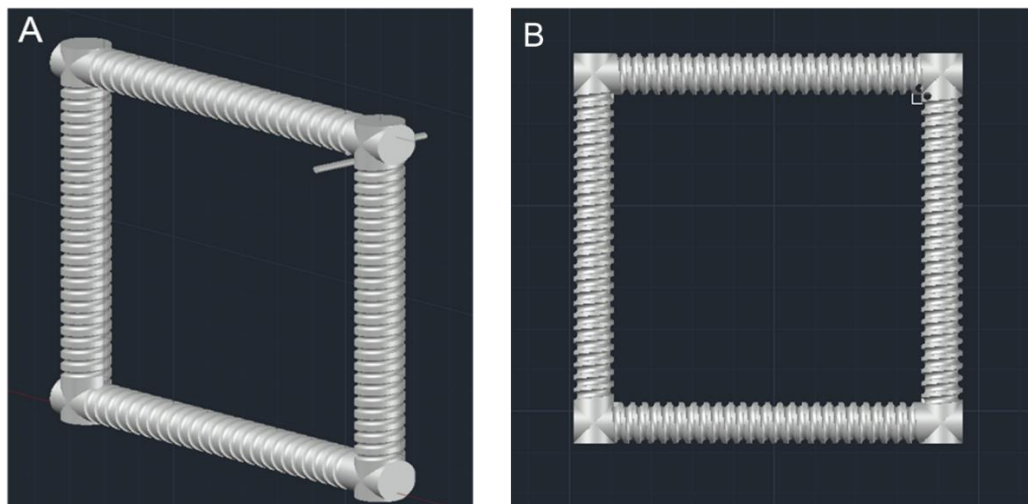


Figure 3.8: (A) Structure with inlet/outlet lines swept through by the 1.6 mm circle, (B) Structure with these sweep throughs subtracted.

6. To complete the square support at the inlet/outlet corner, a straight line of length 10 mm is drawn through the centre of the square, so that a length of 5 mm is on each side of the square. Using this line as a guide, sweep the square and it will form the cuboid support. These 2 steps are shown in **Figure 3.9**.

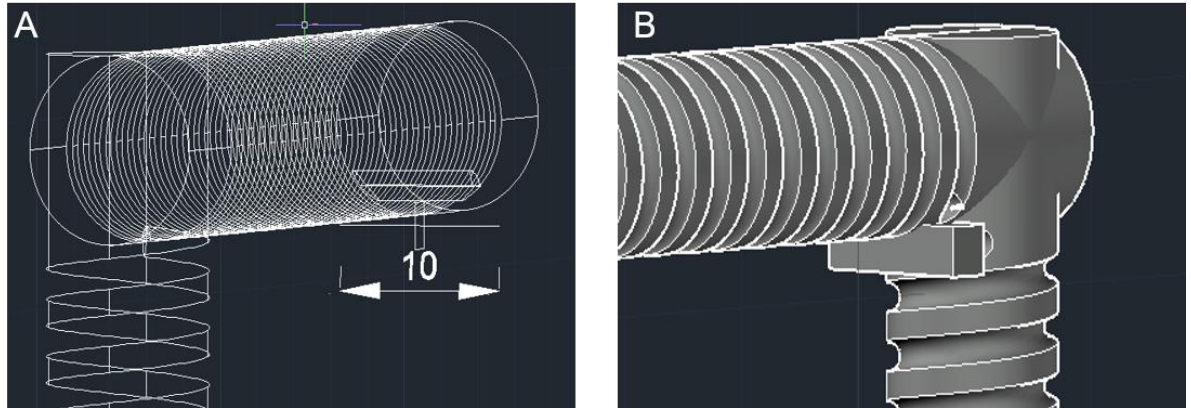


Figure 3.9: (A) Image highlighting the line drawn through the support square in the inlet/outlet corner, (B) Inlet/Outlet corner once the square has been swept through using this line.

7. Finally, to merge all the structures, first highlight all the pieces and use the ‘solid union’ function to combine them. This structure was saved as an STL file and then printed using Formlabs form 2 3D printer with high temp resin, followed by curing with UV light for 8 hours.

3.7.2 Microfluidic connections

Firstly, the tubing needs to be coiled around the CFIR unit. The easiest way to do this is to cut a length of tubing that will be slightly longer than the amount needed for the CFIR, to allow for inputs/outputs to be attached easily. In this case the amount needed for the CFIR was 3.146 m, so 3.5 m was cut to give about 18 cm excess for each side. The tubing is then pushed through one of the inlet holes in the corner (**Figure 3.10**), to then be wrapped fully around the CFIR, before being pushed through the other hole present in the corner. The tubing should be wrapped tightly around the CFIR, ensuring the length of tubing will be correct while also allowing for it to be moved easily.

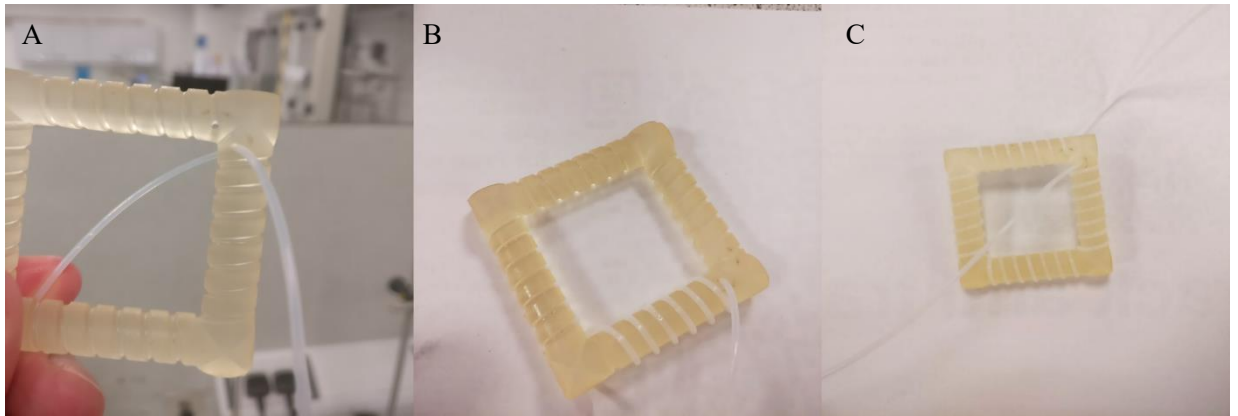


Figure 3.10 (A) The CFIR with tubing pressed through the corner inlet, (B) the CFIR with the tubing wrapped around 1 side, and (C) the fully completed CFIR with the tubing now pressed through the second corner hole.

The next step is to connect the inlet tubing to the syringes. The connecting ports are made of 3 parts: a ferrule, a flangeless fitting and a threaded luer adapter to the syringe (**Figure 3.11A-C**). Firstly, the tubing is inserted through the flangeless fitting, with the thread facing the inlet. The tubing is then also inserted through the ferrule, with the flat side facing into inlet. This is then tightly screwed into the threaded luer adapter, securing the tubing, and ensuring no leakage. The connector is then simply screwed onto the front of a syringe. This is shown in **Figure 3.11D**.

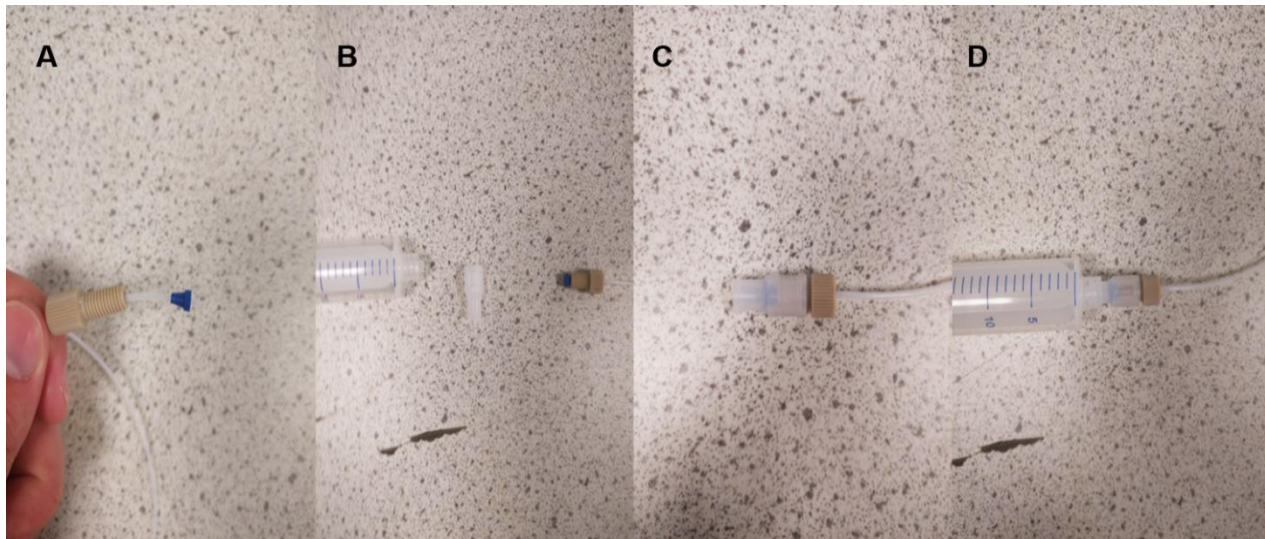


Figure 3.11 (A) Tubing with fitting and ferrule attached (B) Photo showing the syringe, luer adaptor and tubing with the ferrule now tightly attached. (C) Luer adaptor now screwed onto the end of the tubing. (D) Tubing now connected to the syringe.

Once this has been set up, the CFIR unit can be placed in a Duran 900 ml crystallising dish with a stirrer bar placed inside, on top of the magnetic stirrer hotplate. Silicon oil will then be poured over this to cover the reactor, ensuring uniform heating. The outlet tubing will then be placed in a chosen collection vessel, which in this case was 100 ml Duran flasks.

3.7.3 Slurry delivery system

An issue found in this procedure is that the reactant mixture does not fully dissolve at room temperature, and so the suspension collapses over time in the syringe. While it may be well mixed after the sonication, the reactants will not be fully dissolved at room temperature and will crash out of solution over time. This means that the reactant concentration entering the system will be changing over time, giving variable reaction conditions over the course of the run. To ensure that the concentration entering the system is constant, the reactant solution within the syringe needs to be constantly mixed. This can be achieved by placing a very small magnetic stirrer bar inside the syringe and holding a small magnetic stirrer plate over the syringe pump while the reaction process is occurring. This section goes through the steps of setting this up. Firstly, as can be seen in **Figure 3.12A** below, the plunger is pulled out of the syringe to allow the magnet to be placed inside (in this case a 5 mm bar), with the plunger then reinserted.

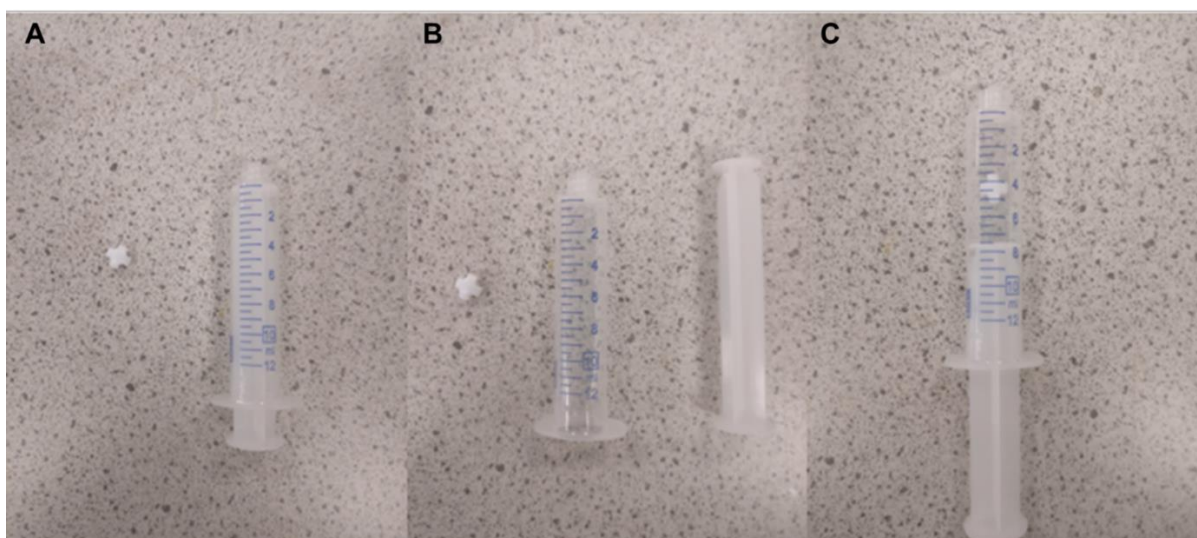


Figure 3.12: (A) Syringe and magnet next to each-other, (B) Image showing syringe with plunger removed, (C) Image showing syringe with magnet placed inside.

Using this syringe, the reaction mixture is drawn up. Some air will be in the syringe when the solution is added, so this needs to be removed before connection to the system. Once it has been connected to the system, place the small stirrer plate above the syringe using a clamp stand. A simple scheme for this is shown in **Figure 3.13**. Turn on the stirrer plate and set it to around 1500 RPM, where the bar will spin constantly in one position, with higher speeds causing the bar to move erratically around the syringe. Once this is setup, the pump can be started.

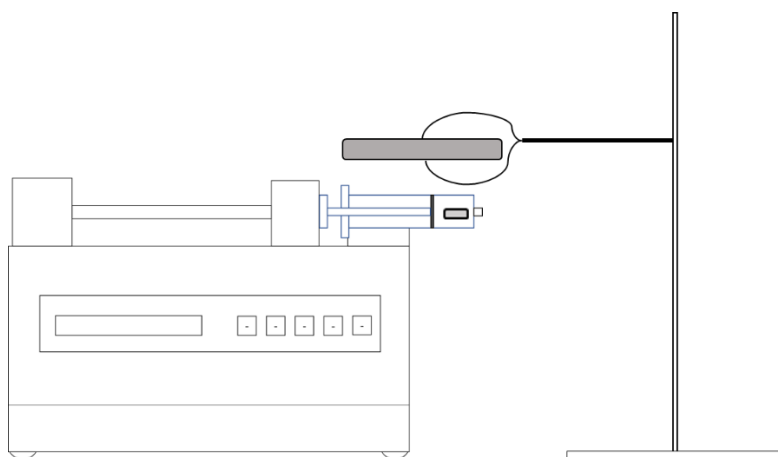


Figure 3.13: Scheme showing the general setup for the slurry delivery system, with the grey rectangle representing the magnetic stirrer plate and the smaller grey cuboid representing the magnetic stirrer bar.

To recover the magnet at the end, fully empty the syringe of any leftover solution and then pull out the plunger. Wash the magnet with acetone and dry in an oven to be ready to use in the next run.

3.7.4 Controlling the residence time

The residence time for this reaction will be controlled by the flowrate used with the syringe pump, which can be calculated by finding the volume of tubing present in the reactor. To quickly go through the calculations of the residence time in this experiment:

$$t = \frac{V}{Q} = \frac{\frac{1}{4}\pi d^2 L}{Q} \quad \text{Equation 4.1}$$

Where t is the residence time, V is the internal volume of the CFIR, d is the inner diameter of the tubing, L is the total length of the CFIR (only considering the part in the oil bath), and Q

is volumetric flow rate. In this work, the inner diameter of the tubing is 0.79×10^{-3} m, the total length of the reactor is 3.146 m, if the volumetric flow rate is set to be 0.052 ml/min, the residence time is then:

$$t = \frac{V}{Q} = \frac{\frac{1}{4}\pi d^2 L}{Q} = \frac{0.25 \times 3.14 \times (0.79 \times 10^{-3})^2 \times 3.146}{0.052 \times 10^{-3}} \quad \text{Equation 4.2}$$

$$= 30 \text{ min}$$

While the residence time may be 30 mins, the overall time for the run will be much longer, as 10 ml of solution has to pass through the system at this rate, giving an overall run time of around 3 hours. The residence time can be easily tuned by changing the volumetric flow rate.

3.8 Experimental Procedure

Firstly, the oil bath containing the CFIR was heated to 140 °C, which was chosen rather than 120 °C due to batch testing at 140 °C showing that increasing the temperature reduces the reaction time needed. ZrCl₄ (0.26 mmol) and benzoic acid (1.28 mmol) were placed in a dry beaker before adding DMF (10 ml), adding a small amount of DMF at the start as a small amount of HCl gas will be released initially, due to the ZrCl₄ reacting with any trace amounts of water present in the beaker/DMF added. This beaker was then sonicated for 1 min. Following this, BPDC (0.26 mmol) and distilled water (0.25 ml) was added to the solution, and then sonicated for a further 3 minutes. The use of water will increase the overall pH of the solution and so increase the deprotonation rate for the linker units, and so increase the rate of formation.¹⁹ While all the reactants will be in the same syringe, this should not affect the result significantly as the reaction is extremely slow at room temperatures. A 10ml syringe with a small magnetic stirrer bar placed inside of it was then used to take up the reactant solution. Before attaching this syringe to the microreactor, 2 ml (which is greater than the total internal volume of the tubing of 1.72 ml) of fresh DMF was quickly pumped through the system, to ensure no previous reactants/products were present. The syringe with the reaction mixture was then attached to the microfluidic reactor and placed in the pump, with a small magnetic stirrer plate set up above the syringe. The pump was then started at a rate of 0.052 ml/min, which

gave a residence time of 30 minutes. The reaction was performed for 2.5 hours before the magnetic stirrer bar stops spinning, at which point the syringe was removed and a new syringe containing 5 ml of fresh DMF was attached. 2 ml of this fresh DMF was pushed through at the same flowrate, to ensure all reactants/products in the system were evacuated in the appropriate residence time. Finally, another 2ml of fresh DMF was pushed through at a flowrate of 1 ml/min, to ensure any settled product/reactant in the system were removed. No severe build-up/blockages have been observed over multiple runs, with the process being repeatable. The product was washed with fresh DMF (2 x 15 ml) and then left to soak in methanol (15 ml) for 72 hours, changing the methanol every 24 hours. The solvent was removed each time by centrifuge (6000 rpm, 20 minutes) and then left to dry overnight in an oven at 110 °C. The product was then collected and analysed by powder X-ray diffraction (PXRD) and scanning electron microscopy (SEM). The PXRD analysed the powder sample from $2\theta = 5^\circ - 45^\circ$, scanning for 45 minutes with a scan interval of 0.033° using Cu Ka radiation. The SEM was performed using a Carl Zeiss EVO MA15, which imaged the particles after being sputter coated with 25 nm of iridium.

3.9 Timing

- Synthesis run: 2.5 hours
- Washing Process: 72 hours
- Drying Process: 12 hours

Currently, the production rate of this process is extremely low, at 0.81 mg h^{-1} , but there are several ways in the future to improve this. The washing and drying times will be the same, independent of the amount of product present, so increasing the amount of product formed in the synthesis time would be vital. This could be achieved by increasing the size of the CFIR and the length of tubing it holds, allowing for higher flowrates while keeping the residence time constant. Multiple parallel reaction lines could be used as well, giving more product in the synthesis time. This process does show promise though, with a space time yield of $524 \text{ kg m}^{-3} \text{ day}^{-1}$, based on the volume of DMF used throughout the process. This is comparable to other continuous MOF production, with a previous plug flow reactor for UiO-66 showing a

STY of $428 \text{ kg m}^{-3} \text{ day}^{-1}$ but can be improved upon by increasing the amount of product formed during the synthesis time.²⁰

3.10 Anticipated results

3.10.1 XRD Patterns

The final product show appears as a white powder, with a yield of ≈ 70 mg achieved in this experiment. **Figure 3.14** is the XRD pattern for the product, with comparison to the expected XRD patterns for a traditional batch UiO-67 product, a batch procedure performed under the same conditions as the CFIR reaction and a simulated spectrum performed in VESTA. All patterns show the key peaks at $2\theta \approx 5.70^\circ$ and 6.6° , confirming the product to be UiO-67, with the smaller peaks appearing also being characteristic of UiO-67. These peak positions are consistent with the simulated results shown and with previous work on UiO-67.²¹ The experimental peaks are slightly shifted to lower angles in the experimental batch results, potentially due to the sample not being completely dry at the time of analysis, with absorbed species from the air expanding the internal structure, leading to a decrease in angle.

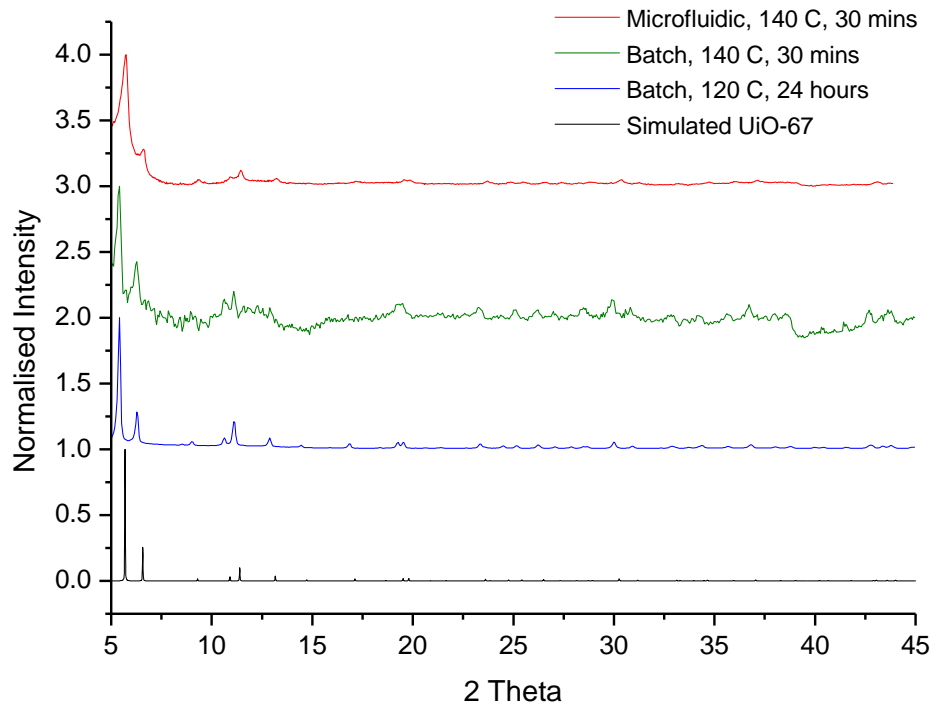


Figure 3.14: (Top to bottom) PXR D patterns for: Microfluidic synthesised UiO-67, Batch synthesised UiO-67 at 140 °C for 30 minutes, traditionally batch synthesised UiO-67 (24 hours, 120 °C), simulated UiO-67 performed by Vesta. All patterns are over $2\theta = 5 - 45^\circ$.

Using the patterns shown, the Scherrer equation was applied, shown below in **Equation 3.3**, to calculate the crystal sizes for the various MOF products.

$$d = \frac{K\lambda}{\beta \cos\theta} \quad \text{Equation 3.3}$$

Where d is the crystal size in Angstroms, K is the shape constant, which is between 0.8 and 1, usually assumed to be 0.9, λ is the wavelength of X-Rays used (1.542 Å), β is the Full-Width Half-Maximum (FWHM) of the peak being analysed, with the instrumental line broadening subtracted, inputted in Radians, and θ is the Bragg angle, also inputted in radians.

As this equation was applied to each synthesised product it gave a calculated crystal sizes of 177 nm, 40 nm, 28 nm for the traditionally synthesised batch UiO-67, the shorter batch process performed at 140 °C and the CFIR microfluidic product respectively. This smaller size is to be expected for the shorter reaction times and higher temperatures, increasing the rate of nucleation and the lack of time stopping the growth. This should not be taken as the particle

size, but to show the general trend in decreasing size, with SEM confirming the true size to be larger.

3.10.2 SEM Images

SEM images were taken for these three samples, which were prepared by sticking to a carbon tab on a SEM stub and then sputter coated with 25 nm of Iridium. **Figure 3.15** shows SEM images for the traditionally synthesised batch UiO-67 and the product obtained using the CFIR. The traditionally synthesised UiO-67 particles (**Figure 3.15a**) show clearly defined edges, with the particles ranging in size from ~ 500 nm to over 3 μm in diameter and separate from each other. The particles formed in the CFIR (**Figure 3.15b**) are much smaller and show a narrower distribution of sizes, ranging from ≈ 200 nm to ≈ 400 nm and appear as separate particles.

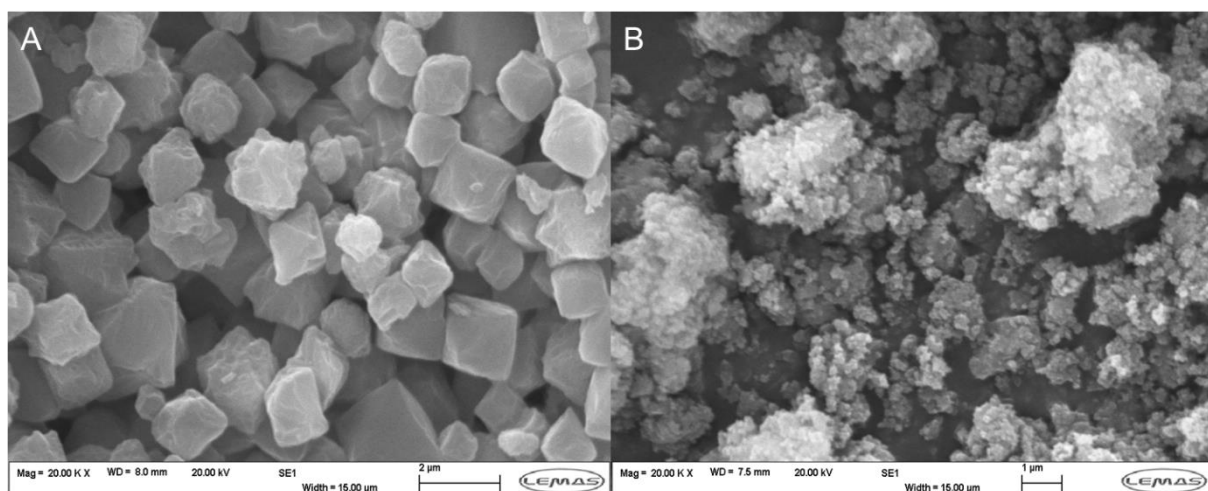


Figure 3.15: (A) SEM image for UiO-67 product formed through traditional 24 hours 120 $^{\circ}\text{C}$ batch process, (B) SEM image for UiO-67 product formed through microfluidic CFIR process.

Figure 3.16 shows the SEM image for the batch synthesised UiO-67 which used the same reaction conditions as the CFIR method (140 $^{\circ}\text{C}$, 30 mins, 50 eq H_2O). As can be seen, the particles here are no longer distinct, with no clear edges present. This suggests that this product has a lower level of crystallinity than the products formed in the CFIR, with use of the CFIR has increasing the rate of reaction through enhanced mass/heat transfer, forming a high-quality

crystalline product in a fraction of the time taken traditionally. It is also worth noting that the 140 °C batch run had to be scaled up considerably (by a factor of 6 when compared to the microfluidic synthesis) in order to form enough product (≈ 50 mg) for XRD and SEM analysis.

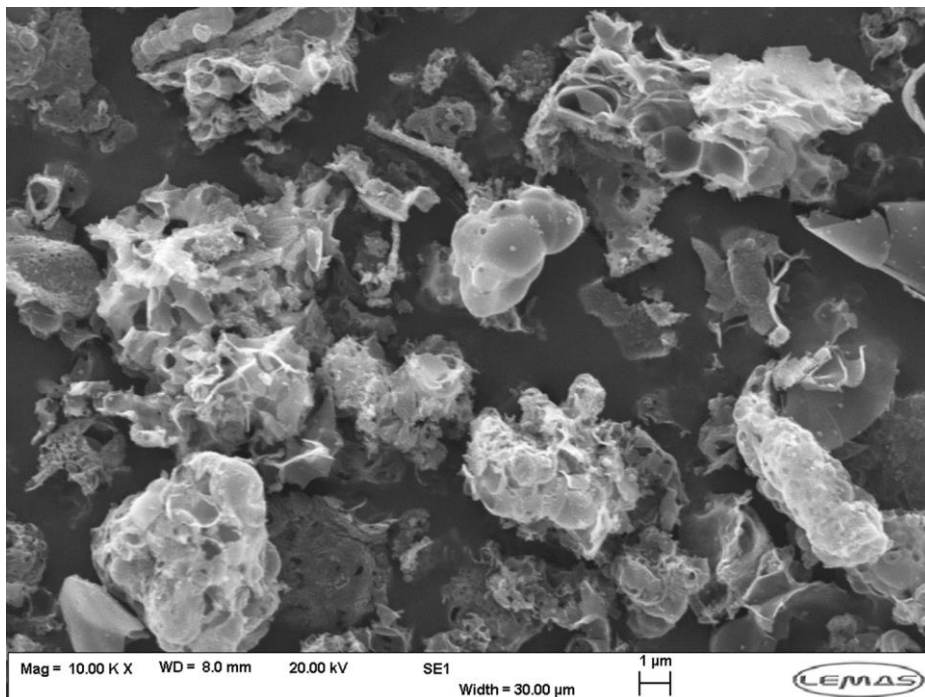


Figure 3.16: SEM image for UiO-67 product from 30 minutes 140 °C batch synthesis.

The characterisation results, incorporating both XRD and SEM, confirm that by using a CFIR microreactor crystalline UiO-67 can be produced, when similar conditions in batch do not. Furthermore, the particles produced using a CFIR are smaller and less varied in size than those produced via the typical batch conditions.

Acknowledgements:

K.W. and N.H. acknowledge financial support from the EU Horizon 2020 (SABADOMA, 862296) and T. B. acknowledges financial support from EPSRC Doctoral Training Partnership.

3.11 Declaration of interests:

The authors declare that they have no known competing financial interests or personal relationships that could have appeared to influence the work reported in this paper.

3.12 References

1. Hoskins, B. F., Robson, R. *J. Am. Chem. Soc.*, 1990, **112**, 1546–1554.
2. Czaja, A. U., Trukhan, N., Müller, U. *Chem. Soc. Rev.*, 2009, **38**, 1284–1293.
3. Chen, D. T., Bi, J. R., Wu, J., Kumar, A. *J. Inorg. Organomet. Polym. Mater.*, 2019.
4. Bai, Y., Dou, Y., Xie, L. H., Rutledge, W., Li, J. R., Zhou, H. C. *Chem. Soc. Rev.*, 2016, **45**, 2327–2367.
5. Bugaev, A. L., Guda, A. A., Lomachenko, K. A., Kamyshova, E. G., Soldatov, M. A., Kaur, G., Øien-Ødegaard, S., Braglia, L., Lazzarini, A., Manzoli, M., Bordiga, S., Olsbye, U., Lillerud, K. P., Soldatov, A. V., Lamberti, C. *Faraday Discuss.*, 2018, 208, 287–306.
6. Yang, Q., Wang, Y., Wang, J., Liu, F., Hu, N., Pei, H., Yang, W., Li, Z., Suo, Y., Wang, J. *Food Chem.*, 2018, **254**, 241–248.
7. Barkhordarian, A. A., Kepert, C. J. *J. Mater. Chem. A*, 2017, **5**, 5612–5618.
8. Faustini, M., Kim, J., Jeong, G. Y., Kim, J. Y., Moon, H. R., Ahn, W. S., Kim, D. P. *J. Am. Chem. Soc.*, 2013, **135**, 14619–14626.
9. Tai, S., Zhang, W., Zhang, J., Luo, G., Jia, Y., Deng, M., Ling, Y. *Microporous Mesoporous Mater.*, 2016, **220**, 148–154.
10. Schaate, A., Roy, P., Godt, A., Lippke, J., Waltz, F., Wiebecke, M., Behrens, P. *Chem. - A Eur. J.*, 2011, **17**, 6643–6651.
11. Zhang, R. Z., Huang, Y. qing, Zhang, W., Yang, J. M. *CrystEngComm*, 2018, **20**, 5672–5676.
12. Hung, L. H., Lee, A. P. *J. Med. Biol. Eng.*, 2007, **27**, 1–6.
13. Jahn, A., Reiner, J. E., Vreeland, W. N., DeVoe, D. L., Locascio, L. E., Gaitan, M. *J. Nanoparticle Res.*, 2008, **10**, 925–934.
14. Uson, L., Sebastian, V., Arruebo, M., Santamaria, J. *Chem. Eng. J.*, 2016, **285**, 286–292.
15. Sounart, T. L., Safier, P. A., Voigt, J. A., Hoyt, J., Tallant, D. R., Matzke, C. M., Michalske, T. A. *Lab Chip*, 2007, **7**, 908–915.
16. Kolmykov, O., Commenge, J. M., Alem, H., Girot, E., Mozet, K., Medjahdi, G., Schneider, R. *Mater. Des.*, 2017, **122**, 31–41.
17. Wu, K. J., Torrente-Murciano, L. *React. Chem. Eng.*, 2018, **3**, 267–276.
18. Kurt, S. K., Warnebold, F., Nigam, K. D. P., Kockmann, N. *Chem. Eng. Sci.*, 2017, **169**, 164–178.
19. Zahn, G., Zerner, P., Lippke, J., Kempf, F. L., Lilienthal, S., Schröder, C. A., Schneider, A. M., Behrens, P. *CrystEngComm*, 2014, **16**, 9198–9207.
20. Rubio-Martinez, M., Avci-Camur, C., Thornton, A. W., Imaz, I., MasPOCH, D., Hill, M. R. *Chem. Soc. Rev.*, 2017, **46**, 3453–3480.
21. Arrozi, U. S. F., Wijaya, H. W., Patah, A., Permana, Y. *Appl. Catal. A Gen.*, 2015, **506**, 77–84.

Chapter 4 Journal of Porous Materials Article,” The controlled microfluidic formation of stable mixed phase HCP/FCC-UiO-67(Zr)-Benzoic acid through modification of water concentration”, Published September 2023, <https://doi.org/10.1007/s10934-023-01513-4>

Tom Bailey, Lina Yang, Eleanor Humphreys, Faye Esat, Ben Douglas, Nicole Hondow

4.1 Abstract

This work reports the synthesis of a mixed crystal phase mesoporous metal-organic framework (MOF) through a new synthesis route. The Hexagonal Centred Planar (HCP)/Face Centred Cubic (FCC) mixed phase UiO-67(Zr) product was microfluidically synthesised using benzoic acid as the acid modulator. This phase ratio can be altered through changing the concentration of water present in the reaction solution. This product shows increased mesoporosity and uptake of N₂ at 77 K and 1 bar of 1083 cm³/g, as compared to 615 cm³/g for the product made via the traditional batch approach. This leads to an increase working capacity due to the change in isotherm type, from type I to type IV, with the uptake occurring more gradually overall as pressure increases. An increased working capacity allows for a greater range of control for the volume of N₂ stored in/released from the material. This product has only been successful in microfluidic conditions, highlighting the potential importance of this method for future synthesis of this MOF.

4.2 Introduction

Metal-Organic Frameworks (MOFs) are crystalline porous materials composed of metal containing nodes, secondary building units (SBUs), joined together by organic linker units. Universitet i Oslo (UiO) MOFs have zirconium based SBUs joined together by dicarboxylic acid linkers.¹ The interest in these MOFs is due to their relatively high stabilities as compared

to non-Zr(IV) carboxylate containing MOFs.² They have found uses in a range of applications, from gas storage³⁻⁶ to catalysis,⁷⁻¹¹ with the UiO series applicable for these applications through modifying the linker units used in synthesis or by altering the UiO product after synthesis.¹²

MOFs have been used, alongside other porous materials, to enhance the storage of gases, through increased overall uptake or by increasing the selectivity for specific gases.¹³ The large surface areas and open pores of the MOF can be filled, allowing for gas to be stored in higher volumes and at lower pressures when compared to storing in traditional bottles.¹³ UiO MOFs in particular have been looked at in gas applications due to the high physical stabilities, allowing them to remain stable in harsher temperatures and pressures when storing or releasing the gas.¹⁴ However, the key limitation to UiO MOFs in gas storage is their microporosity and low density. While they have high uptakes of gas in their structures, the working capacity, defined as the difference between the uptakes at a maximum pressure and that at the lowest controlled pressure, is narrow.¹⁵ This occurs due to the micropores being filled at the low pressures and then not changing, which is a Type I adsorption isotherm.

To improve this, Connolly *et al* formed densely packed monolithic UiO-66, which introduced larger mesopores and macropores into the structure, thereby increasing the overall pore volume of the structure.¹⁵ These larger pores would only fill at higher pressures, allowing for a steady increase of adsorption as the pressure increased, leading to a higher working capacity. Connolly *et al* therefore showed that if mesopores and macropores are introduced into the UiO structure there can be an increase the gas uptake while also raising the working capacity, and this can be achieved through modification or by introducing defects into the structure. Alongside introducing larger pores, they also increased the density of the UiO-66 structure through sol gel synthesis and varying drying conditions, finding a key trend. As density increased, the level of mesoporosity decreased in the structures, leading to N₂ isotherms which followed a Type I shape and with lower overall uptakes.¹⁵ This decrease in mesoporosity is

not due to the mesopores not arising due to defects or change in structure, but due to the spacing between crystalline UiO-66 particles.

Defects may appear in UiO MOFs, either as missing linker unit or as missing cluster units, and are introduced either by design or as a by-product of using certain acid modulator groups.¹⁶ Missing linker defects can occur when there is a “capping” group available, that will bind to the metal cluster instead of the linker unit, making the site unavailable.¹⁷ These capping groups are usually monocarboxylic acids, such as acetic or benzoic acid, but can also other chemicals such as water. By having these groups competing/exchanging with the linker units for space on the clusters, they can have a significant impact on the reaction kinetics and the structure.^{1,17} Defects can have a large effect on the structures pore size, surface area and reactivity, so being able to control these consistently is a point of focus.¹⁸

An engineering focus for the UiO series MOFs has been to introduce enough missing linker defects into the structure that the MOF changes from its usual face centred cubic (FCC) structure to a hexagonal centred planar (HCP) structure.¹⁹ By increasing the number of missing linker defects present in the structure, the metal clusters join together, changing from the 12 linker coordinated $Zr_6O_4OH_4$ (FCC) to the 18 linker coordinated $Zr_{12}O_8OH_{14}$ (HCP) (**Figure 4.1**).²⁰

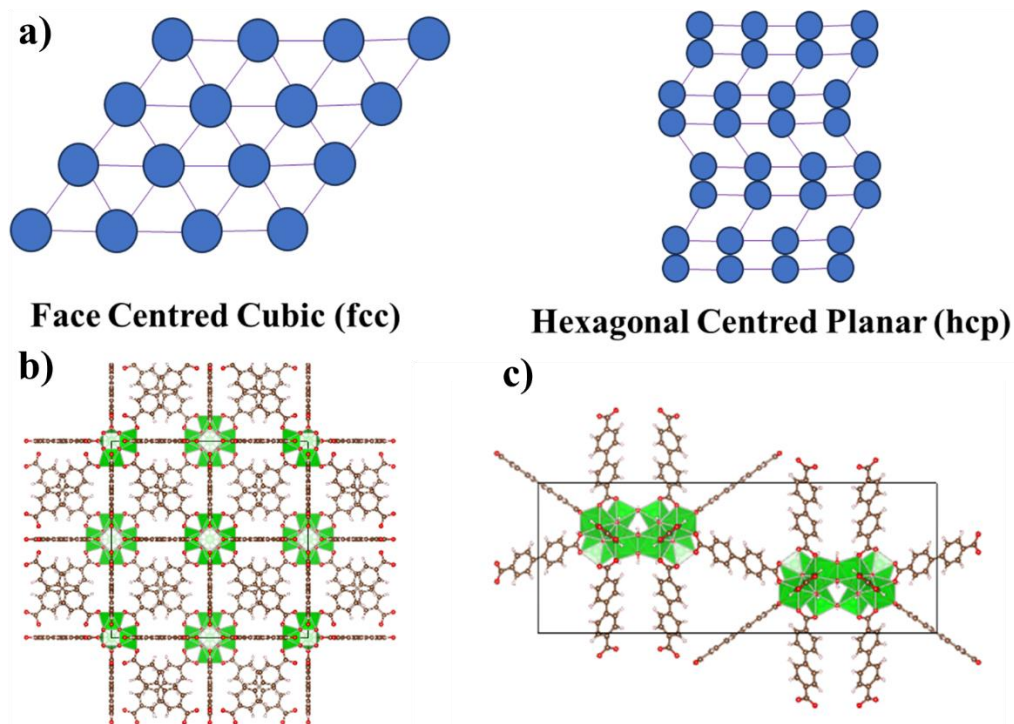


Figure 4.1: a) General 2D representation of face centred cubic (fcc) and hexagonal centred planar (hcp) structures. Blue circles represent SBU's and purple lines represent linkers. b) Crystal structure of FCC-UiO-67 unit cell, with polyhedra highlighted in green. c) Crystal structure of HCP-UiO-67, with double cluster structure visible.

Success in HCP synthesis has been found by increasing the concentration of water present in the reaction to achieve the desired product, in which the water molecules will act as capping agents and promote the formation of HCP²⁰. Previous HCP products have been found to perform better than their traditional FCC counterparts in certain ways, such as increased adsorption of perfluorooctanesulfonate when compared to defect free FCC UiO-66,²¹ or an increase in catalytic activity for ring-opening reactions of epoxides due to a higher density of defect sites.²² While the adsorption has increased, the surface area for the HCP products is usually less than their original FCC forms, due to the loss of linkers and clusters combining, so this increase in adsorption is attributed to some mesopores now being present in these products, allowing for higher uptakes.²³ This has been seen in previous nitrogen isotherms for these products, with a type II isotherm being present instead of type I as usually seen, with larger pores only being filled at higher pressures.²⁰ Distinguishing between these two structures is achieved through X-ray diffraction (XRD), with the FCC product showing (111)

and (200) as key diffraction peaks, while the HCP products shows (002) and (100) diffraction peaks (**Figure 4.2**).

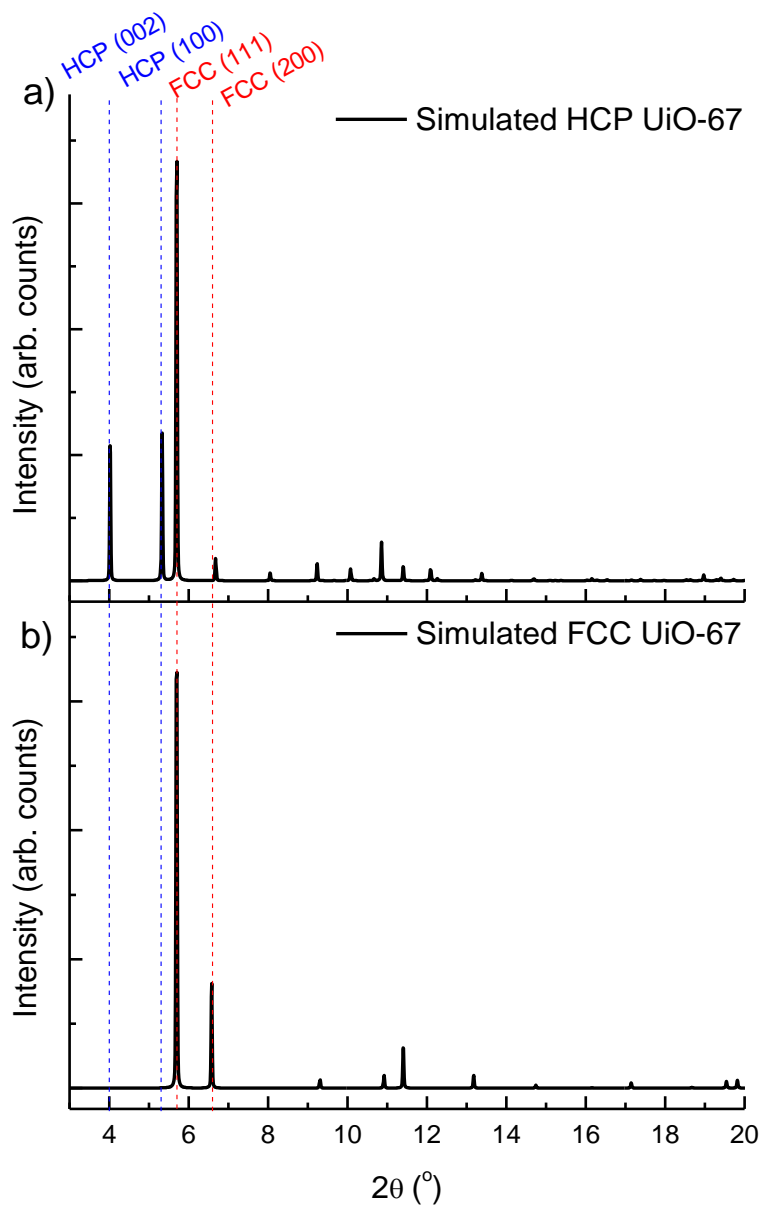


Figure 4.2 Simulated XRD patterns for a) HCP UiO-67 and b) FCC UiO-67. Patterns were simulated in VESTA. CIF for HCP is from Cliffe *et al*'s SI.¹⁹ CIF for the FCC pattern was obtained from the Cambridge Structural Database, from a paper by Goodenough *et al*²⁴.

Previous examples of HCP-UiO-67 have used formic acid as the modulator group, for both Hf and Zr versions.^{19,25} Being able to achieve the HCP structure while using different acid modulator groups would allow for different functional groups to be present in the structure, leading to further applications. Incorporating benzoic acid into the structure would allow

for more ring-based interaction to occur in the pores, such as π - π bonding. Work by Zhang *et al* found that the adsorption of toluene on UiO-67 was increased when using benzoic acid as the modulator, due to the missing linkers increasing the pore size, but also due to the π - π interactions between the benzoic acid and the toluene.²⁶ Density Functional Theory calculations performed by Zhao *et al* found that bonding through these π - π interactions is the most likely pathway for toluene and various other volatile solvents.²⁷

Another key point of interest in developing MOFs for industry use is the transfer of traditionally long and expensive batch synthesis processes to faster continuous synthesis, through the use of microfluidic reactors.²⁸⁻³⁰ These reactors enable a higher level of reaction control by the high surface area to volume ratio of the small channels in which the reaction mixture passes through, which gives increased heat transfer, mass transfer and mixing. Previous work in our group has succeeded in forming FCC-UiO-67(Zr) in a reaction time of 30 minutes of heating as compared to the traditional 24 hours due to this increased heat/mass transfer.³¹ By exploiting the properties possible in microfluidics, it may assist in forming HCP-UiO-67(Zr) while using benzoic acid as the modulator species. Firstly, previous work has shown that higher temperatures increase the formation of metal-oxide clusters with higher nuclearity, with the rate for FCC formation being higher than that for HCP at lower temperature.¹⁹ Therefore, if a reaction gives a product with a higher HCP to FCC ratio then the reaction should be quickly cooled after its heating has been performed, which is possible with microfluidics.

The aim for this work was to synthesise HCP-UiO-67(Zr) using benzoic acid as the modulator species, while varying the water content present to examine the effect this has on the resulting product. The best product found was then re-synthesised using similar conditions in batch, to see if the use of microfluidics influences the product. These products were analysed using XRD and N₂ isotherms, all with comparison to a traditionally batch synthesised FCC-UiO-67(Zr) product. Comments on the synthesis procedure and improvements for future work are provided.

4.3 Materials and Methods

4.3.1 Chemicals

Zirconium chloride (98%, Cat number: L14891) and silicon oil (Cat number: A12728.36) were purchased from Alfa Aesar. Benzoic acid (99%, Cat number: 237766) and biphenyl dicarboxylic acid (BPDC; 95%, Cat number: 091522) were purchased from Fluorochem. Methanol (> 99.9%, Cat number: 34860-2.5L-R) and dimethylformamide (DMF; > 99.9%, Cat number: 27054) were purchased from Sigma Aldrich. DMF and methanol were dried using 3Å molecular sieve beads, to control the water content present in the reactions, purchased from Avantor (L05359.30).

4.3.2 Microfluidic synthesis of UiO-67 products

The general setup for the coiled flow inverter reactor (CFIR) and majority of the synthesis procedure is provided in our previous work³¹. The CFIR had a reactor length of 4.018 m with an inner diameter of 0.79×10^{-3} m, giving a volume of 1.96 ml within the reactor. The residence time used was 30 minutes, leading to a flowrate of 0.0653 ml/min. This results in an overall synthesis time of ~ 2.6 hours.

Briefly, $ZrCl_4$ (60 mg, 0.26 mmol), benzoic acid (160 mg, 1.13 mmol), DMF (10 ml, 128.3 mmol) and ultrapure water were placed into a beaker and sonicated for 3 minutes. The water was varied from 0 to 70 molar equivalents (0 – 350 μ l), increasing every 10 equivalents (50 μ l) in relation to the molar equivalents of $ZrCl_4$. Following sonication, BPDC (62.5 mg, 0.26 mmol) was added and sonicated again for 1 minute. Sonication was performed to assist with dissolving the reactants but stirring was still required within the syringe throughout the run. The reactant solution was then drawn into a 20 ml syringe with a small magnet placed inside. This was then connected to the CFIR which had been filled with dried DMF and heated to 140 °C in the oil bath. A Duran bottle, for product collection, was connected to the reactor and a nitrogen cylinder, the syringe pump was started. As the reactants were pumped through, the

pressure in the system was increased slowly before the reactant solution reached the oil bath (so no reaction started before the desired pressure of 2 bar absolute was reached). This slow increase in pressure was required to ensure that the pump did not stall. Once the reactant solution had been pushed through, 2 ml of dried DMF was pushed through the reactor at the same rate, to ensure any reactant/product left is removed.

As detailed in Section 3.4, this work takes particular care with the use of dried solvents and an increased washing time, with the product soaked in dried methanol over 4 days, with the methanol changed every 24 hours through centrifuge (6000 rpm, 15 mins), before drying overnight at 120 °C. The use of dried solvents and increased washing times were key to avoid issues that are shown later in this work. The product weights ranged from ~5 to ~40 mg, depending on the concentration of water used, with higher concentrations generally leading to more product.

4.3.3 Traditional Batch synthesis of UiO-67 [**Batch**]

Using the procedure given by Schaate *et al*¹, ZrCl₄ (180 mg, 0.77 mmol), BPDC (187.5 mg, 0.77 mmol), benzoic acid (480 mg, 3.93 mmol) and dried DMF (30 ml, 385 mmol) were placed in an autoclave. This was sealed and placed in an oven at 120 °C for 24 hours. The autoclave was then removed and left to cool for 2 hours before opening. The products were washed with fresh DMF (2 x 30 ml) and the left to soak in methanol for 48 hours, changing the methanol after 24h by centrifuge (6000 rpm, 15 mins). The product was then dried overnight at 120 °C, leaving a white powder (138.4 mg).

4.3.4 Batch synthesis: 30 minutes, 140 °C, 60 equivalent water [**Batch60eq**]

ZrCl₄ (180 mg, 0.77 mmol), BPDC (187.5 mg, 0.77 mmol), benzoic acid (480 mg, 3.93 mmol), dried DMF (30 ml, 385 mmol) and ultrapure water (900 µl, 46 mmol) were placed in an autoclave. This was sealed and placed in an oven at 140 °C for 30 minutes. The autoclave was then removed and left to cool for 2 hours before opening. The products were washed with fresh DMF (2 x 30 ml) and the left to soak in methanol for 96 hours, changing the methanol

every 24h by centrifuge (6000 rpm, 15 mins). The product was then dried overnight at 120 °C, leaving white needles (109.3 mg).

4.3.5 Characterisation

XRD was performed on each of the samples formed, using a Bruker D8 with copper k-alpha source ($\lambda = 1.5406 \text{ \AA}$). Scan conditions were $2\theta = 3^\circ\text{-}18^\circ$ at $0.5^\circ/\text{min}$, which is equivalent to a step-size of 0.01649° . Baselines were removed in Highscore using Sonneveld and Visser baseline reduction, with granularity = 15, a bending factor of 0. The data was then automatically smoothed using Fast Fourier smoothing with a degree of smoothing = 5. Before XRD, the samples would be dried overnight at 120 °C. Simulated XRD data were performed using Vesta, with the CIF for the HCP product being taken from the supporting information of the work by Cliffe *et al*¹⁹. The CIF for the FCC product was obtained from the Cambridge Structural Database, from a paper by Goodenough *et al*²⁴. For the N₂ isotherms, the samples would first be dried in air overnight at 120 °C, which was then followed by 3 hours of degassing under N₂ at 220 °C. The N₂ uptake was measured at 77 K using a liquid nitrogen bath. Each isotherm was measured up to 1 bar using a Tristar 3000. Transmission electron microscopy (TEM) was conducted on an FEI Titan³ Themis G2 operating at 300 kV fitted with 4 EDX silicon drift detectors, multiple STEM detectors, and a Gatan One-View CCD. TEM samples were prepared by dispersing the powder in methanol, with a drop placed on a continuous carbon coated copper grid.

4.4 Results and Discussion

4.4.1 Structure analysis

XRD was performed on each sample, with the comparison for each shown in **Figure 4.3**. This clearly shows that as the concentration of water present in the reactant solution increases, the HCP:FCC ratio also increases, with the peak at $5^\circ 2\theta$ indicative of the HCP phase growing in relative intensity. It is proposed that the (002) reflection at $4.0^\circ 2\theta$ and (100) at $5.3^\circ 2\theta$ in the HCP phase are broad and therefore overlap, causing the peak to be at $5^\circ 2\theta$. This broadness and resultant overlapping of the peaks is more likely in these microfluidic products due to their smaller crystallite size (TEM for the 60eq product is shown in **Fig S5.1** and **Fig S5.2**). This decrease in crystallite size was also found in previous work when forming FCC UiO-67 under the same residence time and temperature ³¹.

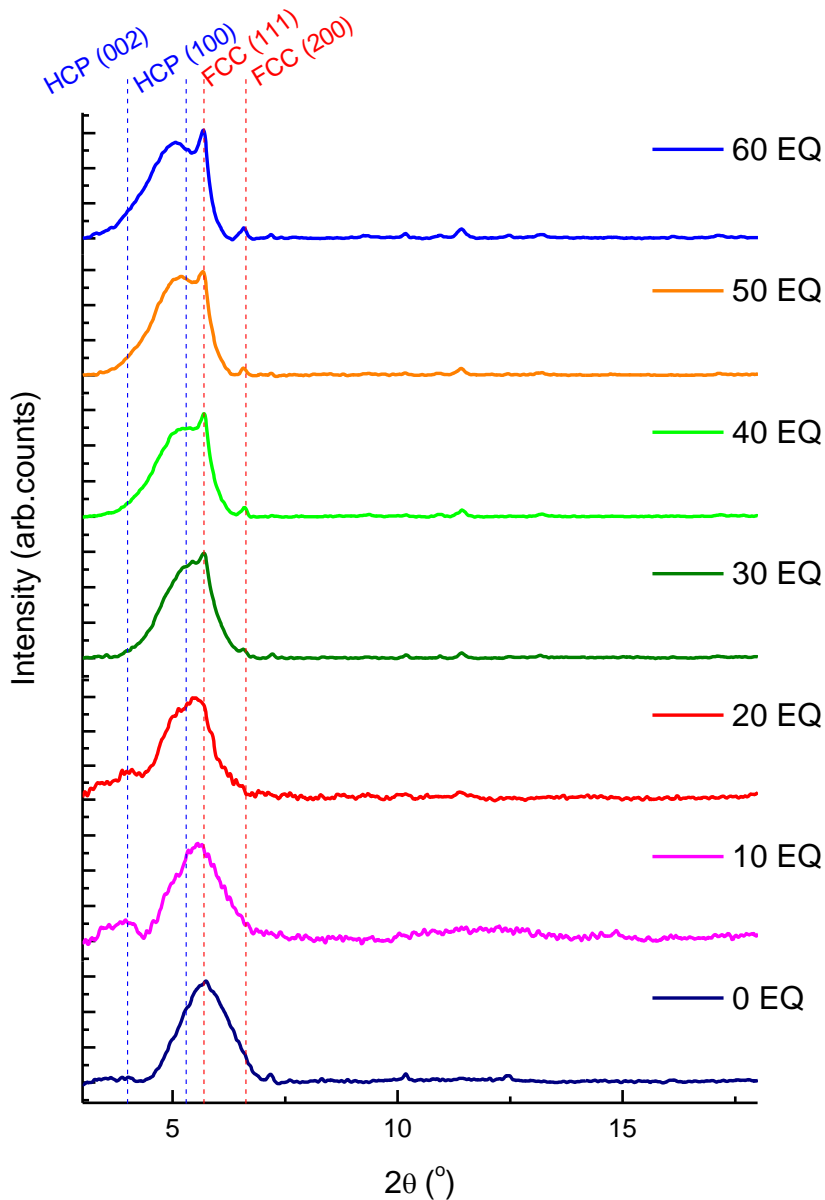


Figure 4.3 XRD patterns for microfluidic UiO-67 products, with the equivalents of H₂O used varying from 0 to 60. Baseline was removed in Highscore using Sonneveld and Visser baseline reduction.

Firstly, for the 0eq and 10eq patterns, a single broad peak appears for them at $\sim 5.7^\circ 2\theta$, which is the (111) reflection for the FCC form. This is to be expected, with uncrystalline FCC-UiO-67 being formed due to the low reaction rate and to lack of defects introduced to form HCP-UiO-67. For the 20eq sample, a new peak starts to appear at lower angles on the initial broad peak, indicating the presence of HCP-UiO-67. The centre of the single XRD peak is shifted to a lower angle, due to the increased formation of HCP phase. For the samples with higher concentrations of water (30 – 60 molar equivalents), that show two key peaks, $5.0^\circ 2\theta$

(combination of (002) and (100) HCP reflections) and $5.7^\circ 2\theta$ ((111) FCC reflection), the position of the overlapping HCP peak continues towards lower angles as the concentration of H_2O increases, while the position of the FCC peak stays the same. This demonstrates that the ratio of HCP:FCC is increasing, with the peak shifting towards the lower angles as the concentration of the (002) and (100) reflections increase in relation to the (111) reflection in the FCC. The central position for the combined HCP 002 and HCP 100 and the central position for the FCC (111) peak, in relation to the equivalents of water used in the synthesis **Figure 4.4**.

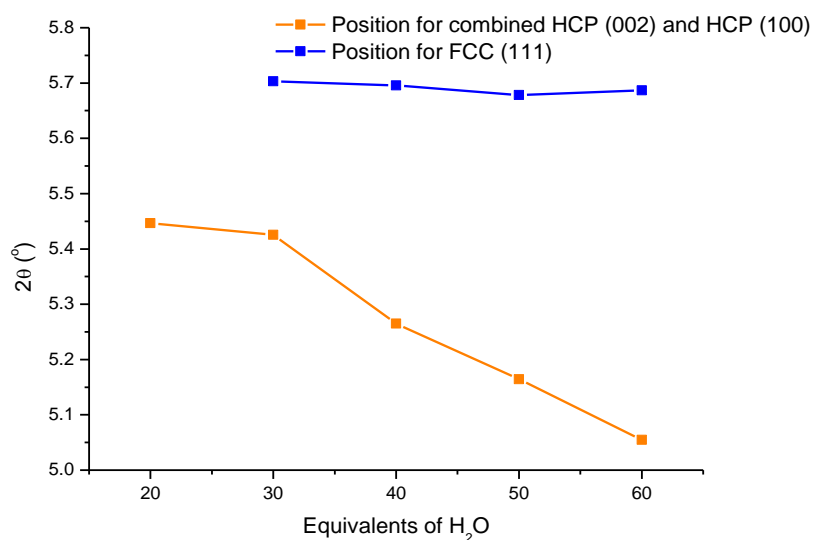


Figure 4.4 HCP and FCC peak positions for microfluidically formed UiO-67, from 20-60 equivalents of water. 20 EQ sample only shows one clear peak, so the centre of this is listed as the HCP peak.

This shift in HCP peak position is due to a secondary effect of the added water to the reaction. The products become more crystalline with increase in water, as this increases the rate formation for Zr MOFs, by “favouring hydrolysis of the zirconium precursor”³². This leads to those samples with higher concentrations of H_2O showing peaks at $\sim 5.0^\circ 2\theta$ and $5.7^\circ 2\theta$ as separate peaks as opposed to one³². The 60 equivalent product shows the highest level of

crystallinity and ratio of HCP:FCC, with the ratio of relative peak intensities (when comparing the HCP $5^\circ 2\theta$ and FCC $5.7^\circ 2\theta$ peaks) being almost 1:1, alongside the decreasing HCP peak position and constant FCC position as shown in **Figure 4.4**. A higher concentration of water (70 equivalents) was attempted; however, resulting issues with its synthesis are discussed in a later section (3.4).

With the 60 equivalent sample being found to contain the highest mixed phase ratio (through the shifting peak positions and peak intensity), the synthesis was repeated using a batch method, to determine the effect of the microfluidic synthesis. As can be seen in **Figure 4.5**, the batch method formed purely FCC product. While the autoclave used for heating the reaction mixture was cooling (~ 2 h to ensure it could be opened safely), the synthesis reactions continued and as discussed earlier, the FCC phase synthesis has a higher reaction rate at lower temperatures¹⁹. The FCC product formed in this cooling stage will be highly crystalline, leading to a completely FCC XRD pattern (due to the high relative intensities of these peaks). From now on, for ease of reading, the traditional batch UiO-67(Zr) shall be referred to as **Batch**, the batch product formed using the similar reaction conditions as the 60 equivalent H₂O microfluidic product shall be referred to as **Batch60eq** and the 60 equivalent H₂O microfluidic UiO-67(Zr) product shall be referred to as **MF60eq**.

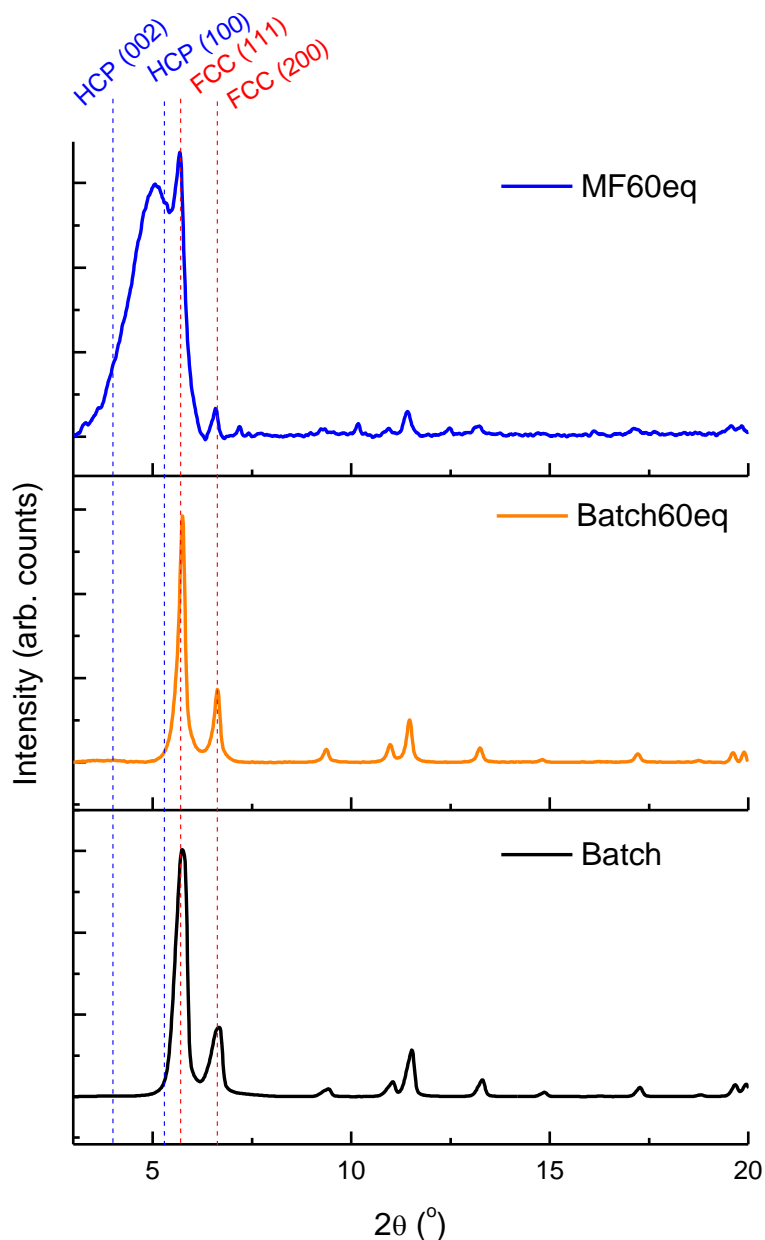


Figure 4.5 XRD patterns for microfluidically synthesised HCP-UiO-67 using 60 equivalents H₂O (**MF60eq**), UiO-67 synthesised in a batch setting using similar reaction conditions to the microfluidic reaction (**Batch60eq**; 60 equivalents H₂O, 30 minutes heating, 140 °C) and FCC-UiO-67 synthesised using the traditional batch method (**Batch**; 0 equivalents of water, 24 hours heating, 120 °C). Key diffraction peaks for the HCP are highlighted at 4.0° 2θ (002) and 5.3° 2θ (100), and for FCC phase at 5.7° 2θ (111) and 6.6° 2θ (200). Baseline was removed in Highscore using Sonneveld and Visser baseline reduction.

Figure 4.6 shows the XRD pattern for MF60eq in more detail, with sections corresponding to each reflection present highlighted. The highlighted sections of the peaks show the contribution of the FCC and HCP phases, with the MF60EQ product clearly being made up of two phases due to the peaks at both 6.63° 2θ and 7.1° 2θ, with the peak at 7.1° 2θ corresponding to the (102) diffraction peak present in the HCP phase. The presence of the hexagonal

nanosheet phase found in the work by Cliffe *et al* was considered due to the presence of a peak at $7.2^\circ 2\theta$ in the theoretical pattern for this product¹⁹. However, it was discounted as two much larger peaks at $5.34^\circ 2\theta$ and $6.47^\circ 2\theta$ should also be present in the pattern and since they are not it can be concluded that the peak at $7.2^\circ 2\theta$ in this pattern is not due to hexagonal nanosheet phase.

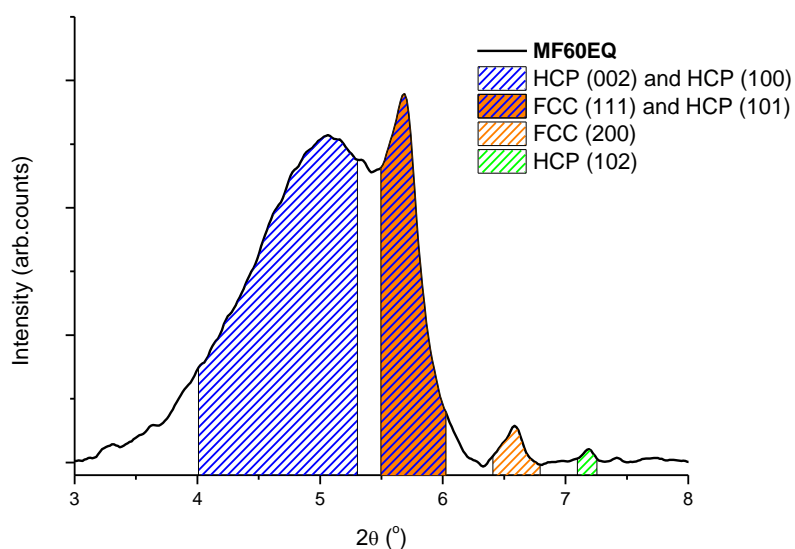


Figure 4.6 XRD pattern for **MF60eq** product. Hashed lines highlight areas corresponding to different diffraction peak contributions. Baseline was removed in Highscore using Sonneveld and Visser baseline reduction

The diffraction peak at $7.2^\circ 2\theta$ is also observed in the Fast Fourier Transform (FFT) taken from TEM images of the **MF60EQ** product (**Fig. S1**)

It may be possible to achieve the same product formed by the microfluidic reactor in a batch synthesis by applying quenching to the reaction vessel to speed up the rate of cooling; however, this would also incur costs and potential hazards.

4.4.2 Gas uptake

For each of the microfluidic products formed, N₂ isotherms were performed to determine how surface area, pore volume and overall gas uptake varied with water content. **Figure 4.7** shows the maximum N₂ uptake for each product produced through the flow synthesis at 1 bar and 77 k.

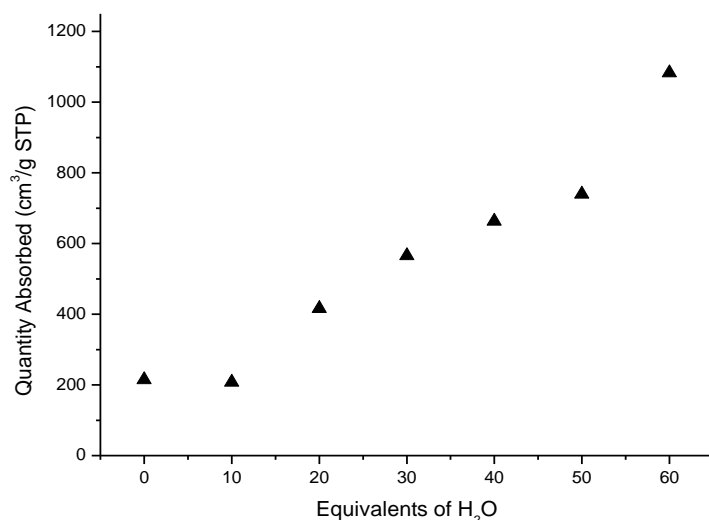


Figure 4.7 Maximum quantity of N₂ adsorbed (cm³/g) vs the molar equivalents of water used in the microfluidic reaction

As shown, the uptake of N₂ steadily increases to 50 equivalents of water with a sudden increase in the overall uptake after this point. This corresponds with the ratio of HCP:FCC increasing in the product, with **MF60eq** showing an N₂ uptake of 1083 cm³/g. Isotherms were also performed on **Batch** and **Batch60eq** for comparison, with key values present in **Table 4.1**. The uptake of the **MF60eq** surpasses the uptake for **Batch** which had an overall uptake of 615 cm³/g. As the HCP:FCC ratio increases, the number of missing linkers present in the structure will increase,²⁰ resulting in a higher frequency of mesopores forming, which correlates with an increasing N₂ uptake. This increase in mesopores/defects is reflected in the N₂ adsorption isotherms, with an increasing level of hysteresis as the equivalents of H₂O used increases, shown in the supporting information. Alongside this, as mentioned earlier, the water will increase the reaction rate to give a more crystalline product,¹⁷ with the resulting increased

surface area and pore volume increasing the N₂ uptake. The adsorption isotherms for **Batch**, **Batch60eq** and **MF60eq** are in **Figure 4.8**. Each microfluidic isotherm shows the same type IV isotherm while **Batch60eq** shows a mostly type I isotherm, similar to **Batch**.

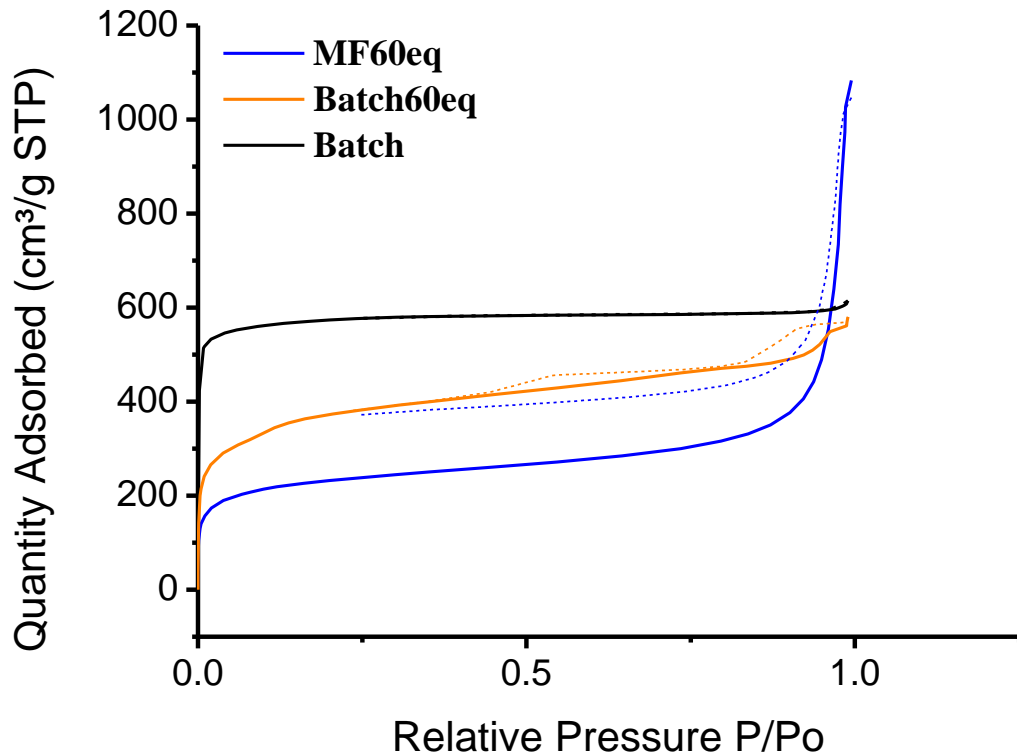


Figure 4.8 N₂ isotherms for microfluidically synthesised HCP-UiO-67 using 60 equivalents H₂O (**MF60eq**), batch synthesised UiO-67 with 60 equivalents of H₂O (**Batch60eq**) and FCC-UiO-67 synthesised using the traditional batch method (**Batch**; 0 equivalents of water, 24 hours heating, 120 °C). Dashed lines are for N₂ desorption.

A type IV isotherm suggests that **MF60eq** has mesopores present in the structure which will fill at higher pressures, whilst at lower pressures the micropores present will be filled. This isotherm type allows for a greater working capacity for the material, with a larger range of uptakes available when altering the pressure, compared to **Batch** where the uptake change is negligible after the initial uptake. This isotherm shape is different to other HCP UiO products found in the literature, with two key examples to compare to. Firstly, the HCP UiO-67 product formed by Cliffe *et al* showed an isotherm mostly consistent with its FCC counterpart, being

mostly type I and only showing a small increase in uptake at the higher pressures.¹⁹ This differs from what is seen here, with the majority of the uptake occurring at the higher pressure, which suggests a higher level of mesoporosity present in this structure when compared to their product. While the MOF made by Cliffe *et al* is Hf based rather than Zr based, these metals are similar analogues that a direct comparison can be made.³³ Only one other example of Zr based HCP-UiO-67 has been found, in work by Dai *et al*.²⁵ They form HCP-UiO-67 in nanoMOF form using formic acid as the modulator, achieving an uptake of $\sim 1300 \text{ cm}^3/\text{g}$ which showing a linear isotherm shape where it does not plateau, suggesting it hasn't reached its saturation pressure yet. This suggests a small level of microporosity due to the sharp initial increase in N_2 uptake, but the linear nature for the majority of the uptake suggests non-porous capture taking place, potentially surface adsorption due too the high surface area to volume ratio of nanoMOFs. While this overall uptake is closer to what is seen in this work, the differing isotherm shapes suggests that the structures are different overall, with the product formed in this work being a blend of the two phases (FCC and HCP) whereas their product was purely HCP.

Figure 4.9 shows how the overall, microporous, mesoporous and external surface area varied across each of the microfluidic products, with the key data for **MF60eq** given in **Table 4.1**, alongside the same values for **Batch** and **Batch60eq** respectively.

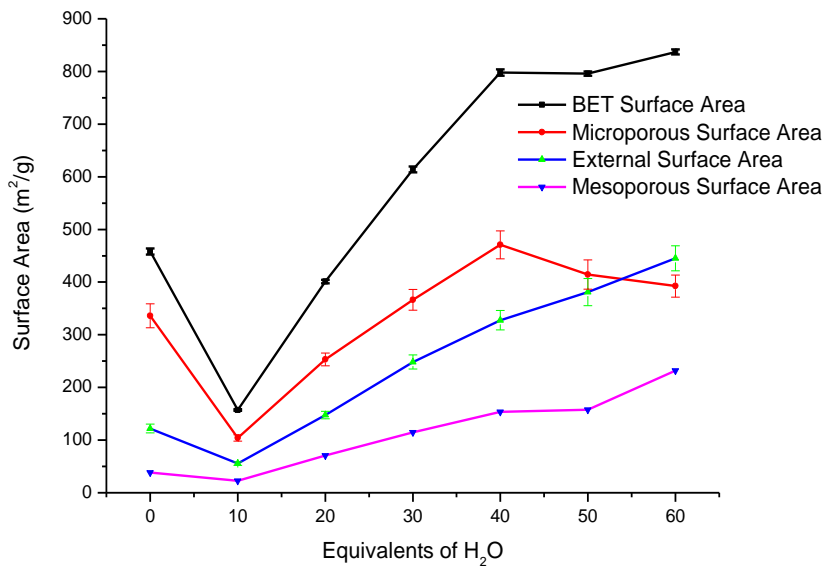


Figure 4.9 Plot showing how BET, Microporous, Mesoporous and External Surface Area (m^2/g) change with the increasing concentration of water in the reaction solution. BET surface area is calculated through Brunauer, Emmett and Teller (BET) calculations, with error bars shown for these. The microporous and external areas have been calculated using t-plot calculations. The mesoporous surface area has been calculated through Barrett, Joyner, and Halenda (BJH) adsorption calculations, giving the surface area for pores with diameters between 1.7 nm and 300 nm. Trendlines for each data set are present to guide the eye

Table 4.1: BET surface area was calculated using several points in the adsorption isotherm. Microporous and External areas are given by the t-plot for each isotherm, with errors provided through the errors on the t-plot intercept and slope. Mesoporous surface area is calculated using the BJH method, giving the surface area for pores with diameters between 1.7 nm and 300 nm. Overall uptake and working capacity are given in cm^3/g of N_2 at standard pressure and temperature (STP). Working capacity is determined by the difference in uptakes from 0.1 to 1 bar.

	BET Surface area (m^2/g)	Microporous surface area (m^2/g)	Mesoporous Surface area (m^2/g)	External Surface Area (m^2/g)	Uptake of N_2 (cm^3/g STP)	Working capacity (cm^3/g STP)
Batch	2108 ± 29	1827 ± 85.4	43	281 ± 13	615	53
Batch60eq	1333 ± 8	380 ± 34.2	261	953 ± 86	581	237
MF60eq	837 ± 4	392 ± 20.2	232	445 ± 23	1083	870

Following a sharp decrease in all surface areas from the 0 equivalents H_2O product, the overall BET surface area, microporous surface area, mesoporous surface area and external surface

area all increase as the water concentration increases. This is likely due to the increased reaction rate leading to more crystalline products being formed, as seen previously in the XRD (**Figure 4.2**). At 40 equivalents of H₂O, the BET surface area stops increasing as rapidly as water concentration increases, and the microporous area starts to decrease from this point also. With increasing water concentration from 40 equivalents, the mesoporous and external surface areas continues to increase, leading to the external surface area exceeding the microporous area. This correlates with the sudden increase in N₂ uptake achieved, with this higher level of mesoporosity being the key, which is reflected in the TEM for the **MF40eq**, **MF50eq** and **MF60eq** with the increased size for **hcp** particles (**Fig. S1**, **Fig. S2**, **Fig. S3**).

Comparing **MF60eq** to the batch products, it has a much higher overall uptake than both, despite its lower BET surface area. **Batch60eq** shows similar surface area values to the microfluidic product, with its external area exceeding its microporous area, but shows the lowest uptake of the three samples. This is due to the structural differences present in the products, which is highlighted by their pore sizes and volumes (**Table 4.2**).

Table 4.2: Average pore diameter (nm), Micropore Volume (cm³/g) and Mesoporous volume (cm³/g) for **Batch**, **Batch60eq**, **MF60eq**. Average pore diameter and Mesoporous volume are calculated by BJH adsorption. Micropore volume is calculated through the t-plot, with errors.

	Average Pore Diameter (nm)	Micropore Volume (cm ³ /g)	Mesoporous volume (cm ³ /g)
Batch	7.22	0.767 ± 0.005	0.079
Batch60eq	6.54	0.166 ± 0.034	0.427
MF60eq	24.52	0.167 ± 0.009	1.42

While **Batch** shows a much higher micropore volume than the microfluidic product, the mesoporous volume for **MF60eq** exceeds it greatly. On the other hand, **Batch60eq** shows lower pore volumes in both categories, explaining its lower uptake even with its higher surface areas. While the pore diameters for **Batch60eq** and **Batch** products are comparable, the reduced microporous volume and increased mesoporous volume for the **Batch60eq** product suggests that it is a lower density product, with a lower number of pores per gram than in the

Batch.³⁴ This may be due to the conversion of the HCP to FCC while cooling, leading to a highly defective MOF structure.

As N₂ is being adsorbed through multilayer adsorption rather than single layer adsorption, which would be found with gases that require specific binding sites to assist their uptake, the volume available to adsorb into is more important than the surface area available. Usually, as surface area increases in MOFs, so will pore volume and therefore higher uptakes of gas. However, by introducing many mesopores, the overall pore volume of **MF60eq** has managed to exceed that of **Batch**, leading to the higher uptakes.

Introducing a number of mesopores into UiO-66 has previously been done to increase the toluene adsorption ability of the material by a factor of 2.6, with the larger pores allowing for larger molecules to be more easily absorbed³⁵. Alongside this, work by Zhang *et al*,²⁶ found that UiO-67 containing Benzoic acid groups and missing linker defects the uptake of toluene increased drastically, due to π - π interactions from the benzene rings on the benzoic acid and the toluene groups and the added pore volume available. From these two pieces of work, the key product formed in this work (**MF60eq**) may be highly successful at adsorbing volatile organic compounds such as toluene, with benzoic acid groups available of its surface and higher overall pore volumes than previous products.

A previous problem found with HCP UiO-66 was its lack of stability, originally degrading in ambient conditions to a hexagonal nanosheet structure after only a few days.¹⁹ While this stability was rectified in later work,²⁰ it is important in this work with to ensure **MF60eq** is stable. XRD was repeated on **MF60eq** after 3 and 5 months to ensure the product had not degraded (**Figure 4.10**).

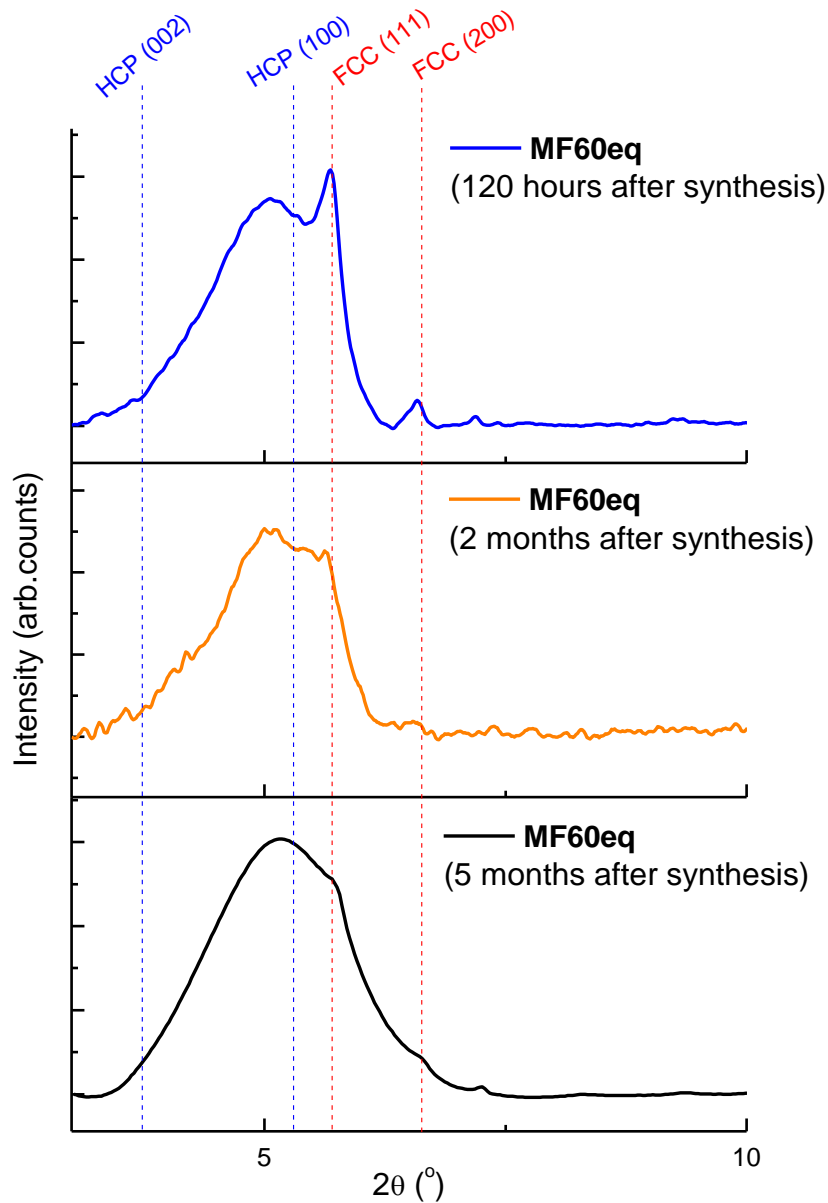


Figure 4.10 XRD pattern for 3 on the day after the initial drying and 3 months after this point. Measured between $3^\circ 2\theta$ and $10^\circ 2\theta$. Key diffraction peaks for the HCP are highlighted at $4.0^\circ 2\theta$ (002) and $5.3^\circ 2\theta$ (100), and for FCC phase at $5.7^\circ 2\theta$ (111) and $6.6^\circ 2\theta$ (200). Baseline was removed in Highscore using Sonneveld and Visser baseline reduction

The degradation shown is different to what occurred in the work by Cliffe *et al*, with the product in their work changing from HCP to a HXL type structure, which resulted in new peaks appearing in the XRD pattern.¹⁹ Two key factors are present in the patterns shown: Firstly, there is a loss in peak definition, which suggests that the crystal structure is amorphised overtime, indicating it may be moisture sensitive. Secondly, the position of the “HCP” peak, which was at $5.0^\circ 2\theta$ originally, has now shifted to a slightly higher angle for both the 3-month

and 5-month products. This fits with the product becoming less crystalline, with a similar shift in the XRD to the MF products synthesised with lower equivalents of water. Rejuvenation of this product has been attempted through washing and drying but to no real success.

4.4.3 Difficulties present in this synthesis

There are some difficulties with the synthesis for this material that are useful for future work to be aware of. These are split into 3 distinct areas, with current or future solutions to each of these issues being given here. Firstly, as is a common issue for microfluidic work, blockages may occur in the tubing, meaning that the reactants/products currently in the reactor will need to be disposed of, as the actual residence time for these products will become unknown. This becomes a problem for this reaction at higher concentrations (70 equivalent and above) of water are used, with the increased reaction rate meaning that more product is formed earlier in the system, giving more time for a blockage to occur. A product for 70 equivalents was formed and while it showed high surface areas/uptakes (N_2 isotherm in **Fig. S10**), its synthesis repeatedly suffered from blockages, meaning it was not possible to keep the residence time consistent, so any product formed would be unreliable for repeat synthesis. The use of both tubing which is slightly wider (to give more space for the products/reactants to move) and a CFIR reactor with a longer pathlength (so that higher flowrates can be used for the same residence time, keeping the product from settling on the tubing) may provide future opportunity.

Secondly, similar to the problem of blockages is the issue of fouling on the tubing surface. While this leftover product may not block the flow in future reactions, it will affect any future product that passes through it. For example, **Figure 4.11**, shows the XRD patterns for two 50 equivalent products, with one being from when the reactor was found to have had some fouling present in the tubing from a previous reaction.

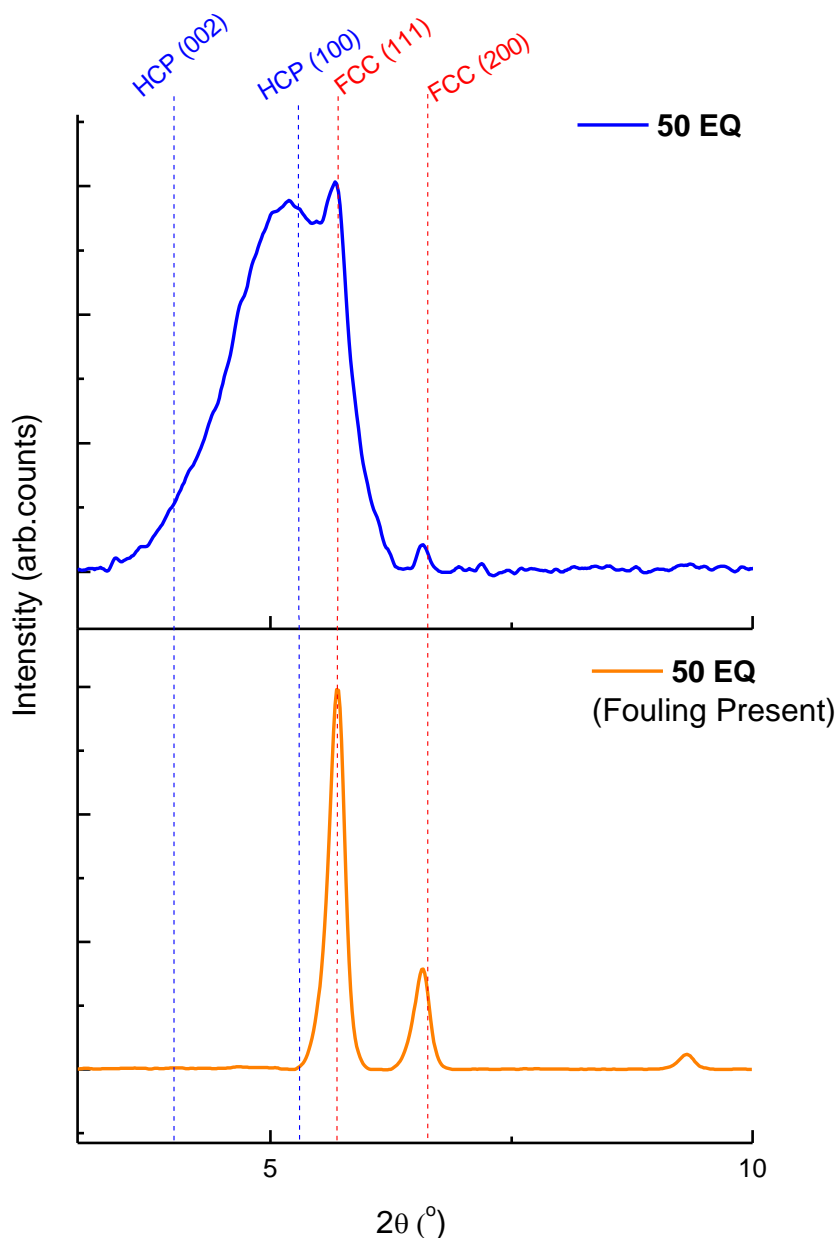


Figure 4.11 XRD patterns for the 50 equivalent H_2O UiO-67 product and for the product formed under the same reaction conditions, except fouling was found to have been present in the reactor. Key diffraction peaks for the HCP are highlighted at 4.0° 2θ (002) and 5.3° 2θ (100), and for FCC phase at 5.7° 2θ (111) and 6.6° 2θ (200). Baseline was removed in Highscore using Sonneveld and Visser baseline reduction

The fouling product left in the tubing continued to react at room temperature, forming FCC-UiO-67 which then reacted with the new reactants through heteronuclear nucleation, giving a product with a very high FCC:HCP ratio. The higher crystallinity of the FCC formed is of much higher intensity compared to the rest of the pattern.

The final challenge can be found in the drying and washing stage. Extra care has to be taken when washing this product, as when a shorter washing method (48 hours soaking in methanol, rather than 96) was attempted for one of the 60 equivalent product, a pattern similar to the FCC batch products was formed (**Figure 4.12**). If there is still DMF present in the structure and it is heated, the exchange reaction between FCC and HCP phases will continue, with the rate for FCC being faster at lower temperatures as mentioned earlier, leading to this structure.¹⁹

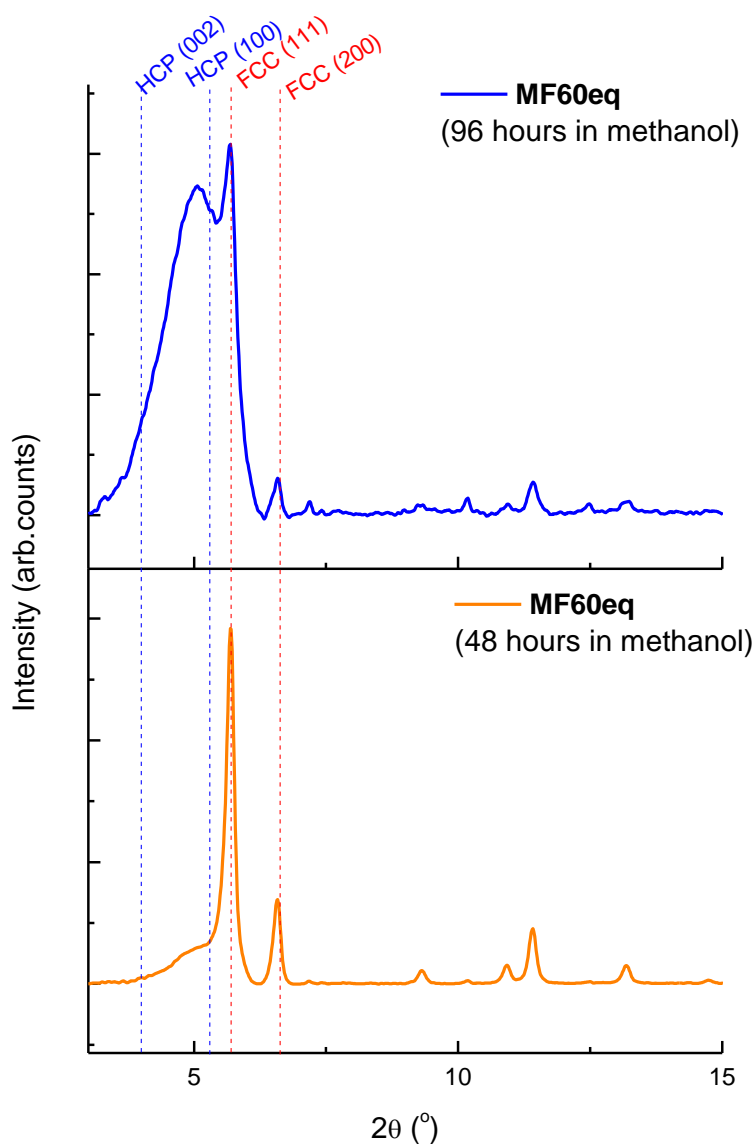


Figure 4.12 XRD pattern for **MF60eq** when using 96 hours washing and for **MF60eq** when using 48 hours washing. Key diffraction peaks for the HCP are highlighted at 4.0° 2θ (002) and 5.3° 2θ (100), and for FCC phase at 5.7° 2θ (111) and 6.6° 2θ (200). Baseline was removed in Highscore using Sonneveld and Visser baseline reduction

The XRD pattern for the product with shorter washing does suggest that the HCP phase is still present, due to the low intensity broad peak appearing at $5^\circ 2\theta$, with the HCP being lower intensity in the pattern when compared to the highly crystalline FCC. The N_2 isotherm for this product supports this theory as well, with a Type IV N_2 isotherm being present (**Fig. S12**).

4.5 Conclusions

A mixed Hexagonal Centred Planar (HCP) and Face Centred Cubic (FCC) phase UiO-67(Zr) product has been formed with benzoic acid as the acid modulating group, using microfluidics. Increasing the volume of water used in the synthesis had two key effects: increasing the synthesis rate and driving the synthesis towards the HCP phase product. Increasing the molar ratio of water to $ZrCl_4$ higher than 60:1 led to an increased level of fouling/blockages within the reactor, so future work should look to adapt the reactor for the use of higher water concentrations, tipping the product towards being purely HCP. Microfluidic synthesis was found to be vital to this process, with its increased heat transfer and rapid cooling allowing for the HCP phase synthesis to be promoted while the FCC phase was suppressed where possible, with synthesis under similar conditions in isothermal batch synthesis resulting in a different product being formed. The microfluidic produced material with 60 equivalents of water (**MF60eq**) showed a higher uptake of N_2 than that found for the traditional UiO-67 product ($1083 \text{ cm}^3/\text{g}$ compared to $615 \text{ cm}^3/\text{g}$), with a type IV isotherm resulting from the increased mesoporosity of the structure. This different isotherm type gives a higher working capacity for N_2 , at $870 \text{ cm}^3/\text{g}$ compared to $53 \text{ cm}^3/\text{g}$ for the traditional batch UiO-67. Various difficulties with this synthesis have been highlighted, with future work aiming to reduce the effect of these issues and synthesise a product with a higher HCP:FCC ratio while still using benzoic acid as the modulating group.

4.6 Declarations

Funding: This work was funded through financial support from EPSRC Doctoral Training Partnership (EP/R513258/1).

Conflict of interest/Competing Interest: Not Applicable

Data Availability: Supplementary Information (including N₂ isotherms for all products) will be provided as a pdf document.

Code Availability: Not Applicable

Authors Contributions: Study conception and design was performed by TB and NH. Material synthesis, data collection and analysis were performed by TB and EH. Assistance in the laboratory was given by LY. FE assisted with the collection and analysis of XRD data. BD assisted in the collection and analysis of N₂ adsorption isotherms. The manuscript was written by TB and NH, with all authors commenting on and approving the manuscript.

4.7 References

1. Schaate, A., Roy, P., Godt, A., Lippke, J., Waltz, F., Wiebcke, M., Behrens, P. *Chem. - A Eur. J.*, 2011, **17**, 6643–6651.
2. Cavka, J. H., Jakobsen, S., Olsbye, U., Guillou, N., Lamberti, C., Bordiga, S., Lillerud, K. P. *J. Am. Chem. Soc.*, 2008, **130**, 13850–13851.
3. Vaidhyanathan, R., Iremonger, S. S., Dawson, K. W., Shimizu, G. K. H. *Chem. Commun.*, 2009, 5230–5232.
4. Han, D., Jiang, F. L., Wu, M. Y., Chen, L., Chen, Q. H., Hong, M. C. *Chem. Commun.*, 2011, **47**, 9861–9863.
5. Chen, Z., Xiang, S., Arman, H. D., Li, P., Zhao, D., Chen, B. *Eur. J. Inorg. Chem.*, 2011, 2227–2231.
6. Sumida, K., Brown, C. M., Herm, Z. R., Chavan, S., Bordiga, S., Long, J. R. *Chem. Commun.*, 2011, **47**, 1157–1159.
7. Lee, J., Farha, O. K., Roberts, J., Scheidt, K. A., Nguyen, S. T., Hupp, J. T. *Chem. Soc. Rev.*, 2009, **38**, 1450–1459.
8. Hou, C. C., Li, T. T., Cao, S., Chen, Y., Fu, W. F. *J. Mater. Chem. A*, 2015, **3**, 10386–10394.
9. Abdel-Mageed, A. M., Rungtaweivoranit, B., Parlinska-Wojtan, M., Pei, X., Yaghi, O. M., Jürgen Behm, R. *J. Am. Chem. Soc.*, 2019, **141**, 5201–5210.
10. Liu, M., Wu, J., Hou, H. *Chem. - A Eur. J.*, 2019, **25**, 2935–2948.

11. Wu, C. De, Zhao, M. *Adv. Mater.*, 2017, **29**.
12. Kutzscher, C., Nickerl, G., Senkowska, I., Bon, V., Kaskel, S. *Chem. Mater.*, 2016, **28**, 2573–2580.
13. Morris, R. E., Wheatley, P. S. *Angew. Chemie - Int. Ed.*, 2008, **47**, 4966–4981.
14. Li, L., Tang, S., Wang, C., Lv, X., Jiang, M., Wu, H., Zhao, X. *Chem. Commun.*, 2014, **50**, 2304–2307.
15. Connolly, B. M., Aragonés-Anglada, M., Gandara-Loe, J., Danaf, N. A., Lamb, D. C., Mehta, J. P., Vulpe, D., Wuttke, S., Silvestre-Albero, J., Moghadam, P. Z., Wheatley, A. E. H., Fairen-Jimenez, D. *Nat. Commun.*, 2019, **10**, 1–11.
16. Atzori, C., Shearer, G. C., Maschio, L., Civalleri, B., Bonino, F., Lamberti, C., Svelle, S., Lillerud, K. P., Bordiga, S. *J. Phys. Chem. C*, 2017, **121**, 9312–9324.
17. Kaur, G., Øien-ødegaard, S., Lazzarini, A., Chavan, S. M., Bordiga, S., Lillerud, K. P., Olsbye, U. *Cryst. Growth Des.*, 2019, **19**, 4246–4251.
18. Shearer, G. C., Chavan, S., Bordiga, S., Svelle, S., Olsbye, U., Lillerud, K. P. *Chem. Mater.*, 2016, **28**, 3749–3761.
19. Cliffe, M. J., Castillo-Martínez, E., Wu, Y., Lee, J., Forse, A. C., Firth, F. C. N., Moghadam, P. Z., Fairen-Jimenez, D., Gaultois, M. W., Hill, J. A., Magdysyuk, O. V., Slater, B., Goodwin, A. L., Grey, C. P. *J. Am. Chem. Soc.*, 2017, **139**, 5397–5404.
20. Firth, F. C. N., Cliffe, M. J., Vulpe, D., Aragonés-Anglada, M., Moghadam, P. Z., Fairen-Jimenez, D., Slater, B., Grey, C. P. *J. Mater. Chem. A*, 2019, **7**, 7459–7469.
21. Clark, C. A., Heck, K. N., Powell, C. D., Wong, M. S. *ACS Sustain. Chem. Eng.*, 2019, **7**, 6619–6628.
22. Chen, X., Lyu, Y., Wang, Z., Qiao, X., Gates, B. C., Yang, D. *ACS Catal.*, 2020, **10**, 2906–2914.
23. Ma, C., Zheng, L., Wang, G., Guo, J., Li, L., He, Q., Chen, Y., Zhang, H. *Aggregate*, 2022, **3**, 1–15.
24. Goodenough, I., Devulapalli, V. S. D., Xu, W., Boyanich, M. C., Luo, T. Y., De Souza, M., Richard, M., Rosi, N. L., Borguet, E. *Chem. Mater.*, 2021, **33**, 910–920.
25. Dai, R., Peng, F., Ji, P., Lu, K., Wang, C., Sun, J., Lin, W. *Inorg. Chem.*, 2017, **56**, 8128–8134.
26. Zhang, X., Shi, X., Zhao, Q., Li, Y., Wang, J., Yang, Y., Bi, F., Xu, J., Liu, N. *Chem. Eng. J.*, 2022, **427**, 131573.
27. Zhao, Q., Du, Q., Yang, Y., Zhao, Z., Cheng, J., Bi, F., Shi, X., Xu, J., Zhang, X. *Chem. Eng. J.*, 2022, **433**, 134510.
28. Hu, G., Yang, L., Li, Y., Wang, L. *J. Mater. Chem. B*, 2018, **6**, 7936–7942.
29. Kolmykov, O., Commenge, J. M., Alem, H., Girot, E., Mozet, K., Medjahdi, G., Schneider, R. *Mater. Des.*, 2017, **122**, 31–41.
30. Faustini, M., Kim, J., Jeong, G. Y., Kim, J. Y., Moon, H. R., Ahn, W. S., Kim, D. P. *J. Am. Chem. Soc.*, 2013, **135**, 14619–14626.
31. Bailey, T., Pinto, M., Hondow, N., Wu, K. J. *MethodsX*, 2021, **8**, 101246.

32. Taddei, M., Van Bokhoven, J. A., Ranocchiari, M. *Inorg. Chem.*, 2020, **59**, 7860–7868.
33. Zaremba, O., Andreo, J., Wuttke, S. *Inorg. Chem. Front.*, 2022, **9**, 5210–5216.
34. Bambalaza, S. E., Langmi, H. W., Mokaya, R., Musyoka, N. M., Ren, J., Khotseng, L. E. *J. Mater. Chem. A*, 2018, **6**, 23569–23577.
35. Zhang, X., Yang, Y., Lv, X., Wang, Y., Liu, N., Chen, D., Cui, L. *J. Hazard. Mater.*, 2019, **366**, 140–150.

4.8 Supporting Information

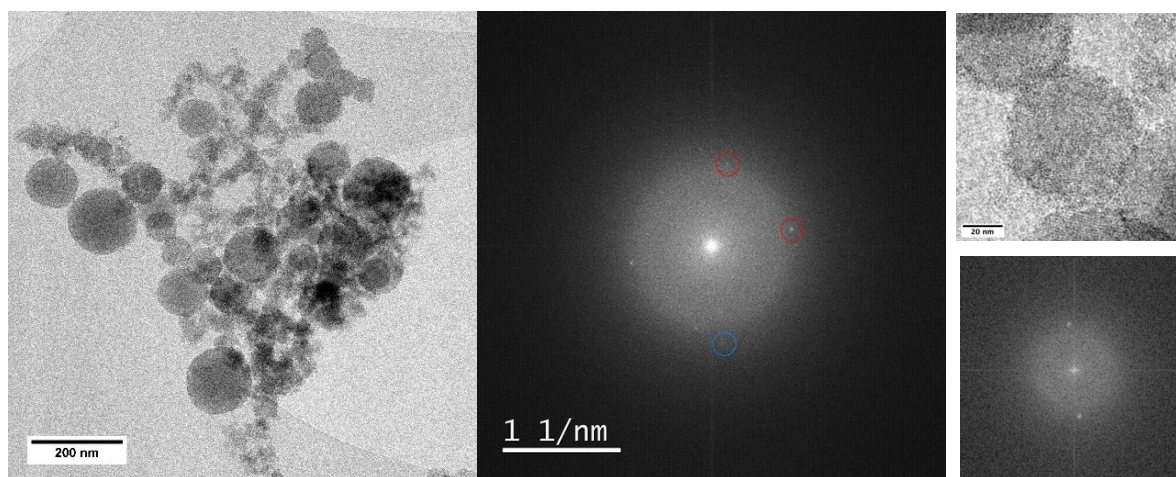
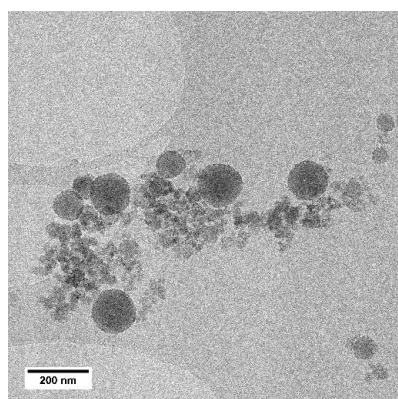
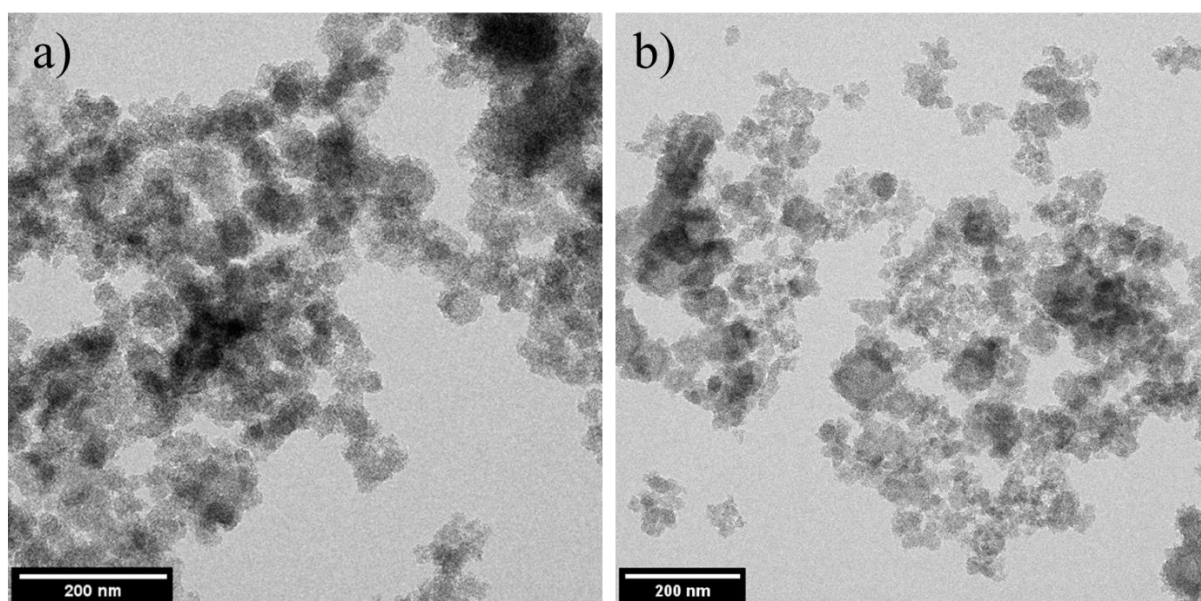


Figure S 4.1 TEM image (left) and FFT (middle) of MF60EQ product. The FFT is taken from the whole TEM image, with the red circles correspond to 14 angstrom spacings (which correspond to $7.2^\circ 2q$ in the XRD pattern), blue circle corresponds to 12 angstrom spacing (which correspond to $6.1\text{--}6.3^\circ 2q$ in the XRD pattern). FFT of one of the larger particles (top right) has spacing corresponding to 14 angstrom spacings (which correspond to $7.2^\circ 2q$ in the XRD pattern), indicating likely structure is HCP



Particle	Average Diameter (nm)	Standard deviation
FCC	29	6
HCP	101	28

Figure S 4.2 TEM image of MF60EQ product showing 2 distinct particles sizes, and table of average sizes



HCP particle diameter	Average Diameter (nm)	Standard deviation
MF40eq	63	13
MF50eq	68	12

Figure S 4.3 TEM images for a) MF40eq product and b) MF50eq product, alongside a table of average particle size for the larger HCP particles.

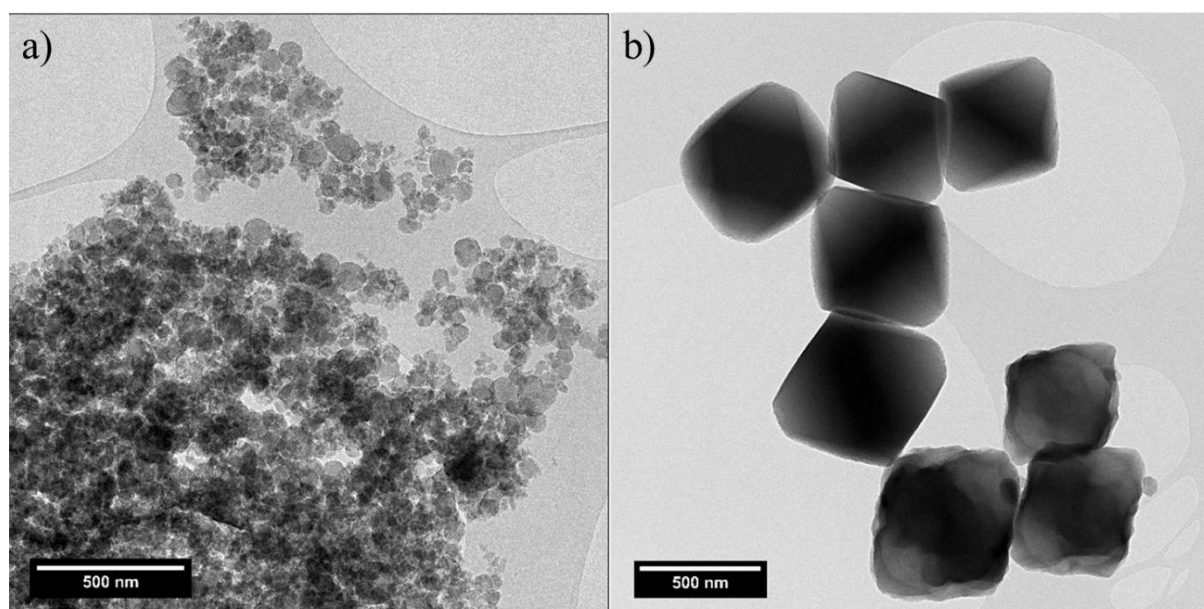


Figure S 4.4 TEM images for a) Batch60eq product and b) Batch product

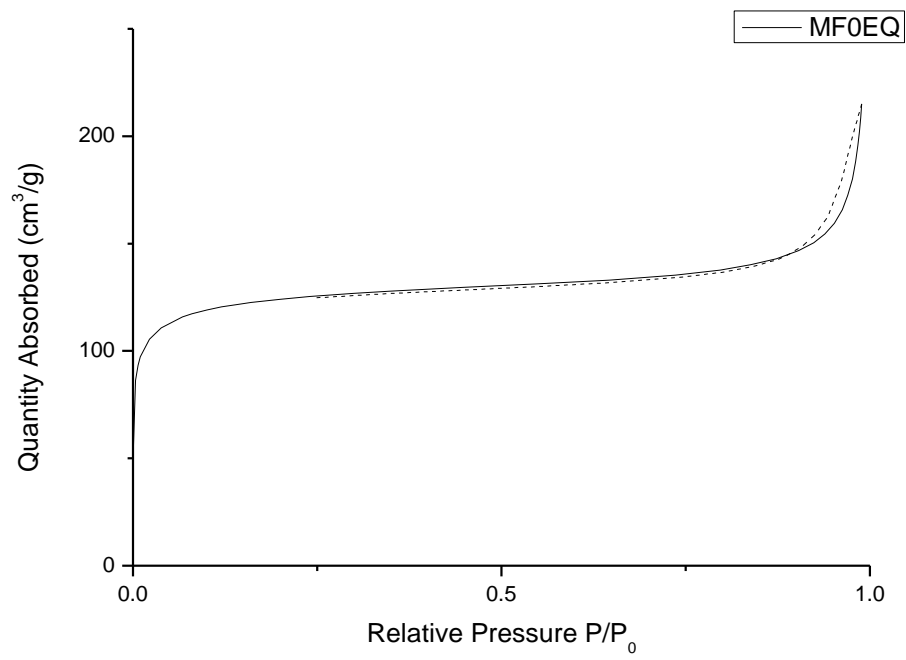


Figure S 4.5 N₂ Absorption isotherm of MF0EQ product

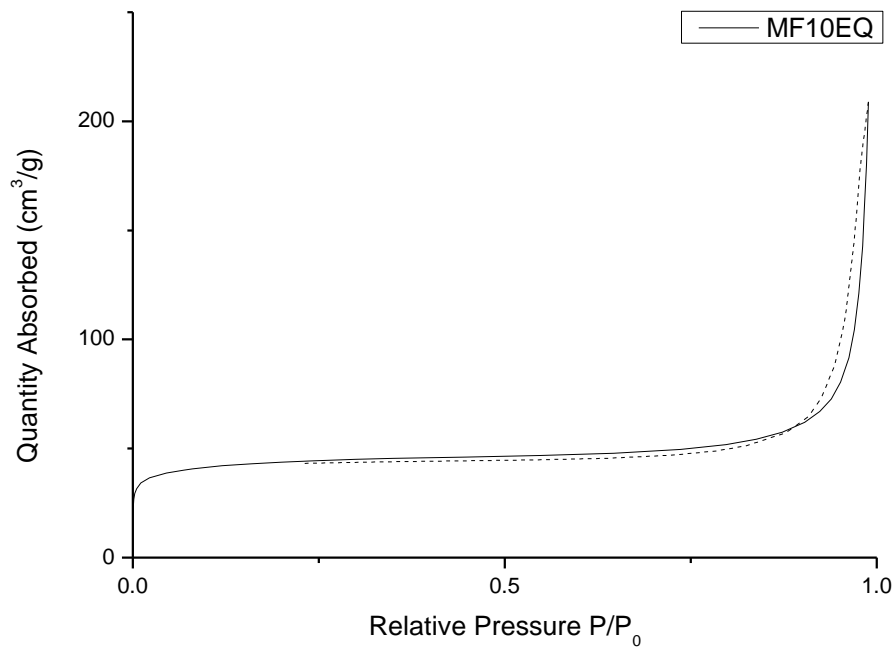


Figure S 4.6 N₂ Absorption isotherm of MF10EQ product

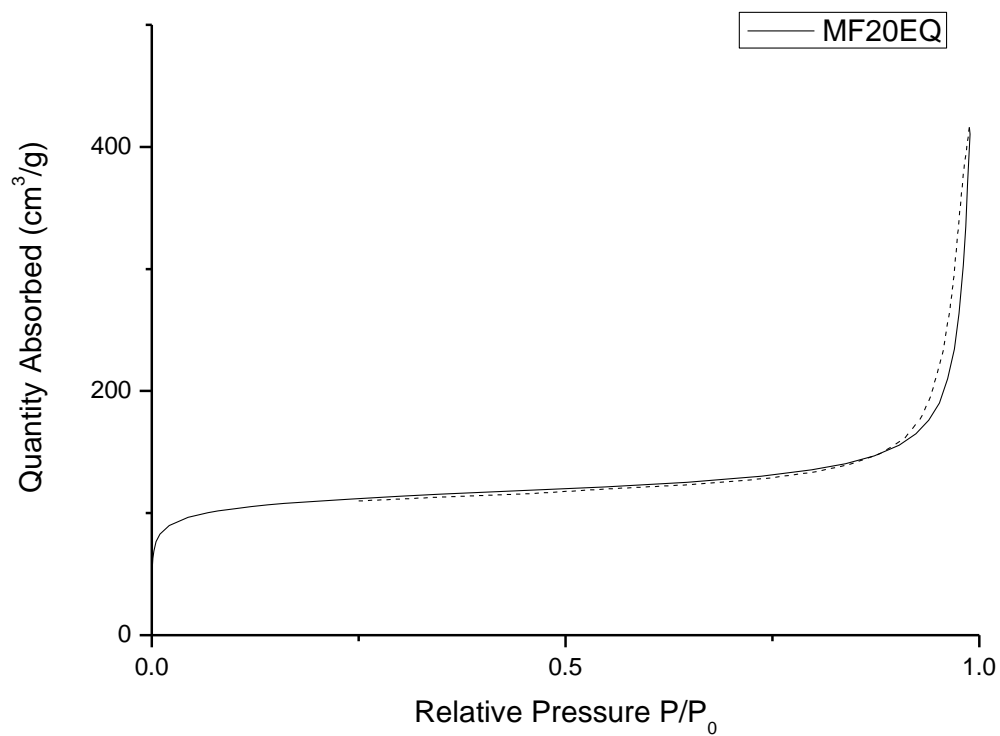


Figure S 4.7 N₂ Absorption isotherm of MF20EQ product

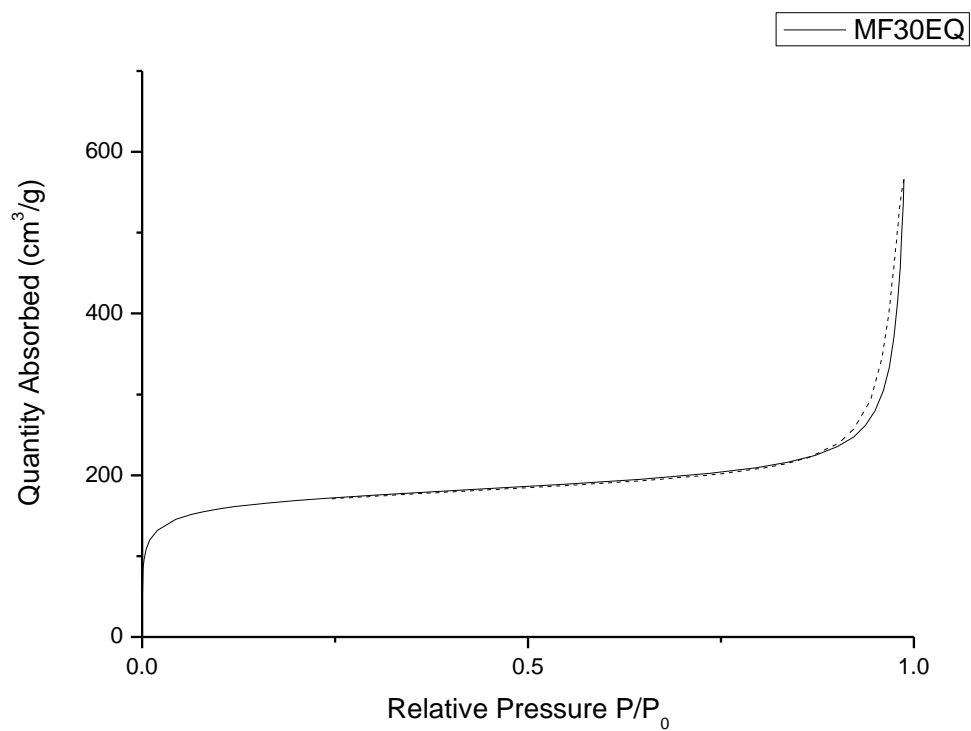


Figure S 4.8 N₂ Absorption isotherm of MF30EQ product

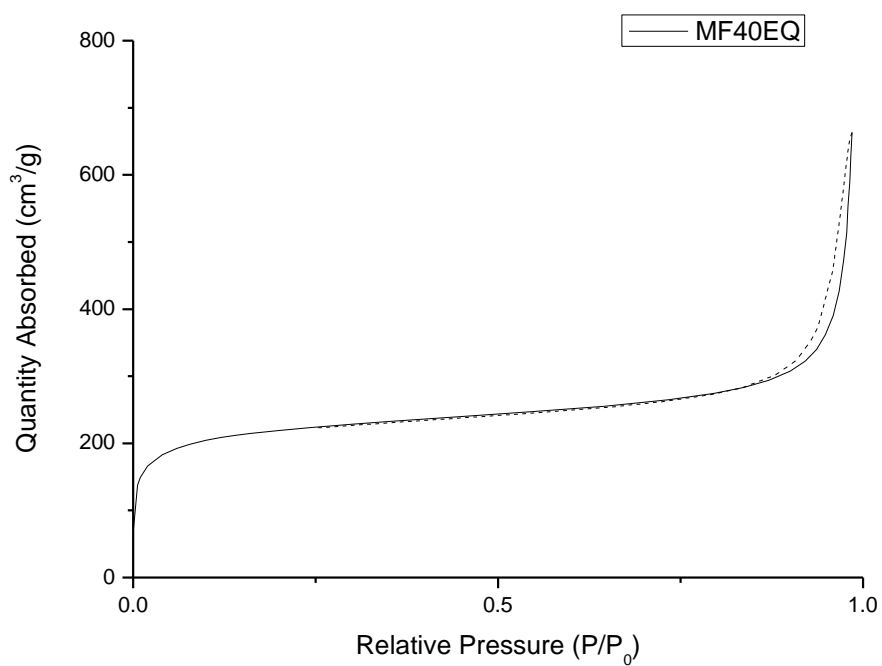


Figure S 4.9 N₂ Adsorption isotherm of MF40EQ product

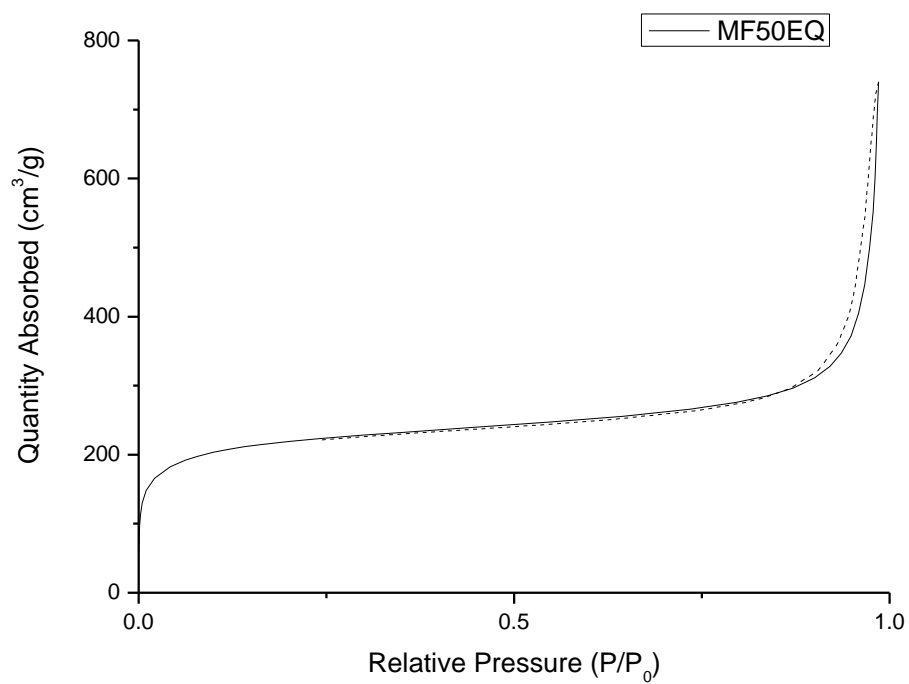


Figure S 4.10 N₂ Adsorption isotherm of MF50EQ product

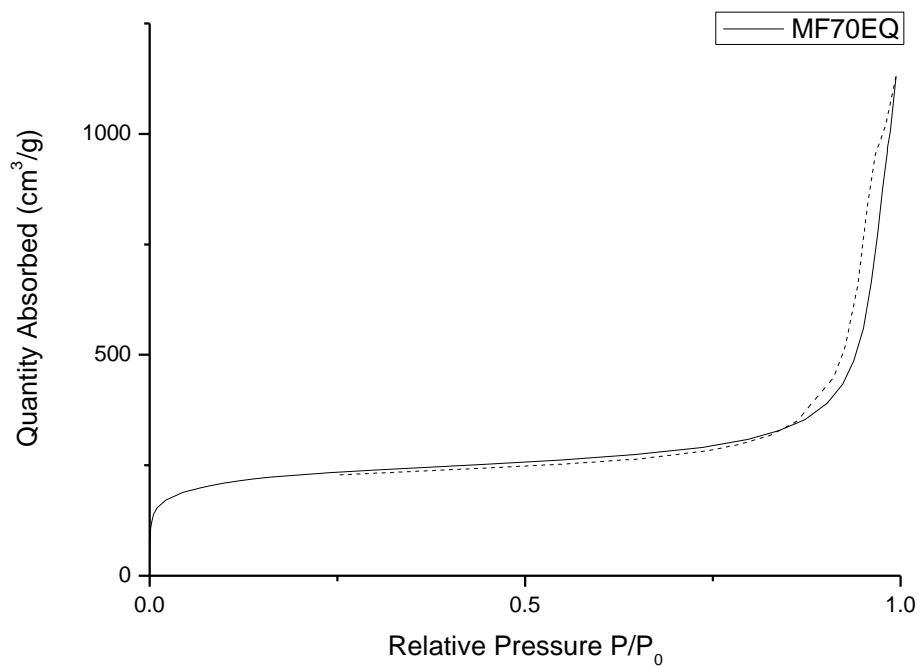


Figure S 4.11 N₂ Absorption isotherm of MF70EQ product

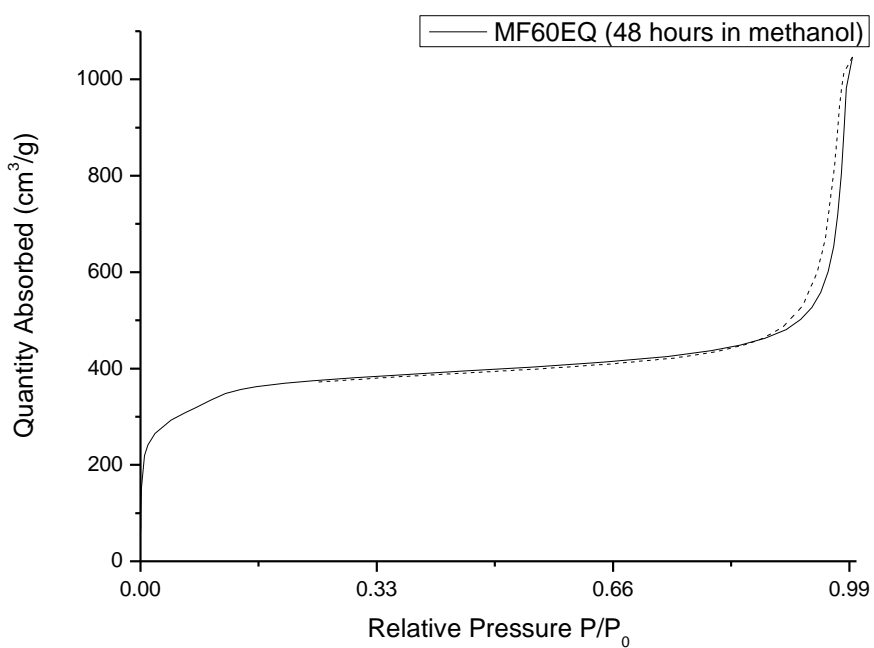


Figure S 4.12 N₂ Absorption isotherm of MF60EQ product (48 hours in methanol)

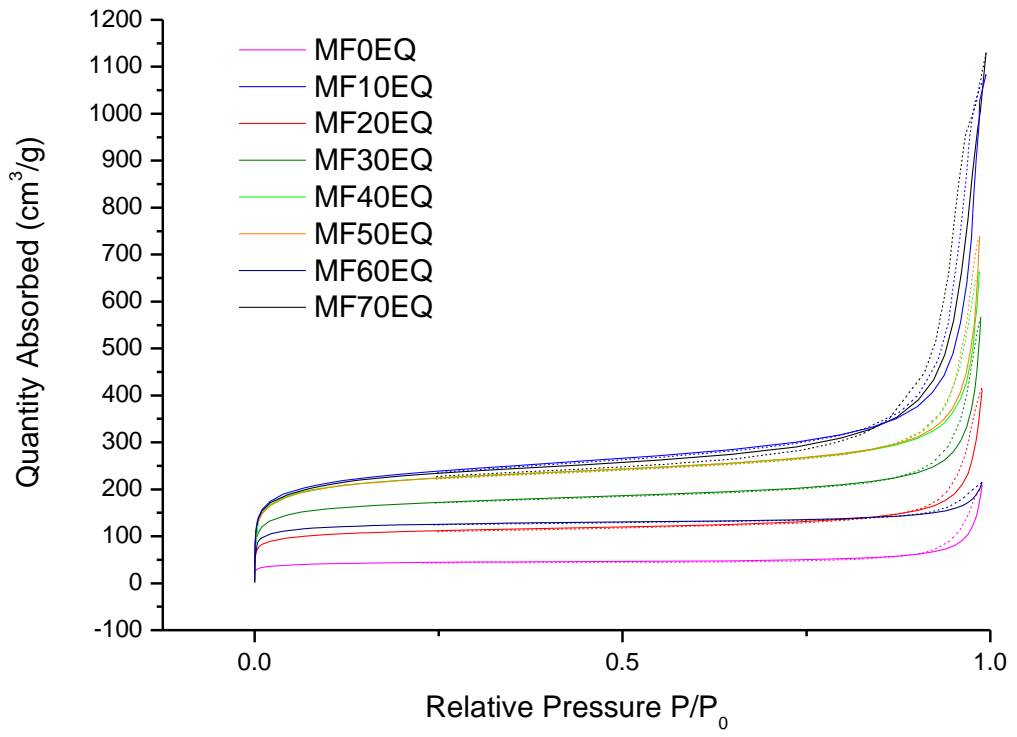


Figure S 4.13 Comparative N₂ isotherm graph for all microfluidic products

Chapter 5 Journal of Porous Materials Article, “Attempts at microfluidic synthesis of UiO-67 with incorporated Pd nanoparticles”, Submitted September 2023

Tom Bailey^{1*}, Dario Luis Fernandez Ainaga¹, Andrew James Britton¹, Nicole Hondow¹

1. School of Chemical and Process Engineering, University of Leeds, Leeds, LS2 9JT

Corresponding Author's Email address:

pmtwb@leeds.ac.uk (Tom Bailey)

5.1 Abstract

This work details the attempted microfluidic synthesis of encapsulated Pd(0) nanoparticles within the pores of a modified UiO-67 metal-organic framework. A microfluidic synthesis approach was used in an attempt to synthesise this product along with other benefits: reduced synthesis time and forming smaller nanoparticles with a smaller particle size distribution. Complications in this attempted synthesis are detailed, with no encapsulated Pd(0) nanoparticles formed. Insight is gained in that the presence of the 2,2'-bipyridine-5,5'-dicarboxylic acid (BPYDC) linker is necessary to contain the Pd(II) precursor within the MOF pores, otherwise it will be reduced outside of the pores and form larger nanoparticles. Secondly, the reducing power of DMF at 130 °C in 0.1 M NaBH₄/Water or 0.1 M NaBH₄/DMF is not strong enough to break the N-Pd bonds in the pores, contrary to literature reports.

5.2 Introduction

Metal nanoparticles have garnered interest for applications in catalysis due to their high surface area to volume ratios and certain catalytic properties not present in the bulk form.¹ Palladium nanoparticles have applications in catalysis for organic coupling reactions, hydrogenation of unsaturated olefins and alcohol oxidation reactions.² Unsupported metal nanoparticles coalesce and aggregate, leading to a loss of catalytic performance due to the

change in size.³ To counter this, supporting materials, such as Metal-Organic Frameworks (MOFs) are used to hold the nanoparticles in place, preventing aggregation. MOFs are particularly suited to this, with the porous structure allowing for nanoparticles to be held in place using non-covalent forces, ensuring a high catalytic activity while also reducing any leaching or aggregation of the Pd catalyst.⁴

Incorporation of nanoparticles into MOFs can be performed by two key methods. Firstly, the nanoparticles can be formed first, with the MOF cages subsequently formed around them.⁵ Secondly, the MOF cages can be built first with the metal precursor incorporated into the structure, which is then followed by a reduction reaction to grow the metal nanoparticles potentially within the pores themselves.⁶ Chen *et al* adapted the second method to incorporate Pd(0) nanoparticles into bipyridine dicarboxylic acid (BPYDC) modified UiO-67 without the need for an external reducing agent.⁷ This method used the increased reducing power of the DMF solvent at higher temperatures, with an initially low temperature used to form the UiO-67 with a $\text{PdCl}_2(\text{CH}_3\text{CN})_2$ precursor bonded to the nitrogen containing BPYDC linkers, followed by a higher temperature to break the N-Pd bonds and grow Pd(0) within the pores (Figure 5.1), with this confirmed through a combination of Transmission-Electron Microscopy (TEM) and X-ray photoelectron spectroscopy (XPS).

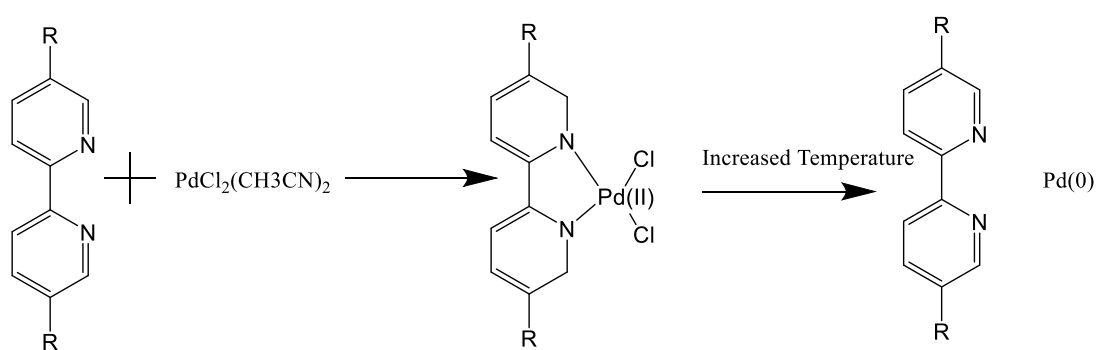


Figure 5.1: Reaction scheme for the incorporation of Pd(0) nanoparticles into UiO-67, using the experimental procedure given by Chen *et al.*⁷ Scheme has been drawn in ChemDraw22.

Microfluidic synthesis methods are known to improve MOF materials in several key ways. Firstly, higher residence time distributions present in batch stirred reactors lead to an increased particle size distribution. This is particularly important as nanoparticle size dictates the

physical and chemical properties.⁸ Secondly, MOF synthesis is traditionally a long process, with the solvothermal batch synthesis of UiO-67 for example requiring 24 hours of heating followed by several stages of washing,⁹ lowering the viability of these materials in an industrial setting as these long synthesis/processing times would ideally be avoided.

Microfluidic synthesis involves the use of sub micrometre sized tubing in a continuous flow synthesis. These low tubing diameters ensure a high level of mixing due to the high surface area to volume ratio, which has been shown to reduce the necessary synthesis time for various MOFs before, including MOF-5, HKUST-1 and UiO-67.^{10,11} Microfluidic synthesis is generally laminar flow which can lead to increased residence time distributions, which is a concern as this can lead to larger particle size distributions. However, using micro-mixing technologies, such as using a Coiled Flow Inverter Reactor (CFIR), will flatten the flow profile and provide lower residence time distributions and improved mixing.¹¹⁻¹³ Exploiting these effects could lead to an improved MOF/metal nanoparticle product, as improved mixing will increase the rate of nucleation for the both the nanoparticles and MOFs, leading to smaller nanoparticles.¹⁴

This research initially aimed to adapt the work by Chen *et al* into a microfluidic setting, aiming to reduce the reaction time needed to synthesise the Pd@UiO-67 product, and reduce the nanoparticle size and size distribution. This paper details the complications present within this system.

5.3 Materials and Methods

5.3.1 Materials

Zirconium chloride (98%, Cat number: L14891) and silicon oil (Cat number: A12728.36) were purchased from Alfa Aesar. Biphenyl dicarboxylic acid (BPDC; 95%, Cat number: 091522) was purchased from Fluorochem. Dimethylformamide (DMF; > 99.9%, Cat number: 27054) and Bis(acetonitrile)dichloropalladium(II) ($\text{PdCl}_2(\text{CH}_3\text{CN})_2$; Cat number: 225657-500MG) were purchased from Sigma Aldrich. Chloroform (CH_3Cl ; Cat number: CHE1574) and

hydrochloric acid (HCl; Cat number: CHE2138) were purchased from Scientific Laboratory Supplies. 2,2'-Bipyridine-5,5'-dicarboxylic Acid (BPYDC; Cat number: 29472-5g-CAY) was purchased from Cambridge Bioscience.

5.3.2 Microfluidic Reactor

The Microfluidic reactor was made of 3 inlets (DMF, $ZrCl_4 + DMF + PdCl_2(CH_3CN)_2$, BPYDC + HCl + DMF), leading to two coiled flow units in sequence. The first unit was made up of 12.6 m of tubing, with an inner diameter of 0.79×10^{-3} m, giving an overall volume of 6.97 ml. The tubing was tightly coiled around four 20 ml syringes, with a diameter of 5 mm and was placed in an 80 °C water bath. The second unit is made up of two 3D printed CFIR units, as described in our groups previous work,¹¹ with an overall volume of 1.97 ml, placed in a silicon oil bath set at 130 °C. The syringes containing reactants had small (5 mm) magnetic stirrer bars placed inside, with a small magnetic stirrer plate clamped above the syringes to keep the reactants suspended throughout the reaction. A N_2 cylinder was connected to the product collection bottle, opened slightly to increase the overall reaction pressure by 1 bar. T_1 was set at 45 minutes and T_2 to 14.38 minutes with an overall flowrate of 0.1374 ml/min.

5.3.3 Microfluidic synthesis of UiO-67-BPDC

Adapting the synthesis procedure by Chen *et al* of UiO-67-BPYDC to initial form UiO-67-BPDC as a test run,⁷ $ZrCl_4$ (67 mg) was added to DMF (8.375 ml) while BPDC (90 mg) and concentrated HCl (1.875 ml) was added to DMF (6.5625 ml) in a separate beaker. Both solutions were sonicated for 20 minutes to ensure all solids were dissolved. These two solutions were then drawn into separate 20 ml syringes, each with a small magnet placed inside, which was stirred throughout the microfluidic reaction, ensuring a consistent reactant solution concentration. These were connected to the microfluidic system, which was cleaned and filled with dry DMF beforehand, with both reaction stages heated to their appropriate temperatures. As the syringe pumps were started, the pressure was slowly increased in the system, with all pressure adjustments performed before the two reactant solutions mixed with each other at the T-Connector. Once the reactant solution had been pushed through at the

appropriate rate (0.1374 ml/min, $T_1 = 45$ minutes, $T_2 = 14.38$ minutes), DMF was pumped through at the same rate to clear any reactants/products in the system while ensuring the residence time was consistent. The product was then centrifuged and washed with DMF (2 x 30 ml) and chloroform (2 x 30ml). The product (51.1 mg) was then dried in a 150 °C oven overnight.

5.3.4 Attempted Microfluidic synthesis of Pd@UiO-67-BPYDC

Adapting the synthesis procedure by Chen *et al.*,⁷ ZrCl₄ (67 mg) and PdCl₂(CH₃CN)₂ (3.8 mg) were added to DMF (8.375 ml) while BPYDC (90 mg) and concentrated HCl (1.875 ml) were added to DMF (6.5625 ml) in a separate beaker. Both solutions were sonicated for 20 minutes to ensure all solids were dissolved. These two solutions were then drawn into separate 20 ml syringes, each with a 5 mm magnet placed inside, which was stirred throughout the microfluidic reaction, ensure a consistent reactant solution concentration. These were connected to the microfluidic system, which had been cleaned and filled with dry DMF beforehand, with both reaction stages heated to their appropriate temperatures. As the syringe pumps started, the pressure was slowly increased in the system, with all pressure adjustments performed before the two reactant solutions mixed with each other at the T-Connector. Once the reactant solution had been pushed through at the appropriate rate (0.1374 ml/min, $T_1 = 45$ minutes, $T_2 = 14.38$ minutes), DMF was pumped through at the same rate to clear any reactants/products in the system while ensuring the residence time was consistent. The product was then centrifuged and washed with DMF (2 x 30 ml) and chloroform (2 x 30ml). The product (54.3 mg) was then dried in a 150 °C oven overnight.

5.3.5 Attempted Batch Synthesis of Pd@UiO-67-BPYDC

Adapting the synthesis procedure by Chen *et al.*,⁷ ZrCl₄ (67.1 mg), PdCl₂(CH₃CN)₂ (4.4 mg), BPYDC (90.4 mg) and HCl (1.875 ml) was added to DMF (15 ml) in a round bottom flask and sonicated for 20 minutes. This was then connected to a condenser and heated/stirred at 80 °C for 20 hours and 130 °C for 4 hours. The product was then centrifuged and washed with

DMF (2 x 30 ml) and chloroform (2 x 30ml). The product (82 mg) was then dried at 150 °C overnight.

5.3.6 Reduction of Pd(II)-UiO-67-BPYDC using NaBH₄/H₂O

Adapting the reduction reaction performed by Cai *et al.*,¹⁵ microfluidically formed Pd(II)-UiO-67-BPYDC (10 mg) was added to Milli-Q water (1.5 ml) in a beaker. This was sonicated for 2 minutes before being placed in an ice bath and stirred for 30 minutes. Following this 0.1 M NaBH₄/water (150 µl) was added and stirred for 2 hours in an ice bath. This was then centrifuged and washed with chloroform (2 x 15 ml) before being dried at 150 °C overnight.

5.3.7 Reduction of Pd(II)-UiO-67-BPYDC using NaBH₄/DMF

Adapting the reduction reaction performed by Chen *et al.*,¹⁵ Pd(II)-UiO-67-BPYDC (25 – 80 mg, full amount synthesised from previous reactions) was added to DMF (2 ml) in a beaker. This was placed in an ice bath and stirred for 30 mins, before the 0.1 M NaBH₄/DMF (1.5 ml) was slowly added. This was stirred for 1 hour before being separated washed with DMF (2 x 15 ml) and then chloroform (2 x 15 ml). The product was then dried at 150 °C overnight.

5.3.8 Reduction of Pd(II)-UiO-67-BPYDC using NaBH₄/DMF (increased reducing agent)

Further adaptation of reduction reaction performed by Chen *et al.*,¹⁵ Pd(II)-UiO-67-BPYDC (25 – 80 mg, full amount synthesised from previous reactions) was added to DMF (2 ml) and then stirred for 30 minutes in an ice bath. 0.1 M NaBH₄/DMF (5 ml) was added slowly before being stirred in the ice bath for 4 hours. This was centrifuged and washed with DMF (5 x 1.5 ml) and chloroform (5 x 1.5 ml) before being dried at 150 °C overnight.

5.3.9 Reduction of Pd(II)-UiO-67-BPYDC using NaBH₄/DMF (increased solvent)

Further adaptation of reduction reaction performed by Chen *et al.*,¹⁵ Pd(II)-UiO-67-BPYDC (25 – 80 mg, full amount synthesised from previous reactions) was added to DMF (20 ml) and

then stirred for 30 minutes in an ice bath. 0.1 M NaBH₄/DMF (15 ml) was added slowly before being stirred in the ice bath for 4 hours. This was centrifuged and washed with DMF (5 x 1.5 ml) and chloroform (5 x 1.5 ml) before being dried at 150 °C overnight.

5.3.10 Attempted Two Stage Batch synthesis of Pd(0)-UiO-67-BPYDC

Combining two of the previous procedures, ZrCl₄ (68.7 mg), PdCl₂(CH₃CN)₂ (5 mg), BPYDC (90.1 mg) and HCl (1.875 ml) was added to DMF (15 ml) in a round bottom flask and sonicated for 20 minutes. This was then connected to a condensation column and heated/stirred at 130 °C for 24 hours. This round bottom flask was then transferred to an ice bath and stirred for 30 minutes. 0.1 M NaBH₄/DMF (15 ml) is added slowly, then was stirred for 4 hours. This was then separated and washed with DMF (2 x 30 ml) and chloroform (2 x 30 ml) before being dried at 150 °C overnight.

5.3.11 Characterisation

XRD was performed using a Bruker D8 with copper K-alpha source ($\lambda = 1.5406 \text{ \AA}$). Scan conditions were $2\theta = 3^\circ\text{-}18^\circ$ at $0.5^\circ/\text{min}$, which is equivalent to a step-size of 0.01649° . Baselines were removed in Highscore using Sonneveld and Visser baseline reduction, with granularity = 15, a bending factor of 0. The data was then automatically smoothed using Fast Fourier smoothing with a degree of smoothing = 5. Before XRD, the samples would be dried overnight at 120 °C. Simulated XRD data were performed using Vesta, with the CIF for the HCP product being taken from the supporting information of the work by Cliffe *et al.*¹⁶ The CIF for the FCC product was obtained from the Cambridge Structural Database, from a paper by Goodnough *et al.*¹⁷ Transmission electron microscopy (TEM) was conducted on an FEI Titan³ Themis G2 operating at 300 kV fitted with 4 EDX silicon drift detectors, multiple STEM detectors, and a Gatan One-View CCD. TEM samples were prepared by dispersing the powder in methanol, with a drop placed on a continuous carbon coated copper grid. For the STEM, High angle annular dark-field (HAADF) STEM was used to form images with atomic number contrast. XPS was performed on a FlexMod UHV-XPS from SPECS, with a pressure of $\sim 1 \times 10^{-9}$ mbar in the chamber. It has a Phoibos 150 hemispherical analyser with 1D-DLD

detectors. The analyser slits were fully open and all measurements were taken in Medium Area mode. Survey spectra were measured at a pass energy of 50 eV and a step size of 1 eV and high resolution spectra were measured at a pass energy of 30 eV and a step size of 0.1 eV. A SPECS XR-50M X-ray source was used with an Al anode (1486.7 eV) at 400 W and 15 kV in an unfocussed mode (spot size 3.5 x 1 mm). Samples were mounted in powder form onto carbon tape attached to standard Omicron plates. Excess powder was knocked off before introducing into the chamber. The sample was charge neutralised using an electron flood gun. In this case, the flood gun was set to a current of 75 μ A and an energy of 4 eV. The XPS spectra was calibrated to the aliphatic C 1S spectra at 284.4 eV. CasaXPS and Origin software were used to analyse the data.

5.4 Results and Discussion

5.4.1 Transfer of synthesis to microfluidics

The synthesis of face centred cubic (FCC) UiO-67-BPDC through microfluidics was performed by adapting the synthesis procedure of Chen *et al.*⁷ UiO-67-BPDC was chosen to be synthesised first as a test due to the high cost of the BPYDC linker, with the aim to make a synthesis procedure for crystalline UiO-67-BPDC that could then be applied to the BPYDC product. This was achieved through varying the HCl volume added to the reactant mixture, leading to a crystalline UiO-67 structure being formed in 1 hour of reaction time, compared to the 24 hours used in the literature batch method. Using the HCl volume as described in the literature (0.5 ml),⁷ yielded an amorphous UiO-67-BPDC product (**Figure 5.2a**). It was possible to either increase the residence time in the reactor or to increase the volume of HCl in the reactant mixture. As the residence time was already 1 hour, increasing this further would lead to a reduction in flow rate for the reactants, potentially resulting in less efficient mixing, and more fouling in the system. For these reasons, the volume of HCl was modified while other reactant volumes/masses being kept consistent with the literature process described by Chen *et al.*⁷

Increasing the volume of HCl produced a more crystalline material but did also result in a change in structure from a purely FCC product to a mixture of FCC and a hexagonal close packed (HCP) product (**Figure 5.2b-c**). HCl is an acid modulator which will increase the crystallinity of the product while increasing the reaction rate, which in contrast to other acid modulators such as benzoic acid where the crystallinity is increased through slowing down the reaction rate.⁹ Increasing the reaction rate too much however with the use of HCl has been previously shown to give this HCP product instead of the FCC.¹⁸ The reaction conditions that gave a crystalline FCC UiO-67-BPDC product (~1 hour residence time, 1.875 ml HCl) were taken forward in the attempts to form Pd(0)-UiO-67-BPYDC.

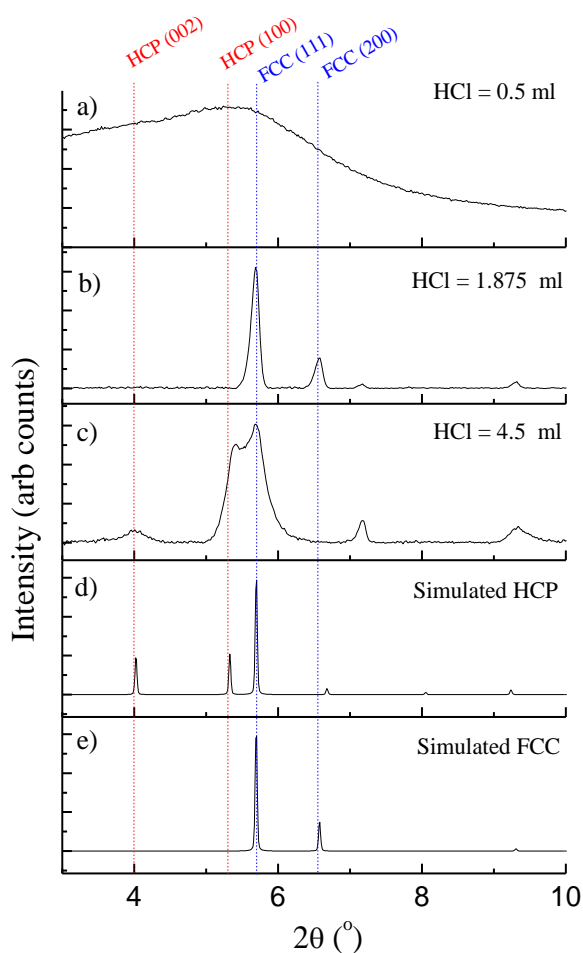


Figure 5.2: XRD patterns for microfluidically synthesised UiO-67-BPDC under varying conditions with simulated patterns for both HCP and FCC phases. All microfluidic products have a residence time ~ 1 hour. a) Microfluidically produced UiO-67-BPDC, HCl volume = 0.5 ml. b) Microfluidically produced UiO-67-BPDC, HCl volume = 1.875 ml. c) Microfluidically produced UiO-67-BPDC, HCl volume = 4.5 ml. d) Simulated XRD pattern for HCP UiO-67-BPDC. Pattern was simulated in VESTA, using a CIF file obtained from Cliff *et al.*'s SI.¹⁶ e) Simulated XRD pattern for FCC UiO-67-BPDC. Pattern was simulated in VESTA, using a CIF file obtained from the Cambridge Structural Database, from a paper by Goodenough *et al.*¹⁷ Key diffraction peaks for the HCP

are highlighted at $4.0^\circ 2\theta$ (002) and $5.3^\circ 2\theta$ (100), and for FCC phase at $5.7^\circ 2\theta$ (111) and $6.6^\circ 2\theta$ (200). Volumes of HCl are related to the specific experimental procedure used, when volume of DMF = 15 ml.

5.4.2 Attempt to incorporate Pd(0) using microfluidic synthesis.

Following the success of forming crystalline UiO-67-BPDC in this reactor using HCl as the acid modulator, an attempted synthesis was made using both the BPYDC linker and the $\text{PdCl}_2(\text{CH}_3\text{CN})_2$ precursor included. BPYDC is used for this synthesis as opposed to BPDC due to the N-Pd bonds that can be formed, aiming to secure the precursor inside the MOF pores before reduction. The product was not dark coloured as described in the work by Chen *et al* for the batch equivalent. Initial XRD results (**Figure 5.3**Error! Reference source not found.) showed the product to be crystalline UiO-67, but through analysis by HAADF STEM and EDX no Pd nanoparticles were imaged within the structure. Using HAADF STEM-EDX, palladium was detected throughout the material but not as nanoparticles. The expected size of these nanoparticles should be ~ 1.5 nm and should be seen within the HAADF STEM images if they have been formed. Other work in the area of supported Pd nanoparticles has clearly imaged their presence for nanoparticles under 5 nm, such as Liu *et al*'s work on supporting Pd nanoparticles on a carbon support.¹⁹ Their TEM images were performed at a magnification lower than shown here, so if Pd nanoparticles were present in this sample they would be clearly imaged. XPS for this product also confirmed a lack of Pd(0) present (**Figure 5.4a**).

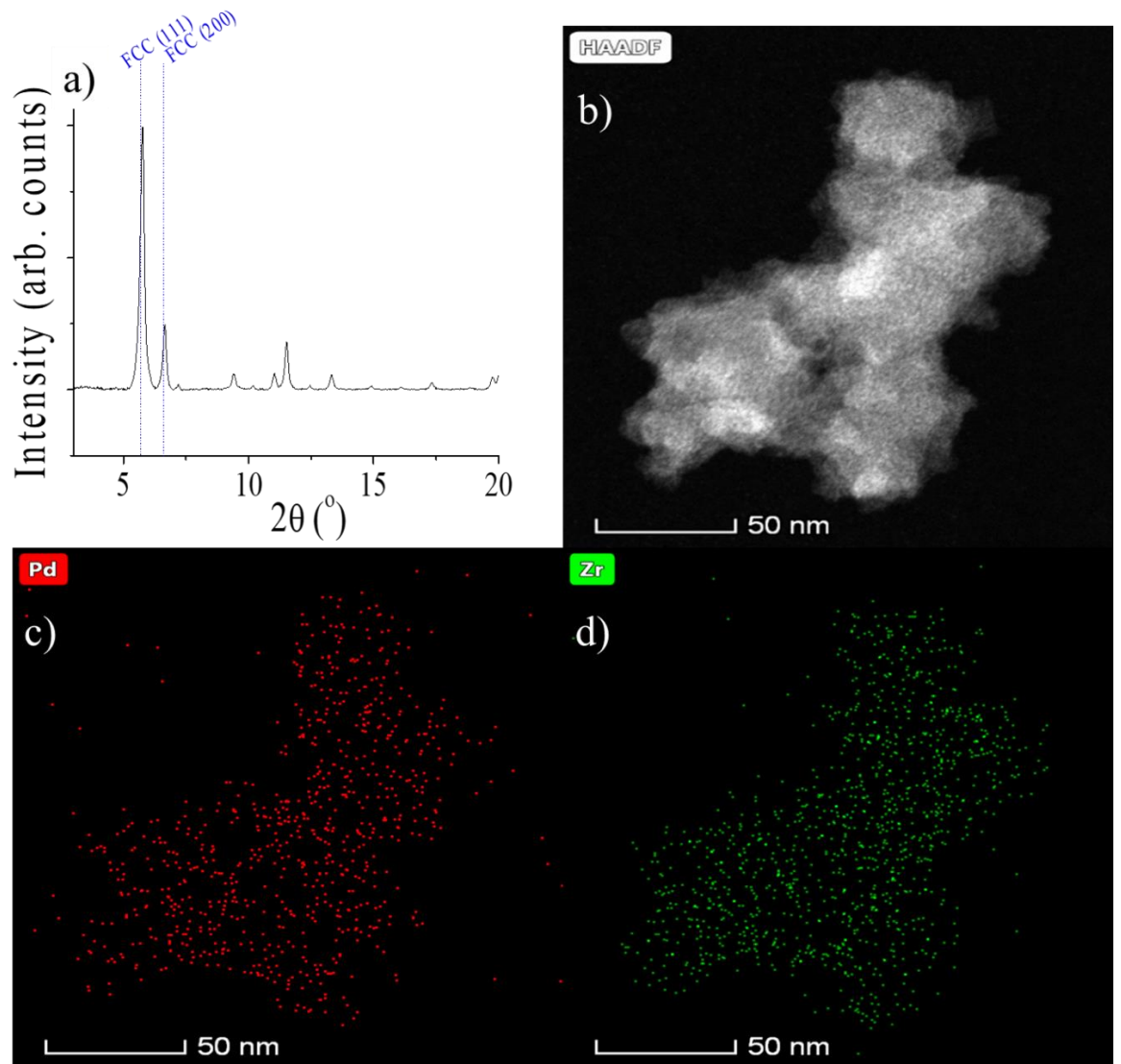


Figure 5.3: a) XRD pattern for microfluidically synthesised Pd(II)-UiO-67-BPYDC. b) HAADF STEM image of microfluidically synthesised Pd(II)-UiO-67-BPYDC. c) EDX map for Pd present in microfluidically synthesised Pd(II)-UiO-67-BPYDC. d) EDX map for Zr present in microfluidically synthesised Pd(II)-UiO-67-BPYDC.

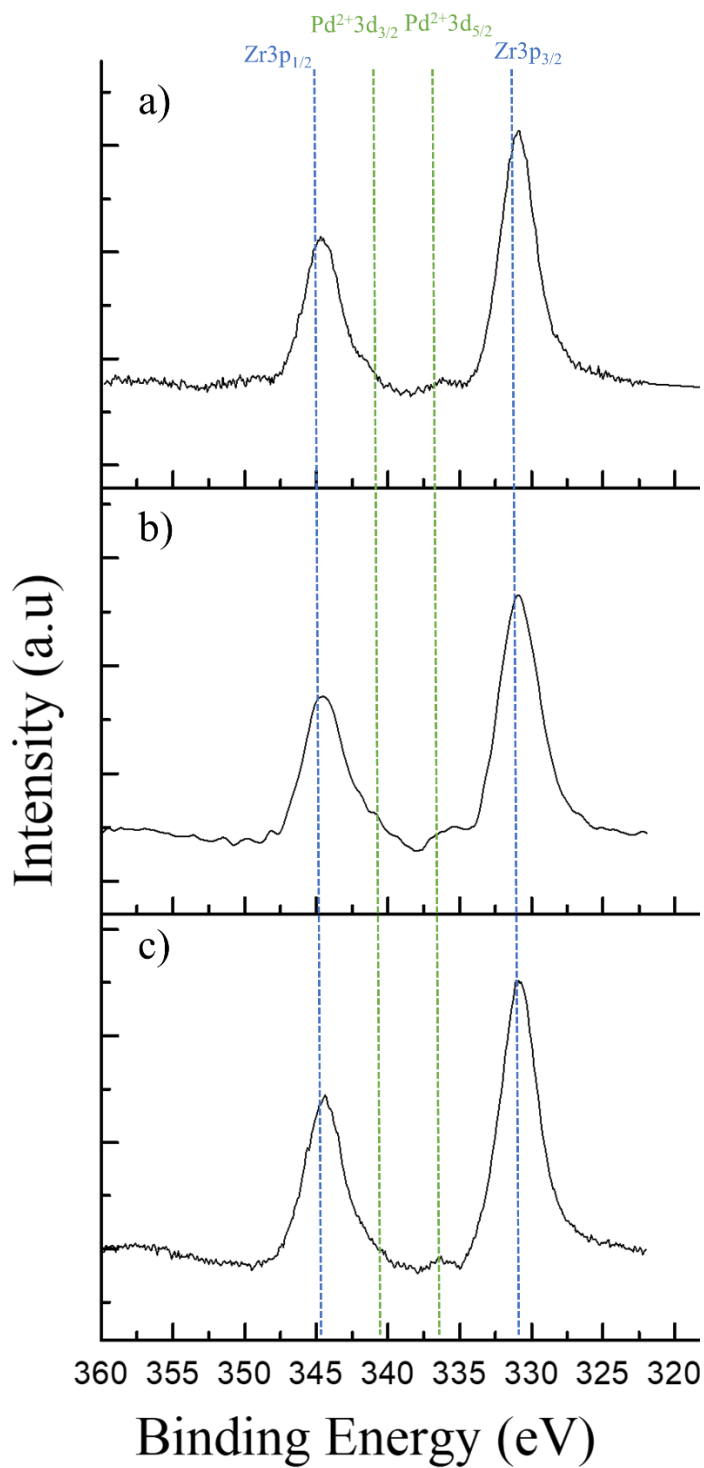


Figure 5.4: X-Ray Photoelectron Spectra for microfluidically formed Pd(II)-UiO-67-BPYDC products. a) XPS for microfluidically formed Pd(II)-UiO-67-BPYDC. b) XPS for microfluidically formed Pd(II)-UiO-67-BPYDC post reduction by $NaBH_4$ /water. c) XPS for microfluidically formed Pd(II)-UiO-67-BPYDC post reduction by $NaBH_4$ /DMF. Blue dashed lines correspond to Zr based signals, green dashed lines correspond to Pd^{2+} based signals.

Time was considered as a factor for why no nanoparticles were produced. This sample was placed in a batch autoclave with DMF and heated for a further 24 hours at 130 °C to align with the time used in the experimental procedure this work is based on. The production of Pd particles were then observed in the TEM and EDX of this product but not within the pores of the UiO-67-BPYDC structure (**Figure 5.5a**). These Pd nanoparticles formed are thought to be the result of reducing unbound Pd(II) precursor, not the Pd(II) connected to the BPYDC linkers, due to HAADF STEM-EDX of just the darker areas showing only a high amount of palladium present (**Figure 5.5c**). HAADF STEM-EDX of other areas showed the high amount of zirconium as expected while still containing some palladium, which will be bonded to the BPYDC linkers (**Figure 5.5d**). If the palladium was being contained within the pores, they would be much smaller, approximately 1.5 nm according to Chen *et al*'s work, rather than the average size of 61 ± 11 nm seen here, with the HAADF STEM-EDX also showing a higher concentration of zirconium compared to palladium throughout the material. The literature pore size for UiO-67 is ~ 2.3 nm for the octahedral pore and ~ 1.2 nm for the tetrahedral pore, with some variance depending on the level of defect present or the crystal phase type.²⁰ Therefore, these larger Pd nanoparticles cannot be encapsulated within the UiO-67 pores.

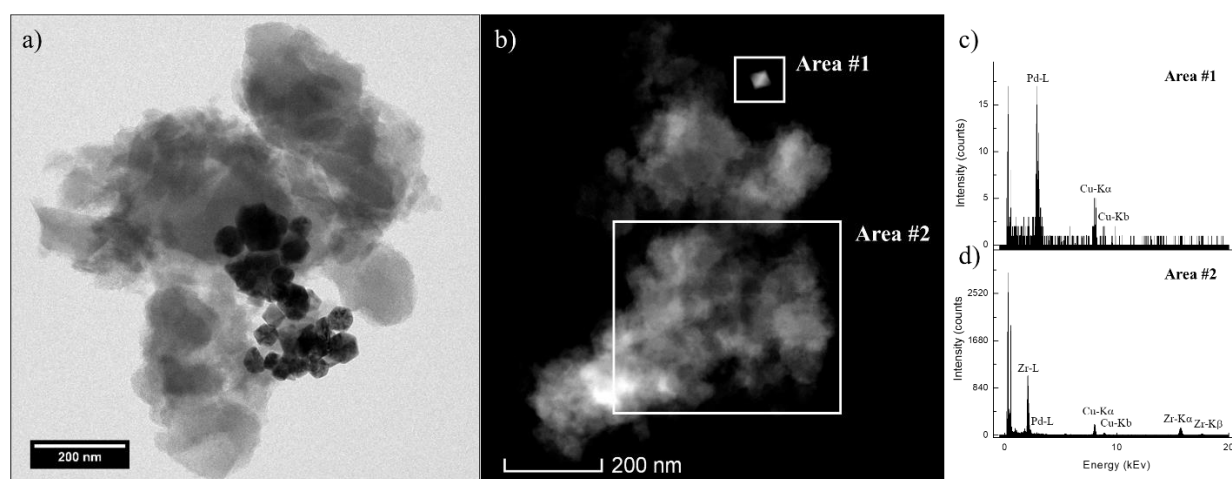


Figure 5.5: a) TEM image of microfluidically synthesised Pd(II)-UiO-67-BPYDC post 24 hours heating in DMF, with Pd particles of 61 ± 11 nm. b) HAADF STEM image of a different area for the same material, with areas for EDX spectra highlighted. c) EDX spectrum for Area #1 with key peaks labelled with a high concentration of palladium labelled compared to d) EDX spectrum for Area #2 with key peaks labelled.

As some reduction was successful of the precursor, this reduction was repeated on a re-washed synthesis product from **Figure 5.3** (30 ml DMF x 2, 30 ml CH₃Cl x 2, centrifuged at 6000 rpm for 15 minutes each time). This washing removed the unbonded Pd(II) precursor leaving only Pd(II) bound to the BPYDC linkers. This synthesis of Pd(0) nanoparticles was unsuccessful due to lack of Pd(0) within the XPS (**Figure S 5.1**).

In the Zr3p XPS spectrum, if Pd(0) was present the current peak for the Pd²⁺3d_{3/2} would be shifted to a lower binding energy and partially overlap with the Zr3p_{3/2} peak.⁷ However, none of the reduction methods used in this section were successful in breaking the N-Pd bonds being formed, with only peaks present that correspond to Pd(II) and no shift to lower energies occurring. Two additional reduction methods were adapted from previous literature methods: Stirring the sample in an ice bath with 0.1 M NaBH₄/H₂O solution added to the sample,¹⁵ and stirring the sample in an ice bath with 0.1 M NaBH₄/DMF solution added to the sample,²¹ with repeated washing (30 ml DMF x 2, 30 ml CH₃Cl x 2) of the Pd(II)-UiO-67-BPYDC products performed beforehand to remove any solvent/unreacted precursor. For this microfluidically synthesised product, the “increased reducing agent” method was used for the 0.1 M NaBH₄/DMF reduction. Neither of the literature methods formed Pd(0) as can be seen in **Figure 5.4b** and **Figure 5.4c**, with no Pd(0) peaks present in the XPS. The 0.1 M NaBH₄/DMF reduction of this product was performed using a higher volume of solvent (20 ml DMF instead of 2 ml, 15 ml 0.1 M NaBH₄/DMF instead of 1.5 ml) using a Pd(II)-UiO-67-BPYDC sample that had not undergone extra washing before reduction, with the idea that increased solvent could solve any potential solubility issues that were present in this reaction and secondly, the presence of unreacted Pd complex was thought to potentially be necessary for the production of Pd(0) nanoparticles. These unreacted complex particles would be reduced first and potentially act as growth sites for the Pd(II) to release and join to, giving a lower energy barrier to the N-Pd bond breaking reaction. However, this attempt was unsuccessful, with TEM taken for this product showing no palladium nanoparticles present (**Figure S 5.2**).

Following the lack of success in reducing the Pd(II) species in the UiO-67-BPYDC product formed through microfluidics, the focus turned to replicating the literature processes in a batch setting, to examine if the use of microfluidics was preventing the formation of Pd(0).

5.4.3 Batch synthesis

To determine if microfluidic synthesis was causing challenges in the formation of Pd(0) nanoparticles within the UiO-67 pores, the microfluidic procedure used was modified to batch, with the reaction length adapted to that of the literature (heating at 80 C⁰ for 20 hours, 130 C⁰ for 4 hours).⁷ It differs from the literature method with the volume of HCl used (1.875 ml rather than 0.5 ml), which was kept consistent with the microfluidic synthesis performed and synthesis was performed with 0.5 ml HCl later on to investigate if this would affect the synthesis. However, TEM showed no Pd(0) nanoparticles present within the pores (**Figure 5.6a-b**). As stated earlier, if Pd nanoparticles were present within the sample, they would be identifiable within the TEM, with a higher magnification image showing no sign of Pd nanoparticles (**Figure 5.6b**).

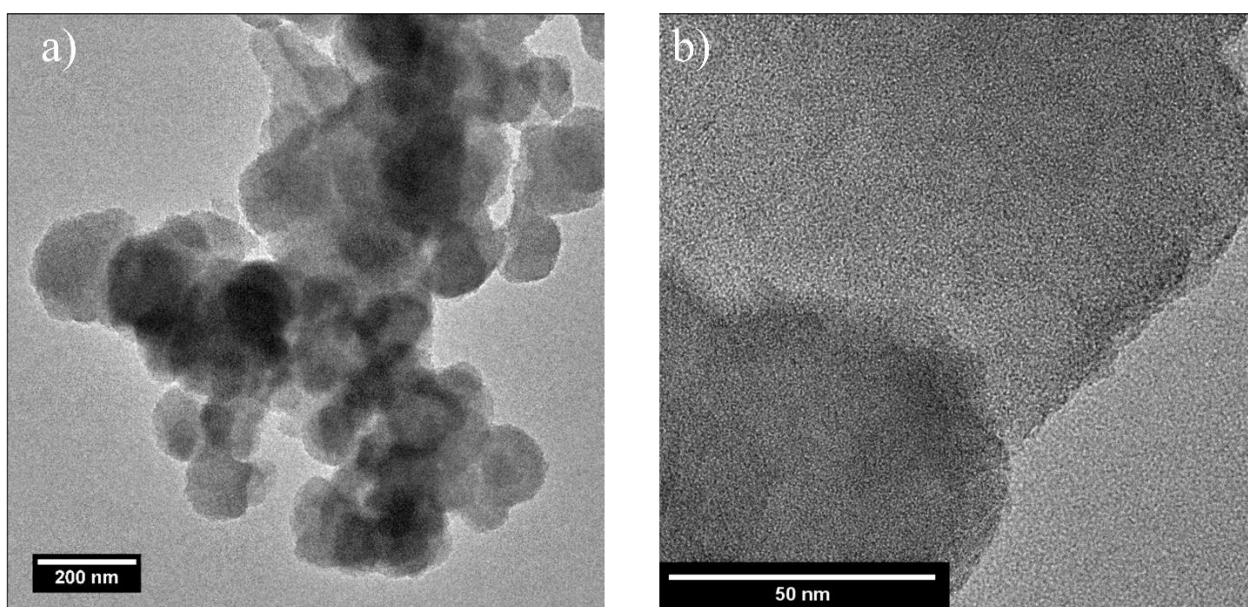


Figure 5.6: a) TEM image of batch synthesised Pd(II)-UiO-67-BPYDC. b) Higher magnification TEM image of batch synthesised Pd(II)-UiO-67-BPYDC.

XPS also confirmed no Pd(0) was present (**Figure 5.7a**), with the Pd²⁺3d_{3/2} and Zr3d_{3/2} peaks remaining separate, as seen in the microfluidic products.

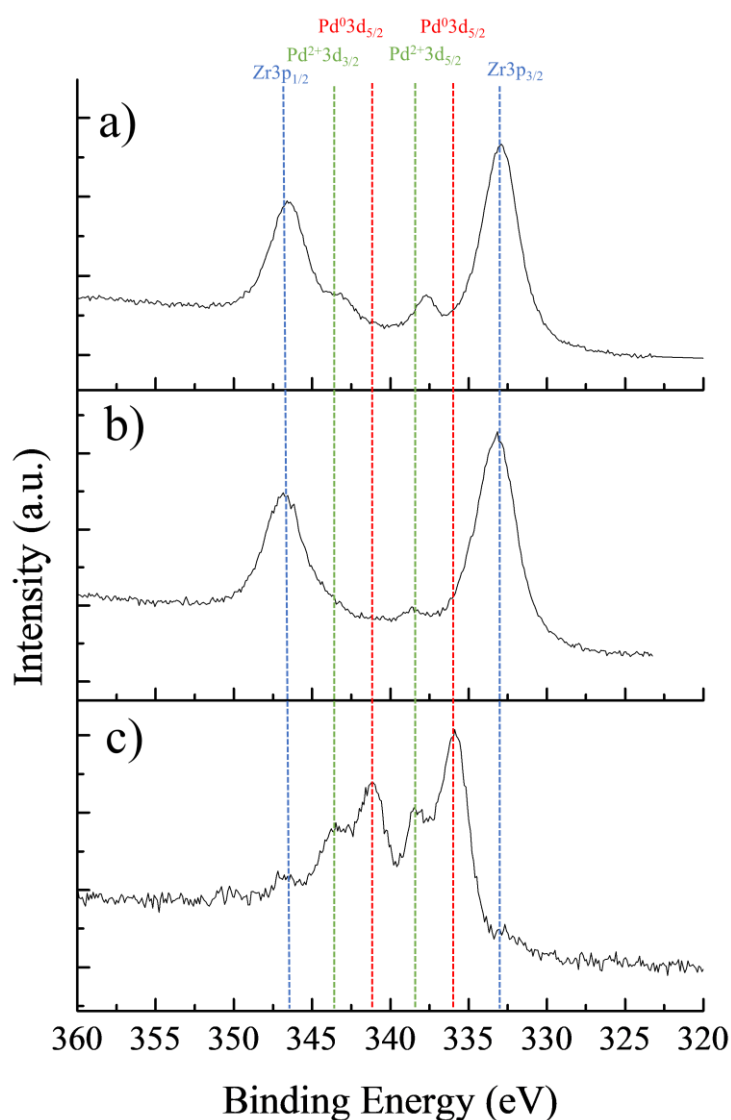


Figure 5.7: X-ray photoelectron spectra for batch synthesised Pd(II)-UiO-67-BPYDC products. a) XPS for batch synthesised Pd(II)-UiO-67-BPYDC. b) XPS for batch synthesised Pd(II)-UiO-67-BPYDC post reduction by NaBH₄/DMF. c) XPS for waste collected from NaBH₄/DMF reduction of batch synthesised Pd(II)-UiO-67-BPYDC.

Following this, the batch produced Pd(II)-UiO-67-BPYDC was reduced using 0.1 M NaBH₄/DMF as performed for the microfluidic products earlier. The reduction using NaBH₄ led to a colour change to black as the reducing agent was added, which is referred to in the literature method.²¹ There was no Pd(0) present based on the XPS (**Figure 5.7b**), suggesting that the colour change was due to unreacted Pd(II) complex in solution being reduced. This colour change being due to the reduction of unbonded Pd(II) complex is confirmed by the XPS (**Figure 5.7c**) of a solid that formed from the waste solution following separation of the

MOF material. The spectrum shows peaks for both Pd(0) and Pd(II). TEM (**Figure 5.8**) of this product also shows that Pd nanoparticles are present, however these appear independently of the UiO-67, not within the pores of the MOF, suggesting the reduction of starting Pd(II) complex. These Pd nanoparticles have an average diameter of $2.5 \text{ nm} \pm 0.6 \text{ nm}$, measured from 166 nanoparticles.

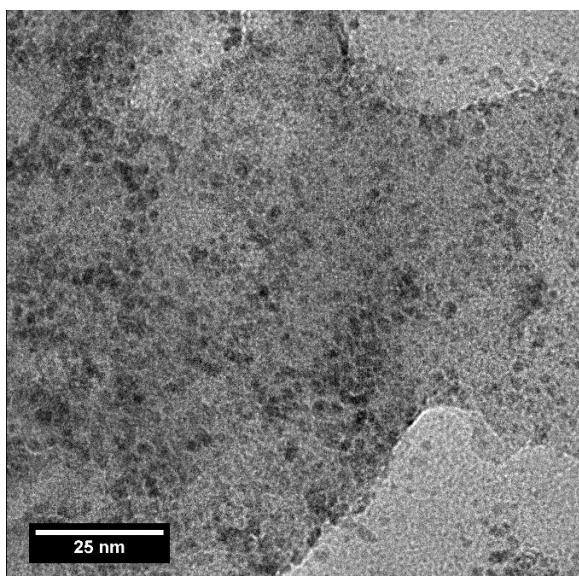


Figure 5.8: TEM image for solid found in the waste solution from the NaBH_4/DMF reduction of batch synthesised Pd(II)-UiO-67-BPYDC following separation of the MOF material.

Alongside this, an attempted batch synthesis of Pd(0)-UiO-67-BPYDC was performed using the exact volume of HCl present in the literature method (0.5 ml), with two external reductions performed. However, none of these three products showed the presence of Pd(0) nanoparticles. TEM for these two reduction products are provided in **Figure S 5.3**.

5.4.4 Two stage batch synthesis

Following observations in the previous experiments and a lack of success in breaking the N-Pd bond present made evident through no Pd(0) peak in the XPS taken for these products, a new experimental protocol was established. Firstly, with the observation of Pd(0) nanoparticles in the waste collected from NaBH_4/DMF reduction of batch synthesised Pd(II)-UiO-67-BPYDC and the colour change to black in this reaction, it was clear that the Pd(II)

precursor could be reduced by this method but the N-Pd bonds were not broken by the method used. Secondly, washing of the product between the reduction stages would remove unreacted Pd(II) precursor, leading to no nanoparticle formation. The new method would take both of these into account, with no separation/washing occurring between the synthesis and the reduction reactions to ensure that the precursor was present to be reduced and form nanoparticles within the pores of the MOF. This lack of separation/washing between the syntheses and reduction is similar to the “one-step” method by Chen *et al* in which this work has been based on.⁷ Alongside this, the BPYDC linker was switched out for the BPDC linker, with no nitrogen present. This would ensure no N-Pd bonds were made, allowing for Pd(II) precursor to be reduced. TEM-EDX (Figure 5.9) of this product shows Pd particles of $\sim 21 \pm 13$ nm, indicating that the N-Pd bonds are required to form a UiO-67 material with Pd of a small (*i.e.* 1-2 nm) size distributed evenly throughout.

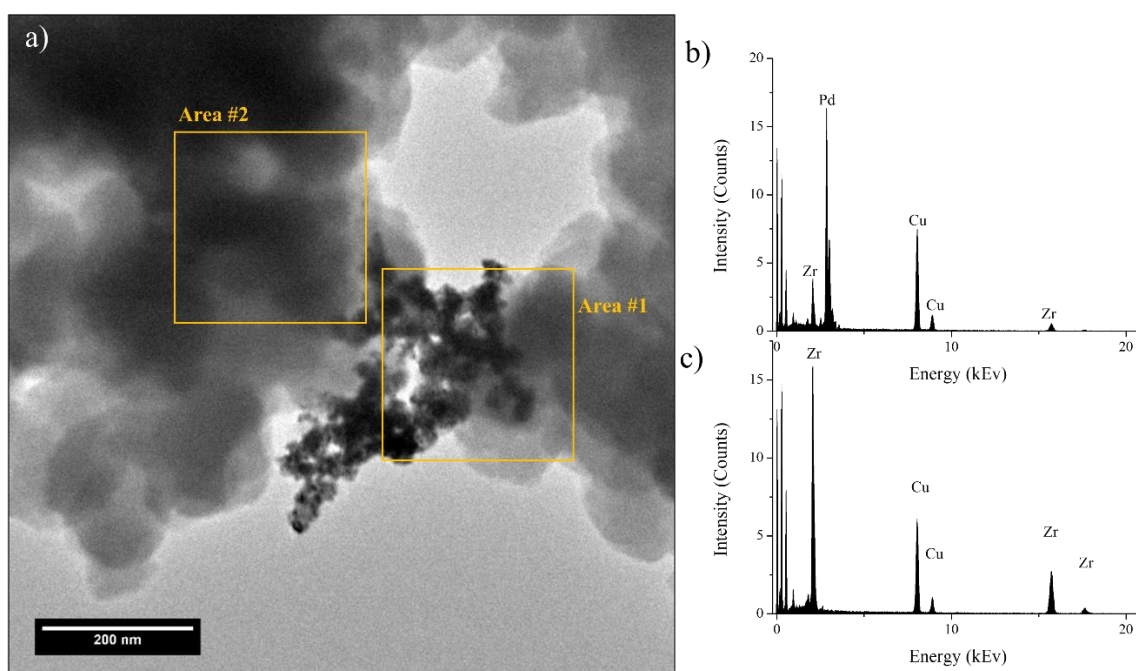


Figure 5.9: a) TEM image of two stage batch synthesised Pd(II)-UiO-67-BPDC with Pd nanoparticles of 21 ± 13 nm, EDX areas are highlighted. b) EDX spectrum taken over Area #1. c) EDX spectrum taken over Area #2.

As the N-Pd bonds are needed to ensure an even distribution of Pd(II) throughout the structure for reduction, the BPYDC linker was used for the two-stage reaction. However, as with all previous Pd(II)-UiO-67-BPYDC products where NaBH₄ had been used as the reducing agent, no Pd nanoparticles are observed in the HAADF STEM-EDX (Figure 5.10a - c). TEM for this product also gave the same conclusion (Figure 5.10d).

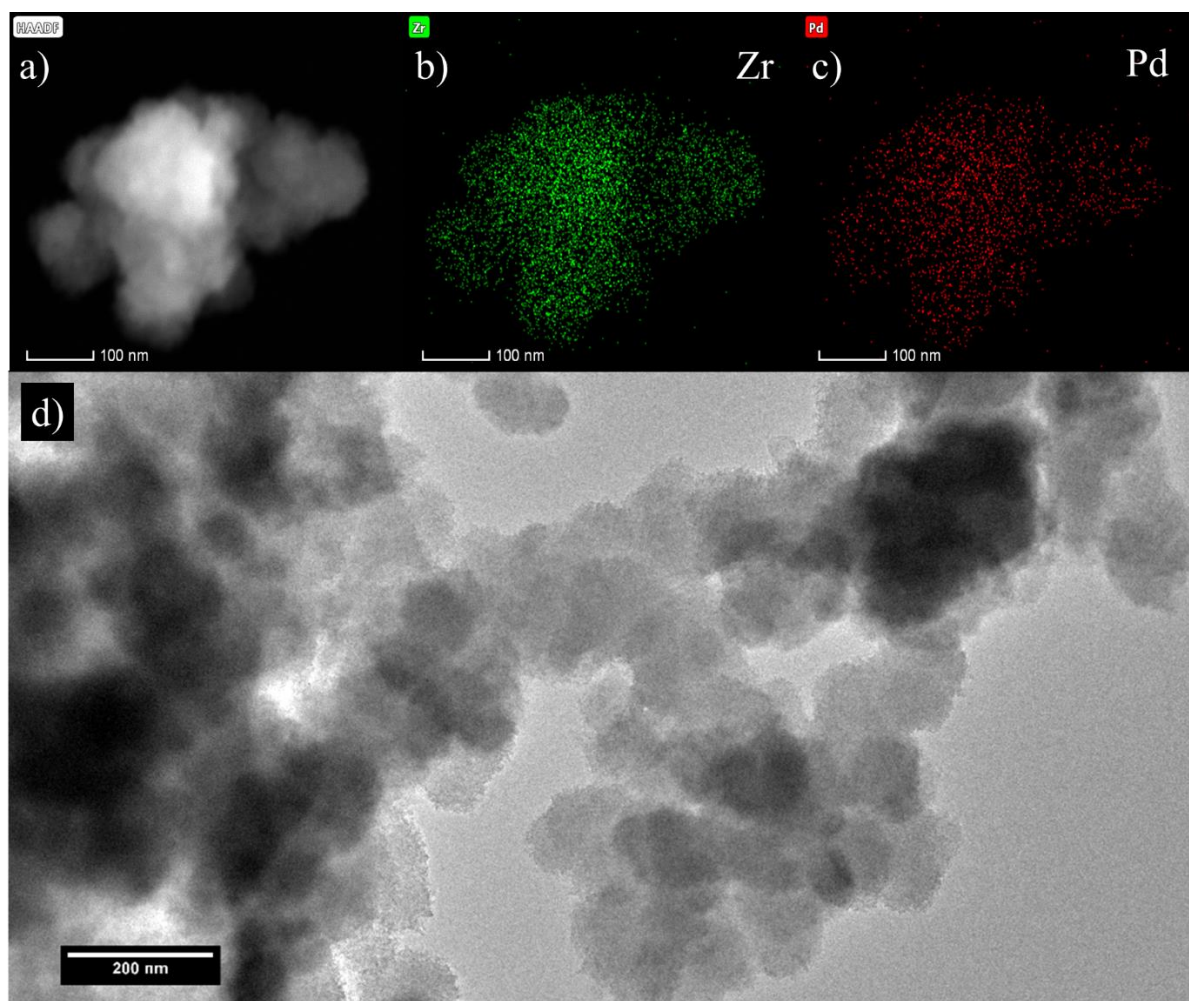


Figure 5.10: a) STEM image of two stage batch synthesised Pd(II)-UiO-67-BPYDC. b) EDX map of Zr present in two stage batch synthesised Pd(II)-UiO-67-BPYDC. c) EDX map of Pd present in two stage batch synthesised Pd(II)-UiO-67-BPYDC, d) TEM image for two stage batch synthesised Pd(II)-UiO-67-BPYDC. The darker features in this TEM image are due to thickness effects.

The HAADF STEM-EDX of this material shows no defined nanoparticles but does show the presence of Pd throughout (Figure 5.10a-c). If Pd nanoparticles had been formed, clear nanoparticles of ~1.5 nm would be present in the image. This result, with no clear nanoparticles, is consistent with the previous materials formed, where the N-Pd bonds have not been broken.

While attempts to replicate the literature work were unsuccessful, it has led to further insight with the issues potentially surrounding the formation of Pd(0) nanoparticles within the UiO-67 structure. Firstly, the presence of nitrogen containing BPYDC or another group that can bind to the Pd(II) precursor is absolutely necessary to trap the precursor within the pores and ensure good distribution of Pd throughout the material. However, the issue of then breaking this bond is one that this work has been unable to achieve, either in the newer microfluidic attempts or through direct replication of previous literature approaches. While reduction of the precursor has been observed in forming larger Pd(0) nanoparticles, the closest product is that of the waste collected from the NaBH₄/DMF reduction of batch synthesised Pd(II)-UiO-67-BPYDC, with Pd nanoparticles observed in the TEM. However, this could not be replicated, and the nanoparticles present were also not isolated within the UiO-67 structure. Previous literature work also cited the presence/flattening of a peak in the N1s XPS spectra was a sign of Pd(0) being present and interacting with the N atoms on the BPYDC linkers.⁷ However, within this work no correlation was found for this peak and the presence of Pd(0), with a sample that was synthesised with no Pd(II) precursor present showing a N 1s spectra that would suggest the presence of Pd(0) nanoparticles according to the literature (**Figure S 5.4**). Future work would need to explore this further, by potentially using a stronger reducing agent, such as NH₃BH₃, a reducing agent used by Chen *et al* to perform this reduction in their first work on this subject, before moving to weaker reducing agents.²²

5.5 Conclusions

A temperature controlled microfluidic synthesis of Pd(0)-UiO-67-BPYDC was attempted. This led to an investigation into the formation of Pd(0) nanoparticles within UiO-67-BPYDC pores with several synthesis/reduction methods being performed, leading to some key conclusions. Firstly, the presence of the BPYDC linker is necessary to contain the Pd(II) precursor within the MOF pores, otherwise it will be reduced outside of the pores and form larger nanoparticles. Secondly, the reducing power of DMF @130 °C, 0.1 M NaBH₄/Water or 0.1 M NaBH₄/DMF is not strong enough to break the N-Pd bonds in the pores, contrary to

literature reports. Thirdly, the use of the BPYDC linker is necessary for Pd nanoparticles to form within the MOF pores, otherwise they will form externally of the MOF. The volume of HCl used should be controlled also to ensure an FCC product rather than a HCP product is formed. Future work aiming to perform this reduction reaction should look to NH_3BH_3 as a potential candidate.

5.6 References

1. Jamkhande, P. G., Ghule, N. W., Bamer, A. H., Kalaskar, M. G. *J. Drug Deliv. Sci. Technol.*, 2019, **53**, 101174.
2. Saldan, I., Semenyuk, Y., Marchuk, I., Reshetnyak, O. *J. Mater. Sci.*, 2015, **50**, 2337–2354.
3. José-Yacamán, M., Gutierrez-Wing, C., Miki, M., Yang, D. Q., Piyakis, K. N., Sacher, E. *J. Phys. Chem. B*, 2005, **109**, 9703–9711.
4. Wang, X., Wang, Y., Ying, Y. *TrAC - Trends Anal. Chem.*, 2021, **143**, 116395.
5. He, L., Dumée, L. F., Liu, D., Velleman, L., She, F., Banos, C., Davies, J. B., Kong, L. *RSC Adv.*, 2015, **5**, 10707–10715.
6. Moon, H. R., Lim, D. W., Suh, M. P. *Chem. Soc. Rev.*, 2013, **42**, 1807–1824.
7. Chen, L., Chen, X., Liu, H., Bai, C., Li, Y. *J. Mater. Chem. A*, 2015, **3**, 15259–15264.
8. Mozaffari, S., Li, W., Dixit, M., Seifert, S., Lee, B., Kovarik, L., Mpourmpakis, G., Karim, A. M. *Nanoscale Adv.*, 2019, **1**, 4052–4066.
9. Schaate, A., Roy, P., Godt, A., Lippke, J., Waltz, F., Wiebcke, M., Behrens, P. *Chem. - A Eur. J.*, 2011, **17**, 6643–6651.
10. Faustini, M., Kim, J., Jeong, G. Y., Kim, J. Y., Moon, H. R., Ahn, W. S., Kim, D. P. *J. Am. Chem. Soc.*, 2013, **135**, 14619–14626.
11. Bailey, T., Pinto, M., Hondow, N., Wu, K. J. *MethodsX*, 2021, **8**, 101246.
12. Capretto, L., Cheng, W., Hill, M., Zhang, X. In *Microfluidics* Springer 2011; pp. 27–68.
13. Wu, K. J., Torrente-Murciano, L. *React. Chem. Eng.*, 2018, **3**, 267–276.
14. Liu, Y., Yang, G., Hui, Y., Ranaweera, S., Zhao, C. X. *Small*, 2022, **18**, 1–33.
15. Cai, X., Pan, J., Tu, G., Fu, Y., Zhang, F., Zhu, W. *Catal. Commun.*, 2018, **113**, 23–26.
16. Cliffe, M. J., Castillo-Martínez, E., Wu, Y., Lee, J., Forse, A. C., Firth, F. C. N., Moghadam, P. Z., Fairen-Jimenez, D., Gaultois, M. W., Hill, J. A., Magdysyuk, O. V., Slater, B., Goodwin, A. L., Grey, C. P. *J. Am. Chem. Soc.*, 2017, **139**, 5397–5404.
17. Goodenough, I., Devulapalli, V. S. D., Xu, W., Boyanich, M. C., Luo, T. Y., De Souza, M., Richard, M., Rosi, N. L., Borguet, E. *Chem. Mater.*, 2021, **33**, 910–920.
18. Clark, C. A., Heck, K. N., Powell, C. D., Wong, M. S. *ACS Sustain. Chem. Eng.*, 2019, **7**, 6619–6628.

19. Vo, T. K., Quang, D. T., Song, M., Kim, D., Kim, J. *Microporous Mesoporous Mater.*, 2020, **306**, 110405.
20. Katz, M. J., Brown, Z. J., Colón, Y. J., Siu, P. W., Scheidt, K. A., Snurr, R. Q., Hupp, J. T., Farha, O. K. *Chem. Commun.*, 2013, **49**, 9449–9451.
21. Chen, L., Chen, X., Liu, H., Li, Y. *Small*, 2015, **11**, 2642–2648.
22. Chen, L., Chen, H., Li, Y. *Chem. Commun.*, 2014, **50**, 14752–14755.

Acknowledgements:

Financial support from the EPSRC is gratefully acknowledged by TB in the form of studentship (EP/R513258/1; Award Number 2282152). We acknowledge support from the Henry Royce Institute (EPSRC grants: EP/P022464/1, EP/R00661X/1), which funded the VXSf Facilities (<https://engineering.leeds.ac.uk/vxsf>) within the Bragg Centre for Materials Research at Leeds.

5.7 Supporting Information

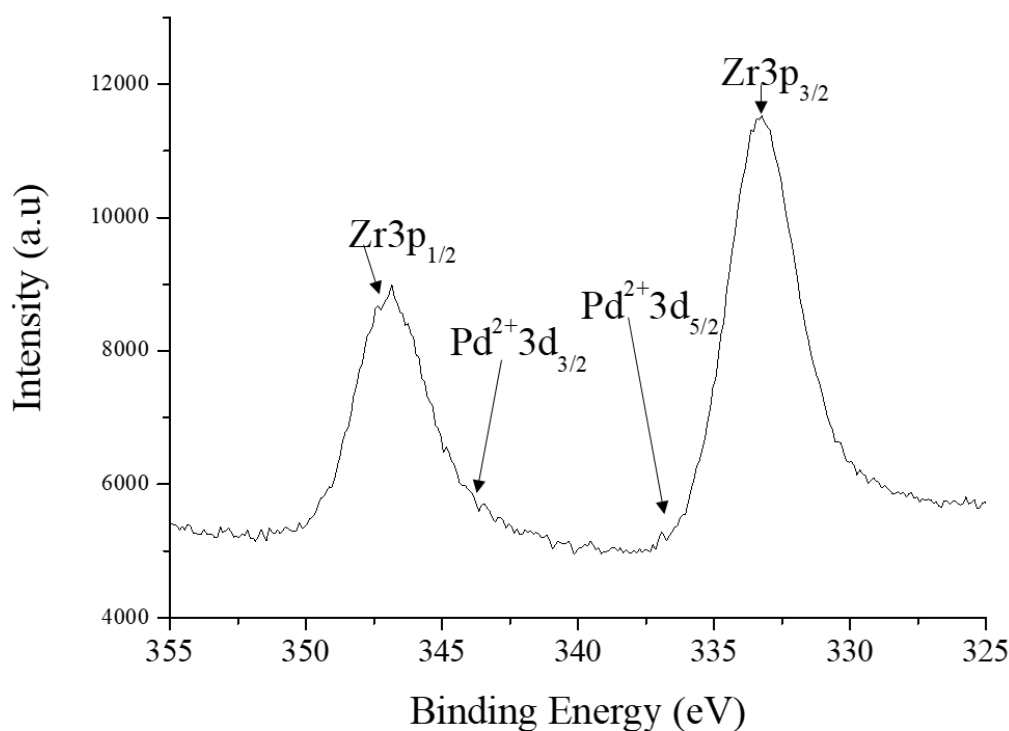


Figure S 5.1: XPS spectrum for rewashed microfluidically synthesised Pd-UiO-67-BPYDC that underwent further reduction with 24hrs heating at 130 °C in DMF

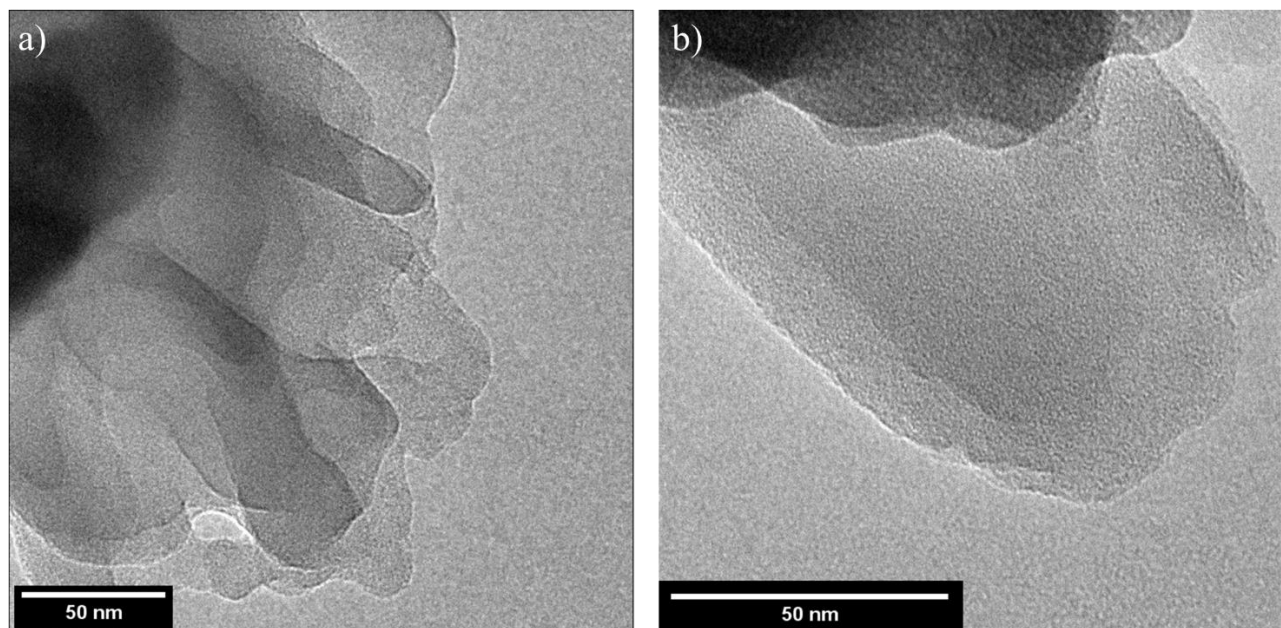


Figure S 5.2: TEM images of Pd(II)-UiO-67-BPYDC sample where further reduction was attempted with 0.1 M NaBH₄/DMF on an unwashed microfluidic synthesis sample. a) Lower magnification TEM image. b) higher magnification TEM image.

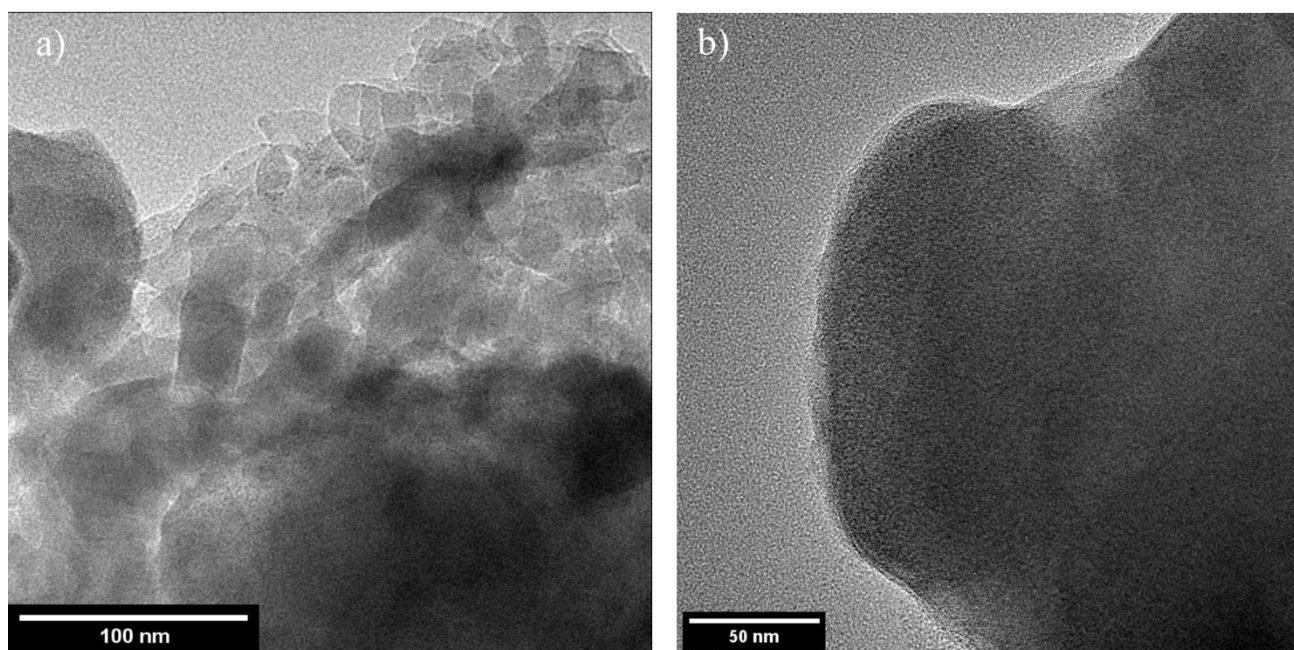


Figure S 5.3: TEM images of two further reduction samples on the batch synthesis product when the literature method was followed exactly (0.5 ml HCl). a) 5 ml 0.1 M NaBH₄/DMF solution in 2 ml DMF, 4 hours in an ice bath. b) 15 ml 0.1 M NaBH₄/DMF solution in 20 ml DMF, 4 hours in ice bath.

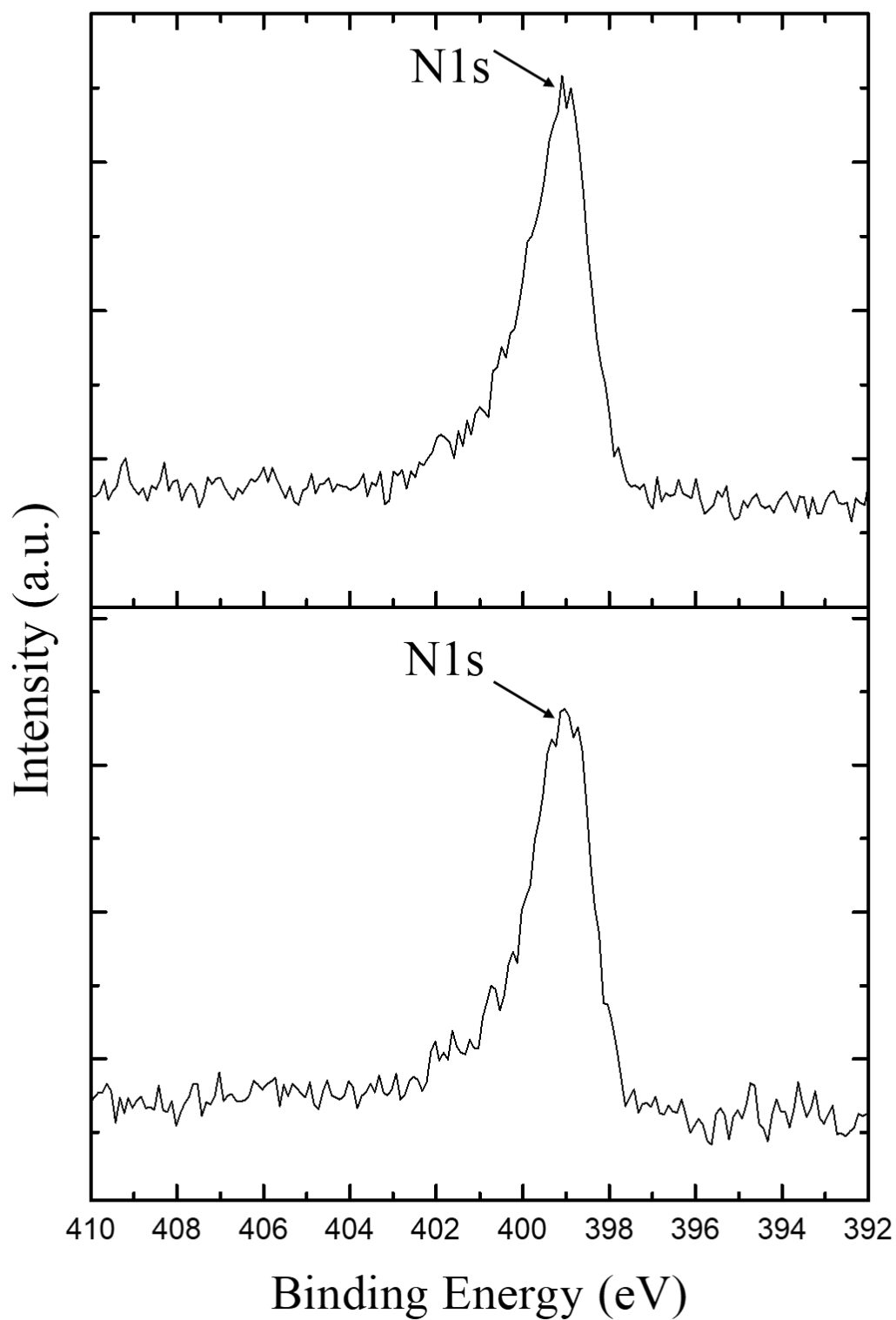


Figure S 5.4: N1s XPS spectra for: a) batch synthesised Pd(II)-UiO-67-BPYDC. b) batch synthesised UiO-67-BPYDC. Both show similar pattern shape, with the broadening to higher energies being unrelated to the Pd present.

Chapter 6 Journal of Chemical Information and Modelling
Article, “Gradient boosted machine learning model to predict H₂,
CH₄ and CO₂ uptake in metal organic frameworks using
experimental data”, Published July 2023,
<https://doi.org/10.1021/acs.jcim.3c00135>

*Tom Bailey,¹ Adam Jackson,¹ Razvan-Antonio Berbece,¹ Kejun Wu,^{*1,2} Nicole Hondow,^{*1} and Elaine Martin^{*1}.*

1. School of Chemical and Process Engineering, University of Leeds, Leeds LS2 9JT
UK

2. Zhejiang Provincial Key Laboratory of Advanced Chemical Engineering
Manufacture Technology, College of Chemical and Biological Engineering, Zhejiang
University, Hangzhou, China, 310027

6.1 Abstract

Predictive screening of Metal-organic Framework (MOF) materials for their gas uptake properties has been previously limited by using data from a range of simulated sources, meaning the final predictions are reliant on the performance of these original models. In this work, experimental gas uptake data has been used to create a Gradient Boosted Tree model for the prediction of H₂, CH₄ and CO₂ uptake over a range of temperatures and pressures in MOF materials. The descriptors used in this database were obtained from literature with no computational modelling needed. This model was repeated 10 times, showing an average R² of 0.86 and a Mean Absolute Error

(MAE) of ± 2.88 wt% across the runs. This model will provide gas uptake predictions for a range of gases, temperatures, and pressures as a one-stop solution, with the data provided being based on previous experimental observations in literature, rather than simulations which may differ from their real-world results. The objective of this work is to create a machine learning model for the inference of gas uptake in MOFs. The basis of model development is experimental as opposed to simulated data to realise its application by practitioners. The real-world nature of this research materialises in a focus on the application of algorithms as opposed to the detailed assessment of the algorithms.

6.2 Introduction

Using porous materials in gas storage has become an increasingly important topic, with effective storage and/or release of gases such as H₂, CH₄ and CO₂ being potentially key in climate change mitigation.¹⁻³ Porous materials, with large surface areas and open spaces, allow for higher uptakes of gas at lower pressures when compared to using traditional bottles.⁴ Metal-organic Framework (MOF) materials have been shown previously to be highly successful in gas absorption,⁵ and in particular are more suited to absorption than other porous materials, such as zeolites, due to an absence of dead volume in the structures, which leads to higher efficiency.⁶ MOF crystalline structures are comprised of repeating metal containing Secondary Building Units (SBUs) joined together by organic linkers. The SBUs and linkers can potentially be combined in an almost limitless number of ways, allowing for extensive design for the application required.⁶ As a result of this, computational screening for MOF materials becomes important to save time and efficiently find a structure suited to the desired application, such as gas uptake/storage. Previous work by Pardakhti *et*

al created a Random Forest (RF) model to predict the methane uptake in ~130,000 simulated MOF structures,⁷ using descriptors gained through Grand Canonical Monte Carlo (GCMC) modelling, such as void fraction, surface area and density. This model had a high predictive performance, with a coefficient of determination (R^2) of 0.98 and a Mean Average Percentage Error (MAPE) of 7.18. However, this model is limited by only predicting for uptake at 35 bar and 298 K, limiting its use for researchers. More recently, Fanourgakis *et al* made an RF based model to predict the CH₄ and CO₂ uptake in ~78,000 structures and achieving an R^2 of 0.96 for predictions on a test set.⁸ A key improvement on the previous work is the ability to predict for two separate gases (CH₄ and CO₂) and at a range of pressures (1 – 65 bar for CH₄, 0.05-2.5 bar for CO₂).

RF models are ensembles of Decision Trees (DT), with the combination of many DTs improving the model performance and decreases certain limitations found in DTs. Briefly, DTs are a simple class of machine learning model that start with all the prediction data being held in a root node, that is then sequentially split through binary decisions by internal nodes until it reaches a terminal node, which will be the prediction.⁹ However, if each output for the training data has a corresponding node, while the performance for the training set will be very high, it may struggle to predict for new data. To counter this, a “minimum leaf size” can be set, where the value for the terminal node will be the average of several outputs rather than just one, with the number of outputs being averaged corresponding to the “minimum leaf size”. This will result in a lack of performance on the training set but should give a model that is more flexible towards new data.

Ensemble models, such as RF or Gradient Boosted Decision Trees (GBDTs), allow for a more flexible model while avoiding a loss of performance. RFs fit many trees

(usually hundreds or thousands), with the average prediction from the trees being given.¹⁰ With the average being taken over many trees it allows for the individual trees to be weaker, to limit overfitting to the training data, with an average prediction over many tree increasing the performance. GBDT is also a technique that uses many decision trees, but rather than have the trees be separate from each other, the trees are built based on the previous iteration to slowly approach a model with high performance.^{9,11} This is achieved by the model firstly taking the average of all the output data and then finding the difference of the output values to this average, with these differences being pseudo residuals. The model will then form a tree to predict for these residuals and not the actual outputs. From this tree, a prediction would be the average output value plus/minus the predicted residual. However, just from this first tree, there could be predictions that are completely accurate, meaning the model is overfitting to the training data and will have reduced performance with new data. To avoid this, a learning gradient can be applied to the model, which acts as a modifier to the predicted residuals. For example, Predicted Output = Average Output + (Gradient x Predicted Residual). Following this first tree, residuals from these predictions will be used to form the second tree and so on. While this learning gradient does mean that the individual decision trees are much weaker now, by gradually building the model performance, overfitting can be reduced while giving a model with more accurate predictions. Friedman, who formed the gradient boosting model, showed that taking lots of these small steps would lead to a better fitting model, while reducing any bias.¹²

These previous models, however, gained initial gas uptake values and several descriptors using GCMC modelling. This limits the transferability of the data to real world applications, as the gas uptake predictions determined through the machine learning (ML) models may be imperfect, due to any errors present in the GCMC

models, which while they might be small, mean that the regression model will be starting from a point of error. For researchers looking to predict the gas uptake on a not yet synthesised MOF, certain physical descriptors, such as pore size and surface area, will only be available through GCMC modelling of the theoretical structure. Since these gas uptake models require these descriptors, researchers would first have to perform these GCMC calculations before a gas uptake prediction could be made.

This work details a predictive ML model for the uptake of multiple gases (H_2 , CH_4 , CO_2) at a range of temperatures (30 – 333 K) and pressures (0.06 – 100 bar). For researchers to use this model for un-synthesised materials, this model will need to be of comparable performance to previous work, while only using predictors that can be gained without the use of GCMC modelling/having already performed a gas isotherm (such as pore size/surface area). The gas uptakes will be obtained from previously published results to remove the errors of GCMC modelling, thus providing an easy-to-use predictive tool for new researchers. The developed ML model shows a high predictive performance while allowing for a range of different predictions to be performed for a single MOF structure. Partial least squares (PLS) regression has been performed to indicate what descriptors are most significant in the prediction of gas uptake.

6.3 Methods and materials

A database was formed using experimental gas uptake data from previously published papers, with a full list of MOF materials and their corresponding references provided in the Supplementary Information. The data was collected by manually searching and reading these papers, giving a total of 589 datapoints, with some datapoints being from the same MOF material but with different gases, temperatures or pressures used. This data was selected from what was available at the time, while

ensuring that the uptakes were not from papers where the aim was to synthesise defective forms of this MOFs, as the model would not be able to account for this currently. The datapoints are split into 205 for H₂ uptake, 268 for CO₂ uptake and 115 CH₄ uptake, corresponding to 304 unique MOFs. The aim was to form a database that represented a wide range of MOF structures while giving multiple datapoints to each MOF structure where possible (with variation in the gas absorbed, temperature and pressure). The wt% values ranged from 1.5 – 74.2 wt%, the temperature ranged from 30 – 313 K and the pressure ranged from 0.1 – 100 bar. By only using gravimetric uptake data, either through collection or calculation from literature, and avoiding papers where the MOF produced was purposefully defective, the literature available was limited. This meant that the database formation was a time-consuming process and a limiting factor in the database size, alongside what literature was available.

Gravimetric uptake data was used rather than volumetric for ease of comparison. The unit used in this work was weight percentage (% wt) uptake, with some values calculated from cm³g⁻¹ using the density of the gas. Wt% was calculated using **Equation 7.1**.

$$wt\% = \frac{\text{Weight of gas absorbed}}{(\text{Weight of gas absorbed}) + (\text{Weight of absorbant material})} \quad \text{Equation 7.1}$$

It was found that different published results for wt% were calculated in two possible ways, with either **Equation 7.1** or by simply dividing the absorbed gas by the weight of the absorbent. At low uptakes (such as those for H₂ absorption), the difference between these two values is small but at larger uptakes (such as those found for CO₂ and CH₄) the difference between the two values is considerable. These values were converted to the same measure, using **Equation 7.1**, to ensure they are comparable and reduce the data range entering the predictive model, which should lead to easier fitting of the data.¹³

The descriptors used can be divided into 3 categories: (1) the type and number of bonds present in the linker unit, (2) the metal present in the SBU and (3) other physical/chemical conditions for the gas absorption (type of gas, temperature, pressure, electronegativity difference between the MOF and the gas). Textural features, such as surface area and pore size, were purposefully not included here to ensure future users would not need to perform other computational modelling before using this model. Overall, 51 descriptor variables (**Table 6.1**) were used with the output being the natural log of the gas uptake wt%. This natural log was used to account for unequal spacing between datapoints.

Table 6.1 A list of the descriptors used in the machine learning models

Type of descriptor	List of descriptors
Primary Building Units (PBU)	C-C, C-C (ring), (ring) C-C (ring), C=C, C-O, C=O, C-N, C=N (ring), N-N (ring), N=N (ring), N=N (ring), (ring) C-O, (ring) C=O, (ring) C-S (ring), (ring) N-S (ring), (ring) C-N, C-N (ring), (ring) C=C (ring), (ring) N-C (ring), (ring) N=C (ring), C≡C, C≡N, N-O, N=O, O-R, C-R, (ring) C-R
Secondary Building Units (SBU)	Al, Cd, Co, Cu, Mg, Mn, Ni, Zr, Zr ₄ O, Sc, Ti, Be, Pd, Y, Er, In, Cr, Fe, Mo, Zn
Physical conditions (PHYS)	largest electronegativity difference, temperature (k), pressure (bar), gas molecular weight (g/mol)

Several machine learning methods, Linear Regression, Quadratic Support Vector Machine (SVM), DT and Gradient Boosted Decision Trees (GBDT), were fitted and tested. In-lieu of using an external test set, 10-fold cross validation was used, with the low amount of data available making it impossible to choose a test set without bias. Machine learning research, performed in relation to materials engineering, has utilised cross-validation as opposed to an external test set for validation, due to a relative lack

of data available.¹⁴⁻¹⁷ The GBDT model had several hyperparameters (number of trees, minimum leaf size and learning rate) manually optimised to give the lowest mean squared error (MSE) on each fold when used as a validation set. This optimisation led to a GBDT model with 600 trees, a learning rate of 0.05 and a minimum leaf size of 3. During optimization, increasing the minimum leaf size from 1 to 2 to 3 did not improve the R^2 significantly as anticipated, with the value decreasing marginally as the leaf size was increased (0.8709 to 0.8669 to 0.8643). However, while it has the lowest R^2 value, a leaf size of 3 was utilised to ensure that if new data is included in the future, this added flexibility should reduce potential overfitting. The Linear Regression, DT and Quadratic SVM models had their hyperparameters optimised using the "OptimiseHyperparameters" function in MATLAB 2020. The full list of hyperparameters is provided in the supporting information.

Each model was run 10 times to give a varied split of the different folds, ensuring that each model was repeatable even when the folds changed. These models were then evaluated by their average R^2 values, the average validation fold MSE (KFold Loss) and the average Mean Absolute Error (MAE) for when the predicted data was converted back from being a logged value and compared with the original value. This MAE was done for each gas as well, to give a more accurate scale of error. Alongside the MAE, mean absolute percentage error (MAPE) was also calculated to give a relative measure of error.

6.4 Results and discussion

The average R^2 , KFold Loss, MAE and MAPE from the four ML methods while predicting for all gases are shown below in **Table 6.2**, with regression plots for each model shown in **Figure 6.1**. The regression plots have been made by converting the

prediction and target wt% values back from natural logs and then taking the average of the prediction values for each datapoint over 10 runs.

Table 6.2 R^2 , Validation MSE (KFold Loss), MAE and MAPE for each of the machine learning models used.

Method	Average R^2	Average KFold Loss	Average MAE	Average MAPE
Linear	0.330	0.605	7.251	87.822
SVM	0.650	0.305	5.309	51.381
DT	0.777	0.195	3.790	35.853
GBDT	0.864	0.117	2.882	26.544

MAE and MAPE are calculated once the data has been converted back from a log values.

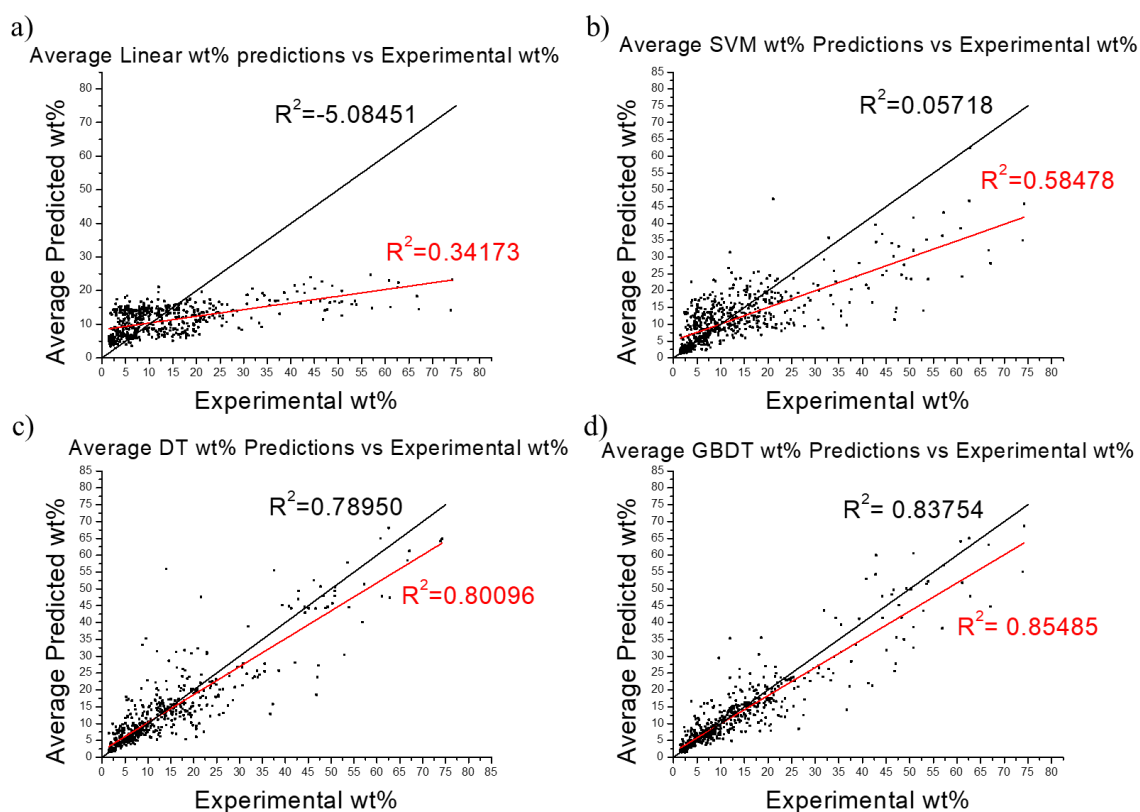


Figure 6.1: Regression plots for the developed ML models a) linear model; b) SVM; c) DT model; d) GBDT model. Each plot uses the average predictions for each datapoint (over 10 runs) versus the real experimental wt% values found in literature. The black line is $y=x$, with the R^2 around this line calculated and shown in black text. The red line is a fitted line of best fit, with the R^2 for this shown in red text.

The GBDT model shows the highest level of performance across the board ($R^2 = 0.86$, Average KFold Loss = 0.117, Average MAE = 2.882 wt%, Average MAPE = 26.54%), which is to be expected from a more complex machine learning model. The

KFold Loss being the lowest shows this model to be the best at predicting for new data, with the lowest MSE for the held-out folds, which is key for a new researcher to use this model. In relation to previous literature examples by Pardakhti *et al* and Fanourgakis *et al*,^{7,8} this does show a slightly lower level of performance ($R^2 = 0.86$ compared to 0.98 or 0.96 respectively), but with the added flexibility available for this model in which multiple gases and conditions can be predicted, it is a success. The GBDT performed consistently across the 10 runs, with the relative standard deviation for each error shown in **Table 6.3**.

Table 6.3 Relative Standard Deviation (%) for R^2 , KFold Loss, MAE and MAPE across the 10 runs.

	R^2	KFold Loss	MAE	MAPE
Relative Standard Deviation (%)	0.6	3.6	1.4	1.9

In terms of MAPE, there is a deviation from the model by Pardakhti *et al*, with 26.544% compared to 7.18%. Again however, with the limited of data used and the flexibility of the model formed for new user, it is still a success. The predictions for this work being based on previous literature results should also give predictions that are more applicable in a real-world setting. An average MAE of ± 2.882 wt% is given for all the datapoints but there is variation depending on the gas being predicted (**Table 6.4**), which new researchers can apply to their predictions. Note here that these errors are for the specific datapoints for different gasses when predictions are being performed on the full dataset, not for separate models for each gas. Being able to perform calculations for any of the gasses while not changing the training database is a key aspect of the model's flexibility.

Table 6.4: Average MAE and Average MAPE when fitting data for each gas in the GBDT model, over 10 runs.

Gas Type	Average MAE	Average MAPE
H ₂	0.759	20.70%
CO ₂	4.598	32.26%
CH ₄	2.667	23.64%
All gases	2.882	26.54%

GBDT is the most accurate model, fitting was repeated while limiting the descriptors used, to examine how each category contributed to the fitting. For each of these, the adjusted R^2 was also collected, to observe if overfitting through the number of descriptors was occurring (**Table 6.5**). Adjusted R^2 is calculated using **Equation 7.2** and is used to measure R^2 in relation to the number of descriptors used, only increasing if the increase in R^2 is significant in relation to the increase in descriptors.¹⁸

$$\text{Adjusted } R^2 = 1 - \frac{(1 - R^2)(N - 1)}{(N - d - 1)} \quad \text{Equation 7.2}$$

Table 6.5 Comparison of R², Adjusted R², Kfold loss, average MAE, average MAPE when different combinations of primary building unit (PBU), secondary building unit (SBU) and physical conditions (PHYS) were used in the fitting of the GBDT model.

	Average R ²	Average Adjusted R ²	Average Kfold Loss	Average MAE	Average MAPE
PBU (27)	0.062	0.017	0.9016	8.200	100.600
SBU (20)	0.023	-0.012	0.848	8.280	97.180
PHYS (4)	0.743	0.741	0.222	4.431	40.858
PHYS + PBU (31)	0.842	0.8340	0.1356	3.217	29.049
PHYS + SBU (24)	0.803	0.795	0.1702	3.646	34.001
PBU + SBU (47)	0.064	-0.017	0.9100	8.324	102.249
All Descriptors (51)	0.864	0.851	0.117	2.882	26.544

The set of descriptors with the highest adjusted R² has been highlighted. The number of descriptors used in each category is shown in brackets.

As can be seen in **Table 6.6** R², Adjusted R², Kfold Loss, MAE and MAPE for GBDT models fitting using only the descriptors with VIPScores >1, VIPScores > 0.5 and fitting using all 51 descriptors., the physical uptake conditions (PHYS; pressure, temperature, type of gas, electronegativity difference) play the biggest role in the prediction for the overall uptake, which is understandable as the way a gas behaves is affected drastically by the environment, as seen in the ideal gas equation for example. Following this, predicting using just the primary building unit (PBU) descriptors gives the next most accurate predictions (when using one category of predictors at a time), with the SBU descriptors giving the least accurate. When combining these descriptors, the model with the highest predictive performance is formed, with the highest adjusted R², indicating that overfitting through too many descriptors is not occurring. If this database is expanded, leading to an increase in runtimes, then limiting to the physical conditions and the PBU descriptors, which would reduce the predictors from 51 to 31, could give a comparatively accurate result in less time.

Partial Least Squares (PLS) fitting was performed to give Variable Importance Scores (VIPScores) for each descriptor, with a higher score meaning that descriptor

contributes more to the Percentage Variance explained. Firstly, PLS was performed to find the minimum number of components needed for the model to predict accurately. The results for this are shown in **Figure 6.2**, with the Estimated Mean Squared Prediction Error plotted against the number of components used.

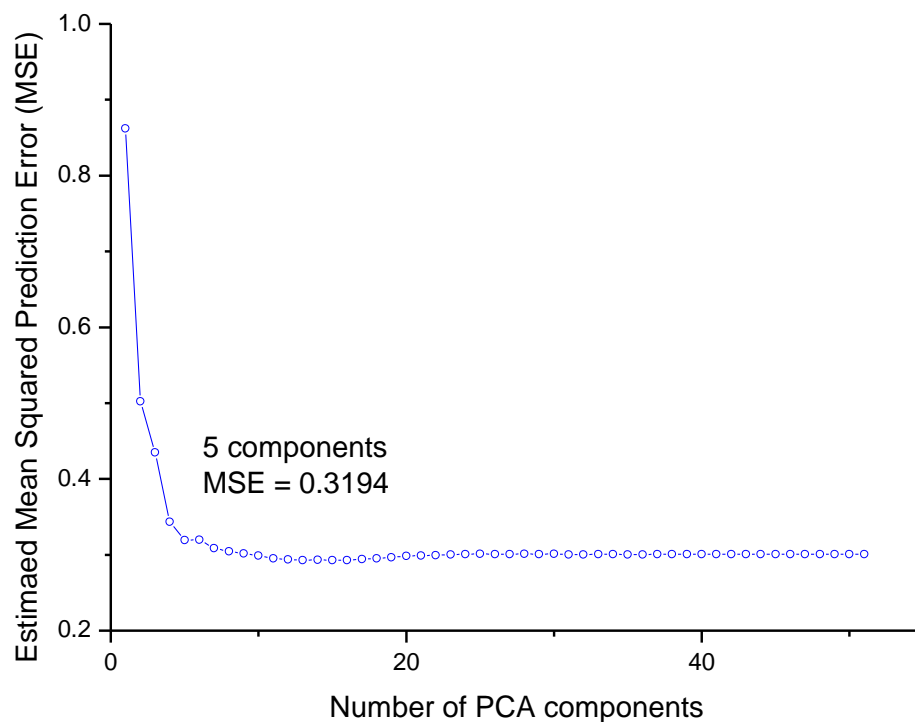


Figure 6.2. Estimated mean squared prediction error vs number of PLS components. The datapoint at 5 components has been highlighted.

In this principle component analysis (PCA) plot (**Figure 6.2**), the “elbow”, being the point at which the error starts to level off is at 7 components, with the Elbow Method of choosing the number of components being well documented.¹⁹ This method is performed to ensure that overfitting is not occurring through including too many components and because after this point the increase in performance for increasing components has been reduced drastically. Following this, PLS was repeated using 6 components to give accurate VIPScores for the descriptors, which should be comparable to the variable importance found earlier when using different datasets.

These VIP Scores are shown in **Figure 6.3** with the descriptors showing a score of 0.5 or higher labelled. While in the literature a score > 1 is used as indication that a descriptor is important,²⁰ this would only leave the temperature, pressure and type of gas in this case. As shown in **Table 6.6**, using other descriptors alongside the physical conditions do increase the performance of the model while not overfitting, as seen with the increasing adjusted R^2 , so some of these must also be important.

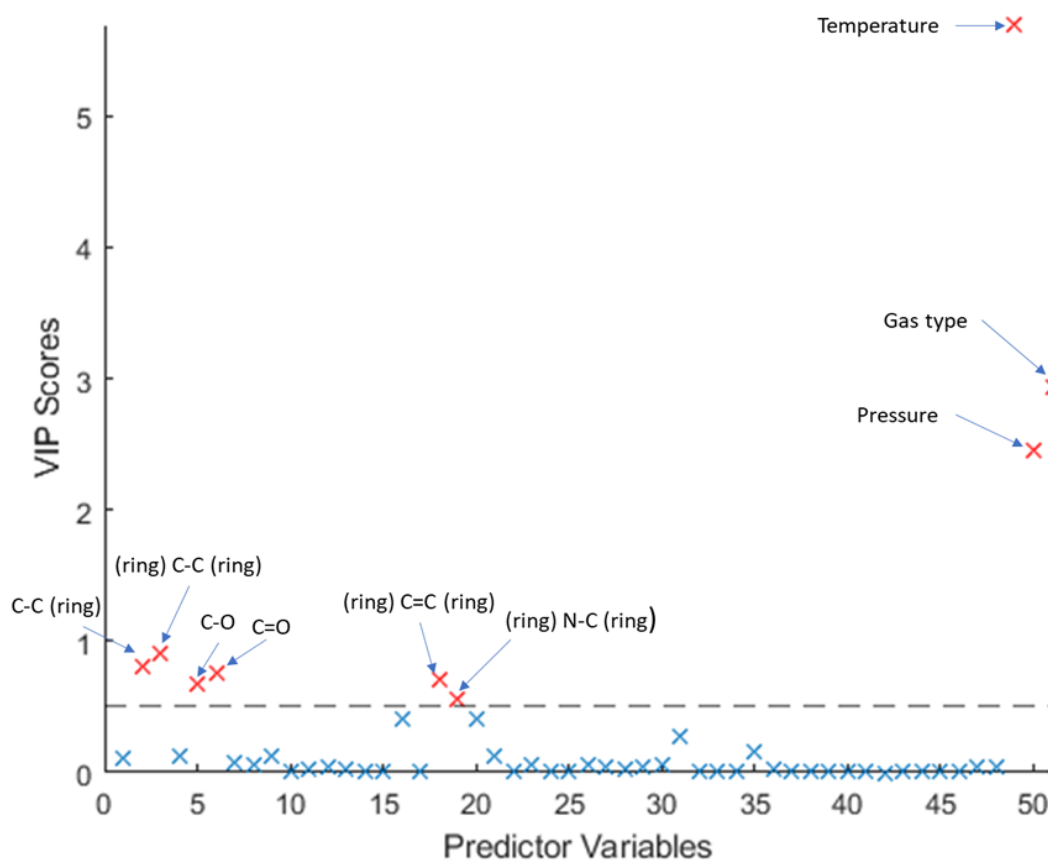


Figure 6.3. Variable importance scores for each of the 51 descriptors. Those with a score > 0.5 are labelled and highlighted in red.

After the physical conditions (except electronegativity difference), the descriptors that show the highest contribution are those relating to certain linker bonds in the PBUs as highlighted in **Figure 6.3**. The bonds with the highest contribution to the uptake being carbon bonded to other atoms is sensible, as a higher number of C-C bonds for example would usually result in a longer linker, increasing the surface area

and the pore size.²¹ Fitting the GBDT model was repeated using these descriptors with VIPScores > 1 and >0.5, to see how their inclusion affected performance, with their errors shown in **Table 6.6**.

Table 6.6 R², Adjusted R², Kfold Loss, MAE and MAPE for GBDT models fitting using only the descriptors with VIPScores >1, VIPScores > 0.5 and fitting using all 51 descriptors.

	R2	Adjusted R2	Kfold Loss	Average MAE	Average MAPE
VIPScores > 1	0.737	0.736	0.228	4.521	41.415
VIPScores > 0.5	0.804	0.801	0.169	3.651	33.139
All Descriptors	0.864	0.851	0.117	2.882	26.544

When limited to these 9 descriptors, the model has comparable performance to that found when using the full 51, whereas only using the physical conditions yield a model with lower performance. Future work using larger databases could benefit from using just these 9 descriptors to reduce the computing power required.¹³

An interesting finding from the PLS and fitting the GBDT model with certain descriptor sets, is that the SBU metal type shows a very low impact on the predicted gas uptake. This is unexpected, as the metal type is one of the key features of a MOF structure so was thought necessary to include in prediction of the gas uptake. There are two potential reasons for this lack of impact. Firstly, the type of metal is not as important as the linker bonds that are present when it comes to gas uptake, with longer/larger linker units potentially leading to higher surface areas/pore sizes. In general, higher surface areas and/or pore volumes will lead to higher gas uptakes so this does make sense why they are so important. The second reason could be due to

the limited dataset that is present in this work, with a larger dataset potentially showing trends for the metal type that can't currently be seen for this model.

With the completed GBDT model formed, new researchers can use this database and model to form gas uptake predictions on new MOF structures quickly and easily, as a one stop preliminary model. This model differs itself from others through its flexibility, being able to predict for different gases, temperatures and pressures without the researcher first needing to perform any other modelling work, only needing to provide the descriptors for the linker, SBU and the physical conditions for the gas uptake. The use of experimental data in the models fitting should provide results that are more in line with real world observations, rather than theoretical structures. The errors found for each gas have been provided so researchers using this model may accurately determine a predicted uptake range for their chosen MOF and gas. Future work expanding this database, especially with datapoints at the temperature/pressure extremes, will help to improve the performance of this model, as it is a relatively small dataset compared to other works.^{7,8}

6.5 Conclusions

In this work a GBDT model has been formed to predict the uptake of H₂, CO₂ and CH₄ in MOF materials and is able to predict these for a range of temperatures and pressure. The average R² of this model is found to be 0.864 with an average MAE of ± 2.88 wt% for the uptakes. This model's high performance while using experimental data should provide researchers with predictions more in line with real world observations, with the added flexibility to vary physical parameters quickly and easily. Future work should aim to expand this database to give greater predictive performance.

6.6 References

1. Figueroa, J. D., Fout, T., Plasynski, S., McIlvried, H., Srivastava, R. D. *Int. J. Greenh. Gas Control*, 2008, **2**, 9–20.
2. Connolly, B. M., Aragones-Anglada, M., Gandara-Loe, J., Danaf, N. A., Lamb, D. C., Mehta, J. P., Vulpe, D., Wuttke, S., Silvestre-Albero, J., Moghadam, P. Z., Wheatley, A. E. H., Fairen-Jimenez, D. *Nat. Commun.*, 2019, **10**, 1–11.
3. Ma, S., Zhou, H. C. *Chem. Commun.*, 2010, **46**, 44–53.
4. Morris, R. E., Wheatley, P. S. *Angew. Chemie - Int. Ed.*, 2008, **47**, 4966–4981.
5. Li, H., Wang, K., Sun, Y., Lollar, C. T., Li, J., Zhou, H. C. *Mater. Today*, 2018, **21**, 108–121.
6. Czaja, A. U., Trukhan, N., Müller, U. *Chem. Soc. Rev.*, 2009, **38**, 1284.
7. Pardakhti, M., Moharreri, E., Wanik, D., Suib, S. L., Srivastava, R. *ACS Comb. Sci.*, 2017, **19**, 640–645.
8. Fanourgakis, G. S., Gkagkas, K., Tylianakis, E., Froudakis, G. E. *J. Am. Chem. Soc.*, 2020, **142**, 3814–3822.
9. Elith, J., Leathwick, J. R., Hastie, T. *J. Anim. Ecol.*, 2008, **77**, 802–813.
10. Svetnik, V., Liaw, A., Tong, C., Christopher Culberson, J., Sheridan, R. P., Feuston, B. P. *J. Chem. Inf. Comput. Sci.*, 2003, **43**, 1947–1958.
11. Schapire, R. E. *Nonlinear Estim. Classif.*, 2003, 149–171.
12. Friedman, J. *Ann. Stat.*, 2001, **29**, 1189–1232.
13. Obaid, H. S., Dheyab, S. A., Sabry, S. S. In 2019 9th Annual Information Technology, Electromechanical Engineering and Microelectronics Conference (IEMECON) 2019; 279–283.
14. Yao, L., Li, Y., Cheng, Q., Chen, Z., Song, J. *Desalination*, 2022, **532**, 115729.
15. Borboudakis, G., Stergiannakos, T., Frysali, M., Klontzas, E., Tsamardinos, I., Froudakis, G. E. *npj Comput. Mater.*, 2017, **3**, 1–6.
16. Townsend, J., Micucci, C. P., Vogiatzis, K. D., Hymel, J. H. *Nat. Commun.*, 2020, **11**, 1–9.
17. Takahashi, K., Miyazato, I. 2018, 2405–2408.
18. Lepš, J. In *Biostatistics with R 2020*; pp. 219–238.
19. Dmitrienko, A., Chuang-Stein, C., D’Agostino Sr, R. B. *Pharmaceutical statistics using SAS: a practical guide*, SAS Institute, 2007.
20. Galindo-Prieto, B., Eriksson, L., Trygg, J. *Chemom. Intell. Lab. Syst.*, 2015, **146**, 297–304.
21. Wang, R., Meng, Q., Zhang, L., Wang, H., Dai, F., Guo, W., Zhao, L., Sun, D. *Chem. Commun.*, 2014, **50**, 4911–4914.

6.7 Supporting Information

Table S 6.1 MOF structures with literature H₂ uptakes

MOF Name	Common Name	Pressure (Bar)	Temperature (K)	Uptake (%wt)	Reference
Be ₁₂ (OH) ₁₂ (BTB) ₄		1	77	1.6	Sumida et al., 2009 ¹
		20	77	6	
		100	77	9.2	
		95	298	2.3	
Cd ₄ (TCPM) ₂		1	77	2.8	Chun et al., 2004 ²
Co(BDP)		30	77	3.1	Jin Choi, Dincă and Long, 2008 ³
Co(BTC)(4,4'-bpy)		72	77	2.05	Li.Y et al., 2008 ⁴
Co ₂ (BDC) ₂ (dabco)		44.2	77	4.11	Suh et al, 2012 ⁵
Co ₃ (bpdc) ₃ (4,4'-bpy)		1	77	1.98	Lee et al., 2005 ⁶
Co ₃ (NDC) ₃ (dabco)		1	77	2.45	Chun et al., 2008 ⁷
Co ₃ [(Co ₄ Cl) ₃ (BTT) ₈ (H ₂ O) ₁₂] ₂		1	77	1.8	Liao et al., 2013 ⁸
Cr ₃ (BTC) ₂		1	77	1.9	Sumida, Her, et al., 2011 ⁹
Cu(dccptp)(NO ₃)		20	77	1.91	Yang et al., 2008 ¹⁰
Cu(peip)		1	77	2.51	Liu, Oh and Soo Lah, 2011 ¹¹
		40	77	4.14	
Cu(pmip)		1	77	2.36	Liu, Oh and Soo Lah, 2011 ¹¹
Cu(TZI) ₃		1	77	2.4	Nouar et al., 2008 ¹²
Cu ₂ (BDC) ₂ (dabco)		1	77	1.8	Lee et al., 2007 ¹³
		33.7	77	2.7	
Cu ₂ (BDDC)		0.95	77	1.64	Bing Zheng et al., 2010 ¹⁴
		17	77	3.98	
Cu ₂ (dhtp)	Cu-MOF-74	5	77	2.22	García-Holley et al., 2018 ¹⁵
		100	77	3.15	
		100	160	2.87	

Cu ₂ (DAIA)(H ₂ O) ₂	Cu-MOPF	1	77	2.8	Maity, Karan and Biradha, 2018 ¹⁶ García-Holley et al., 2018 ¹⁵
Al(OH)(SDC)	CYCU-3-Al	5	77	3.37	
		100	77	8.24	
		100	160	7.92	
Fe ₃ (OH)(pbpc) ₂		1	77	1.6	Jia et al., 2007 ¹⁷
		20	77	3.05	
Fe ₄ O ₂ (BTB) _{8/3}		1	77	2.1	Choi et al., 2007 ¹⁸
Zn ₆ (BTB) ₄ (4,4'-bpy) ₃	FJI-1	37	77	6.52	Han et al., 2011 ¹⁹
HCu[(Cu ₄ Cl) ₃ (BTT) ₈]	Cu-BTT	1.2	77	2.42	Dincă et al., 2007 ²⁰
		20	77	4.1	
Cu ₃ (BTC) ₂	HKUST-1	5	77	3.53	García-Holley et al., 2018 ¹⁵
		100	77	5.31	
		100	160	4.91	
Zn ₄ O(CH ₃ PhTDC) ₃	IFMC-29	1	77	1.75	Cheng et al., 2018 ²¹
Zn ₄ O(dobdc) ₂	IRMOF-6	45	77	4.63	Wong-Foy, Matzger and Yaghi, 2006 ²²
Zn ₄ O(NDC) ₃	IRMOF-8	1	77	1.5	Rowell et al., 2004 ²³
Zn ₄ O(HPDC) ₂	IRMOF-11	1	77	1.62	Rowell et al., 2004 ²³
		33.7	77	3.4	Wong-Foy, Matzger and Yaghi, 2006 ²²
Zn ₄ O(pyrdc) ₂	IRMOF-13	1	77	1.73	Rowell and Yaghi, 2006 ²⁴
Zn ₄ O(ttdc) ₂	IRMOF-20	77.6	77	6.25	Wong-Foy, Matzger and Yaghi, 2006 ²²
Cd ₃ (bpdc) ₃	JUC-48	40	77	2.8	Fang et al., 2007 ²⁵
Cu ₃ (BTAT)	MFM-132a	1	77	2.83	Yan et al., 2018 ²⁶
		20	77	6.3	
Mg ₂ (dobdc)	Mg-MOF-74	1	77	2.2	Sumida, Brown, et al., 2011 ²⁷
		100	77	4.9	
Al(OH)(bdc)	MIL-53(Al)	16	77	3.8	Férey et al., 2003 ²⁸
Cr(OH)(bdc)	MIL-53(Cr)	16	77	3.1	Férey et al., 2003 ²⁸
Cr ₃ OF(BTC) ₂	MIL-100	26.5	77	3.28	Latroche et al., 2006 ²⁹
Cr ₃ O(BDC) ₂	MIL-101(Cr)	1	77	1.92	Ren et al., 2014 ³⁰
Mn ₃ [(Mn ₄ Cl) ₃ (BTT) ₈] ₂	Mn(BTT)	1.2	77	2.2	Dincă et al., 2007 ²⁰

		90	77	6.9	
Zn ₄ O(bdc) ₃	MOF-5, IRMOF-1	50	77	4.7	Panella et al., 2006 ³¹
Pd(bdc)	MOF-5 (Pd)	1	77	1.86	Sabo et al., 2007 ³²
Zn ₂ (dhtp)	Zn-MOF-74, CPO-27-Zn	1	77	1.77	Rowsell and Yaghi, 2006 ²⁴
		30	77	2.8	Liu et al., 2008 ³³
		70	77	7.5	Wong-Foy, Matzger and Yaghi, 2006 ²²
Zn ₄ O(BBC) ₂ (H ₂ O) ₃	MOF-200	80	77	7.4	Furukawa et al., 2010 ³⁴
Zn ₄ O(BTB) ₄ /3(NDC)	MOF-205	80	77	7	Furukawa et al., 2010 ³⁴
Zn ₄ O(BTE) ₄ /3(bpdc)	MOF-210	80	77	8.6	Furukawa et al., 2010 ³⁴
Cu ₂ (bptc)	MOF-505, NOTT-100	1	77	2.47	Chen et al., 2005 ³⁵
		20	77	4.02	Lin et al., 2009 ³⁶
Zn ₄ O(AZD) ₃	MOF-646	1	77	1.75	Barman et al., 2010 ³⁷
	MOF-808	1	77	2.78	Xia et al., 2016 ³⁸
Ni(dhtp) ₂	Ni-MOF-74	70	77	1.8	Dietzel et al., 2006 ³⁹
Ni(BTC) ₄ /3(4'-bpy)		72	77	3.42	Y. Li et al., 2008 ⁴
Ni ₃ (OH)(pbpc) ₃		1	77	1.99	Jia et al., 2007 ¹⁷
		20	77	4.15	
Ni ₃ [(Co ₄ Cl) ₃ (BTT) ₈ (H ₂ O) ₁₂] ₂		1	77	1.5	Liao et al., 2013 ⁸
NJU-bai12-ac		1	77	1.91	Zheng et al., 2013 ⁴⁰
		20	77	5.9	
Cu ₂ (tptc)	NOTT-101	1	77	2.52	Lin et al, 2009 ³⁶
		20	77	6.06	
		60	77	6.6	
Cu ₂ (qptc)	NOTT-102	1	77	2.24	Lin et al, 2009 ³⁶
		20	77	6.07	
		60	77	7.2	
Cu ₂ (NddIP)	NOTT-103	1	77	2.63	Lin et al, 2009 ³⁶
		20	77	6.51	

		60	77	7.78	
Cu ₂ (DFTP)	NOTT-105	1	77	2.52	Lin et al, 2009 ³⁶
		20	77	5.4	
Cu ₂ (DMTP)	NOTT-106	1	77	2.29	Lin et al, 2009 ³⁶
		20	77	4.5	
Cu ₂ (TMTP)	NOTT-107	1	77	2.26	Lin et al, 2009 ³⁶
		20	77	4.46	
Cu ₂ (ndip)	NOTT-109	1	77	2.33	Lin et al, 2009 ³⁶
		20	77	4.15	
Cu ₂ (pdip)	NOTT-110	1	77	2.64	Yang et al., 2009 ⁴¹
		20	77	6.59	
		55	77	7.62	
Cu ₂ (dpdip)	NOTT-111	1	77	2.56	Yang et al., 2009 ⁴¹
		20	77	6.48	
		48	77	7.36	
Cu ₃ (BDDC)	NOTT-112	1	78	2.3	Yan et al., 2009 ⁴²
		37.5	77	7.07	
		100	77	8.74	García-Holley et al., 2018 ¹⁵
		100	160	8.31	
Cu ₃ (tbtt)	NOTT-113	1	78	2.39	Yan, Blake, et al., 2011 ⁴³
		30	78	5.1	
Cu ₃ (abtt)	NOTT-114	1	78	2.39	Yan, Blake, et al., 2011 ⁴³
		30	78	5	
Cu ₃ (NTBD)	NOTT-115	1	78	2.39	Yan, Blake, et al., 2011 ⁴³
		33	78	5.6	
Cu ₃ (btti)	NOTT-119, PCN-69	1	77	1.44	Yan, Yang, et al., 2011 ⁴⁴
		44	77	5.6	
Cu ₄ (TDTM)	NOTT-140	1	77	2.5	Tan.C et al., 2011 ⁴⁵
		20	77	6	
Sc ₂ (bptc)(OH) ₂	NOTT-400	1	77	2.14	Ibarra et al., 2011 ⁴⁶

Sc(TDA)(OH)	NOTT-401	20	77	3.84	
		1	77	2.31	Ibarra et al., 2011 ⁴⁶
		20	77	4.44	
Cu ₃ (ttei)	NU-100	1	77	1.82	Farha et al., 2010 ⁴⁷
		56	77	9.95	
Cu ₃ (TIPTB)	NU-125, NOTT-122	1	77	2.61	Yan et al., 2014 ⁴⁸
		5	77	4.6	García-Holley et al., 2018 ¹⁵
		100	77	8.2	
		100	160	7.76	
Zr(TBAPy) ₂	NU-1000	5	77	3.37	García-Holley et al., 2018 ¹⁵
		100	77	7.98	
		100	160	7.62	
Zr(Py-XP)	NU-1101	100	77	9.5	Gómez-Gualdrón et al., 2017 ⁴⁹
Zr(Por-PP)	NU-1102	100	77	9.9	Gómez-Gualdrón et al., 2017 ⁴⁹
Zr(Py-PTP)	NU-1103	100	77	13	Gómez-Gualdrón et al., 2017 ⁴⁹
Cu ₃ (TATB) ₂ (catenated)	PCN-6	1	77	1.9	Sun, Ma, et al., 2006 ⁵⁰
		50	77	7.2	S. Ma et al., 2008 ⁵¹
Cu ₂ (aobtc)	PCN-10	1	77	2.34	X.-S. Wang, Ma, Rauch, et al., 2008 ⁵²
		3.5	30	6.84	
		45	77	5.23	
Cu ₂ (sbtc)	PCN-11	1	77	2.55	X.-S. Wang, Ma, Rauch, et al., 2008 ⁴⁹
		3.5	30	7.89	
		45	77	5.97	
Cu ₂ (mdip)	PCN-12	1	77	3.05	X.-S. Wang, Ma, Forster, et al., 2008 ⁴⁹
Cu ₂ (adip)	PCN-14	1	77	2.7	Ma et al., 2009 ⁵³
		45	77	4.42	
Cu ₂ (ebdc)	PCN-16	1	77	2.6	Sun et al., 2010 ⁵⁴
		45	77	5.1	
Cu ₂ (PMTB)	PCN-21	1	77	1.6	Zhuang et al., 2010 ⁵⁵

Cu ₂ (bdi)	PCN-46	1	77	1.95	Zhao et al., 2010 ⁵⁶
		32	77	5.31	
Cu ₃ (btei)	PCN-61	1	77	2.25	Yuan et al., 2010 ⁵⁷
		33	77	6.24	
Cu ₃ (ntei)	PCN-66	1	77	1.79	Yuan et al., 2010 ⁵⁷
		45	77	6.65	
Cu ₃ (ptei)	PCN-68, NOTT-116	1	77	1.87	Yuan et al., 2010 ⁵⁷
		50	77	7.32	
Fe ₂ (abtc)	PCN-250	5	77	3.77	García-Holley et al., 2018 ¹⁵
		100	77	5.37	
		100	160	4.93	
Cu ₂ (bdpb)	PMOF-3	1	77	2.47	Zhang et al., 2011 ⁵⁸
Cu ₃ (TDPAT)	rht-MOF-7	5	77	3.23	García-Holley et al., 2018 ¹⁵
		100	77	4.89	
		100	160	4.5	
Sc(BDC) ₃		1	77	1.5	Perles et al., 2005 ⁵⁹
Zn ₄ O(NTB) ₂	SNU-1	1	77	1.9	Young Lee, Yeon Jang and Paik Suh., 2005 ⁶⁰
Zn ₂ (abtc)(DMF) ₂	SNU-4	1	77	2.07	Lee et al., 2008 ⁶¹
		50	77	3.7	
Cu ₂ (abtc)(DMF) ₂	SNU-5'	1	77	1.83	Lee et al., 2008 ⁶¹
		50	77	5.22	
Cu ₂ (BPnDC) ₂ (4,4'-bpy)	SNU-6	1	77	1.68	Park and Suh., 2008 ⁶²
		70	77	4.87	
Cu ₂ (TCM)	SNU-21S	1	77	1.95	Kim and Suh., 2011 ⁶³
		70	77	4.37	
Zn ₂ (TCPBDA)(H ₂ O) ₂	SNU-30	61	77	3.27	Park, Cheon and Suh, 2010 ⁶²
Cu ₂ (bdcppi)	SNU-50'	1	77	2.1	Prasad, Hong and Suh, 2010 ⁶⁴
		1	87	1.39	
		60	77	5.53	

Zn4O(CVB)3	SNU-70	20	77	7	Ahmed et al., 2019 ⁶⁵
		100	77	10.5	
Zn4O(TCBPA)2	SNU-77H	1	77	1.79	Park H. J. et al., 2011 ⁶⁶
		90	77	8.1	
Mo3(BTC)2	TUDMOF-1	1	77	1.75	Kramer, Schwarz and Kaskel, 2006 ⁶⁷
Zr(BPDC)2	UiO-67	5	77	3.23	García-Holley et al., 2018 ¹⁵
		100	77	5.86	
		100	160	5.53	
Zr(ACDB)2	UiO-68-Ant	5	77	3.81	García-Holley et al., 2018 ¹⁵
		100	77	7.58	
		100	160	7.18	
Zn4O(T2DC)(BTB)4/3	UMCM-2	46	77	6.9	Koh, Wong-Foy and Matzger, 2009 ⁶⁸
Zn4O(bpdc)1.5(NDC)1.5	UMCM-9	20	77	7.5	Ahmed et al., 2019 ⁶⁵
		100	77	11.5	
Cu3(BHB)	UTSA-20	1	77	2.9	Guo et al., 2011 ⁶⁹
		15	77	4.1	
Cu3(bhtc)2	UMCM-150	1	77	2.1	Wong-Foy, Lebel and Matzger, 2007 ⁷⁰
		45	77	5.7	
Y(BTC)		1	77	1.57	Luo et al., 2008 ⁷¹
		10	77	2.1	
Zn(MeIM)2	ZIF-8	55	77	3.01	Zhou et al., 2007 ⁷²
		30	77	3.3	
Co(MeIM)2	ZIF-67	1	77	1.53	Panchariya et al., 2018 ⁷³
Zn(NDC)(bpe)0.5		40	77	2	Chen, Ma, et al., 2006 ⁷⁴
Zn(peip)		1	77	2.27	Liu, Oh and Soo Lah, 2011b ⁷⁵
Zn2(BDC)(tmbdc)(dabco)		1	77	2.08	Chun et al., 2005 ⁷⁶
Zn2(BDC)2(dabco)		1	77	2.1	Lee et al., 2007 ¹³
		83.2	77	3.17	Takei et al., 2008 ⁷⁷
Zn2(btatb)		1	77	2.2	Farha et al., 2008 ⁷⁸
Zn2(NDC)2(dabco)		1	77	1.7	Chun et al., 2005 ⁷⁶

Zn ₂ (tftpa) ₂ (dabco)		1	77	1.78	Chun et al., 2005 ⁷⁶
Zn ₂ (tmbdc) ₂ (4,4'-bpy)		1	77	1.68	Chun et al., 2005 ⁷⁶
Zn ₂ (tmbdc) ₂ (dabco)		1	77	1.85	Chun et al., 2005 ⁷⁶
Zn ₃ (bpdc) ₃ (4,4'-bpy)		1	77	1.74	Lee et al., 2005 ⁷⁹
Zn(5-AT) ₂	ZTF-1	1	77	1.6	Panda et al., 2011 ⁸⁰
Zn(Mlai)	IMOF-3	1	77	1.5	Debatin et al., 2010 ⁸¹

Table S 6.2 MOF structures with literature CH₄ uptakes

MOF Name	Common Name	Pressure (Bar)	Temperature (K)	Uptake (%wt)	Reference
Al ₃ (TCPT)6	Alsoc-MOF-1	65	270	33.8	Alezi et al., 2015 ⁸²
		65	270	29	
Cd(bpydb)		35	298	5.5	Sharma et al., 2011 ⁸³
Co ₂ (4,4'-bpy) ₃ (NO ₃) ₄		30	298	3.56	Kondo et al., 1997 ⁸⁴
Co ₂ (azpy) ₃ (NO ₃) ₄		36	298	2.9	Kondo et al., 2000 ⁸⁵
Co ₂ (BDC) ₂ (dabco)		35	303	11.4	H. Wang et al., 2008 ⁸⁶
		75	303	12.28	H. Wang et al., 2008 ⁸⁶
Co ₂ (dobdc)	Co-MOF-74	35	298	11	Mason, Veenstra and Long, 2014 ⁸⁷
Cu ₂ (BDC) ₂ (dabco)		35	293	10.8	Seki and Mori, 2002 ⁸⁸
		35	298	13.2	Seki, 2001 ⁸⁹
Cu ₃ (BTC) ₂		35	303	12.7	Senkovska and Kaskel, 2008 ⁹⁰
Cu ₃ (TDPAT)	Cu-TDPAT	35	298	13.2	Li et al., 2012 ⁹¹
Al(OH)(NDC)	DUT-4	35	303	8.8	Senkovska et al., 2009 ⁹²
Al(OH)(bpdc)	DUT-5	35	303	9.8	Senkovska et al., 2009 ⁹²
Co ₂ (NDC) ₂ (dabco)	DUT-8(Co)	60	298	4.5	Klein et al., 2012 ⁹³
Cu ₂ (NDC) ₂ (dabco)	DUT-8(Cu)	60	298	12.8	Klein et al., 2012 ⁹³
Zn ₂ (NDC) ₂ (dabco)	DUT-8(Zn)	60	298	3.7	Klein et al., 2012 ⁹³
Ni ₅ O ₂ (BTB) ₂	DUT-9	30	298	12	Gedrich et al., 2010 ⁹⁴
		70	298	17.3	
Zn ₄ O(TCPBDA) _{3/2}	DUT-13	50	298	13.9	Grünker et al., 2011 ⁹⁵
Co ₂ (bipy) ₃ (BTB) ₄	DUT-23(Co)	100	298	21.1	Klein et al., 2011 ⁹⁶
Cu ₂ (BBCDC)	DUT-49	35	298	19.2	Stoek et al., 2012 ⁹⁷
Zn ₆ (BTB) ₄ (4,4'-bpy) ₃	FJI-1	35	273	20.6	Han et al., 2011 ¹⁹
		35	298	15.2	
Cu ₃ (BTC) ₂	HKUST-1	35	298	15.5	Peng, Krungleviciute, et al., 2013 ⁹⁸
		65	298	17.8	
Zn ₄ O(NH ₂ -bdc) ₃	IRMOF-3	36.5	298	13	Eddaoudi et al., 2002 ⁹⁹

Zn ₄ O(C ₂ H ₄ -bdc) ₃	IRMOF-6	36.5	298	19.4	Eddaoudi et al., 2002 ⁹⁹
Zn ₄ O(NDC) ₃	IRMOF-8	35	298	12.2	Feldblyum et al., 2013 ¹⁰⁰
Mg ₂ (dobdc)	Mg-MOF-74, CPO-27-Mg	35	298	13.62	Mason, Veenstra and Long, 2014 ⁸⁷
Al(OH)(bdc)	MIL-53(Al)	35	298	10.6	Bolinois et al, 2017 ¹⁰¹
Cr(OH)(bdc)	MIL-53(Cr)	30	304	8.8	Bourrelly et al., 2005 ¹⁰²
Cr ₃ OF(BTC) ₂	MIL-100(Cr)	35	303	10.7	Llewellyn et al., 2008 ¹⁰³
Fe ₃ OF(BTC) ₂	MIL-100(Fe)	35	303	8.8	Wiersum et al., 2013 ¹⁰⁴
Cr ₃ OF(H ₂ O) ₂ (bdc) ₃	MIL-101(Cr)	35	303	9.3	Wiersum et al., 2013 ¹⁰⁴
Ti ₈ O ₈ (OH) ₄ (bdc) ₆	MIL-125	35	303	9.7	Wiersum et al., 2013 ¹⁰⁴
Mn ₂ (dobdc)	Mn-MOF-74, CPO-27-Mn	35	297	9.6	Wu, Zhou and Yildirim, 2009 ¹⁰⁵
Zn ₄ O(bdc) ₃	MOF-5 or IRMOF-1	36.5	298	15.1	Eddaoudi et al., 2002 ⁹⁹
Zn ₄ O(BTB) ₂	MOF -177	35	298	13.8	Furukawa et al., 2010 ³⁴
		65	298	19.5	
Zn ₄ O(BBC) ₂	MOF -200	10	298	5.12	Furukawa et al., 2010 ³⁴
		35	298	11.5	
		65	298	17.5	
Zn ₄ O(BTB) _{4/3} (NDC)	MOF -205	10	298	5.7	Furukawa et al., 2010 ³⁴
		35	298	14.9	
		65	298	20	
Zn ₄ O(BTE) _{4/3} (bpdcc)	MOF -210	35	298	13.2	Furukawa et al., 2010 ³⁴
		65	298	19.3	
Cu ₂ (bptc)	MOF -505, NOTT -100	35	300	13.3	He, Zhou, et al., 2013 ¹⁰⁶
		65	270	16.2	
Ni ₂ (dobdc)	Ni -MOF -74, CPO -27 -Ni	35	298	12.2	Mason, Veenstra and Long, 2014 ⁸⁷
Cu ₆ (BDPP) ₃ (H ₂ O) ₆	NJU -Bai10	35	290	17.6	Lu et al., 2013 ¹⁰⁷
Cu ₂ (tptc)	NOTT -101	35	300	17	He, Zhou, et al., 2013 ¹⁰⁶
		65	300	19.8	
Cu ₂ (qptc)	NOTT -102	35	300	18.1	He, Zhou, et al., 2013 ¹⁰⁶

		65	300	22.2	
Cu 2(2,6 -nddi)	NOTT -103	35	300	17.9	He, Zhou, et al., 2013 ¹⁰⁶
		65	300	20.8	
Cu 2(C26 H20 O 8)	NOTT -107	35	298	15.7	He,Zhou et al., 2014 ¹⁰⁸
Cu 2(1,4 -nddi)	NOTT -109	35	300	15.1	He,Zhou et al., 2014 ¹⁰⁸
		65	300	18	
Cu 3(C66 H36 O12)	NOTT -119	35	298	16.2	Yan, Yang, et al., 2011 ⁴⁴
Cu 3 (btdi)(H 2O) 3	NU -111	35	298	19.8	Peng, Srinivas, et al., 2013 ¹⁰⁹
		65	270	32.9	
Cu 3(TIPTB)	NU -125, NOTT -122	35	298	18.3	Wilmer et al., 2013 ¹¹⁰
		65	298	22	
Cu 3(TIPTPB)(H 2O) 3	NU -140	65	270	29.6	Barin et al., 2014 ¹¹¹
		65	300	25.4	
Zr 6 O 4(OH) 4(TPT)	NU -800	35	298	15.2	Gomez -Gualdron et al., 2014 ¹¹²
		65	270	27.7	
Cu 2(sbtc)	PCN -11	35	298	14.5	X. -S. Wang, Ma, Rauch, et al., 2008 ⁵²
Cu 2(adip)	PCN -14	65	270	33.3	Peng, Srinivas, et al., 2013 ¹⁰⁹
		65	298	26.4	
Cu 2(ebdc)	PCN -16	35	300	15.9	He,Zhou et al., 2014 ¹⁰⁸
Cu 2(bdi)	PCN -46	35	298	19.4	Zhao et al., 2010 ⁵⁶
Cu 3(btei)	PCN -61	35	298	16.7	Yuan et al., 2010 ⁵⁷
Cu 3(ntei)	PCN -66	35	298	16.6	Yuan et al., 2010 ⁵⁷
Cu 3(ptei)	PCN -68	35	298	17.9	Yuan et al., 2010 ⁵⁷
Cu 2(bttd)	PCN -80	35	296	15	Lu et al., 2012 ¹¹³
Zn 2 (TCPBDA)	SNU -30	50	194	6.4	Park, Cheon and Suh, 2010 ⁶²
		50	298	4.5	
Zn 2(TCPBDA)(bpta)	SNU -31	50	298	1.5	Park, Cheon and Suh, 2010 ⁶²
Cu 2(bdcppi)	SNU -50	1	195	10.6	Prasad, Hong and Suh, 2010 ⁶⁴
		61	298	14.5	

Zn 4O(CVB) 3	SNU -70	1	195	3.8	Prasad and Suh, 2012 ¹¹⁴
		45	298	18.3	
Zn 4O(CEB) 3	SNU -71	1	195	4.7	Prasad and Suh, 2012 ¹¹⁴
		45	298	10.8	
Zn 4O(TCBPA) 2	SNU -77H	1	195	8.04	H. J. Park et al., 2011 ⁶⁶
		35	298	17.8	
		60	298	18.08	
Zr 6 O 4(OH) 4(bdc) 6	UiO -66	35	303	6.7	Wiersum et al., 2013 ¹⁰⁴
Zr6O4(OH)4(NH2-bdc)6	UiO-66-NH2	35	303	7.5	Wiersum et al., 2013 ¹⁰⁴
Cu3(BHB)	UTSA-20a	35	298	12.5	He,Zhou et al., 2014 ¹⁰⁸
		65	298	14.2	
Cu3(TIPAB)	UTSA-34	35	290	11.9	He,Zhou et al., 2014 ¹⁰⁸
Zn4O(NDC)3	UTSA-38	35	300	7.5	Das et al., 2011 ¹¹⁵
Cu2(dcei)	UTSA-40	35	300	12	He, Xiang, et al., 2013 ¹¹⁶
Cu2(PDD)(H2O)2	UTSA-75	65	298	20.4	Li et al., 2015 ¹¹⁷
Cu2(PDDP)(H2O)2	UTSA-76	65	298	20.8	Li et al., 2015 ¹¹⁷
Cu2(tptc)(PDDP)(H2O)2	UTSA-77	65	298	20.4	Li et al., 2015 ¹¹⁷
Cu2(DCPAI)(H2O)2	UTSA-80	65	298	19.4	Wen et al., 2014 ¹¹⁸
Cu2(DFMTP)(H2O)2	UTSA-88	65	298	17.1	Chang et al., 2015 ¹¹⁹
Zn(MeIM)2	ZIF-8	36	300	7	Zhou et al., 2007 ⁷²
Cu2(BDPP)(H2O)2	ZJU-5	65	298	20.8	Li et al., 2015 ¹¹⁷
Cu2(FDDI)	ZJU-25	35	300	17.2	He,Zhou et al., 2014 ¹⁰⁸
Cu2(cpda)	ZJU-36	35	300	17	He,Zhou et al., 2014 ¹⁰⁸
		65	300	22.7	
Cu6(CTIA)2	ZJU-70	35	298	12.7	Duan et al., 2015 ¹²⁰
		65	270	16.3	
Cu2(BDEDI)(H2O)2	ZJUN-50	35	298	17.6	Song, Ling, et al., 2015 ¹²¹
		65	298	21.5	
Zn2(BDC)2(dabco)		35	303	12.5	Senkovska and Kaskel, 2008 ⁹⁰
Zn3O(2,7-ndc)2		35	298	7.3	Park et al., 2009 ¹²²

Zn ₂ (dobdc)	Zn-MOF-74, CPO-27-Zn	35	298	9.1	Wu, Zhou and Yildirim, 2009 ¹⁰⁵
-------------------------	----------------------	----	-----	-----	--

Table S 6.3 MOF structures with literature CO₂ uptakes

MOF Name	Common Name	Pressure (Bar)	Temperature (K)	Uptake (%wt)	Reference
Al3(TCPT)6	Alsoc-MOF1	40	298	66.7	Alezi et al., 2015 ⁸²
Zn8(ad)4(BPDC)6O.2Me2NH2	Bio-MOF-1	1	313	5.48	An and Rosi, 2010 ¹²³
Co2(ad)2(CO2CH3)2·2DMF	Bio-MOF-11	1	298	15.3	An, Geib and Rosi, 2010 ¹²³
Al4(OH)2(OCH3)4(NH2-bdc)3	CAU-1	1	273	24.1	Si et al., 2011 ¹²⁴
Cd(DBNBVP)2(ClO4)2		1	273	12.3	Wu and Lin, 2005 ¹²⁵
Cd2(HFIDP)(H2O)2		1	195	12.7	Hou et al., 2011 ¹²⁶
		1	293	8.5	
Cd6(CPOM)3(H2O)6		1	297	5.6	Tian, J et al., 2010 ¹²⁷
		30	297	14	
Cd(ADA)(4,4'-bipy)0.5.(DMF)	Cd-ADA-1	1	298	3.4	Pachfule et al., 2010 ¹²⁸
Cd(MeIm)2	CdIF-1	1	273	5.6	Tian, Y.-Q et al., 2010 ¹²⁹
Cd(eIm)2	CdIF-4	1	273	4	Tian, Y.-Q et al., 2010 ¹²⁹
Cd(nIm)2	CdIF-9	1	273	8.8	Tian, Y.-Q et al., 2010 ¹²⁹
Co(BDP)		40	313	41.3	Herm et al., 2011 ¹³⁰
Co(tImb)		1	298	7.2	Chen, S.-S et al., 2011 ¹³¹
Co(tImb).DMF.H2O		1	298	11.7	Chen, S.-S et al., 2011 ¹³¹
Co2(dobdc)	Co-MOF-74	0.1	296	10.36	Caskey, Wong-Foy and Matzger, 2008 ¹³²
		1	296	23.6	
Zn(BTT)	CPF-6	1	273	16.2	Lin et al., 2012 ¹³³
Cu2(pmddc)2(bpy)	CPL-2	1	298	6.6	García-Ricard and Hernández Maldonado, 2010 ¹³⁴
Ni3(OH)(bdc)3(tpt)	CPM-33a	1	273	21.2	Zhao et al., 2015 ¹³⁵
		1	298	12.7	
Ni3(OH)(dobdc)3(tpt)	CPM-33b	1	273	25.6	Zhao et al., 2015 ¹³⁵
		1	298	19.8	

(CH ₃) ₂ NH ₂][In ₃ O(BTC) ₂ (H ₂ O) ₃] ₂ [In ₃ (BTC) ₄] ₇ DMF·23H ₂ O	CPM-5	1	273	13.7	S.-T. Zheng et al., 2010 ¹³⁶
		1	299	9.6	
Cu(2-pymo) ₂		0.86	293	3.8	Navarro et al., 2006 ¹³⁷
Cu(BDC-OH)		2	296	8.9	Xiang et al., 2012 ¹³⁸
Cu ₂ (pmde) ₂ (pz)		1	300	6.4	Kitaura et al., 2005 ¹³⁹
Cu ₃ (BTB)		20	273	61.1	Zheng et al., 2012 ¹⁴⁰
Cu ₃ (BTC) ₂		1	296	18.8	Xiang et al., 2012 ¹³⁸
Cu ₄ O(OH) ₂ (Me ₂ trzpba) ₄		1	298	5.8	Lincke et al., 2011 ¹⁴¹
Cu-BTTri		1	298	12.3	Demessence et al., 2009 ¹⁴²
		40	313	42.8	
Cu ₃ (TDPAT)(H ₂ O) ₃	Cu-TDPAT	0.1	298	5.8	Li et al., 2012 ⁹¹
		1	298	20.6	
Cu ₃ (TPBTM)(H ₂ O) ₃	Cu-TPBTM	20	298	50.8	Baishu Zheng et al., 2011 ¹⁴³
Fe ₃ [(Fe ₄ Cl) ₃ (BTT) ₈ (MeOH) ₄] ₂	Fe-BTT	1	298	12	Sumida et al., 2010 ¹⁴⁴
Fe ₃ O(OH)(BTC) ₂	Fe-MIL-100	0.9	298	6.6	Mason et al., 2015 ¹⁴⁵
Fe(pz)Ni(CN) ₄		1	298	9.3	Sumida et al 2012 ¹⁴⁶
Cu(BTTA)(H ₂ O)	FJI-H14	1	195	35.5	Liang et al., 2017 ¹⁴⁷
		1	298	22.2	
Zn(bcphfp)	FMOF-2	1	298	4.5	Fernandez et al., 2010 ¹⁴⁸
Cu ₃ (BTC) ₂	HKUST-1	1	298	15.3	Millward and Yaghi, 2005 ¹⁴⁹
		30	298	31.9	
[Zn ₃ (pbdc) ₂] ₂ ·HPIP·H ₃ O·5H ₂ O	HPIP@ZnPC -2	0.15	298	4.6	Ling et al., 2013 ¹⁵⁰
[Zn ₃ (pbdc) ₂] ₂ ·HPYR·H ₃ O·4H ₂ O	HPYR@ZnP C-2	0.15	298	3	Ling et al., 2013 ¹⁵⁰
Zn(BHTHT)	IFMC-1	1	195	24.8	Qin et al., 2012 ¹⁵¹
		1	273	15.3	
		1	298	10.6	
Zn(Mlai)	IMOF-3	1	273	7.2	Debatin et al., 2010 ⁸¹
In ₂ (OH) ₂ (obb) ₂		1	298	8.6	Y.-X. Tan et al., 2011 ¹⁵²
In ₃ O(abtc) _{1.5} (H ₂ O) ₃ (NO ₃)	socMOF M080	1	273	17.9	Moellmer et al., 2010 ¹⁵³

In ₃ (BTC) ₄ (choline)		1	273	12.3	Chen et al., 2009 ¹⁵⁴
Zn ₄ O(NH ₂ -BDC) ₂	IRMOF-3	1.1	298	5.1	Millward and Yaghi, 2005 ¹⁴⁹
		35	298	45.1	
Zn ₄ O(dobdc) ₂	IRMOF-6	1.2	298	4.6	Millward and Yaghi, 2005 ¹⁴⁹
		40	298	46.6	
Zn ₄ O(NDC) ₃	IRMOF-8	1	273	12.2	Orefuwa et al., 2013 ¹⁵⁵
		30	273	38.6	
		30	298	34	
Zn ₄ O(HPDC) ₂	IRMOF-11	1.1	298	7.3	Millward and Yaghi, 2005 ¹⁴⁹
		35	298	39.3	
Zn ₄ O(TPDC) ₃	IRMOF-16	1	298	5.4	Bae et al., 2009 ¹⁵⁶
Mg ₂ (DH ₃ PhDC)-CH ₂ NH ₂	IRMOF-74- III- CH ₂ NH ₂	1	298	12.3	Fracaroli et al., 2014 ¹⁵⁷
Fe ₃ O(TCDC)(H ₂ O) ₃	LIFM-26	1	273	19.2	C.-X Chen et al., 2017 ¹⁵⁸
		1	298	12.7	
Zr ₆ O ₈ (TDA)(H ₂ O) ₈	LIFM-29	1	273	9.9	C.-X. Chen et al., 2016 ¹⁵⁹
		1	298	6.13	
Zr ₆ O ₈ (tftpa)(H ₂ O) ₈	LIFM-30	1	273	10.3	C.-X. Chen et al., 2016 ¹⁵⁹
		1	298	4.9	
Zr ₆ O ₈ (NDC)(H ₂ O) ₈	LIFM-31	1	273	10.3	C.-X. Chen et al., 2016 ¹⁵⁹
		1	298	6.5	
Zr ₆ O ₈ (dhbpdC)(H ₂ O) ₈	LIFM-32	1	273	10.6	C.-X. Chen et al., 2016 ¹⁵⁹
		1	298	5.25	
Zr ₆ O ₈ (dabpdC)(H ₂ O) ₈	LIFM-33	1	273	13.7	C.-X. Chen et al., 2016 ¹⁵⁹
		1	298	7.08	
Cu(etz)	MAF-2	1	298	3.6	Zhang and Chen, 2009 ¹⁶⁰
		1	273	8.84	
Zn ₂ (btm) ₂	MAF-23	1	273	12.7	Liao et al., 2012 ¹⁶¹
		1	298	9.9	

Co(dpt24)2	MAF-25	1	195	18.6	Lin, Zhang and Chen, 2010 ¹⁶²
		1	273	4.83	
		1	283	3	
Co(mdpt24)2	MAF-26	1	195	14.3	Lin, Zhang and Chen, 2010 ¹⁶²
		1	273	3.75	
		1	283	2.9	
Zn(atz)2	MAF-66	1	273	21.7	Lin et al., 2012 ¹⁶³
		1	298	16.2	
Mg(TCPBDA)		1	195	20.9	Cheon et al 2009 ¹⁶⁴
		1	273	8.3	
		1	298	6.2	
Mg2(dobpdc)		0.15	298	12.1	McDonald et al., 2012 ¹⁶⁵
		1	298	14.5	
Mg(3,5-pdc)	Mg-MOF-1	1	298	2.7	Mallick et al., 2010 ¹⁶⁶
Mg2(dobdc)	Mg-MOF74, MgCPO-27	0.1	298	20.3	Bao et al., 2011 ¹⁶⁷ Dietzel, Besikiotis and Blom, 2009 ¹⁶⁸
		1	298	27.5	
		36	278	40.8	
Al(OH)(bdc)	MIL-53(Al), USO-1-Al	1	303	9.2	Rallapalli et al., 2011 ¹⁶⁹ Bourrelly et al., 2005 ¹⁰²
		25	304	30.6	
Cr(OH)(bdc)	MIL-53(Cr)	1	304	8.1	Bourrelly et al., 2005 ¹⁰²
		25	304	30.8	
Al12O(OH)18(Al2(OH)4)(BTC)6	MIL-96(Al)	10	303	16.2	Loiseau et al., 2006 ¹⁷⁰
		20	303	18.6	
Cr3OF(H2O)3(BTC)2	MIL-100(Cr)	50	304	44.2	Llewellyn et al., 2008 ¹⁰³
Cr3OF(H2O)2(BDC)3	MIL-101(Cr)	1	296	5.8	Chowdhury et al., 2012 ¹⁷¹ Llewellyn et al., 2008 ¹⁰³
		50	304	56.9	
Cr3OF(H2O)2(NTC)1.5	MIL-102(Cr)	30	304	12	Surbly et al., 2006 ¹⁷²
Al4(OH)8(C10O8H2)	MIL-120	10	303	15.6	Volkringer et al., 2009 ¹⁷³
mmen-Cu-BTtri		1	298	15.6	McDonald et al., 2011 ¹⁷⁴

Mn(bdc)(dpe)		1	195	17.7	Foo et al., 2016 ¹⁷⁵
Mn(NDC)(DEF)		1	195	11.7	Hoi, Kobayashi and Myunghyun., 2006 ¹⁷⁶
		1	273	6.2	
Mn(pmde)		0.9	293	7.3	Beobide et al., 2008 ¹⁷⁷
[Mn ₂ (2,6-ndc) ₂ (bpda) ₂]-5DMF	Mn-bpda	1	195	24.5	Lee et al., 2016 ¹⁷⁸
		35	298	21.6	
Zn ₃ (bdc) ₃	MOF-2	1	298	2.4	Millward and Yaghi, 2005 ¹⁴⁹
		30	298	11.97	
Zn ₄ O(bdc) ₃	MOF-5 or IRMOF-1	1	296	3.94	Millward and Yaghi, 2005 ¹⁴⁹
		35	298	48.8	
Zn ₄ O(BTB) ₂	MOF-177	1	298	6.5	Saha et al., 2010 ¹⁷⁹
		50	298	60.8	Furukawa et al., 2010 ³⁴
Zn ₄ O(BBC) ₂ (H ₂ O) ₃	MOF-200	50	298	73.9	Furukawa et al., 2010 ³⁴
Zn ₄ O(BTB)(NDC)(H ₂ O) ₃	MOF-205	50	298	62.6	Furukawa et al., 2010 ³⁴
Zn ₄ O(BTE)(BPDC)(H ₂ O) ₃	MOF-210	50	298	74.2	Furukawa et al., 2010 ³⁴
Al(OH)(bpydc)	MOF-253	1	298	6.2	Bloch et al., 2010 ¹⁷⁷
Cu ₂ (bptc)(H ₂ O) ₂ (DMF) ₃	MOF-505	1.1	298	12.6	Millward and Yaghi, 2005 ¹⁴⁹
Zn ₂ (BDC) ₂ (4,4'-bpy)	MOF-508	5	303	20.6	Bárcia et al., 2008 ¹⁸⁰
Al(ABDC)(OH)	NH ₂ -MIL53(Al)	5	303	8.4	Couck et al., 2009 ¹⁸¹
		13	303	22.8	
Ti(NH ₂ -bdc) ₂	NH ₂ -MIL125	1	273	15	Kim et al., 2013 ⁶³
		1	298	8.8	
Ni(DBNBVP) ₂ Cl ₂		1	273	8.1	Wu and Lin, 2006 ¹⁸²
Ni ₃ (L-TMTA) ₂ (bpy) ₄		1	298	8.2	Z. Chen et al., 2011 ¹⁸³
Ni-4Pyc		10	298	26.5	Nandi et al., 2015 ¹⁸⁴
Ni ₂ (dobdc)	Ni-MOF-74, CPO-27-N	0.1	296	10.3	Caskey, Wong-Foy and Matzger, 2008 ¹³²
		1	296	20.3	
		22	278	34.4	Dietzel, Besikiotis and Blom, 2009 ¹⁶⁸

Cu ₃ (cobai) ₂ (H ₂ O) ₅	NJU-Bai3	1	273	21.5	Duan et al., 2012 ¹⁸⁵
		20	273	49.3	
		20	298	44.3	
[Cu ₂ (H ₂ O) ₂ (obaddi)]·4 H ₂ O·2 DMA	NOTT-125	1	273	28.6	Alsmail et al., 2014 ¹⁸⁶
		1	298	15.4	
		20	273	50.3	
		20	298	48.3	
Cu ₄ (TDTM)	NOTT-140	1	293	11.7	C. Tan et al., 2011 ⁴⁵
		20	293	47.7	
		20	283	46.2	
Me ₂ NH ₂) _{1.75} [In(btpc)] _{1.75} (DMF) ₁₂	NOTT-202a	1	195	46.8	Yang et al., 2012 ¹⁸⁷
Cu ₃ (btDi)(H ₂ O) ₃	NU-111	30	298	62.8	Peng, Srinivas, et al., 2013 ¹⁰⁹
Zr(TBAPy) ₂	NU-1000	1	298	10.7	Farha et al., 2010 ⁴⁷
		40	298	67.1	
Cu ₃ (TATB) ₂ (catenated)	PCN-6	1	273	25.65	Kim et al., 2011 ⁶³
		1	298	15.9	
		30	298	53.9	
Cu ₃ (btei)	PCN-61	35	298	50.8	Yuan et al., 2010 ⁵⁷
Cu ₃ (ntei)	PCN-66	35	298	53.6	Yuan et al., 2010 ⁵⁷
Cu ₃ (ptei)	PCN-68	35	298	57.2	Yuan et al., 2010 ⁵⁷
Cu(NddIP) _{0.5}	PCN-88	1	273	23.8	Li et al., 2013 ¹⁸⁸
		1	296	15.6	
Zn(PDAT)	PCN-123	1	295	3.9	J. Park et al., 2012 ¹⁸⁹
Zr(TCPP) ₂	PCN-222, MOF-545	1	298	4.9	Lv et al., 2018 ¹⁹⁰
		30	298	37.6	
Pd(2-pymo) ₂		0.86	293	6.8	Navarro et al., 2006 ¹³⁷
Pd(F-pymo) ₂		0.86	293	9.7	Navarro et al., 2007 ¹⁹¹
		1.2	273	13.5	
Sc ₂ (BDC) ₃		1	303	3	Miller et al., 2009 ¹⁹²
(Me ₂ NH ₂)[In(ABDC) ₂]	SHF-61	20	298	9.6	Carrington et al., 2017 ¹⁹³

Zn ₃ (NTB) ₂	SNU-3	1	195	22.9	Suh, Cheon and Lee, 2007 ¹⁹⁴
		1	273	6.5	
Zn ₂ (abtc)(DMF) ₂	SNU-4	1	195	35.5	Lee et al., 2008 ⁶¹
		1	273	17.3	
Cu ₂ (abtc) ₃	SNU-5	1	195	52.9	Lee et al., 2008 ⁶¹
		1	273	27.8	
Cu ₂ (BPnDC) ₂ (4,4'-bpy)	SNU-6	1	273	9.9	Park and Suh, 2008 ¹⁹⁵
Zn ₂ (BPnDC) ₂ (bpy)	SNU-9	30	298	23	Park and Suh, 2010 ¹⁹⁶
Co ₂ (MTB)	SNU-15	1	273	6.5	Cheon and Suh, 2009 ¹⁹⁷
Cu ₂ (TCM)	SNU-21S	1	298	10	Kim and Suh, 2011 ⁶³
Zn ₂ (TCPBDA)(H ₂ O) ₂	SNU-30	1	195	31.6	Park, Cheon and Suh, 2010 ⁶²
		1	273	10.3	
		1	298	4.9	
		50	298	18	
Zn ₂ (TCPBDA)(bpta)	SNU-31	1	195	14.6	Park, Cheon and Suh, 2010 ⁶²
		1	273	5	
		1	298	2.6	
		40	298	8.8	
Cu ₂ (bdcppi)	SNU-50	1	195	47.2	Prasad, Hong and Suh, 2010 ⁶⁴
		1	273	19.1	
		1	298	13.7	
		46	298	42.9	
Zn ₄ O(CEB) ₂	SNU-71	1	195	36.7	Prasad and Suh, 2012 ¹¹⁴
		1	298	4.2	
Ni ₂ (CYC-2C-CYC)(bptc)	SNU-M10	1	195	19.5	Choi and Suh, 2009 ¹⁹⁸
		1	273	12.7	
		1	298	8.5	
Ni ₂ (CYC-4C-CYC)(bptc)	SNU-M11	1	195	19.5	Choi and Suh, 2009 ¹⁹⁸
[Zn ₄ O(bdc) ₃].(ZnO) _{0.125}	SUMOF-2	1	273	15.9	Yao et al., 2012 ¹⁹⁹
Zn ₄ O(NDC) ₃	SUMOF-3	1	273	13	Yao et al., 2012 ¹⁹⁹

Zn4O(bdc)2(bpdc)(H2O)	SUMOF-4	1	273	13.7	Yao et al., 2012 ¹⁹⁹
Cu(bpy)2(EDS)	TMOF-1	1	200	22.9	Zhang et al., 2016 ²⁰⁰
		1	273	9	
		1	298	5.8	
		1	308	4.9	
Zn2(obb)2(bppta)	TMU-22	1	203	24.1	Safarifard et al., 2016 ²⁰¹
Zn2(obb)2(bpfm)	TMU-24	1	203	21.7	Safarifard et al., 2016 ²⁰¹
Zr6O4(OH)4(bpdc)12	UiO(bpdc)	20	303	42.1	Li et al., 2014 ²⁰²
Zn4O(BDC)(BTB)4/3	UMCM-1	1	298	3.8	Yazaydin et al., 2009 ²⁰³
		24	298	50.8	Mu, Schoenecker and Walton, 2010 ²⁰⁴
Cu3(BPT)2	UMCM-150	1	298	10.2	Yazaydin et al., 2009 ²⁰³
Ni2(BDC)2(DABCO)	USO-2-Ni	1	298	10	Arstad et al., 2008 ²⁰⁵
Ni2(2-amino-BDC)2(DABCO)	USO-2-Ni-A	1	298	14	Arstad et al., 2008 ²⁰⁵
In(OH)(BDC)	USO-3-In-A	1	298	8	Arstad et al., 2008 ²⁰⁵
Al(OH)(Sbpdc)	USTC-253	1	273	14	Jiang et al., 2015 ²⁰⁶
		1	298	8.5	
Al(OH)(Sbpdc)(TFA)	USTC-253- TFA	1	273	21.2	Jiang et al., 2015 ²⁰⁶
		1	298	11.3	
Cu(BDC-OH)(4,4'-bipy)	UTSA-15a	1	296	5.1	Z. Chen, Xiang, Hadi D. Arman, et al., 2011a ²⁰⁷
Cu3(BHB)	UTSA-20a	1	296	17	Guo et al., 2011 ⁶⁹
Zn(BDC-OH)(DABCO)0.5	UTSA-25a	1	296	12	Z. Chen, Xiang, Hadi D Arman, et al., 2011b ²⁰⁸
Zn4(TIPAB)(DMA)4	UTSA-33a	1	273	8.9	He, Zhang, Xiang, Fronczek, et al., 2012 ²⁰⁹
Zn2(btbb)(diPyNI)	YO-MOF	1	273	14.4	Mulfort et al., 2010 ²¹⁰
		1	298	4.5	
Zn(MeIm)2	ZIF-8	1	298	4.3	Yazaydin et al., 2009 ²⁰³
Zn(nIm)(bIm)	ZIF-68	1	298	6.4	Banerjee et al., 2009 ²¹¹
Zn(nIm)(cbIm)	ZIF-69	1	298	7.9	Banerjee et al., 2009 ²¹¹
Zn(nIm)(Im)	ZIF-70	1	298	4.43	Banerjee et al., 2009 ²¹¹
Zn(nbIm)(nIm)	ZIF-78	2	298	9.52	Banerjee et al., 2009 ²¹¹

Zn(nIm)(mbIm)	ZIF-79	1.1	298	5.9	Banerjee et al., 2009 ²¹¹
Zn(nIm)(cnIm)	ZIF-82	1	298	7.84	Banerjee et al., 2009 ²¹¹
Zn(almeIm)	ZIF-93	1	298	6.7	Morris et al., 2010 ²¹²
Zn(cyamIm)	ZIF-96	1	298	8.5	Morris et al., 2010 ²¹²
Cu ₂ (BTADD)(H ₂ O) ₂	ZJNU-40	1	273	24.9	Song et al., 2014 ²¹³
		1	296	16.3	
[Cu ₂ (qdip)(H ₂ O) ₂] ₃ DMF·2EtOH	ZJNU-43	1	273	24.9	Song, Hu, et al., 2015 ²¹⁴
		1	296	17.2	
[Cu ₂ (qodip)(H ₂ O) ₂] ₃ DMF·3MeOH Z	ZJNU-45	1	273	23.5	Song, Hu, et al., 2015 ²¹⁴
		1	296	16.1	
Zn(BDC-NH ₂)(dabco) _{0.5}		1	298	8.8	Zhao et al., 2011 ²¹⁵
Zn(BDC-OH)(dabco) _{0.5}		1	298	11.7	Zhao et al., 2011 ²¹⁵
Zn(BPZNO ₂)		1.2	298	18	Mosca et al., 2018 ²¹⁶
Zn(dtp)		1	195	14	J.-R. Li et al., 2008 ²¹⁷
Zn(MIai)		1	298	7.9	Debatin et al., 2010 ⁸¹
Zn ₂ (2,5-BME-bdc) ₂ (dabco)		1	195	16.8	Henke et al., 2012 ²¹⁸
Zn ₂ (BDC) ₂ (dabco)		1	294	8.1	Mishra et al., 2012 ²¹⁹
		25	294	37.3	
Zn ₂ (BME-bdc) ₂ -(bipy)		1	195	23.6	Henke and Fischer, 2011 ²²⁰
		1	273	9.2	
		1	298	5.56	
Zn ₂ (BMOE-bdc) ₂ (dabco)		1	195	25.4	Henke et al., 2010 ²²¹
Zn ₂ (BMOP-bdc) ₂ (dabco)		1	195	8.6	Henke et al., 2010 ²²¹
Zn ₂ (bpdc) ₂ (bpe)		1	273	7.3	J. Zhang et al., 2010 ²²²
		1	298	4.7	
Zn ₂ (DB-bdc) ₂ (dabco)		1	195	9.9	Henke et al., 2012 ²¹⁸
Zn ₂ (MOE-bdc) ₂ (dabco)		1	195	30.7	Henke et al., 2010 ²²¹
Zn ₂ (NDC) ₂ (diPyNI)		1	298	5.8	Bae et al., 2011 ²²³
Zn ₂ (ox)(atz) ₂		1.2	273	16.1	Vaidhyanathan et al., 2009 ²²⁴
		1.2	293	14.2	

Zn ₄ (OH) ₂ (BTC) ₂		1	295	6.7	Z. Zhang et al., 2010 ²²⁵
Zn ₄ O(BMOE-bdc) ₃		1	195	18.1	Henke et al., 2010 ²²¹
Zn ₄ O(BMOP-bdc) ₃		1	195	11.9	Henke et al., 2010 ²²¹
Zn ₄ O(FMA) ₃		2	296	3.8	Xiang et al., 2012 ¹³⁸
Zn ₄ O(MOE-bdc) ₃		1	195	47	Henke et al., 2010 ²²¹
[Zn ₄ (BDC) ₄ (BPDA) ₄]·5DMF·3H ₂ O	Zn-bpda	1	298	7.5	Lee et al., 2013 ²²⁶
		35	298	13.2	
Zn ₂ (dobdc)	Zn-MOF-74	0.1	296	5.4	Caskey, Wong-Foy and Matzger, 2008 ¹³²
		1	296	19.5	
Zn(5-AT) ₂	ZTF-1	1	273	19.8	Panda et al., 2011 ⁸⁰

Table S 6.4 Individual coefficient of determination values for each fold in the 10 runs

Run	Fold number									
	1	2	3	4	5	6	7	8	9	10
1	0.91	0.87	0.87	0.92	0.87	0.87	0.92	0.86	0.90	0.85
2	0.86	0.88	0.89	0.90	0.84	0.86	0.86	0.92	0.84	0.92
3	0.86	0.86	0.93	0.91	0.90	0.83	0.92	0.90	0.87	0.83
4	0.85	0.87	0.89	0.91	0.92	0.82	0.87	0.87	0.89	0.88
5	0.89	0.90	0.93	0.83	0.89	0.88	0.87	0.85	0.84	0.92
6	0.89	0.90	0.82	0.94	0.86	0.89	0.86	0.87	0.89	0.85
7	0.88	0.87	0.87	0.91	0.91	0.89	0.79	0.86	0.90	0.87
8	0.89	0.84	0.92	0.86	0.88	0.88	0.88	0.85	0.86	0.88
9	0.79	0.91	0.87	0.87	0.92	0.90	0.82	0.91	0.90	0.86
10	0.88	0.89	0.83	0.81	0.88	0.88	0.87	0.89	0.91	0.91

Hyperparameters for other machine learning models

Linear Regression

This was fitted using the “fitrlinear” function in MATLAB 2020. All other parameters that are not stated are set to their default values.

Lambda = 0.048818

Learner type = Least Squares

Regularisation = Ridge

Decision Trees

This was fitted using the “fitrtrees” function in MATLAB 2020. All other parameters that are not stated are set at their default values.

Minimum Leaf size = 3

Maximum number of splits = 195

Support Vector Mechanism

This was fitted using the “fitrsvm” function in MATLAB 2020. All other parameters that are not stated are set at their default values.

Box Constraint = 0.11404

Epsilon = 0.18408

Kernel Function = Linear

Standardize data = False

6.8 References for uptake data

1. Sumida, K., Hill, M. R., Horike, S., Dailly, A., Long, J. R. *J. Am. Chem. Soc.*, 2009, **131**, 15120–15121.
2. Chun, H., Kim, D., Dybtsev, D. N., Kim, K. *Angew. Chemie*, 2004, **116**, 989–992.
3. Choi, H. J., Dinca, M., Long, J. R. *J. Am. Chem. Soc.*, 2008, **130**, 7848–7850.
4. Li, Y., Xie, L., Liu, Y., Yang, R., Li, X. *Inorg. Chem.*, 2008, **47**, 10372–10377.
5. Myunghyun Paik Suh, Hye Jeong Park, T. K. P. *Chem. Rev.*, 2012, **112**, 782–835.
6. Lee, J. Y., Pan, L., Kelly, S. P., Jagiello, J., Emge, T. J., Li, J. *Adv. Mater.*, 2005, **17**, 2703–2706.
7. Chun, H., Jung, H., Koo, G., Jeong, H., Kim, D.-K. *Inorg. Chem.*, 2008, **47**, 5355–5359.
8. Liao, J. H., Chen, W. T., Tsai, C. S., Wang, C. C. *CrystEngComm*, 2013, **15**, 3377–3384.
9. Sumida, K., Her, J.-H., Dinca, M., Murray, L. J., Schloss, J. M., Pierce, C. J., Thompson, B. A., FitzGerald, S. A., Brown, C. M., Long, J. R. *J. Phys. Chem. C*, 2011, **115**, 8414–8421.
10. Yang, W., Lin, X., Jia, J., Blake, A. J., Wilson, C., Hubberstey, P., Champness, N. R., Schröder, M. *Chem. Commun.*, 2008, 359–361.
11. Liu, X., Oh, M., Lah, M. S. *Cryst. Growth Des.*, 2011, **11**, 5064–5071.
12. Nouar, F., Eubank, J. F., Bousquet, T., Wojtas, L., Zaworotko, M. J., Eddaoudi, M. *J. Am. Chem. Soc.*, 2008, **130**, 1833–1835.
13. Lee, J. Y., Olson, D. H., Pan, L., Emge, T. J., Li, J. *Adv. Funct. Mater.*, 2007, **17**, 1255–1262.
14. Zheng, B., Liang, Z., Li, G., Huo, Q., Liu, Y. *Cryst. Growth Des.*, 2010, **10**, 3405–3409.
15. García-Holley, P., Schweitzer, B., Islamoglu, T., Liu, Y., Lin, L., Rodriguez, S., Weston, M. H., Hupp, J. T., Gómez-Gualdrón, D. A., Yildirim, T., Farha, O. K. *ACS Energy Lett.*, 2018, **3**, 748–754.
16. Maity, K., Karan, C. K., Biradha, K. *Chem. - A Eur. J.*, 2018, **24**, 10988–10993.
17. Jia, J., Lin, X., Wilson, C., Blake, A. J., Champness, N. R., Hubberstey, P., Walker, G., Cussen, E. J., Schröder, M. *Chem. Commun.*, 2007, **3**, 840–842.
18. Choi, S. B., Seo, M. J., Cho, M., Kim, Y., Jin, M. K., Jung, D. Y., Choi, J. S., Ahn, W. S., Rowsell, J. L. C., Kim, J. *Cryst. Growth Des.*, 2007, **7**, 2290–2293.
19. Han, D., Jiang, F. L., Wu, M. Y., Chen, L., Chen, Q. H., Hong, M. C. *Chem. Commun.*, 2011, **47**, 9861–9863.
20. Dincă, M., Han, W. S., Liu, Y., Dailly, A., Brown, C. M., Long, J. R. *Angew. Chemie - Int. Ed.*, 2007, **46**, 1419–1422.
21. Cheng, C., Yang, G. S., Yan, L. H., Wang, X., Jiang, C. J., Li, N., Su, Z. M. *Inorg. Chem. Commun.*, 2018, **93**, 25–28.
22. Wong-Foy, A. G., Matzger, A. J., Yaghi, O. M. *J. Am. Chem. Soc.*, 2006, **128**, 3494–3495.
23. Rowsell, J. L. C., Millward, A. R., Park, K. S., Yaghi, O. M. *J. Am. Chem. Soc.*, 2004, **126**, 5666–5667.
24. Rowsell, J. L. C., Yaghi, O. M. *J. Am. Chem. Soc.*, 2006, **128**, 1304–1315.
25. Fang, Q.-R., Zhu, G.-S., Jin, Z., Ji, Y.-Y., Ye, J.-W., Xue, M., Yang, H., Wang, Y., Qiu, S.-L.

- Angew. Chemie*, 2007, **119**, 6758–6762.
26. Yan, Y., Da Silva, I., Blake, A. J., Dailly, A., Manuel, P., Yang, S., Schröder, M. *Inorg. Chem.*, 2018, **57**, 12050–12055.
 27. Sumida, K., Brown, C. M., Herm, Z. R., Chavan, S., Bordiga, S., Long, J. R. *Chem. Commun.*, 2011, **47**, 1157–1159.
 28. Férey, G., Latroche, M., Serre, C., Millange, F., Loiseau, T., Percheron-Guégan, A. *Chem. Commun.*, 2003, **3**, 2976–2977.
 29. Latroche, M., Surblé, S., Serre, C., Mellot-Draznieks, C., Llewellyn, P. L., Lee, J.-H., Chang, J.-S., Jhung, S. H., Férey, G. *Angew. Chemie*, 2006, **118**, 8407–8411.
 30. Ren, J., Musyoka, N. M., Langmi, H. W., Segakweng, T., North, B. C., Mathe, M., Kang, X. *Int. J. Hydrogen Energy*, 2014, **39**, 12018–12023.
 31. Panella, B., Hirscher, M., Pütter, H., Müller, U. *Adv. Funct. Mater.*, 2006, **16**, 520–524.
 32. Sabo, M., Henschel, A., Fröde, H., Klemm, E., Kaskel, S. *J. Mater. Chem.*, 2007, **17**, 3827–3832.
 33. Liu, Y., Kabbour, H., Brown, C. M., Neumann, D. A., Ahn, C. C. *Langmuir*, 2008, **24**, 4772–4777.
 34. Furukawa, H., Ko, N., Go, Y. B., Aratani, N., Choi, S. B., Choi, E., Yazaydin, A. Ö., Snurr, R. Q., O’Keeffe, M., Kim, J., Yaghi, O. M. *Science (80-.)*, 2010, **329**, 424–428.
 35. Chen, B., Ockwig, N. W., Millward, A. R., Contreras, D. S., Yaghi, O. M. *Angew. Chemie - Int. Ed.*, 2005, **44**, 4745–4749.
 36. Lin, X., Telepeni, I., Blake, A. J., Dailly, A., Brown, C. M., Simmons, J. M., Zoppi, M., Walker, G. S., Thomas, K. M., Mays, T. J., Hubberstey, P., Champness, N. R., Schröder, M. *J. Am. Chem. Soc.*, 2009, **131**, 2159–2171.
 37. Barman, S., Furukawa, H., Blacque, O., Venkatesan, K., Yaghi, O. M., Berke, H. *Chem. Commun.*, 2010, **46**, 7981–7983.
 38. Xia, L., Liu, Q., Wang, F., Lu, J. *J. Mol. Model.*, 2016, **22**.
 39. Dietzel, P. D. C., Panella, B., Hirscher, M., Blom, R., Fjellvåg, H. *Chem. Commun.*, 2006, **1**, 959–961.
 40. Zheng, B., Yun, R., Bai, J., Lu, Z., Du, L., Li, Y. *Inorg. Chem.*, 2013, **52**, 2823–2829.
 41. Yang, S., Lin, X., Dailly, A., Blake, A. J., Hubberstey, P., Champness, N. R., Schröder, M. *Chem. - A Eur. J.*, 2009, **15**, 4829–4835.
 42. Yan, Y., Lin, X., Yang, S., Blake, A. J., Dailly, A., Champness, N. R., Hubberstey, P., Schröder, M. *Chem. Commun.*, 2009, 1025–1027.
 43. Yan, Y., Blake, A. J., Lewis, W., Barnett, S. A., Dailly, A., Champness, N. R., Schröder, M. *Chem. - A Eur. J.*, 2011, **17**, 11162–11170.
 44. Yan, Y., Yang, S., Blake, A. J., Lewis, W., Poirier, E., Barnett, S. A., Champness, N. R., Schröder, M. *Chem. Commun.*, 2011, **47**, 9995–9997.
 45. Tan, C., Yang, S., Champness, N. R., Lin, X., Blake, A. J., Lewis, W., Schröder, M. *Chem. Commun.*, 2011, **47**, 4487–4489.
 46. Ibarra, I. A., Yang, S., Lin, X., Blake, A. J., Rizkallah, P. J., Nowell, H., Allan, D. R., Champness, N. R., Hubberstey, P., Schröder, M. *Chem. Commun.*, 2011, **47**, 8304–8306.

47. Farha, O. K., Yazaydin, A. Ö., Eryazici, I., Malliakas, C. D., Hauser, B. G., Kanatzidis, M. G., Nguyen, S. T., Snurr, R. Q., Hupp, J. T. *Nat. Chem.*, 2010, **2**, 944–948.
48. Yan, Y., Yang, S., Blake, A. J., Schröder, M. *Acc. Chem. Res.*, 2014, **47**, 296–307.
49. Gómez-Gualdrón, D. A., Wang, T. C., García-Holley, P., Sawelewa, R. M., Argueta, E., Snurr, R. Q., Hupp, J. T., Yildirim, T., Farha, O. K. *ACS Appl. Mater. Interfaces*, 2017, **9**, 33419–33428.
50. Sun, D., Ma, S., Ke, Y., Collins, D. J., Zhou, H. C. *J. Am. Chem. Soc.*, 2006, **128**, 3896–3897.
51. Ma, S., Eckert, J., Forster, P. M., Ji, W. Y., Young, K. H., Chang, J. S., Collier, C. D., Parise, J. B., Zhou, H. C. *J. Am. Chem. Soc.*, 2008, **130**, 15896–15902.
52. Wang, X. Sen, Shengqian, M., Rauch, K., Simmons, J. M., Yuan, D., Wang, X., Yildirim, T., Cole, W. C., López, J. J., De Meijere, A., Zhou, H. C. *Chem. Mater.*, 2008, **20**, 3145–3152.
53. Ma, S., Simmons, J. M., Sun, D., Yuan, D., Zhou, H. C. *Inorg. Chem.*, 2009, **48**, 5263–5268.
54. Sun, D., Ma, S., Simmons, J. M., Li, J. R., Yuan, D., Zhou, H. C. *Chem. Commun.*, 2010, **46**, 1329–1331.
55. Zhuang, W., Ma, S., Wang, X. Sen, Yuan, D., Li, J. R., Zhao, D., Zhou, H. C. *Chem. Commun.*, 2010, **46**, 5223–5225.
56. Zhao, D., Yuan, D., Yakovenko, A., Zhou, H. C. *Chem. Commun.*, 2010, **46**, 4196–4198.
57. Yuan, D., Zhao, D., Sun, D., Zhou, H.-C. *Angew. Chemie*, 2010, **122**, 5485–5489.
58. Zhang, P., Li, B., Zhao, Y., Meng, X., Zhang, T. *Chem. Commun.*, 2011, **47**, 7722–7724.
59. Perles, J., Iglesias, M., Martín-Luengo, M. Á., Monge, M. A., Ruiz-Valero, C., Snejko, N. *Chem. Mater.*, 2005, **17**, 5837–5842.
60. Lee, E. Y., Jang, S. Y., Suh, M. P. *J. Am. Chem. Soc.*, 2005, **127**, 6374–6381.
61. Lee, Y.-G., Moon, H. R., Cheon, Y. E., Suh, M. P. *Angew. Chemie*, 2008, **120**, 7855–7859.
62. Park, H. J., Cheon, Y. E., Suh, M. P. *Chem. - A Eur. J.*, 2010, **16**, 11662–11669.
63. Kim, T. K., Suh, M. P. *Chem. Commun.*, 2011, **47**, 4258–4260.
64. Prasad, T. K., Hong, D. H., Suh, M. P. *Chem. - A Eur. J.*, 2010, **16**, 14043–14050.
65. Ahmed, A., Seth, S., Purewal, J., Wong-Foy, A. G., Veenstra, M., Matzger, A. J., Siegel, D. J. *Nat. Commun.*, 2019, **10**, 1568.
66. Park, H. J., Lim, D. W., Yang, W. S., Oh, T. R., Suh, M. P. *Chem. - A Eur. J.*, 2011, **17**, 7251–7260.
67. Kramer, M., Schwarz, U., Kaskel, S. *J. Mater. Chem.*, 2006, **16**, 2245–2248.
68. Koh, K., Wong-Foy, A. G., Matzger, A. J. *J. Am. Chem. Soc.*, 2009, **131**, 4184–4185.
69. Guo, Z., Wu, H., Srinivas, G., Zhou, Y., Xiang, S., Chen, Z., Yang, Y., Zhou, W., O’Keeffe, M., Chen, B. *Angew. Chemie - Int. Ed.*, 2011, **50**, 3178–3181.
70. Wong-Foy, A. G., Lebel, O., Matzger, A. J. *J. Am. Chem. Soc.*, 2007, **129**, 15740–15741.
71. Lou, J., Xu, H., Liu, Y., Zhao, Y., Daemen, L. L., Brown, C., Timofeeva, T. V., Ma, S., Zhou, H. C. *J. Am. Chem. Soc.*, 2008, **130**, 9626–9627.
72. Zhou, W., Wu, H., Hartman, M. R., Yildirim, T. *J. Phys. Chem. C*, 2007, **111**, 16131–16137.
73. Panchariya, D. K., Rai, R. K., Anil Kumar, E., Singh, S. K. *ACS Omega*, 2018, **3**, 167–175.

74. Chen, B., Ma, S., Zapata, F., Lobkovsky, E. B., Yang, J. *Inorg. Chem.*, 2006, **45**, 5718–5720.
75. Liu, X., Oh, M., Lah, M. S. *Inorg. Chem.*, 2011, **50**, 5044–5053.
76. Chun, H., Dybtsev, D. N., Kim, H., Kim, K. *Chem. - A Eur. J.*, 2005, **11**, 3521–3529.
77. Takei, T., Kawashima, J., Ii, T., Maeda, A., Hasegawa, M., Kitagawa, T., Ohmura, T., Ichikawa, M., Hosoe, M., Kanoya, I., Mori, W. *Bull. Chem. Soc. Jpn.*, 2008, **81**, 847–856.
78. Farha, O. K., Mulfort, K. L., Hupp, J. T. *Inorg. Chem.*, 2008, **47**, 10223–10225.
79. Lee, J., Li, J., Jagiello, J. *J. Solid State Chem.*, 2005, **178**, 2527–2532.
80. Panda, T., Pachfule, P., Chen, Y., Jiang, J., Banerjee, R. *Chem. Commun.*, 2011, **47**, 2011–2013.
81. Debatin, F., Thomas, A., Kelling, A., Hedin, N., Bacsik, Z., Senkovska, I., Kaskel, S., Junginger, M., Müller, H., Schilde, U., Jäger, C., Friedrich, A., Holdt, H.-J. *Angew. Chemie*, 2010, **122**, 1280–1284.
82. Alezi, D., Belmabkhout, Y., Suyetin, M., Bhatt, P. M., Weseliński, L. J., Solovyeva, V., Adil, K., Spanopoulos, I., Trikalitis, P. N., Emwas, A. H., Eddaoudi, M. *J. Am. Chem. Soc.*, 2015, **137**, 13308–13318.
83. Sharma, M. K., Senkovska, I., Kaskel, S., Bharadwaj, P. K. *Inorg. Chem.*, 2011, **50**, 539–544.
84. Kondo, M., Yoshitomi, T., Matsuzaka, H., Kitagawa, S., Seki, K. *Angew. Chemie Int. Ed. English*, 1997, **36**, 1725–1727.
85. Kondo, M., Shimamura, M., Noro, S. I., Minakoshi, S., Asami, A., Seki, K., Kitagawa, S. *Chem. Mater.*, 2000, **12**, 1288–1299.
86. Wang, H., Getzschmann, J., Senkovska, I., Kaskel, S. *Microporous Mesoporous Mater.*, 2008, **116**, 653–657.
87. Mason, J. A., Veenstra, M., Long, J. R. *Chem. Sci.*, 2014, **5**, 32–51.
88. Seki, K., Mori, W. *J. Phys. Chem. B*, 2002, **106**, 1380–1385.
89. Seki, K. *Chem. Commun.*, 2001, **1**, 1496–1497.
90. Senkovska, I., Kaskel, S. *Microporous Mesoporous Mater.*, 2008, **112**, 108–115.
91. Li, B., Zhang, Z., Li, Y., Yao, K., Zhu, Y., Deng, Z., Yang, F., Zhou, X., Li, G., Wu, H., Nijem, N., Chabal, Y. J., Lai, Z., Han, Y., Shi, Z., Feng, S., Li, J. *Angew. Chemie - Int. Ed.*, 2012, **51**, 1412–1415.
92. Senkovska, I., Hoffmann, F., Fröba, M., Getzschmann, J., Böhlmann, W., Kaskel, S. *Microporous Mesoporous Mater.*, 2009, **122**, 93–98.
93. Klein, N., Hoffmann, H. C., Cadiou, A., Getzschmann, J., Lohe, M. R., Paasch, S., Heydenreich, T., Adil, K., Senkovska, I., Brunner, E., Kaskel, S. *J. Mater. Chem.*, 2012, **22**, 10303–10312.
94. Gedrich, K., Senkovska, I., Klein, N., Stoeck, U., Henschel, A., Lohe, M. R., Baburin, I. A., Mueller, U., Kaskel, S. *Angew. Chemie - Int. Ed.*, 2010, **49**, 8489–8492.
95. Grünker, R., Senkovska, I., Biedermann, R., Klein, N., Lohe, M. R., Müller, P., Kaskel, S. *Chem. Commun.*, 2011, **47**, 490–492.
96. Klein, N., Senkovska, I., Baburin, I. A., Grünker, R., Stoeck, U., Schlichtenmayer, M., Streppel, B., Mueller, U., Leoni, S., Hirscher, M., Kaskel, S. *Chem. - A Eur. J.*, 2011, **17**, 13007–13016.
97. Stoeck, U., Krause, S., Bon, V., Senkovska, I., Kaskel, S. *Chem. Commun.*, 2012, **48**, 10841–10843.

98. Peng, Y., Krungleviciute, V., Eryazici, I., Hupp, J. T., Farha, O. K., Yildirim, T. *J. Am. Chem. Soc.*, 2013, **135**, 11887–11894.
99. Eddaoudi, M., Kim, J., Rosi, N., Vodak, D., Wachter, J., O’Keeffe, M., Yaghi, O. M. *Science (80-)*, 2002, **295**, 469–472.
100. Feldblyum, J. I., Dutta, D., Wong-Foy, A. G., Dailly, A., Imirzian, J., Gidley, D. W., Matzger, A. *J. Langmuir*, 2013, **29**, 8146–8153.
101. Bolinois, L., Kundu, T., Wang, X., Wang, Y., Hu, Z., Koh, K., Zhao, D. *Chem. Commun.*, 2017, **53**, 8118–8121.
102. Bourrelly, S., Llewellyn, P. L., Serre, C., Millange, F., Loiseau, T., Férey, G. *J. Am. Chem. Soc.*, 2005, **127**, 13519–13521.
103. Llewellyn, P. L., Bourrelly, S., Serre, C., Vimont, A., Daturi, M., Hamon, L., De Weireld, G., Chang, J.-S., Hong, D.-Y., Kyu Hwang, Y., others *Langmuir*, 2008, **24**, 7245–7250.
104. Wiersum, A. D., Chang, J. S., Serre, C., Llewellyn, P. L. *Langmuir*, 2013, **29**, 3301–3309.
105. Wu, H., Zhou, W., Yildirim, T. *J. Am. Chem. Soc.*, 2009, **131**, 4995–5000.
106. He, Y., Zhou, W., Yildirim, T., Chen, B. *Energy & Environ. Sci.*, 2013, **6**, 2735–2744.
107. Lu, Z., Du, L., Tang, K., Bai, J. *Cryst. growth & Des.*, 2013, **13**, 2252–2255.
108. He, Y., Zhou, W., Qian, G., Chen, B. *Chem. Soc. Rev.*, 2014, **43**, 5657–5678.
109. Peng, Y., Srinivas, G., Wilmer, C. E., Eryazici, I., Snurr, R. Q., Farha, O. K., Yildirim, T. *Chem. Commun.*, 2013, **49**, 2992–2994.
110. Wilmer, C. E., Farha, O. K., Yildirim, T., Eryazici, I., Krungleviciute, V., Sarjeant, A. A., Snurr, R. Q., Hupp, J. T. *Energy Environ. Sci.*, 2013, **6**, 1158–1163.
111. Barin, G., Krungleviciute, V., Gomez-Gualdron, D. A., Sarjeant, A. A., Snurr, R. Q., Hupp, J. T., Yildirim, T., Farha, O. K. *Chem. Mater.*, 2014, **26**, 1912–1917.
112. Gomez-Gualdron, D. A., Gutov, O. V., Krungleviciute, V., Borah, B., Mondloch, J. E., Hupp, J. T., Yildirim, T., Farha, O. K., Snurr, R. Q. *Chem. Mater.*, 2014, **26**, 5632–5639.
113. Lu, W., Yuan, D., Makal, T. A., Li, J.-R., Zhou, H.-C. *Angew. Chemie*, 2012, **124**, 1612–1616.
114. Prasad, T. K., Suh, M. P. *Chem. - A Eur. J.*, 2012, **18**, 8673–8680.
115. Das, M. C., Xu, H., Wang, Z., Srinivas, G., Zhou, W., Yue, Y. F., Nesterov, V. N., Qian, G., Chen, B. *Chem. Commun.*, 2011, **47**, 11715–11717.
116. He, Y., Xiang, S., Zhang, Z., Xiong, S., Wu, C., Zhou, W., Yildirim, T., Krishna, R., Chen, B. *J. Mater. Chem. A*, 2013, **1**, 2543–2551.
117. Li, B., Wen, H. M., Wang, H., Wu, H., Yildirim, T., Zhou, W., Chen, B. *Energy Environ. Sci.*, 2015, **8**, 2504–2511.
118. Wen, H. M., Li, B., Yuan, D., Wang, H., Yildirim, T., Zhou, W., Chen, B. *J. Mater. Chem. A*, 2014, **2**, 11516–11522.
119. Chang, G., Li, B., Wang, H., Bao, Z., Yildirim, T., Yao, Z., Xiang, S., Zhou, W., Chen, B. *Chem. Commun.*, 2015, **51**, 14789–14792.
120. Duan, X., Wu, C., Xiang, S., Zhou, W., Yildirim, T., Cui, Y., Yang, Y., Chen, B., Qian, G. *Inorg. Chem.*, 2015, **54**, 4377–4381.
121. Song, C., Ling, Y., Feng, Y., Zhou, W., Yildirim, T., He, Y. *Chem. Commun.*, 2015, **51**, 8508–

- 8511.
122. Park, M., Moon, D., Yoon, J. W., Chang, J. S., Lah, M. S. *Chem. Commun.*, 2009, 2026–2028.
123. An, J., Rosi, N. L. *J. Am. Chem. Soc.*, 2010, **132**, 5578–5579.
124. Si, X., Jiao, C., Li, F., Zhang, J., Wang, S., Liu, S., Li, Z., Sun, L., Xu, F., Gabelica, Z., Schick, C. *Energy Environ. Sci.*, 2011, **4**, 4522–4527.
125. Wu, C. De, Lin, W. *Angew. Chemie - Int. Ed.*, 2005, **44**, 1958–1961.
126. Hou, L., Shi, W. J., Wang, Y. Y., Guo, Y., Jin, C., Shi, Q. Z. *Chem. Commun.*, 2011, **47**, 5464–5466.
127. Tian, J., Motkuri, R. K., Thallapally, P. K., McGrail, B. P. *Cryst. Growth Des.*, 2010, **10**, 5327–5333.
128. Pachfule, P., Panda, T., Dey, C., Banerjee, R. *CrystEngComm*, 2010, **12**, 2381–2389.
129. Tian, Y. Q., Yao, S. Y., Gu, D., Cui, K. H., Guo, D. W., Zhang, G., Chen, Z. X., Zhao, D. Y. *Chem. - A Eur. J.*, 2010, **16**, 1137–1141.
130. Herm, Z. R., Swisher, J. A., Smit, B., Krishna, R., Long, J. R. *J. Am. Chem. Soc.*, 2011, **133**, 5664–5667.
131. Chen, S. S., Chen, M., Takamizawa, S., Wang, P., Lv, G. C., Sun, W. Y. *Chem. Commun.*, 2011, **47**, 4902–4904.
132. Caskey, S. R., Wong-Foy, A. G., Matzger, A. J. *J. Am. Chem. Soc.*, 2008, **130**, 10870–10871.
133. Lin, Q., Wu, T., Zheng, S. T., Bu, X., Feng, P. *J. Am. Chem. Soc.*, 2012, **134**, 784–787.
134. García-Ricard, O. J., Hernández-Maldonado, A. J. *J. Phys. Chem. C*, 2010, **114**, 1827–1834.
135. Zhao, X., Bu, X., Zhai, Q. G., Tran, H., Feng, P. *J. Am. Chem. Soc.*, 2015, **137**, 1396–1399.
136. Zheng, S. T., Bu, J. T., Li, Y., Wu, T., Zuo, F., Feng, P., Bu, X. *J. Am. Chem. Soc.*, 2010, **132**, 17062–17064.
137. Navarro, J. A. R., Barea, E., Salas, J. M., Masciocchi, N., Galli, S., Sironi, A., Ania, C. O., Parra, J. B. *Inorg. Chem.*, 2006, **45**, 2397–2399.
138. Xiang, S., He, Y., Zhang, Z., Wu, H., Zhou, W., Krishna, R., Chen, B. *Nat. Commun.*, 2012, **3**, 1–9.
139. Kitaura, R., Matsuda, R., Kubota, Y., Kitagawa, S., Takata, M., Kobayashi, T. C., Suzuki, M. *J. Phys. Chem. B*, 2005, **109**, 23378–23385.
140. Zheng, B., Yang, Z., Bai, J., Li, Y., Li, S. *Chem. Commun.*, 2012, **48**, 7025–7027.
141. Lincke, J., Lässig, D., Möllmer, J., Reichenbach, C., Puls, A., Möller, A., Gläser, R., Kalies, G., Staudt, R., Krautscheid, H. *Microporous mesoporous Mater.*, 2011, **142**, 62–69.
142. Demessence, A., D'Alessandro, D. M., Foo, M. L., Long, J. R. *J. Am. Chem. Soc.*, 2009, **131**, 8784–8786.
143. Zheng, B., Bai, J., Duan, J., Wojtas, L., Zaworotko, M. J. *J. Am. Chem. Soc.*, 2011, **133**, 748–751.
144. Sumida, K., Horike, S., Kaye, S. S., Herm, Z. R., Queen, W. L., Brown, C. M., Grandjean, F., Long, G. J., Dailly, A., Long, J. R. *Chem. Sci.*, 2010, **1**, 184–191.
145. Mason, J. A., McDonald, T. M., Bae, T. H., Bachman, J. E., Sumida, K., Dutton, J. J., Kaye, S.

- S., Long, J. R. *J. Am. Chem. Soc.*, 2015, **137**, 4787–4803.
146. Sumida, K., Rogow, D. L., Mason, J. A., McDonald, T. M., Bloch, E. D., Herm, Z. R., Bae, T.-H., Long, J. R. *Chem. Rev.*, 2012, **112**, 724–781.
147. Liang, L., Liu, C., Jiang, F., Chen, Q., Zhang, L., Xue, H., Jiang, H.-L., Qian, J., Yuan, D., Hong, M. *Nat. Commun.*, 2017, **8**, 1–10.
148. Fernandez, C. A., Thallapally, P. K., Motkuri, R. K., Nune, S. K., Sumrak, J. C., Tian, J., Liu, J. *Cryst. Growth Des.*, 2010, **10**, 1037–1039.
149. Millward, A. R., Yaghi, O. M. *J. Am. Chem. Soc.*, 2005, **127**, 17998–17999.
150. Ling, Y., Deng, M., Chen, Z., Xia, B., Liu, X., Yang, Y., Zhou, Y., Weng, L. *Chem. Commun.*, 2013, **49**, 78–80.
151. Qin, J. S., Du, D. Y., Li, W. L., Zhang, J. P., Li, S. L., Su, Z. M., Wang, X. L., Xu, Q., Shao, K. Z., Lan, Y. Q. *Chem. Sci.*, 2012, **3**, 2114–2118.
152. Tan, Y. X., Wang, F., Kang, Y., Zhang, J. *Chem. Commun.*, 2011, **47**, 770–772.
153. Möllmer, J., Celer, E. B., Luebke, R., Cairns, A. J., Staudt, R., Eddaoudi, M., Thommes, M. *Microporous Mesoporous Mater.*, 2010, **129**, 345–353.
154. Chen, S., Zhang, J., Wu, T., Feng, P., Bu, X. *J. Am. Chem. Soc.*, 2009, **131**, 16027–16029.
155. Orefuwa, S., Iriowen, E., Yang, H., Wakefield, B., Goudy, A. *Microporous Mesoporous Mater.*, 2013, **177**, 82–90.
156. Bae, Y. S., Dubbeldam, D., Nelson, A., Walton, K. S., Hupp, J. T., Snurr, R. Q. *Chem. Mater.*, 2009, **21**, 4768–4777.
157. Fracaroli, A. M., Furukawa, H., Suzuki, M., Dodd, M., Okajima, S., Gándara, F., Reimer, J. A., Yaghi, O. M. *J. Am. Chem. Soc.*, 2014, **136**, 8863–8866.
158. Chen, C. X., Zheng, S. P., Wei, Z. W., Cao, C. C., Wang, H. P., Wang, D., Jiang, J. J., Fenske, D., Su, C. Y. *Chem. - A Eur. J.*, 2017, **23**, 4060–4064.
159. Chen, C.-X., Wei, Z., Jiang, J.-J., Fan, Y.-Z., Zheng, S.-P., Cao, C.-C., Li, Y.-H., Fenske, D., Su, C.-Y. *Angew. Chemie*, 2016, **128**, 10086–10090.
160. Zhang, J. P., Chen, X. M. *J. Am. Chem. Soc.*, 2009, **131**, 5516–5521.
161. Liao, P. Q., Zhou, D. D., Zhu, A. X., Jiang, L., Lin, R. B., Zhang, J. P., Chen, X. M. *J. Am. Chem. Soc.*, 2012, **134**, 17380–17383.
162. Lin, J.-B., Zhang, J.-P., Chen, X.-M. *J. Am. Chem. Soc.*, 2010, **132**, 6654–6656.
163. Lin, R. B., Chen, D., Lin, Y. Y., Zhang, J. P., Chen, X. M. *Inorg. Chem.*, 2012, **51**, 9950–9955.
164. Cheon, Y. E., Park, J., Suh, M. P. *Chem. Commun.*, 2009, 5436–5438.
165. McDonald, T. M., Lee, W. R., Mason, J. A., Wiers, B. M., Hong, C. S., Long, J. R. *J. Am. Chem. Soc.*, 2012, **134**, 7056–7065.
166. Mallick, A., Saha, S., Pachfule, P., Roy, S., Banerjee, R. *J. Mater. Chem.*, 2010, **20**, 9073–9080.
167. Bao, Z., Yu, L., Ren, Q., Lu, X., Deng, S. *J. Colloid Interface Sci.*, 2011, **353**, 549–556.
168. Dietzel, P. D. C., Besikiotis, V., Blom, R. *J. Mater. Chem.*, 2009, **19**, 7362–7370.
169. Rallapalli, P., Prasanth, K. P., Patil, D., Somani, R. S., Jasra, R. V., Bajaj, H. C. *J. Porous Mater.*, 2011, **18**, 205–210.

170. Loiseau, T., Lecroq, L., Volkringer, C., Marrot, J., Férey, G., Haouas, M., Taulelle, F., Bourrelly, S., Llewellyn, P. L., Latroche, M. *J. Am. Chem. Soc.*, 2006, **128**, 10223–10230.
171. Chowdhury, P., Mekala, S., Dreisbach, F., Gumma, S. *Microporous Mesoporous Mater.*, 2012, **152**, 246–252.
172. Surblé, S., Millange, F., Serre, C., Düren, T., Latroche, M., Bourrelly, S., Llewellyn, P. L., Férey, G. *J. Am. Chem. Soc.*, 2006, **128**, 14889–14896.
173. Volkringer, C., Loiseau, T., Haouas, M., Taulelle, F., Popov, D., Burghammer, M., Riekel, C., Zlotea, C., Cuevas, F., Latroche, M., Phanon, D., Knöfelv, C., Llewellyn, P. L., Férey, G. *Chem. Mater.*, 2009, **21**, 5783–5791.
174. McDonald, T. M., D'Alessandro, D. M., Krishna, R., Long, J. R. *Chem. Sci.*, 2011, **2**, 2022–2028.
175. Foo, M. L., Matsuda, R., Hijikata, Y., Krishna, R., Sato, H., Horike, S., Hori, A., Duan, J., Sato, Y., Kubota, Y., Takata, M., Kitagawa, S. *J. Am. Chem. Soc.*, 2016, **138**, 3022–3030.
176. Hoi, R. M., Kobayashi, N., Myunghyun, P. S. *Inorg. Chem.*, 2006, **45**, 8672–8676.
177. Bloch, E. D., Britt, D., Lee, C., Doonan, C. J., Uribe-Romo, F. J., Furukawa, H., Long, J. R., Yaghi, O. M. *J. Am. Chem. Soc.*, 2010, **132**, 14382–14384.
178. Lee, C. H., Huang, H. Y., Lee, J. J., Huang, C. Y., Kao, Y. C., Lee, G. H., Peng, S. M., Jiang, J. C., Chao, I., Lu, K. L. *ChemistrySelect*, 2016, **1**, 2923–2929.
179. Saha, D., Bao, Z., Jia, F., Deng, S. *Environ. Sci. & Technol.*, 2010, **44**, 1820–1826.
180. Barcia, P. S., Bastin, L., Hurtado, E. J., Silva, J. A. C., Rodrigues, A. E., Chen, B. *Sep. Sci. Technol.*, 2008, **43**, 3494–3521.
181. Couck, S., Denayer, J. F. M., Baron, G. V., Rémy, T., Gascon, J., Kapteijn, F. *J. Am. Chem. Soc.*, 2009, **131**, 6326–6327.
182. Wu, C. De, Lin, W. *Dalt. Trans.*, 2006, 4563–4569.
183. Chen, Z., Liu, X., Zhang, C., Zhang, Z., Liang, F. *Dalt. Trans.*, 2011, **40**, 1911–1918.
184. Nandi, S., De Luna, P., Daff, T. D., Rother, J., Liu, M., Buchanan, W., Hawari, A. I., Woo, T. K., Vaidhyanathan, R. *Sci. Adv.*, 2015, **1**, 1–10.
185. Duan, J., Yang, Z., Bai, J., Zheng, B., Li, Y., Li, S. *Chem. Commun.*, 2012, **48**, 3058–3060.
186. Alsmail, N. H., Suyetin, M., Yan, Y., Cabot, R., Krap, C. P., Lü, J., Easun, T. L., Bichoutskaia, E., Lewis, W., Blake, A. J., Schröder, M. *Chem. - A Eur. J.*, 2014, **20**, 7317–7324.
187. Yang, S., Lin, X., Lewis, W., Suyetin, M., Bichoutskaia, E., Parker, J. E., Tang, C. C., Allan, D. R., Rizkallah, P. J., Hubberstey, P., Champness, N. R., Mark Thomas, K., Blake, A. J., Schröder, M. *Nat. Mater.*, 2012, **11**, 710–716.
188. Li, J. R., Yu, J., Lu, W., Sun, L. B., Sculley, J., Balbuena, P. B., Zhou, H. C. *Nat. Commun.*, 2013, **4**, 1–8.
189. Park, J., Yuan, D., Pham, K. T., Li, J. R., Yakovenko, A., Zhou, H. C. *J. Am. Chem. Soc.*, 2012, **134**, 99–102.
190. Lv, D., Shi, R., Chen, Y., Chen, Y., Wu, H., Zhou, X., Xi, H., Li, Z., Xia, Q. *Ind. Eng. Chem. Res.*, 2018, **57**, 12215–12224.
191. Navarro, J. A. R., Barea, E., Salas, J. M., Masciocchi, N., Galli, S., Sironi, A., Ania, C. O., Parra, J. B. *J. Mater. Chem.*, 2007, **17**, 1939–1946.

192. Miller, S. R., Wright, P. A., Devic, T., Serre, C., Férey, G., Llewellyn, P. L., Denoyel, R., Gaberova, L., Filinchuk, Y. *Langmuir*, 2009, **25**, 3618–3626.
193. Carrington, E. J., McAnally, C. A., Fletcher, A. J., Thompson, S. P., Warren, M., Brammer, L. *Nat. Chem.*, 2017, **9**, 882–889.
194. Suh, M. P., Cheon, Y. E., Lee, E. Y. *Chem. - A Eur. J.*, 2007, **13**, 4208–4215.
195. Park, H. J., Suh, M. P. *Chem. - A Eur. J.*, 2008, **14**, 8812–8821.
196. Park, H. J., Suh, M. P. *Chem. Commun.*, 2010, **46**, 610–612.
197. Cheon, Y. E., Suh, M. P. *Chem. Commun.*, 2009, 2296–2298.
198. Choi, H. S., Suh, M. P. *Angew. Chemie - Int. Ed.*, 2009, **48**, 6865–6869.
199. Yao, Q., Su, J., Cheung, O., Liu, Q., Hedin, N., Zou, X. *J. Mater. Chem.*, 2012, **22**, 10345–10351.
200. Zhang, G., Wei, G., Liu, Z., Oliver, S. R. J., Fei, H. *Chem. Mater.*, 2016, **28**, 6276–6281.
201. Safarifard, V., Rodríguez-Hermida, S., Guillerm, V., Imaz, I., Bigdeli, M., Tehrani, A. A., Juanhuix, J., Morsali, A., Casco, M. E., Silvestre-Albero, J., Ramos-Fernandez, E. V., Maspocho, D. *Cryst. Growth Des.*, 2016, **16**, 6016–6023.
202. Li, L., Tang, S., Wang, C., Lv, X., Jiang, M., Wu, H., Zhao, X. *Chem. Commun.*, 2014, **50**, 2304–2307.
203. Yazaydin, A. Ö., Snurr, R. Q., Park, T. H., Koh, K., Liu, J., LeVan, M. D., Benin, A. I., Jakubczak, P., Lanuza, M., Galloway, D. B., Low, J. J., Willis, R. R. *J. Am. Chem. Soc.*, 2009, **131**, 18198–18199.
204. Mu, B., Schoenecker, P. M., Walton, K. S. *J. Phys. Chem. C*, 2010, **114**, 6464–6471.
205. Arstad, B., Fjellvåg, H., Kongshaug, K. O., Swang, O., Blom, R. *Adsorption*, 2008, **14**, 755–762.
206. Jiang, Z. R., Wang, H., Hu, Y., Lu, J., Jiang, H. L. *ChemSusChem*, 2015, **8**, 878–885.
207. Chen, Z., Xiang, S., Arman, H. D., Mondal, J. U., Li, P., Zhao, D., Chen, B. *Inorg. Chem.*, 2011, **50**, 3442–3446.
208. Chen, Z., Xiang, S., Arman, H. D., Li, P., Zhao, D., Chen, B. *Eur. J. Inorg. Chem.*, 2011, 2227–2231.
209. He, Y., Zhang, Z., Xiang, S., Fronczek, F. R., Krishna, R., Chen, B. *Chem. - A Eur. J.*, 2012, **18**, 613–619.
210. Mulfort, K. L., Farha, O. K., Malliakas, C. D., Kanatzidis, M. G., Hupp, J. T. *Chem. - A Eur. J.*, 2010, **16**, 276–281.
211. Banerjee, R., Furukawa, H., Britt, D., Knobler, C., O’Keeffe, M., Yaghi, O. M. *J. Am. Chem. Soc.*, 2009, **131**, 3875–3877.
212. Morris, W., Leung, B., Furukawa, H., Yaghi, O. K., He, N., Hayashi, H., Houndonougbo, Y., Asta, M., Laird, B. B., Yaghi, O. M. *J. Am. Chem. Soc.*, 2010, **132**, 11006–11008.
213. Song, C., He, Y., Li, B., Ling, Y., Wang, H., Feng, Y., Krishna, R., Chen, B. *Chem. Commun.*, 2014, **50**, 12105–12108.
214. Song, C., Hu, J., Ling, Y., Feng, Y., Krishna, R., Chen, D., He, Y. *J. Mater. Chem. A*, 2015, **3**, 19417–19426.

215. Zhao, Y., Wu, H., Emge, T. J., Gong, Q., Nijem, N., Chabal, Y. J., Kong, L., Langreth, D. C., Liu, H., Zeng, H., Li, J. *Chem. - A Eur. J.*, 2011, **17**, 5101–5109.
216. Mosca, N., Vismara, R., Fernandes, J. A., Tuci, G., Di Nicola, C., Domasevitch, K. V., Giacobbe, C., Giambastiani, G., Pettinari, C., Aragones-Anglada, M., Moghadam, P. Z., Fairen-Jimenez, D., Rossin, A., Galli, S. *Chem. - A Eur. J.*, 2018, **24**, 13170–13180.
217. Li, J. R., Tao, Y., Yu, Q., Bu, X. H., Sakamoto, H., Kitagawa, S. *Chem. - A Eur. J.*, 2008, **14**, 2771–2776.
218. Henke, S., Schneemann, A., Wütscher, A., Fischer, R. A. *J. Am. Chem. Soc.*, 2012, **134**, 9464–9474.
219. Mishra, P., Mekala, S., Dreisbach, F., Mandal, B., Gumma, S. *Sep. Purif. Technol.*, 2012, **94**, 124–130.
220. Henke, S., Fischer, R. a *J. Am. Chem. Soc.*, 2011, **133**, 2064–2067.
221. Henke, S., Schmid, R., Grunwaldt, J. D., Fischer, R. A. *Chem. - A Eur. J.*, 2010, **16**, 14296–14306.
222. Zhang, J., Wu, H., Emge, T. J., Li, J. *Chem. Commun.*, 2010, **46**, 9152–9154.
223. Bae, Y. S., Hauser, B. G., Farha, O. K., Hupp, J. T., Snurr, R. Q. *Microporous Mesoporous Mater.*, 2011, **141**, 231–235.
224. Vaidhyanathan, R., Iremonger, S. S., Dawson, K. W., Shimizu, G. K. H. *Chem. Commun.*, 2009, 5230–5232.
225. Zhang, Z., Xiang, S., Rao, X., Zheng, Q., Fronczek, F. R., Qian, G., Chen, B. *Chem. Commun.*, 2010, **46**, 7205–7207.
226. Lee, C. H., Huang, H. Y., Liu, Y. H., Luo, T. T., Lee, G. H., Peng, S. M., Jiang, J. C., Chao, I., Lu, K. L. *Inorg. Chem.*, 2013, **52**, 3962–3968.

Chapter 7 Overall Discussion and Future work

The overall aim of this thesis was to further the study of MOF materials through the lens of microfluidic synthesis, with an additional objective of forming a machine learning model to predict the uptake of gases in MOFs using only experimentally determined data and easy to determine chemical descriptors being added later. Both have been achieved with varying degrees of success and contributing to an overall aim of developing research into MOFs.

7.1 Progress achieved

In the experimental work, the focus was on developing a method for the synthesis of UiO-67 using a CFIR reactor, before analysing how the effects of microfluidic reactors could be used to form new/improved products that were not obtained through solvothermal batch synthesis. This was a success, with the MethodsX paper detailing the synthesis of UiO-67 while using a CFIR and the Journal of Porous Materials paper discussing the effects of water concentration and microfluidic effects on the formation of HCP/FCC-UiO-67-Benzoic acid. UiO-67 had not previously been formed through a microfluidic synthesis in the literature and the MethodsX paper detailing this process has been cited by 9 other works. This paper is being cited as a recent example of developments in microfluidics and MOF based chemistry in a paper published in the Annual Review of Chemical and Biomolecular Engineering.¹ The HCP/FCC-UiO-67-Benzoic acid is a product that had previous not been synthesised within the literature, with the published paper detailing how microfluidic synthesis is necessary for this product to be formed. This builds upon previous works, in which the formation of an HCP based UiO-67 with benzoic acid has not been performed,² with attempts to form HCP based UiO-66 with benzoic acid being unsuccessful in previous published literature.³

The final experimental paper on the formation of Pd nanoparticles within the UiO-67 pores was not as successful as hoped, with a lack of success in synthesising the intended Pd(0)-UiO-67-BPYDC product. However, the discussion present within this paper may be used to inform future researchers if they attempt this process. All three of these papers have contributed to the overall thesis aims, being the further study of MOF materials through the lens of microfluidic synthesis.

For the computational side, a machine learning model was built to predict the uptake of gases in MOFs using only experimentally determined uptake data and basic chemical descriptors, achieving the computational objective for the thesis. This model can predict for a range of gases, pressures, and temperatures, providing a high level of flexibility for new users and has been made readily available in an open access journal (Journal of Chemical Information and Modelling).

7.2 Difficulties encountered in the research

In terms of difficulties present within this work, the transference of batch synthesis processes to a microfluidic flow synthesis introduced various challenges. Firstly, solubility became far more important, as found with a lot of the early work in this thesis when trying to synthesise UiO-67. Initially, a molar ratio of 1:80 ZrCl₄: DMF was used, as is used in the work by Faustini *et al* in their microfluidic synthesis of UiO-66.⁴ The product synthesised however was determined to be the starting linker BPDC by XRD. When this molar ratio was increased to 1:300, as was initially used by Schaate *et al* in their batch synthesis of UiO-67,⁵ the correct product was seen in the XRD pattern. The increased mixing present within the two phase-flow reactor used by Faustini *et al* allowed them to use this higher concentration and successfully form crystalline UiO-66. What also allowed them to form crystalline UiO-66 in this higher concentration and lower reaction time (15 minutes compared to 30 minutes) is the choice of acid modulator, which plays a more important role in the microfluidic formation of UiO MOFs than it does in the longer solvothermal batch synthesis.

As detailed in Chapter 1.1.3, acid modulators are used to increase the crystallinity of the UiO-67 product by reducing the synthesis rate through competing with the linkers to bind with the SBUs and reducing the rate deprotonation. In a solvothermal batch setting, varying the acid modulator used will not affect if a crystalline product is formed, as with synthesis times of ~24 hrs, even if the reaction is slower, it will still be completed within this time period. For microfluidic synthesis however, this choice of acid modulator is very important, as with reaction times of 30 minutes or less, an acid modulator that slows down the process too much and will result in an amorphous product being formed. This is why in the Journal of Porous Materials paper when there is no water present to speed up the formation an amorphous UiO-67 product is formed due to the reduced reaction rate from the benzoic acid. For the

final experimental paper however, crystalline UiO-67 is formed within the same time frame when using only HCl as the acid modulator. This necessity for longer reaction times/additives when using benzoic acid has been noted in work by Vo *et al*, in which the flow formation of UiO-67 through microfluidic heating was achieved with various acids (formic, propanoic and acetic) within 10 minutes of microwave heating.⁶

A challenge in this work that is not mentioned in other literature work is the boiling of solvents within the microfluidic reactor, with the gas bubbles formed causing variance in residence time. This was rectified through the attachment of a N₂ cylinder to the reactor and increasing the overall pressure by 1 bar, resulting in the bubbles disappearance. With the loss of these bubbles however came another problem, fouling of the tubing. These bubbles, while disruptive in terms of residence times, did help to ensure no reactants/products dropped out of the solution and stayed on the tubing, causing blockages or changes in product down the line. The formation of a larger CFIR unit as well as its subsequent combination with the smaller unit was performed to decrease this issue, with the increased tubing lengths allowing for higher flow rates while ensuring the residence time remained constant.

For the computational work, there were several difficulties. Firstly, a certain level of competence with MATLAB and an understanding of machine learning methods had to be achieved before work could begin. Once GBDT had been chosen as the ideal model type for this dataset, with neural networks and other methods tested before, it had to then be optimised by varying the parameters manually. Decisions had to be made to sacrifice some precision of the model to ensure its adaptability to new datapoints in the future. The model was found to perform poorly for weight percentage uptakes below 1.5% so many datapoints were sacrificed to ensure the model would perform accurately within a set range (1.5 – 74.2 wt%, 30 – 313 k, 0.1 – 100 bar).

7.3 Conclusions

Alongside the specific conclusions present in each paper, several more overarching conclusions can be drawn. Firstly, alongside reducing the synthesis time necessary and improving the product size distribution of MOF materials, the intrinsic properties of microfluidic synthesis may allow for new materials to be synthesised that are not possible in solvothermal batch settings, with the HCP/FCC-UiO-67-Benzoic acid product being a key example of this. Secondly, the transfer of literature batch processes to new microfluidic reactions can lead to various unexpected issues, as detailed in Chapter 8.2. These potential issues should be considered by future researchers if they decide to use microfluidics for their MOF synthesis. To expand from this, while the use of microfluidics may reduce the synthesis time from ~24 hrs to 30 minutes or below, the washing and drying times for these products are still extensive, usually at least involving being dried overnight. Until these backend parts of the synthesis are streamlined and optimised, the use of microfluidic synthesis for MOF materials would only be recommended for materials where the use of microfluidics is required for their development or results in a much more consistent product. If for that specific MOF material, a consistent product can be achieved through batch reactions, with no specific product benefits being seen in the microfluidic product, such as size consistency, crystal phase or surface area, then the batch reaction would be recommended, as it would avoid many issues that will need to be solved before microfluidic synthesis is possible.

7.4 Future Research

For future experimental work available there are several paths that could be investigated. Firstly, the microfluidic synthesis of a completely HCP-UiO-67-Benzoic Acid rather than a mixture of phases could be attempted, with an increased tubing length allowing for the flow rates necessary to avoid clogging being a necessity when increasing the concentration of water further. Using 3-5 CFIR units stacked on top of each other could provide the necessary tubing length to achieve this. The use of different acid modulators and the minimum times necessary for each UiO-67 product to be synthesised could also be investigated, providing the fastest synthesis possible for industrial users. In terms of industry, the parallel scale of up any synthesis performed within this work can be attempted, with many separate and

recombining CFIR units used to achieve this. The successful microfluidic growth of Pd(0) nanoparticles within the pores of UiO-67 can be further researched with its success providing a continuous pathway to supported Pd(0) nanoparticles on UiO-67-BPYDC. A potential approach to achieve this synthesis could be to use a stronger reducing agent, such as NH_3BH_3 , to break the N-Pd bonds that form. NH_3BH_3 has previously been used to form Pd(0) nanoparticles in UiO-67 in the literature,⁷ before weaker reducing agents were used.⁸

The procedures could be adapted to a new heating source, such as microwave heating or ultrasonic bath, could introduce new effects into the synthesis products or result in lower synthesis times being necessary. Ultrasonic baths have been used to synthesise various MOFs in both batch and flow systems, and have shown increased crystallisation rate within both, due to the acoustic cavitation which occurs through this process (collapse of bubbles resulting in high temperature and pressure hotspots in the solvent).⁹⁻¹⁵ These techniques can be applied to the experimental procedures established in this thesis, potentially reducing the necessary residence time or allowing new products to be formed.

Attempts to use microwave heating were attempted within this work and were unsuccessful, with the heating being too effective for a microfluidic reactor and the solvent boiling almost instantly. Introducing a water-cooling unit to constantly pump through cold water and absorb some of the microwaves may work to make this process viable. Using a much longer reactor may also rectify this issue, with the higher flow rates providing cooling for the solvent/reactant mixture. The formation of UiO MOFs in a microwave heated flow reactor by setting the modified microwave oven to a lower wattage (350W) has been achieved in the literature.¹⁶ However, lowering the wattage of a domestic microwave oven does not lower the output power, but instead lowers the average output power over a period, by introducing pauses when no heating will be occurring.¹⁷ These pauses will mean the reactor is not being consistently heated over the time period, but is instead being heated in short bursts. For a future researcher to be successful in implementing a microwave oven into their reactor it would either need to be water cooled as mentioned before or by modified in a way to control the power output of the synchrotron directly, using the method described by van der Merwe *et al.*¹⁷

For future computational work, there are two pathways that could be taken. Firstly, more experimental uptake data for previously synthesised MOFs can be collected to introduce into the database, improving the model's performance and prediction range. Alternatively, a new MOF material could have a gas uptake predicted in the model, before being synthesised and tested. If the predicted value and the experimental value match it could be used to validate the model's performance with new materials.

7.5 References

1. Volk, A. A., Campbell, Z. S., Ibrahim, M. Y. S., Bennett, J. A., Abolhasani, M. *Annu. Rev. Chem. Biomol. Eng.*, 2022, **13**, 45–72.
2. Ma, C., Zheng, L., Wang, G., Guo, J., Li, L., He, Q., Chen, Y., Zhang, H. *Aggregate*, 2022, **3**, 1–15.
3. Ermer, M., Mehler, J., Kriesten, M., Avadhut, Y. S., Schulz, P. S., Hartmann, M. *Dalt. Trans.*, 2018, **47**, 14426–14430.
4. Faustini, M., Kim, J., Jeong, G. Y., Kim, J. Y., Moon, H. R., Ahn, W. S., Kim, D. P. *J. Am. Chem. Soc.*, 2013, **135**, 14619–14626.
5. Schaate, A., Roy, P., Godt, A., Lippke, J., Waltz, F., Wiebcke, M., Behrens, P. *Chem. - A Eur. J.*, 2011, **17**, 6643–6651.
6. Vo, T. K., Quang, D. T., Song, M., Kim, D., Kim, J. *Microporous Mesoporous Mater.*, 2020, **306**, 110405.
7. Chen, L., Chen, H., Li, Y. *Chem. Commun.*, 2014, **50**, 14752–14755.
8. Chen, L., Chen, X., Liu, H., Li, Y. *Small*, 2015, **11**, 2642–2648.
9. Wu, H. Y., Wu, C. L., Liao, W., Matsagar, B. M., Chang, K. Y., Huang, J. H., Wu, K. C. W. *J. Mater. Chem. A*, 2023, **11**.
10. Masoomi, M. Y., Morsali, A., Junk, P. C. *RSC Adv.*, 2014, **4**, 47894–47898.
11. Tehrani, A. A., Safarifard, V., Morsali, A., Bruno, G., Rudbari, H. A. *Inorg. Chem. Commun.*, 2015, **59**, 41–45.
12. Karizi, F. Z., Safarifard, V., Khani, S. K., Morsali, A. *Ultrason. Sonochem.*, 2015, **23**, 238–245.
13. Haque, E., Khan, N. A., Park, J. H., Jhung, S. H. *Chem. Eur. J.*, 2010, **16**, 1046–1052.
14. Haque, E., Jhung, S. H. *Chem. Eng. J.*, 2011, **173**, 866–872.
15. Gordon, J., Kazemian, H., Rohani, S. *Microporous Mesoporous Mater.*, 2012, **162**, 36–43.
16. Vo, T. K., Le, V. N., Yoo, K. S., Song, M., Kim, D., Kim, J. *Cryst. Growth Des.*, 2019, **19**, 4949–4956.
17. van der Merwe, J. P., De Swardt, J. B. In *2017 IEEE AFRICON 2017*; 574–578.